Quantifying Impaired Metabolism following Acute Ischaemic Stroke using Chemical Exchange Saturation Transfer Magnetic Resonance Imaging

D. Phil. thesis, University of Oxford

Yunus K. Msayib

BEng, MSc

Lincoln College, Oxford

Quantifying Impaired Metabolism following Acute Ischaemic Stroke using Chemical Exchange Saturation Transfer Magnetic Resonance Imaging

D. Phil. thesis *University of Oxford*
Yunus K. Msayib Lincoln College

Trinity Term 2017

In ischaemic stroke a disruption of cerebral blood flow leads to impaired metabolism and the formation of an ischaemic penumbra in which tissue at risk of infarction is sought for clinical intervention. In stroke trials, therapeutic intervention has largely been based on perfusion-weighted measures, but these have not been shown to be good predictors of tissue outcome. The aim of this thesis was to develop analysis techniques for magnetic resonance imaging (MRI) of chemical exchange saturation transfer (CEST) in order to quantify metabolic signals associated with tissue fate in patients with acute ischaemic stroke. This included addressing robustness for clinical application, and developing quantitative tools that allow exploration of the *in-vivo* complexity.

Tissue-level analyses were performed on a dataset of 12 patients who had been admitted to the John Radcliffe Hospital in Oxford with acute ischaemic stroke and recruited into a clinical imaging study. Further characterisation of signals was performed on stroke models and tissue phantoms.

A comparative study of CEST analysis techniques established a model-based approach, Bloch-McConnell model analysis, as the most robust for measuring pH-weighted signals in a clinical setting. Repeatability was improved by isolating non-CEST effects which attenuate signals of interest. The Bloch-McConnell model was developed further to explore whether more biologically-precise quantification of CEST effects was both possible and necessary. The additional model complexity, whilst more reflective of tissue biology, diminished contrast that distinguishes tissue fate, implying the biology is more complex than pH alone. The same model complexity could be used reveal signal patterns associated with tissue outcome that were otherwise obscured by competing CEST processes when observed through simpler models.

Improved quantification techniques were demonstrated which were sufficiently robust to be used on clinical data, but also provided insight into the different biological processes at work in ischaemic tissue in the early stages of the disease. The complex array of competing processes in pathological tissue has underscored a need for analysis tools adequate for investigating these effects in the context of human imaging. The trends herein identified at the tissue level support the use of quantitative CEST MRI analysis as a clinical metabolic imaging tool in the investigation of ischaemic stroke.

In the name of God, The Beneficent, The Merciful

This is a mercy from my Lord

The Glorious Qur'an – [1:1] and [18:98]

To my family.

Acknowledgements

I am indebted to a number of individuals for their help and support in the writing of this thesis. In particular I must thank my supervisor, Professor Michael Chappell, for his guidance and generous support over the duration of my research degree. I have benefited enormously from his knowledge and wisdom. I am also grateful to my clinical advisor, Professor James Kennedy, for the guiding clinical insight he has provided during the course of this work.

To the team at the Centre for Doctoral Training (CDT) in Healthcare Innovation I am grateful, especially to the CDT Director Professor Vicente Grau for facilitating my research through this programme, and enabling me to disseminate this work at relevant conferences and workshops. I would also like to thank the previous Director of the CDT, Professor Gari Clifford, and Professor Chappell, for admitting me onto the CDT from which my research has benefited immensely. I am grateful to Ms Jo Armitage for her thoughtful assistance with administrative matters and conference arrangements.

I have received valuable input from colleagues involved with the AMICI imaging study. Specifically, I would like to express my thanks to Dr George Harston, Professor Peter Jezzard, and Dr Thomas Okell. I am indebted to Dr Harston for providing meticulously-defined masks of normal and pathological tissue, used for analysing the clinical data. I gratefully acknowledge the helpful feedback Dr Harston provided in relation to Chapter 5 and Chapter 6. For the work in Chapter 8 and Chapter 9, I am indebted to Kevin Ray for supplying high-field preclinical and phantom datasets. When I embarked on this project I inherited a rich set of analysis tools which were developed by Professor Chappell and Dr Yee Kai Tee; I am grateful for these foundational technical contributions which enabled me to explore a greater breadth of questions in the time I that had than I otherwise could have. I would also like to thank my D. Phil. examiners, Professor Penny Gowland and Professor Stephen Payne, for their thoughtful consideration of this work and informative feedback.

I would like to express my thanks to Mr Ian Kemp and to my lecturers at The University of Manchester; Professor Trevor York, Mr Peter Green, and Professor Patrick Gaydecki, who afforded me exceptional support and opportunities for advancing my academic aspirations as an undergraduate. I am deeply grateful to Professor Gaydecki for taking me on as a Research Assistant in the Signal Processing group for one year during my undergraduate degree. I would like to thank Professor Payne for subsequently admitting me onto the Master's programme in Biomedical Engineering.

Finally, I would like to thank my family for their support and encouragement. I am grateful for my parents' lifelong inspiration and backing.

This work was financially supported by the Engineering and Physical Sciences Research Council (EPSRC) through the Research Councils UK (RCUK) Digital Economy Programme[1].

[1]Grant number EP/G036861/1 (Oxford Centre for Doctoral Training in Healthcare Innovation).

Abbreviations

ADC	apparent diffusion coefficient
AMICI	Acute Magnetic Resonance Imaging in Cerebral Ischaemia
ANOVA	analysis of variance
APT	amide proton transfer
APTR	APT ratio
APTR*	apparent APT ratio
AREX	apparent exchange dependent relaxation
ASL	arterial spin labelling
ATP	adenosine triphosphate
AVIC	Acute Vascular Imaging Centre
BALB/c	a laboratory-bred strain of house mouse
BayCEST	Bayesian CEST analysis tool
`bet`	brain extraction tool
BM	Bloch-McConnell
BMM	Bloch-McConnell model
BOLD	blood oxygen level dependent
BSA	bovine serum albumin
CBF	cerebral blood flow
CEST	chemical exchange saturation transfer
CI	confidence interval
CNAWM	contralateral normal-appearing white matter
CNR	contrast-to-noise ratio
CO	contralateral
CSF	cerebrospinal fluid
CoV	coefficient of variation
DOF	degrees of freedom
DS	direct saturation
DWI	diffusion-weighted image
EEG	electroencephalogram
EDS	evenly-distributed sampling

EMR	extrapolated semisolid MT reference
EPI	echo planar imaging
FA	flip angle
`fabber`	fast ASL and BOLD Bayesian estimation routine
`fast`	FMRIB automatic segmentation tool
FE	frequency encoding
FFE	fast field echo
FGE	fast gradient echo
FID	free induction decay
FLAIR	fluid-attenuated inversion recovery
`flirt`	FMRIB linear image registration tool
FMRIB	Oxford Centre for Functional MRI of the Brain
FOV	field of view
FSL	FMRIB Software Library
FT	Fourier transform
FWER	family-wise error rate
FWHM	full-width half-maximum
GE	gradient echo
GM	grey matter
HWHM	half-width half-maximum
IC	ischaemic core
IQR	interquartile range
IR	inversion recovery
LDA	Lorentzian difference analysis
LLA	local linear approximation
LMM	large mobile macromolecule
MCAO	middle cerebral artery occlusion
MP-RAGE	magnetisation-prepared rapid gradient echo
MR	magnetic resonance
MRI	magnetic resonance imaging
MRS	magnetic resonance spectroscopy
MT	magnetisation transfer
MTR	magnetisation transfer ratio

MVN	multivariate normal
NIHSS	National Institutes of Health Stroke Scale
NMR	nuclear magnetic resonance
NOE	nuclear Overhauser effect
NOER	NOE ratio
NOER*	apparent NOE ratio
NOESY	NOE spectroscopy
paLDA	post-acquisition Lorentzian difference analysis
PC	phosphatidylcholine
pCASL	pseudo-continuous arterial spin labelling
PD	proton density
PE	phase encoding
PET	positron emission tomography
PDM	perfusion-diffusion mismatch
ppm	parts per million
PV	partial volume
PVc	PV correction or PV-corrected
PVE	PV estimate
PWI	perfusion-weighted image
RF	radiofrequency
RMS	root mean square
ROI	region of interest
rtPA	recombinant tissue plasminogen activator
SAR	specific absorption rate
SD	standard deviation
SE	spin echo
Semi-OSS	semi-optimal sampling scheme
semisolidR*	apparent semisolid effects ratio
SNR	signal-to-noise ratio
SS	slice selection
TE	echo time
TR	repetition time
VB	variational Bayes
WASSR	water saturation shift referencing
WM	white matter

Publications arising from this thesis

Conference abstracts

Y. Msayib, G. W. J. Harston, Y. K. Tee, F. Sheerin, N. P. Blockley, T. W. Okell, P. Jezzard, S. Payne, J. Kennedy, and M. A. Chappell, "Repeatability study of APT CEST quantification techniques for identification of ischaemic penumbra in stroke", *Proceedings of the 25th ISMRM Annual Meeting and Exhibition*, vol. 25, no. 3752, 2017.

Y. Msayib, G. W. J. Harston, K. J. Ray, J. R. Larkin, B. A. Sutherland, F. Sheerin, N. P. Blockley, T. W. Okell, P. Jezzard, A. Baldwin, N. R. Sibson, J. Kennedy, and M. A. Chappell, "Downfield CEST signals of the ischaemic core in quantitative imaging of hyperacute stroke", ESMRMB 2017, 34th Annual Scientific Meeting, *Magnetic Resonance Materials in Physics, Biology and Medicine*, vol. 30, no. 447, 2017.

Y. Msayib, G. W. J. Harston, Y. K. Tee, N. P. Blockley, T. W. Okell, S. Payne, P. Jezzard, J. Kennedy, , and M. A. Chappell, "Assessing the suitability of common NOE modelling approximations in quantitative imaging of hyperacute stroke", ESMRMB 2015, 32nd Annual Scientific Meeting, *Magnetic Resonance Materials in Physics, Biology and Medicine*, vol. 28, no. 442, pp. 277-418, 2015.

P. L. Croal, **Y. Msayib**, K. J. Ray, J. R. Larkin, B. A. Sutherland, G. W. J. Harston, A. Buchan, P. Jezzard, J. Kennedy, N. R. Sibson, and M. A. Chappell, "Clinically feasible model-based analysis of amide proton transfer MRI in acute ischaemic stroke", *Proceedings of the Joint Annual Meeting ISMRM–ESMRMB*, no. 358, 2018.

P. L. Croal, **Y. Msayib**, K. J. Ray, M. Craig, and M. A. Chappell, "QuantiCEST: Bayesian model-based analysis of CEST MRI", *Proceedings of the Joint Annual Meeting ISMRM–ESMRMB*, no. 4803, 2018.[1]

[1] QuantiCEST is a visual tool that provides the quantitative CEST analysis methods used in this thesis. It is available within the Quantiphyse biomedical image analysis suite, at www.quantiphyse.org.

P. L. Croal, K. J. Ray, **Y. Msayib**, J. R. Larkin, B. A. Sutherland, G. W. J. Harston, A. Baldwin, A. M. Buchan, P. Jezzard, J. Kennedy, N. R. Sibson, and M. A. Chappell, "Model-based analysis of partial z-spectra for rapid quantification of amide proton transfer MRI", *Proceedings of the 25th ISMRM Annual Meeting and Exhibition*, vol. 25, no. 3779, 2017.

G. W. J. Harston, Y. K. Tee, N. P. Blockley, **Y. Msayib**, F. Sheerin, P. Mathieson, I. Reckless, K. Shah, U. Schulz, S. Payne, P. Jezzard, M. A. Chappell, and J. Kennedy, "Novel imaging of protein integrity to better define ischemic injury after stroke", *Stroke*, vol. 47, no. 63, 2016.

Workshop abstracts

Y. Msayib, G. W. J. Harston, F. Sheerin, N. P. Blockley, T. W. Okell, P. Jezzard, J. Kennedy, and M. A. Chappell, "Separating NOEs and semisolid MT in quantitative imaging of hyperacute stroke", Music City International CEST Symposium. Vanderbilt University, Nashville, TN. August 2017.

G. W. J. Harston, D. Carone, **Y. Msayib**, A. Baldwin, M. A. Chappell, and J. Kennedy, "Identifying cerebral injury in acute stroke using metabolic imaging biomarkers", National Institute for Health Research Stroke Research Workshop, Clare College, Cambridge, September 2017.

Contents

List of Figures

List of Tables

Chapter 1

Introduction

1.1 Stroke background

STROKE is a pathology associated with rapid loss of brain function due to a sudden disruption of cerebral blood flow (CBF), caused by haemorrhage or ischaemia. Haemorrhagic stroke is the result of internal bleeding into or around the brain. Ischaemic stroke is caused by a vascular occlusion, usually with a clot, and comprises 85% of stroke cases [1,2].

Stroke is the third largest cause of death in the UK after heart disease and cancer, with an annual incidence of approximately 161, 000 of which one in five leads to a fatality [2–4]. There are approximately 1.2 million stroke survivors living in the UK with half living dependent on others for day-to-day activities, making stroke the largest single cause of severe adult disability in the UK [2,5,6]. It is estimated that the annual cost of stroke to the UK economy is around £9 billion, and accounts for 5% of the National Health Service (NHS) budget [7].

1.2 Pathophysiology of acute ischaemic stroke

The energy needs of healthy brain tissue are met almost exclusively by the oxidation of glucose, for which the oxygen supply is provided through CBF [8]. CBF is impeded

in ischaemic stroke, reducing oxygen supply and thereby impairing energy production. This first impairs functional activity of the brain, followed, at a more severe degree of hypoxia, by the suppression of metabolic activity that is required to maintain the structural integrity of cells [8]. The final stage is cerebral infarction, defined as brain cell death due to prolonged ischaemia [8].

In focal ischaemia (confined to a certain region of the brain), brain functions break down over a wide range of CBF levels [8]. The metabolic disturbances leading up to infarction proceed as follows (Fig. 1.1) [8]. Protein synthesis becomes inhibited to half its capacity by a CBF of about 0.55 ml/g/min, and is completely suppressed below 0.35 ml/g/min. Below this level of CBF, anaerobic glycolysis is stimulated, which is a process that transforms glucose into energy in the presence of a limited supply of oxygen. Glucose utilisation temporarily increases, before sharply declining when CBF decreases below 0.25 ml/g/min. This range corresponds to the beginning of acidosis and the subsequent accumulation of lactate byproducts. Tissue acidosis becomes very pronounced at CBF rates below 0.26 ml/g/min, and adenosine triphosphate (ATP), the predominant source of energy in the cell, begins to decline [8,9]. The breakdown of energy state occurs at about 0.20 ml/g/min. The first change in functional disturbance is the suppression of brain activity when observed through an electroencephalogram (EEG), occurring between 0.15–0.23 ml/g/min. The progressive and uncontrollable depolarisation of cell membranes, anoxic depolarisation, occurs below 0.15 ml/g/min [8]. Cerebral infarction progresses to surrounding cells if no intervention is taken [10].

In the acute phase of stroke, tissue injury is a direct consequence of energy failure and cell depolarisation, generally happening within the first few minutes of stroke [10]. The sub-acute phase starts with anoxic depolarisation, where there is a spreading depolarisation occurring through tissue. Cell death in the sub-acute phase is preceded by impaired metabolism and the formation of an ischaemic penumbra where tissue at risk of infarction is sought for clinical intervention. If timely reperfusion does not occur the infarct core expands into peri-infarct penumbra. The largest increment in infarct

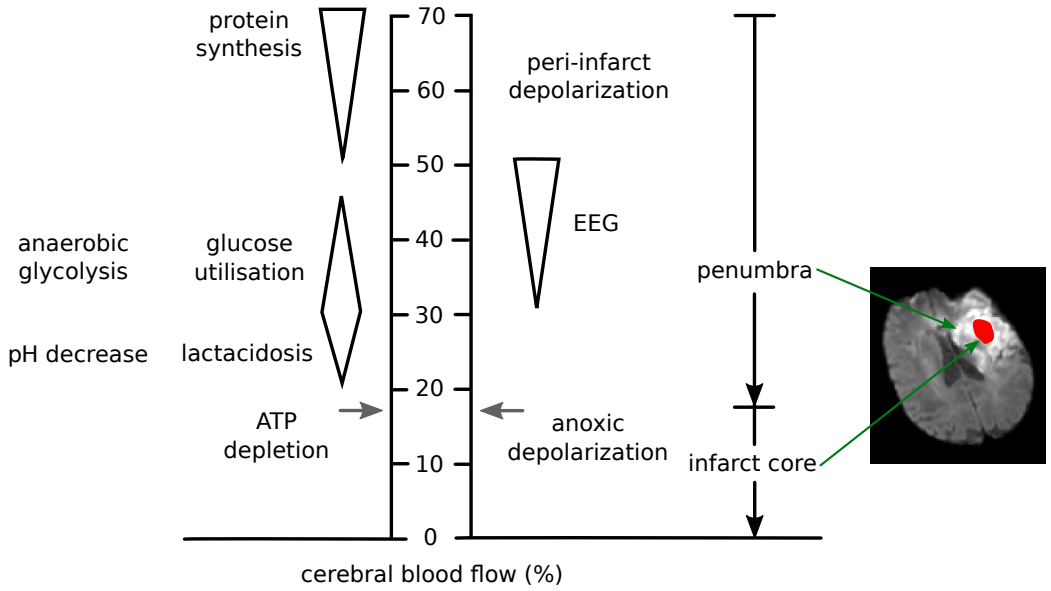

Figure 1.1: Thresholds of metabolic (left axis) and electrophysiological (right axis) disturbances which precipitate tissue infarction during a graded reduction in CBF. A stroke patient diffusion-weighted image is used to illustrate the penumbra; a region of reduced blood supply in which energy state is preserved, and the infarct core; a region in which blood flow decreases below the threshold of energy failure. Adapted from refs. [8,10].

volume can be seen during this phase [10]. The primary clinical objective is to restore adequate perfusion to the brain within a time window of three to 4.5 hours of symptom onset [11]. The third phase is the delayed phase of injury, which may last for days or weeks, mediated by secondary phenomena such as inflammation, oedema, and reperfusion injury [10].

1.3 Stroke treatment and its challenges

The main early treatment option for ischaemic stroke is to thrombolyse the clot by intravenously administering recombinant tissue plasminogen activator (rtPA) [12]. Thrombolysis has been shown to have overall benefit when administered within the first 3–4.5 hours after onset of symptoms [12,13]. This is in an attempt to salvage at-risk penumbral tissue, the classical definition of which is a region of tissue around the ischaemic core that is hypoperfused and metabolically stressed [14–16]. Treatment rates with intravenous rtPA are low, at approximately 5% of stroke patients [11], and the main ob-

stacle that prevents wider clinical use of thrombolysis is the restrictive therapeutic time window [12]. Medical contraindications and complexity in determining eligibility criteria also contribute to this [10,11,17]. The main complication risk is intracranial haemorrhaging which increases significantly with the administration of thrombolytic therapy [10]. Mechanical removal of the thrombus using a catheter (mechanical thrombectomy) is an alternative treatment with a therapeutic window of six hours, which has been recently commissioned by the NHS [18]. In most cases of ischaemic stroke CBF improves over time. Recanalisation of the vascular occlusion is observed in half of stroke patients within four days after stroke, but often reperfusion is initiated at too late a stage to reverse ischaemic injury [8]. In treating stroke a time-critical assessment and treatment decision must therefore be made—"time is brain", and brain tissue is rapidly lost (1.9 million neurons per minute) as the disease progresses [19].

1.4 MR imaging of ischaemic stroke

1.4.1 Perfusion-diffusion mismatch

Magnetic resonance imaging (MRI) of the mismatch between intracranial diffusion and perfusion is used to assist treatment decisions by defining the ischaemic penumbra [20]. Metabolic disturbances in focal ischaemia drive water from the extracellular space into intracellular space. The decrease in fluid volume of the extracellular compartment can be detected through diffusion-weighted imaging (DWI), used to help delineate the ischaemic core [21]. Perfusion-weighted images (PWI) quantify the adequacy of blood perfusion to tissue, with at-risk penumbral tissue being hypoperfused [20]. Subtraction of the two images yields a PWI-DWI mismatch (PDM) image which is used to characterise the quantity of potentially salvageable penumbral tissue [20]. The modern concept of the ischaemic penumbra is illustrated in Fig. 1.2. This may be useful in helping to identify patients who will benefit from recanalisation of the occluded artery using thrombolysis, and may extend the time window for treatment [13].

In stroke trials, therapeutic intervention has largely been based on perfusion-weighted measures, but these have not been shown to be good predictors of tissue outcome [20]. PDM was thought to delineate the ischaemic penumbra in stroke patients, however it is not clear which areas of PDM mismatch are simply benign oligaemia (hypoperfused but not at risk of infarction), or are viable but at risk of subsequent infarction if early thrombolytic intervention is not administered. PWI overestimates the ischaemic penumbra and alone is not a good predictor of tissue fate, reflected in clinical results where final lesion size is normally smaller than the apparent perfusion deficit. Two hours after vascular occlusion the threshold of the rise in signal intensity on DWI is 0.41 ml/g/min. This threshold is distinctly higher than the thresholds of energy failure, indicating that the DWI lesion is larger than the infarct core and includes parts of the peri-infarct penumbra [8,22]. DWI thus also overestimates the infarct core [20]. PDM does not, therefore, optimally define the ischaemic penumbra, and PDM alone has been found not to be a good predictor of tissue outcome for making treatment decisions [15,20,23].

1.4.2 Metabolic imaging

There is evidence that cell pH dynamics are related to ischaemic damage [24]. During ischaemic oxygen depletion, metabolism in underperfused tissue is sustained for a short period of time by anaerobic glycolysis which produces acidic lactate byproducts. Without timely reperfusion, cells ultimately depolarise and are recruited into the infarct core. The accumulation of lactate leads to a decrease in the intracellular pH, which is a physiological change that can be observed through metabolic imaging [10]. Measurement of metabolites and metabolic reactions has typically been the preserve of positron emission tomography (PET) imaging, which, in stroke studies, has traditionally been the modality of choice for metabolic imaging [25]. MRI does not involve ionising radiation but there are few MRI-based alternatives to PET for metabolic imaging [25]. Blood oxygen level dependent (BOLD) techniques generate a signal based on the differences in mag-

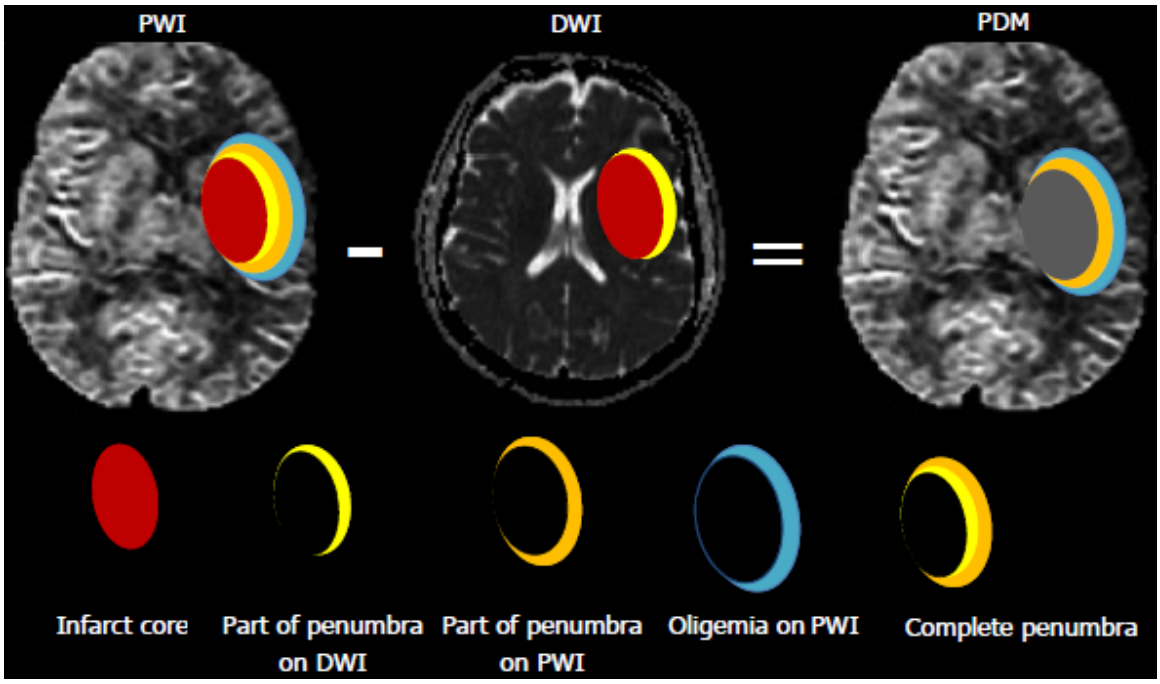

Figure 1.2: Modern concept of the ischaemic penumbra, reproduced from ref. [20] with permission from Baishideng Publishing Group. The presenting DWI scan shows the ischaemic core and part of the penumbra. Perfusion deficiency on the PWI scan includes the infarct core, part of the penumbra, and benign oligaemia. The PWI-DWI mismatch image does not optimally identify the ischaemic penumbra.

netic susceptibility between oxyhaemoglobin and deoxyhaemoglobin [25,26]. BOLD techniques can be impractical as they often require gaseous stimuli for meaningful calibration and they rely heavily on the perfusion of blood [25]. MR spectroscopy (MRS) has been used to provide detailed information about molecular profiles and metabolism within individual voxels [25]. However, MRS can only sample relatively large volumes (*ca*. 1 cm^3) in humans which does not give sufficient spatial resolution to be used in a clinically meaningful way [25,27]. Phosphorus MRS has been used to investigate the metabolism of human stroke within single voxels, providing information on pH and the concentrations of phosphorous metabolites, but without spatial resolution [25]. Hydrogen MRS has been used in stroke studies with some spatial resolution (*ca*. 1 cm^3) to detect lactate, which appears after an infarct, and has been observed before and after changes on DWI [25,28].

MRI of chemical exchange saturation transfer (CEST) is a relatively recent technique which allows indirect measurement of chemical groups by exploiting the chemical ex-

change of spin magnetization between metabolites and water [29,30]. This offers a way of measuring metabolites using MRI but with a resolution comparable to perfusion MRI measures, and at millimolar concentrations [31]. CEST images achieve contrast endogenously, have good resolution (*ca.* 0.06 cm^3), can be acquired in under three minutes, and do not require specialised hardware (such as the phosphorous coils used in phosphorous MRS). The last decade has seen the development of many *in-vivo* CEST contrast mechanisms for investigating a variety of labile macromolecules and metabolites which have previously been undetectable using MRI due to their low concentrations [32,33]. Amide proton transfer (APT) imaging, where contrast originates from backbone amide protons of mobile proteins and peptides within cells, is the most developed of the endogenous CEST contrast modes [34,35]. Quantification of amide proton chemical exchange rates in brain tissue has been used to measure pH-related changes associated with impaired metabolism and cell death, as the chemical exchange rate is dependent on intracellular pH [36]. APT CEST has been used in clinical studies for generating pH-weighted maps of brain tissue, with findings suggesting that it may have a role in improving imaging definition of penumbral tissue in patients with acute ischaemic stroke [37]. CEST MRI is highly flexible as a metabolic imaging tool as a single acquisition can capture spectral information from a range of hydrogen-bound chemical groups, which have not been explored in detail in the context of tissue fate following stroke [34,38]. Information on tissue metabolism that may be afforded through CEST imaging could provide insights on tissue outcome by highlighting cell death pathways on different timescales, thus potentially enabling discrimination of tissue at risk.

1.5 Thesis aim

The aim of this thesis was to develop analysis techniques for CEST MRI data in order to quantify metabolic signals associated tissue fate in patients with acute ischaemic stroke. This included addressing the need for robustness and repeatability for clinical

application, and developing quantitative tools that exploit competing CEST processes and enable exploration of the *in-vivo* complexity.

1.6 Thesis outline

The theoretical background to MR imaging of CEST is developed in Chapter 2. In Chapter 3 a literature review of quantification techniques, and the application of CEST imaging to ischaemic stroke, is presented and used to set up the research direction pursued in this thesis. The general methods used for data collection and analysis are outlined in Chapter 4.

This thesis first sets out to address the question of robustness of CEST analysis techniques for clinical application, commencing with a comparative study of analysis techniques in Chapter 5 whereat the Bloch-McConnell model analysis technique was identified as the most repeatable measure of CEST signals. The Bloch-McConnell model analysis technique was extended in Chapter 6 to explore whether more biologically-precise quantification was both possible and necessary in as far as its clinical utility. This was followed with the implementation of a quantification technique, in Chapter 7, that sought to correct for the effects of tissue partial volumes and thereby to effect more robust measurement.

Competing CEST processes, and their association with tissue outcome, were explored in Chapter 8 using the extended Bloch-McConnell model. Animal stroke models and tissue-mimicking phantoms were used to inform a discussion on the biophysical characteristics of CEST processes. In Chapter 9, this approach was refined for a specific subset of signals which were revealed through prior analyses. A summary of the main findings of this thesis is presented in Chapter 10, along with a discussion of study limitations and areas of future work.

Chapter 2

Theoretical framework

MAGNETIC resonance imaging (MRI) uses the natural magnetic properties of tissue in order to construct detailed images of their structure and composition, exploiting the large abundance of hydrogen atoms tissue [39]. The principles of nuclear magnetic resonance (NMR) underlie MRI and are discussed first. The behaviour of a single proton in the presence of a static magnetic field is explored, then extended to an ensemble of protons. Image formation by spatial encoding of the NMR signal is then introduced, followed by a discussion of MRI pulse sequences. The CEST mechanism is presented in the final section, along with CEST MRI pulse sequences relevant to this thesis.

2.1 Nuclear magnetic resonance

2.1.1 Quantum mechanical description

The theory developed in this section is based on ref. [26]. Atomic nuclei exhibit an intrinsic angular momentum called spin, represented by the vector **J**. The magnitude of the spin angular momentum is given by

$$|\mathbf{J}| = \hbar\sqrt{I(I+1)} \tag{2.1}$$

where $\hbar$ is the reduced Planck constant, and I is the spin quantum number associated with the spin angular momentum. Depending on the composition of the nucleus in terms of elementary particles, the value of I can be zero, a half-integer, or an integer. Net nuclear spin ($I > 0$) is required for NMR. A nucleus with spin quantum number I gives rise to $2I+1$ energy levels in the presence of an external magnetic field, where the individual energy levels are described by the quantum number $m_I = \{-I, -I+1, ..., I-1, I\}$. The quantum number m_I describes the discrete orientation of the spin angular momentum. For an external magnetic field applied along the z-axis, $B_0\hat{\boldsymbol{z}}$, the z-component of $\mathbf{J}$ is given by

$$J_z = m_I\hbar \tag{2.2}$$

In MRI the primary nucleus of interest is that of hydrogen (^{1}H) owing to its high level of natural abundance in biological tissue [39]. The hydrogen nucleus is composed of a single proton, for which $I = \frac{1}{2}$, and there are two energy levels or spin states: $m_I = \pm\frac{1}{2}$. Therefore, by equation (2.2), there are two possible orientations of J_z, corresponding to $J_z = \pm\hbar/2$. This is referred to as a spin-$\frac{1}{2}$ (spin-half) system, where $m_I = +\frac{1}{2}$ corresponds to a spin orientation parallel to B_0 ('spin-up', or α state), and $m_I = -\frac{1}{2}$ corresponds to a spin orientation anti-parallel to B_0 ('spin-down', or β state).

Classically, the hydrogen nucleus can be viewed as a rotating charged sphere, thus it also possesses a magnetic dipole moment $\boldsymbol{\mu}$. The magnetic dipole moment is related to the spin angular momentum via a nucleus-specific proportionality constant γ, referred to as the gyromagnetic ratio ($\gamma = 42.57$ MHz/T for ^{1}H):

$$\boldsymbol{\mu} = \gamma\mathbf{J} \tag{2.3}$$

The z-component of $\boldsymbol{\mu}$ is given by $\mu_z = \gamma\hbar m_I$ using equation (2.2). In the presence of the external magnetic field $B_0\hat{\boldsymbol{z}}$, the nucleus acquires energy $E = -\mu_z B_0$. Substituting for μ_z shows that each spin state will have a distinct energy level: $E_{+\frac{1}{2}} = -\gamma\hbar B_0$ for the parallel spin state (lower energy state), and $E_{-\frac{1}{2}} = +\gamma\hbar B_0$ for the anti-parallel orientation. The

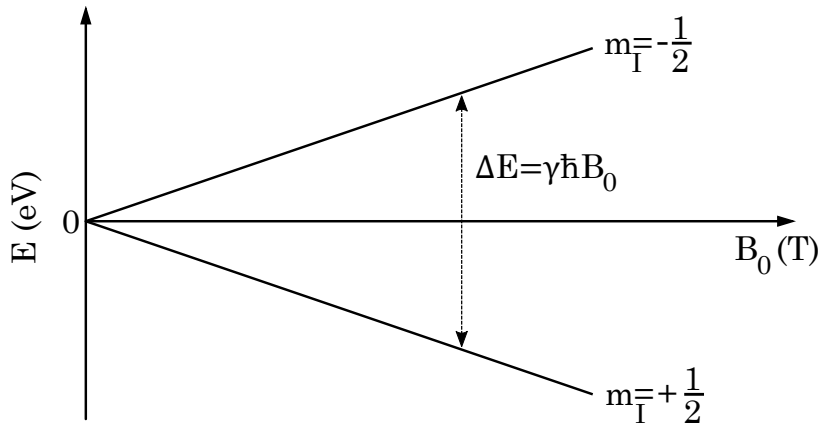

Figure 2.1: Zeeman splitting of ^{1}H. In the absence of an external magnetic field the energy levels of the two spin states are equal. When an external magnetic field is applied, the spin states exhibit distinct energy levels, with the difference ΔE being proportional to B_0.

separation of energy levels in the presence of a magnetic field is known as Zeeman splitting (Fig. 2.1). The difference between the two energy levels is:

$$\Delta E = \gamma \hbar B_0 \tag{2.4}$$

ΔE is directly proportional to the applied magnetic field, and therefore in the absence of B_0, no splitting of energy levels occurs. ΔE corresponds to the energy that can be absorbed or emitted by the spin system (inducing transitions between the spin states), and when expressed in terms of frequency, is known as the Larmor frequency ω_0:

$$\omega_0 = 2\pi f_0 = \gamma B_0 \tag{2.5}$$

The Larmor frequency for ^{1}H is 127.7 MHz at 3 T, 298.0 MHz at 7 T, and 400.2 MHz at 9.4 T. Equation (2.4) applies to a single nuclear spin. In a typical MRI voxel of $2 \times 2 \times 3$ mm there are on the order of 8×10^{20} protons (a single volume of spins can be referred to as an isochromat). The Boltzmann distribution describes the population ratio of energy levels of the protons at thermal equilibrium:

$$\frac{N_{-\frac{1}{2}}}{N_{+\frac{1}{2}}} = e^{-\Delta E/kT} \tag{2.6}$$

where $N_{-\frac{1}{2}}$ and $N_{+\frac{1}{2}}$ are the number of spins in the spin-up and spin-down orientations respectively, k is the Boltzmann constant (1.38×10^{-23} J/K), and T is the temperature in Kelvin. In the high temperature limit, $\Delta E \ll kT$, and equation (2.6) can be approximated by a first-order Taylor expansion:

$$\frac{N_{-\frac{1}{2}}}{N_{+\frac{1}{2}}} \approx 1 - \frac{\gamma\hbar B_0}{kT} \tag{2.7}$$

The total number of spins is given by $N = N_{+\frac{1}{2}} + N_{-\frac{1}{2}} \approx 2N_{+\frac{1}{2}}$, and therefore the population difference, n, using equation (2.7) is

$$n = N_{+\frac{1}{2}} - N_{-\frac{1}{2}} = \frac{N_{+\frac{1}{2}}\gamma\hbar B_0}{kT} \approx \frac{N\gamma\hbar B_0}{2kT} \tag{2.8}$$

The net equilibrium magnetisation within a voxel ($\mathbf{M_0} = M_0\hat{\boldsymbol{z}}$) will have a magnitude proportional to the number of spins (n) and the magnetic moment of each spin (μ_z): $M_0 = n\mu_z$. Substituting for n and μ_z yields:

$$M_0 = \frac{N(\gamma\hbar)^2 B_0}{4kT} \tag{2.9}$$

In the absence of an external magnetic field ($B_0 = 0$), the magnetic dipoles are oriented randomly and there is zero net equilibrium magnetisation ($M_0 = 0$, Fig. 2.2a). In the presence of a magnetic field, there is a slightly higher proportion of spins aligned parallel to the field (equation 2.8), and therefore voxels exhibit a net equilibrium magnetisation ($M_0 > 0$, Fig. 2.2b). Equation 2.9 indicates that net magnetisation (and hence the signal-to-noise ratio, SNR) is proportional to B_0.

2.1.2 Classical description

The theory developed in this section is based on ref. [26]. A classical description of what is a quantum excitation and relaxation process is used hereon, and is sufficient when describing the macroscopic net magnetisation of an ensemble of ^{1}H nuclei [40]. The

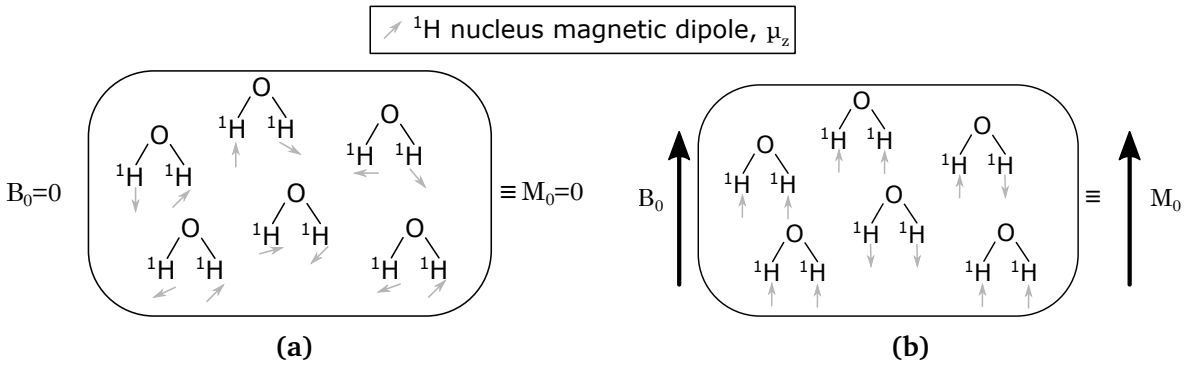

Figure 2.2: Illustration of magnetic dipoles in the presence of an external magnetic field, shown for a small volume of water. **(a)** In the absence of an external magnetic field B_0, the magnetic dipoles $\boldsymbol{\mu}$ of the nuclear spins are randomly-oriented and there is no net magnetisation. **(b)** In the presence of an external magnetic field the individual dipoles line up, with a small majority in parallel (as opposed to anti-parallel), to give a net equilibrium magnetisation within the tissue of M_0.

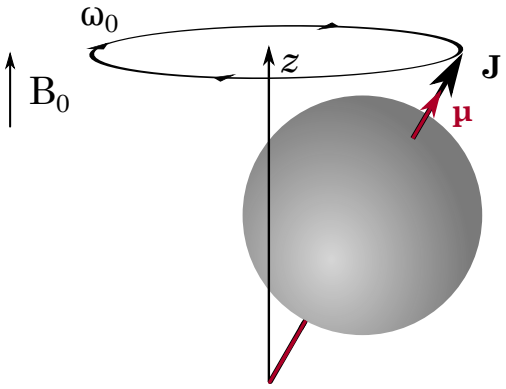

Figure 2.3: Classical representation of spin angular momentum **J** and associated magnetic dipole $\boldsymbol{\mu}$. In the presence of a static magnetic field $B_0\hat{\boldsymbol{z}}$, the torque exerted on $\boldsymbol{\mu}$ causes **J** to precess about the axis of B_0 (defined as the z-axis), at the Larmor frequency $\omega_0 = \gamma B_0$ [26,41].

magnetic moment $\boldsymbol{\mu}$, when placed in an external static magnetic field **B**, will experience a torque $\boldsymbol{\mu} \times \mathbf{B}$:

$$\frac{d\mathbf{J}}{dt} = \boldsymbol{\mu} \times \mathbf{B} \tag{2.10}$$

For $\mathbf{B} = (0, 0, B_0)$, the spin angular momentum **J** associated with $\boldsymbol{\mu}$ (equation 2.3) will precess about B_0, as illustrated in Fig. 2.3. This can be expressed in terms of net magnetisation $\mathbf{M} = (M_x, M_y, M_z)$ using equation (2.3) and that $\mathbf{M} \propto \boldsymbol{\mu}$:

$$\frac{d\mathbf{M}}{dt} = \gamma \mathbf{M} \times \mathbf{B} \tag{2.11}$$

The individual vector components of equation (2.11) are, for this case of **B**:

$$\begin{aligned}\frac{d\mathrm{M}_x(t)}{dt} &= \omega_0 \mathrm{M}_y(t) \\ \frac{d\mathrm{M}_y(t)}{dt} &= -\omega_0 \mathrm{M}_x(t) \\ \frac{d\mathrm{M}_z(t)}{dt} &= 0\end{aligned} \tag{2.12}$$

M exhibits a torque from B_0 which causes it to precess about the axis of B_0. The angular frequency at which **M** precesses about $\hat{\boldsymbol{z}}$ is the Larmor frequency, $\omega_0 = \gamma \mathrm{B}_0$, corresponding to the resonance frequency defined in equation (2.5). When the external magnetic field **B** is simply described by a static field B_0 along z, this yields a constant magnetisation component along $\hat{\boldsymbol{z}}$, $\mathrm{M}_z(t) = \mathrm{M}_0$, with $\mathrm{M}_x(t)$ and $\mathrm{M}_y(t)$ rotating in the xy plane at frequency ω_0. This is illustrated in Fig. 2.4. In particular, for an initial magnetisation of $\mathbf{M}(t=0) = (\mathrm{M}_x^0,\ \mathrm{M}_y^0,\ \mathrm{M}_z^0)$ and assuming an initial phase shift of zero in the xy plane:

$$\begin{aligned}\mathrm{M}_z(t) &= \mathrm{M}_0 \\ \mathrm{M}_x(t) &= \mathrm{M}_{xy}(0)\cos(\omega_0 t) \\ \mathrm{M}_y(t) &= -\mathrm{M}_{xy}(0)\sin(\omega_0 t) \\ \mathrm{M}_{xy}(0) &= \sqrt{\mathrm{M}_x(0)^2 + \mathrm{M}_y(0)^2}\end{aligned} \tag{2.13}$$

2.1.3 RF excitation and the rotating frame

Thus far the only external magnetic field that has been considered is a uniform B_0 in the $\hat{\boldsymbol{z}}$ direction, which results in a net equilibrium magnetisation M_0 in the tissue along $\hat{\boldsymbol{z}}$. Tilting **M** away from the z-axis is done by applying an RF field $\mathrm{B}_x(t)$ along $\hat{\boldsymbol{x}}$ and $\mathrm{B}_y(t)$ along $\hat{\boldsymbol{y}}$ as follows:

$$\begin{aligned}\mathrm{B}_x(t) &= \mathrm{B}_1 \cos(\omega_{\mathrm{RF}} t) \\ \mathrm{B}_y(t) &= -\mathrm{B}_1 \sin(\omega_{\mathrm{RF}} t)\end{aligned} \tag{2.14}$$

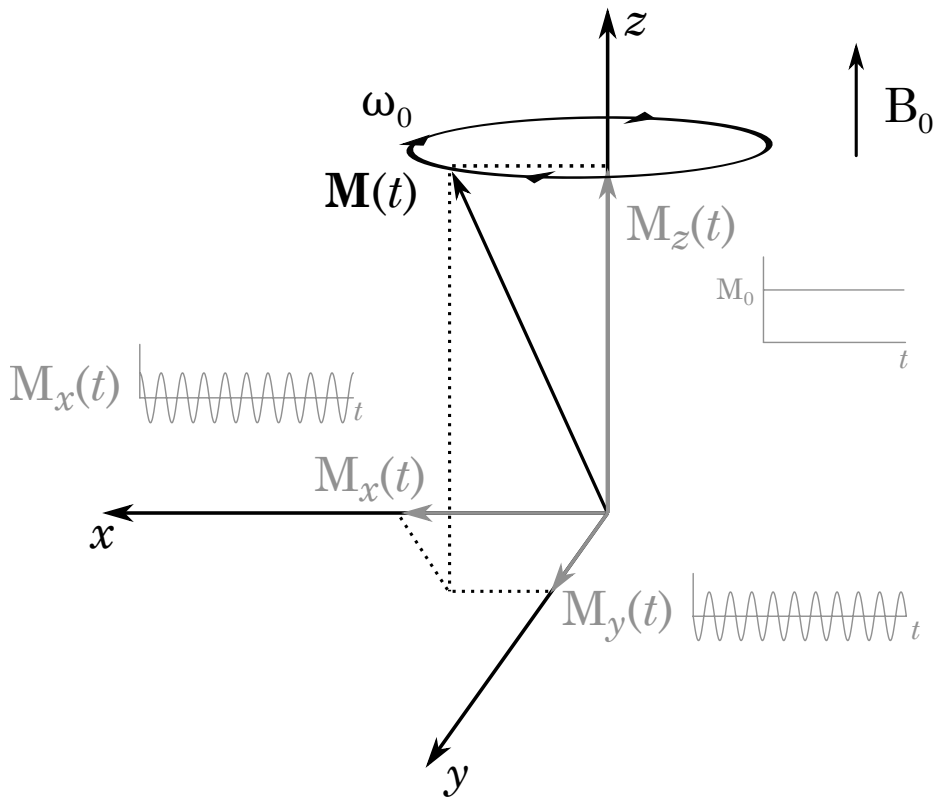

Figure 2.4: Precession of the tissue magnetisation vector **M** about the z-axis due to the external magnetic field, B_0, applied along $\hat{\boldsymbol{z}}$. Precession is at frequency ω_0.

where B_1 is the amplitude of the RF field and ω_{RF} is the frequency of the applied excitation. The new external magnetic field interacting with **M** is therefore $\mathbf{B}(t) = \big(B_x(t),\ B_y(t),\ B_0\big)$, and substituting into equation (2.11) shows that application of the RF pulse introduces rotation about y with time-dependent frequency $\gamma B_x(t)$, and rotation about x at frequency $\gamma B_y(t)$, in addition to precession about $\boldsymbol{hatz}$ at the Larmor frequency ω_0 (Fig. 2.5). In this case **M** is simpler to analyse in a rotating frame of reference, $x'y'z'$, where the observer rotates about $\hat{\boldsymbol{z}}$ at frequency ω_{RF} in the same sense as precession, such that when $\omega_{RF} = \omega_0$ the transverse components appear stationary. In the rotating frame of reference, the equivalent of $\mathbf{M} = (M_x,\ M_y,\ M_z)$ is, $\mathbf{M}^r = (M_{x'},\ M_{y'},\ M_{z'})$. It is first useful to write the transverse components of **M** in complex form:

$$\mathbf{M}_{xy} = M_x + iM_y = M_{xy}(0)e^{-i\omega_0 t} \tag{2.15}$$

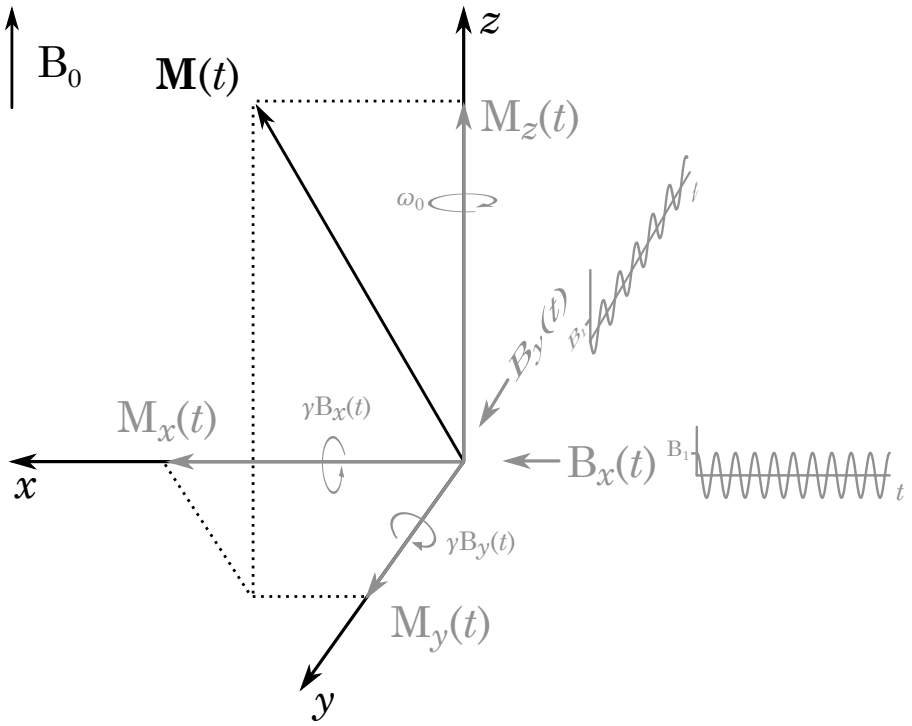

Figure 2.5: Illustration of RF excitation in the laboratory frame. The magnetisation vector **M** rotates about all three axes, making excitation and relaxation complex to analyse, and some frequencies are time-dependent.

In the laboratory frame of reference, $\mathbf{M}_{xy}$ rotates clockwise in the xy-plane at the Larmor frequency. In a frame that rotates at an angular frequency of ω_{RF} in the same sense as $\mathbf{M}_{xy}$, then to the observer, $\mathbf{M}_{xy}$ can be expressed as the rotating-frame equivalent:

$$\mathbf{M}_{x'y'} = \mathbf{M}_{xy} e^{i\omega_{\mathrm{RF}} t} \tag{2.16}$$

from which the separate x' and y' components are extracted as follows: $\mathrm{M}_{x'} = \mathrm{Re}\{\mathbf{M}_{x'y'}\} = \mathrm{M}_x \cos(\omega_{\mathrm{RF}} t) - \mathrm{M}_y \sin(\omega_{\mathrm{RF}} t)$, $\mathrm{M}_{y'} = \mathrm{Im}\{\mathbf{M}_{x'y'}\} = \mathrm{M}_y \cos(\omega_{\mathrm{RF}} t) + \mathrm{M}_x \sin(\omega_{\mathrm{RF}} t)$, and $\mathrm{M}_{z'} = \mathrm{M}_z$. The time derivatives of the rotating-frame terms depend on the laboratory-frame terms in equation (2.11) and the definitions in equation (2.14). Substituting as

required yields the rotating-frame description of the isochromat:

$$\begin{aligned}\frac{dM_{x'}}{dt} &= -\Delta\omega M_{y'} \\ \frac{dM_{y'}}{dt} &= \Delta\omega M_{x'} + \omega_1 M_{z'} \\ \frac{dM_{z'}}{dt} &= -\omega_1 M_{y'}\end{aligned} \tag{2.17}$$

where the following definitions have been used:

$$\Delta\omega = \omega_{RF} - \omega_0 \tag{2.18}$$

$$\omega_1 = \gamma B_1 \tag{2.19}$$

The rotating frame equivalent of Fig. 2.5 is shown in Fig. 2.6a. In the rotating frame there are now only two planes of rotation: rotation in the $x'y'$-plane at the 'off-resonance' frequency $\Delta\omega$, and rotation in the $y'z'$-plane at angular frequency ω_1. The evolution of longitudinal magnetisation is identical in both the laboratory and rotating frames ($\hat{\boldsymbol{z}}' = \hat{\boldsymbol{z}}$), with the rotating frame offering the advantage of a simplified trajectory in the transverse plane. A key insight from this simplified representation is to observe the effect that the B_1 field has on $\mathbf{M}^r$: if the sample is irradiated on resonance ($\Delta\omega = 0$) with an RF amplitude of B_1, for a duration Δt seconds, $\mathbf{M}^r$ will simply rotate in the $y'z'$ plane through an angle, α, proportional to B_1 and Δt:

$$\alpha = \gamma B_1 \Delta t = \omega_1 \Delta t \tag{2.20}$$

α is known as the flip angle (FA). Therefore, on resonance, the effect on longitudinal magnetisation is:

$$M_z(\Delta t) = M_z(0)\cos(\alpha) \tag{2.21}$$

Mathematically, the rotating frame is equivalent to viewing ω_{RF} as a magnetic field (equation 2.5), ω_{RF}/γ, which directly opposes the B_0 field to give a reduced magnetic field along $\hat{\boldsymbol{z}}'$ of $B_0' = B_0 - \omega_{RF}/\gamma = -\Delta\omega/\gamma$ [42]. In the absence of RF excitation,

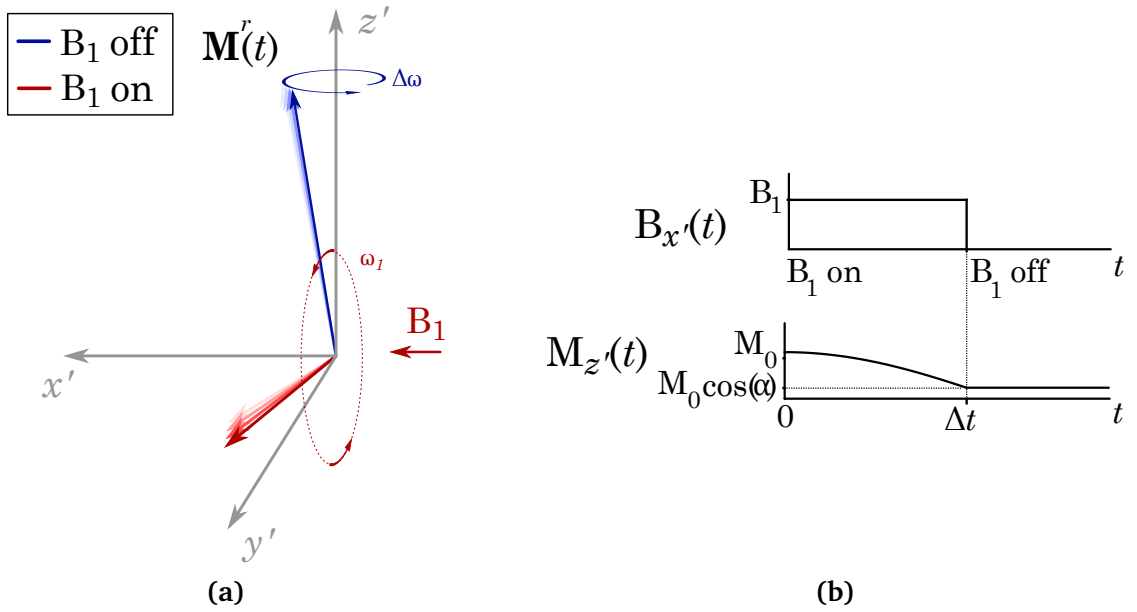

Figure 2.6: Illustration of on-resonance RF excitation in the rotating frame **(a)**, and example waveforms in **(b)**. In the rotating frame, dependence on the excitation frequency ω_{RF} is simplified. Rotation of the rotating frame magnetisation vector $\mathbf{M}^r$ occurs only in two planes, and with time-independent frequencies: $\Delta\omega_0$ about $\hat{\boldsymbol{z}}'$, and ω_1 about $\hat{\boldsymbol{x}}'$. In this frame of reference RF excitation reduces to an equivalent static field, and along $\hat{\boldsymbol{x}}'$ only.

$B_0' = B_0$ and $\mathbf{M}^r$ simply precesses about the z'-axis (constant $M_{z'}$). In the presence of on-resonance RF excitation, $\Delta\omega = 0$, and the only field acting on $\mathbf{M}^r$ is $B_1\hat{\boldsymbol{x}}'$. In this case, the effect of B_1 on $M_{z'}$ is maximal (resonance condition), and $\mathbf{M}^r$ experiences a flip angle nutates about the x'-axis.

RF pulses that are regularly used in NMR pulse sequences are an excitation pulse ($\alpha = 90°$), and an inversion pulse ($\alpha = 180°$). If the RF envelope is non-rectangular, a more general expression of FA is $\alpha = \gamma \int_0^t B_1(t)dt$. In an NMR experiment, detection of M_0 (Fig. 2.7a) takes place exclusively in the transverse plane, meaning that the spin isochromat needs to be rotated into the $x'y'$ plane in order to be measured. An excitation pulse (Fig. 2.7b) achieves this by rotating longitudinal magnetisation through an angle of 90°. An inversion pulse (Fig. 2.7c) serves to invert the sign of M_0 by rotating longitudinal magnetisation through 180°, onto the $-z'$-axis.

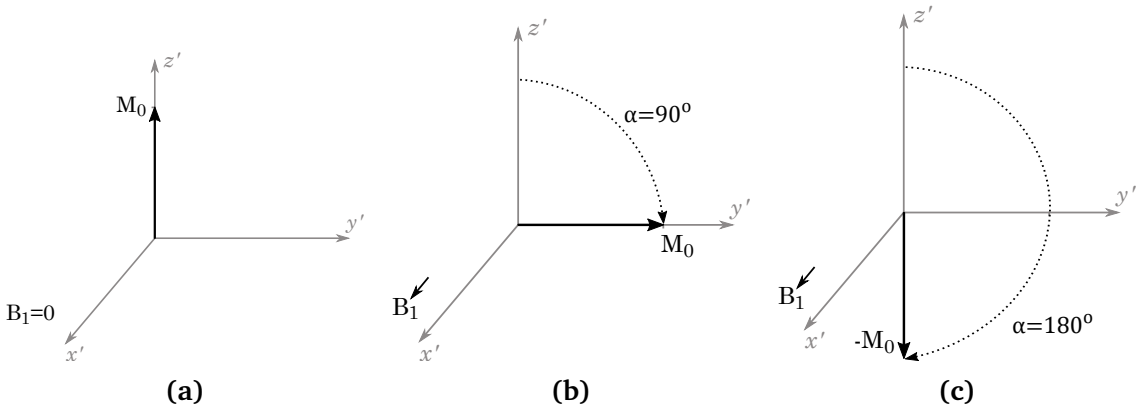

Figure 2.7: Types of RF pulses commonly used in NMR. In an NMR experiment, detection of M_0 in **(a)** requires magnetisation to be rotated onto the transverse plane; this is achieved by the 90° RF excitation pulse in **(b)**. A 180° RF inversion pulse, shown in **(c)**, inverts longitudinal magnetisation by flipping it onto the $-z'$ axis.

2.1.4 Relaxation mechanisms and the Bloch equations

At equilibrium, macroscopic net magnetisation is oriented only along $\hat{\boldsymbol{z}}$: $\mathbf{M}_0 = (0,\ 0,\ M_0)$. Application of an RF pulse at the Larmor frequency disturbs the equilibrium distribution of spin states, which on a macroscopic level leads to a change in longitudinal magnetisation $\mathbf{M}_z$. The RF pulse also induces a degree of phase coherence between the individual spins, which is observed as an increase in transverse magnetisation $\mathbf{M}_{xy}$. When the RF pulse is turned off, longitudinal and transverse relaxation mechanisms restore $\mathbf{M}$ to its equilibrium state.

2.1.4.1 Longitudinal relaxation

Longitudinal relaxation describes the return of longitudinal magnetisation towards M_0 from an initial value of $M_z(0)$ at $t = 0$. It is characterised by a time constant T_1 as follows:

$$\frac{dM_z(t)}{dt} = \frac{M_0 - M_z(t)}{T_1} \quad \rightarrow \quad M_z(t) = M_0 - \big(M_0 - M_z(0)\big)e^{-t/T_1} \tag{2.22}$$

Equation (2.22) is an extension of equation (2.12) to include T_1 relaxation, or spin-lattice relaxation. T_1 provides a measure by which tissue types can be differentiated, as it is affected by tissue properties such as water concentration and the concentration

Table 2.1: Average T_1, T_2, and T_2^* relaxation times in human brain tissue at 3 T (based on 19 healthy subjects) [45]. The T_1 and T_2 values are averages from nine anatomical regions, and the T_2^* values are averages from within the frontal lobe.

tissue type	T_1 (ms)	T_2 (ms)	T_2^* (ms)
grey matter	1331	110	51.8
white matter	832	79.6	44.7

of macromolecules. T_1 relaxation is a process by which energy is transferred from the excited spin to the surrounding molecular environment [43]. The excited spin is surrounded by random molecular motion, such as molecular rotation (tumbling), which is characterised by a correlation time τ_c (the average time taken for a molecule to rotate through one radian) [44]. Molecular tumbling leads to fluctuations in the local magnetic field experienced by a spin. A tumbling rate close to the Larmor frequency of the spin ($1/\tau_c \approx \omega_0$) promotes effective energy exchange between the spin and the environment and therefore more efficient relaxation (T_1 minimised), re-establishing Boltzmann equilibrium. Rates of tumbling that are significantly higher (fast molecular motion) or lower (slow molecular motion) than ω_0 are less effective at promoting spin-lattice relaxation, leading to a larger T_1 and slower regrowth of M_z towards M_0. Recovery of $\mathbf{M}_z$ is illustrated in Fig. 2.8. Average T_1 values in brain tissue are listed in Table 2.1.

2.1.4.2 Transverse relaxation

Application of a 90° RF pulse tips $\mathbf{M}_0$ into the transverse plane, such that immediately after the excitation pulse, $\mathbf{M}_{xy} = \mathbf{M}_0$. The individual nuclear spins that comprise $\mathbf{M}_{xy}$ are initially all in alignment and rotating at the same frequency ω_0. Random fluctuations in local magnetic field, caused by neighbouring spins, leads to a range of Larmor frequencies, and the spins begin to dephase with respect to each other having initially been aligned [44]. This irreversible loss of synchronisation between spins is observed as a decay in the amplitude of net transverse magnetisation, characterised by a time

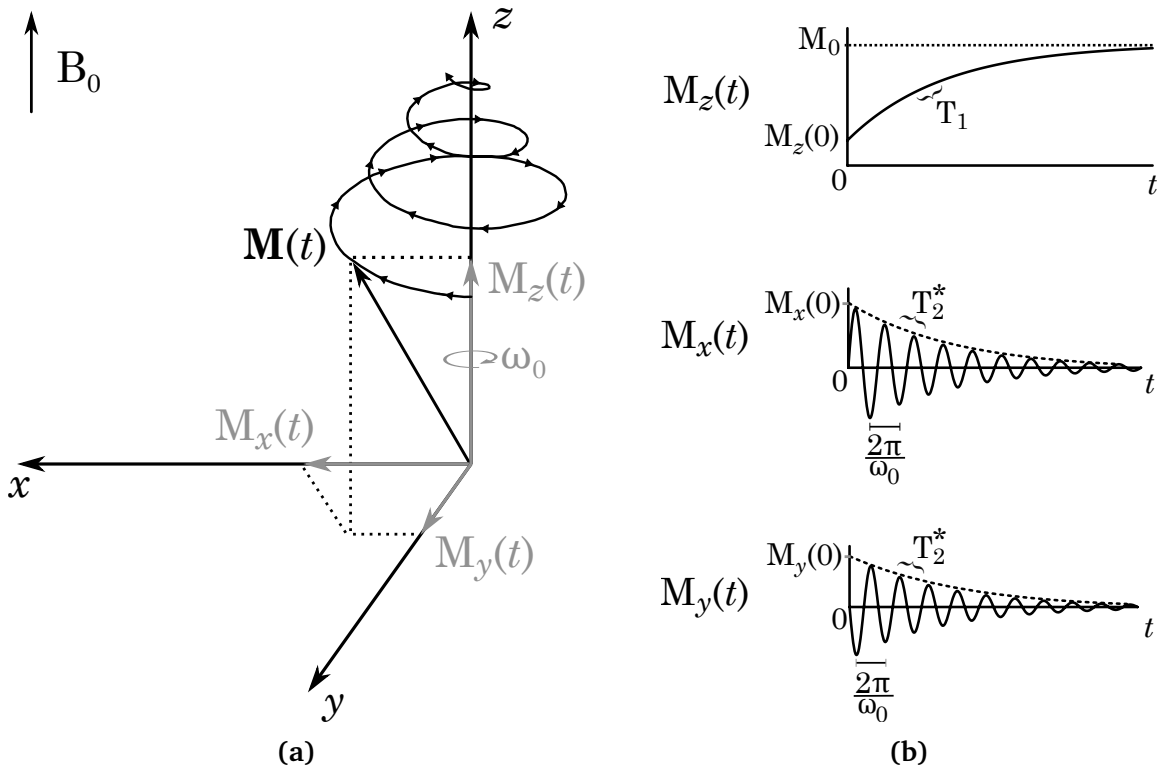

Figure 2.8: Relaxation of tissue magnetisation in the laboratory frame. **(a)** Precession of the tissue magnetisation vector **M** about the z axis due to the main magnetic field B_0 applied in that direction. Precession is at frequency ω_0. When relaxation terms are included, and the magnetisation vector is perturbed from equilibrium, it will return to equilibrium via a decay in oscillation in the xy-plane with time constant T_2^* and a growth in the longitudinal component with time constant T_1, shown in **(b)**.

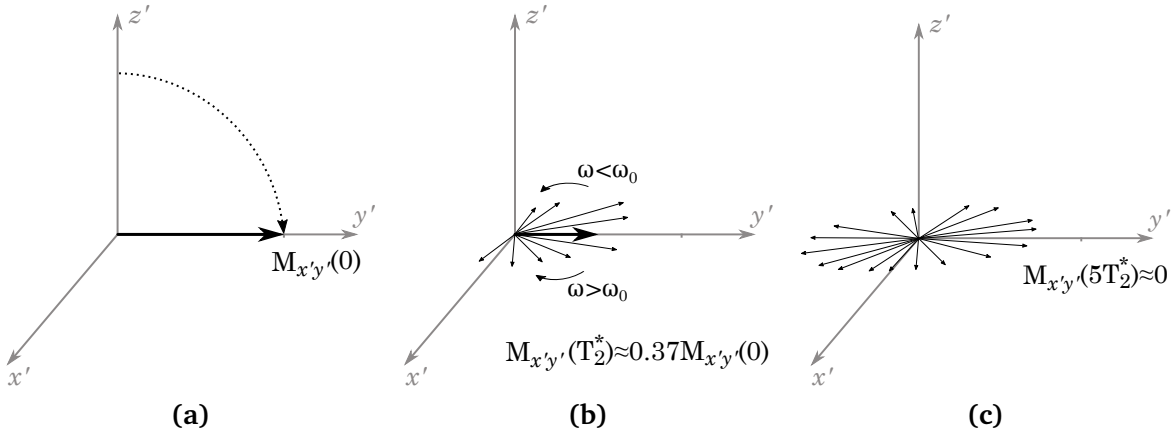

Figure 2.9: Illustration of spin dephasing leading to transverse relaxation. Transverse relaxation with time constant T_2^* is viewed in the rotating frame. **(a)** The magnetisation vector (black arrow) is tipped into the $x'y'$ plane, whereat the individual spins are initially in phase. **(b)** Random field fluctuations and static field inhomogeneities cause the individual spins (thin arrows) to dephase with respect to each other: some rotate at frequencies higher than ω_0, and others at lower frequencies. The vector sum of the individual spins is less than $M_{x'y'}(0)$. **(c)** The spins continue to fan out, and after about $5T_2^*$, phase coherence is lost such that $M_{x'y'} \approx 0$.

constant T_2:

$$\begin{aligned} \frac{dM_x}{dt} &= \omega_0 M_y - M_x/T_2 \quad \rightarrow \quad M_x(t) = M_0 \cos(\omega_0 t) e^{-t/T_2} \\ \frac{dM_y}{dt} &= -\omega_0 M_x - M_y/T_2 \quad \rightarrow \quad M_y(t) = -M_0 \sin(\omega_0 t) e^{-t/T_2} \end{aligned} \tag{2.23}$$

T_2 varies by tissue type and relaxation is more efficient in environments with slower molecular motion where local field differences persist for longer. Fluctuations in the local field observed by a spin tend to average out at higher tumbling rates, preserving coherence between spins and therefore prolonging T_2 relaxation [46,47]. In addition to the random time-varying causes of dephasing, described by T_2, there are also static spatial variations in the applied B_0 field (B_0 field inhomogeneity) that cause additional dephasing, characterised by a time constant T_2'. B_0 inhomogeneity is caused by imperfections in magnet construction and susceptibility effects from the patient in the field. The overall rate of signal decay, $1/T_2^*$, is a combination of these two rates:

$$\frac{1}{T_2^*} = \frac{1}{T_2} + \frac{1}{T_2'} \tag{2.24}$$

The process of transverse relaxation is illustrated in Fig. 2.9, and T_2^* decay waveforms are shown in Fig. 2.8b. Average T_2 and T_2^* values in brain tissue are listed in Table 2.1.

2.1.4.3 Bloch equations

Incorporating T_1 and T_2 relaxation times into the vector product terms of equation (2.11) gives the Bloch equations, which describe precession of **M** with relaxation:

$$\begin{aligned} \frac{dM_x}{dt} &= \gamma\left(M_y B_0 - M_z B_y\right) - \frac{M_x}{T_2} \\ \frac{dM_y}{dt} &= \gamma\left(M_z B_x - M_x B_0\right) - \frac{M_y}{T_2} \\ \frac{dM_z}{dt} &= \gamma\left(M_x B_y - M_y B_x\right) - \frac{M_z - M_0}{T_1} \end{aligned} \tag{2.25}$$

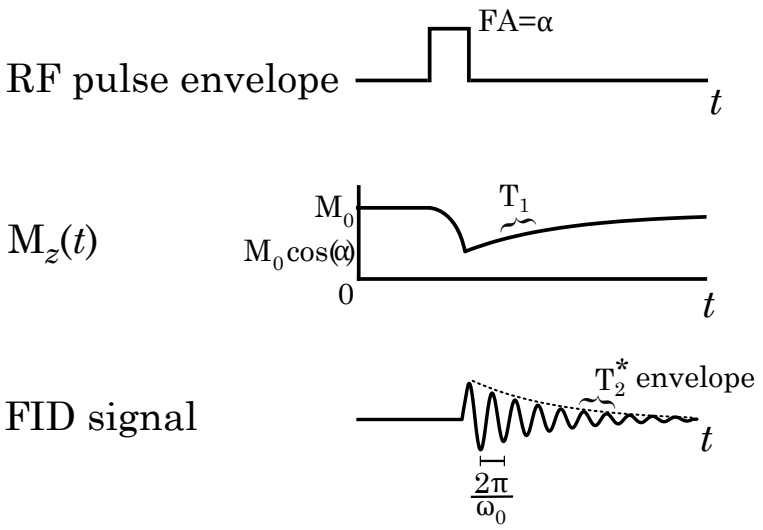

Figure 2.10: A basic NMR pulse sequence for generating FID. An NMR signal is obtained by tipping sample magnetisation into the transverse plane using an RF pulse. After excitation, transverse magnetisation undergoes damped oscillation at the Larmor frequency, with a T_2^* decay envelope. The FID signal is recorded as a voltage across detector coils.

In the rotating frame, assuming the RF field takes the form as in equation (2.17), the rotating frame Bloch equations are [42]:

$$\begin{aligned}
\frac{dM_{x'}}{dt} &= -\Delta\omega M_{y'} - \frac{M_{x'}}{T_2} \\
\frac{dM_{y'}}{dt} &= \Delta\omega M_{x'} + \omega_1 M_{z'} - \frac{M_{y'}}{T_2} \\
\frac{dM_{z'}}{dt} &= -\omega_1 M_{y'} - \frac{M_{z'} - M_0}{T_1}
\end{aligned} \tag{2.26}$$

2.1.5 Free induction decay

In order to detect sample magnetisation, an RF pulse rotates **M** into the transverse plane. Oscillation of the magnetisation vectors in the transverse plane induces an oscillating electromotive force across receiver coils oriented co-axially to the x and y axes via Faraday's law of electromagnetic induction [26]. The damped oscillation decays with time constant T_2^* and is known as the free induction decay (FID). Oscillations in the recorded FID signal occur at frequencies equal to the difference between the Larmor and carrier frequencies (Fig. 2.10) [26]. FID is the basic form of MR signals that are formed using a single RF pulse [26].

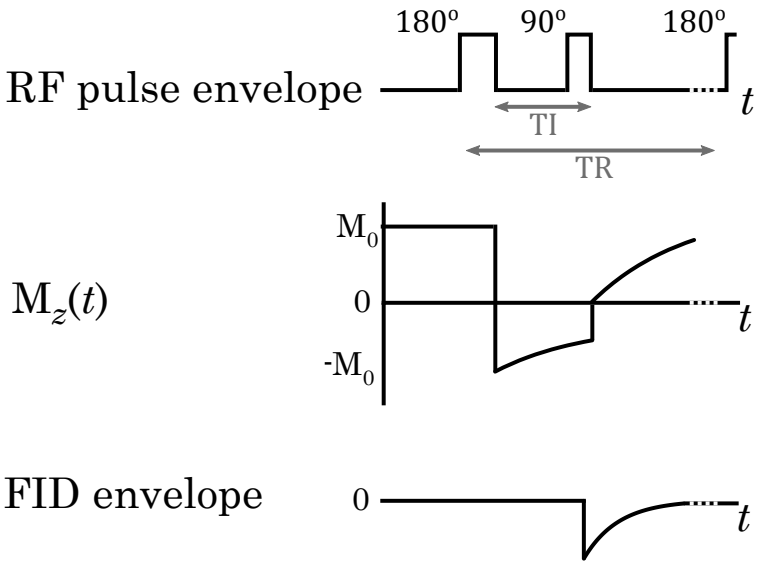

Figure 2.11: Inversion recovery NMR pulse sequence. A 180° pulse inverts longitudinal magnetisation, after which longitudinal magnetisation begins to recover. After a short period of recovery, TI, an excitation pulse is applied to rotate M_z onto the transverse plane for detection. Every TR seconds, this process is repeated for a different value of TI.

2.1.6 Inversion recovery

An inversion recovery (IR) pulse sequence is often used to measure the T_1 of a sample (Fig. 2.11). In an IR experiment, an inversion pulse is used to rotate $\mathbf{M}_0$ onto the $-z$-axis ($M_z(0) = -M_0$), whereat it begins to recover according to equation (2.22). A short delay (inversion time, TI) allows for some recovery of $\mathbf{M}_z$, before a 90° excitation pulse rotates $\mathbf{M}_z(t = \text{TI})$ onto the transverse plane for signal detection. When $\mathbf{M}_z$ returns to equilibrium (or within every repetition period, TR), this process of inversion and excitation is repeated for a different value of TI. T_1 can be estimated by fitting the data to equation (2.22).

2.1.7 Spin echo generation

The T_2 of a sample can be measured using a spin echo (SE) pulse sequence, which reverses the loss of phase coherence caused by static T_2' effects. Static inhomogeneities cause some spins to precess at a frequency slightly higher than ω_0 (positive phase accumulation), whilst other spins precess at a slightly lower frequency than ω_0 (negative

phase accumulation). These phase differences lead to a reversible loss of coherence, and are reversed by applying a 180° refocusing pulse along $\hat{\boldsymbol{y}}'$, which flips transverse magnetisation by 180° about the y' axis (applied at half the echo time, TE/2). This causes the spins to accumulate phase at the same rate but in the opposite sense. The amount of dephasing between 0 to TE/2 is cancelled out by the rephasing between TE/2 to TE, such that at TE the spins are refocused, forming a spin echo (Fig. 2.12). A basic SE NMR pulse sequence is shown in Fig. 2.13.

2.2 Magnetic resonance imaging

This section extends the principles of NMR to MRI by showing how spatial localisation of signals is achieved, followed by an outline of MRI pulse sequences.

2.2.1 Gradient fields

Thus far a uniform external magnetic field along the z-axis has been assumed, $\mathbf{B}_z = \mathrm{B}_0$, which means that all spins in the sample precess with the same Larmor frequency ω_0 according to equation (2.5). In MRI, spatial localisation of voxels requires making B_z spatially-dependent, so that Larmor frequency becomes a function of position. B_z is made to vary linearly in space by introducing a linearly-varying magnetic field (via gradient coils) which is superimposed onto B_0. This addition to B_z is known as a gradient field, defined by the magnetic field gradient $\mathbf{G}$, as follows:

$$\mathbf{G} = (\mathrm{G}_x,\ \mathrm{G}_y,\ \mathrm{G}_z) = \nabla \mathrm{B}_z \tag{2.27}$$

In the presence of a gradient field $\mathbf{G}$, B_z at position $\boldsymbol{r} = (x, y, z)$ in object space is given by

$$\mathrm{B}_z(\boldsymbol{r}) = \mathrm{B}_0 + \mathbf{G} \cdot \boldsymbol{r} = \mathrm{B}_0 + \mathrm{G}_x x + \mathrm{G}_y y + \mathrm{G}_z z \tag{2.28}$$

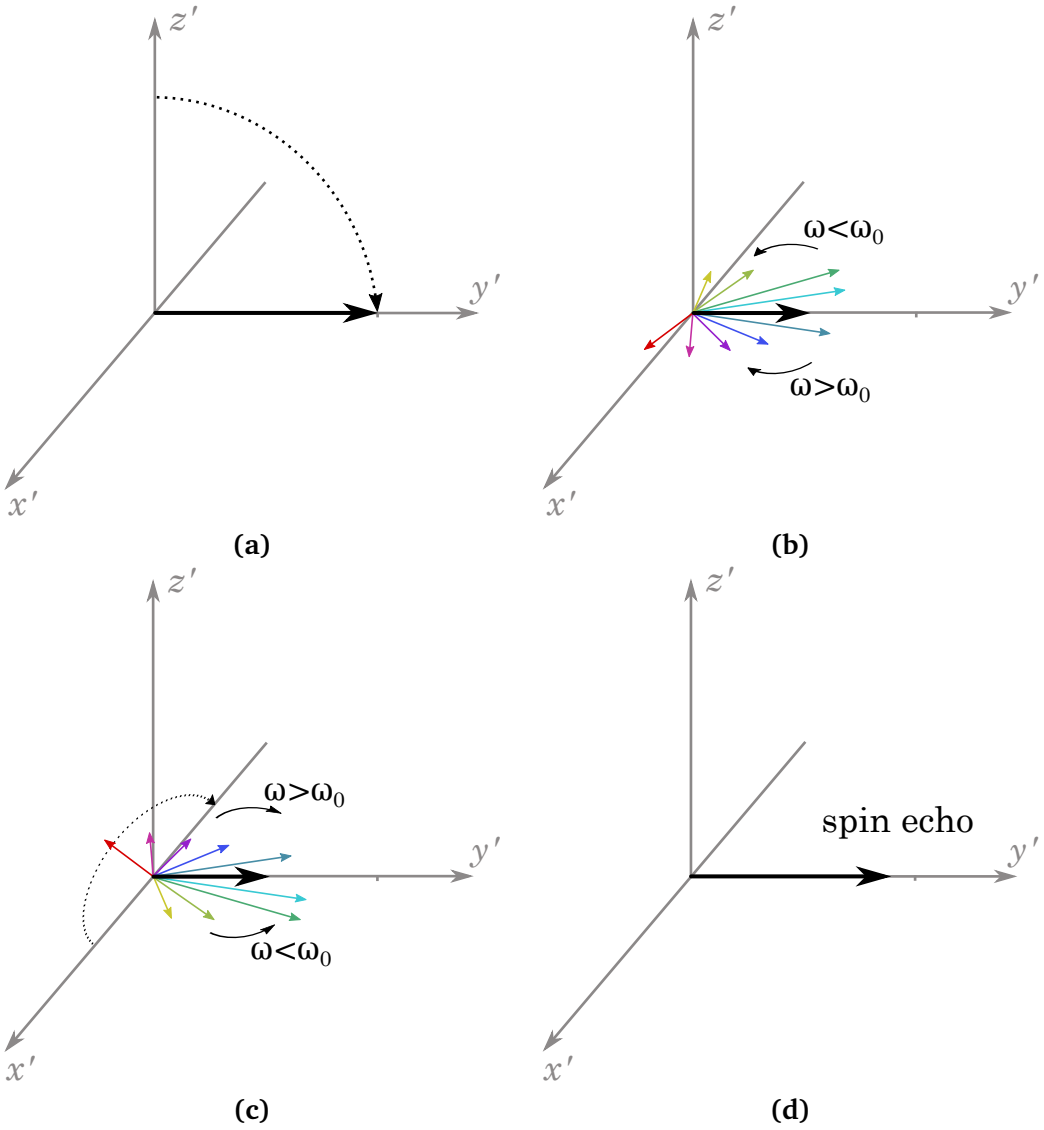

Figure 2.12: Illustration of spin echo formation in the rotating frame, using a 180° refocusing pulse. **(a)** When the magnetisation vector (black arrow) is rotated onto the transverse plane, the individual spins are initially in phase. **(b)** Transverse magnetisation decays as the spins (coloured arrows) dephase owing to T_2 and T_2' processes. **(c)** The T_2' contribution to dephasing can be reversed by applying a 180° refocusing pulse along the y' axis at time TE/2, causing the spins to flip by 180° about $\hat{\boldsymbol{y}}'$ and accumulate phase in the opposite sense. **(d)** At TE, net phase accumulation is zero, and the spins converge to form a spin echo. The spin echo is smaller in amplitude than the initial signal due to random T_2 dephasing which cannot be refocused.

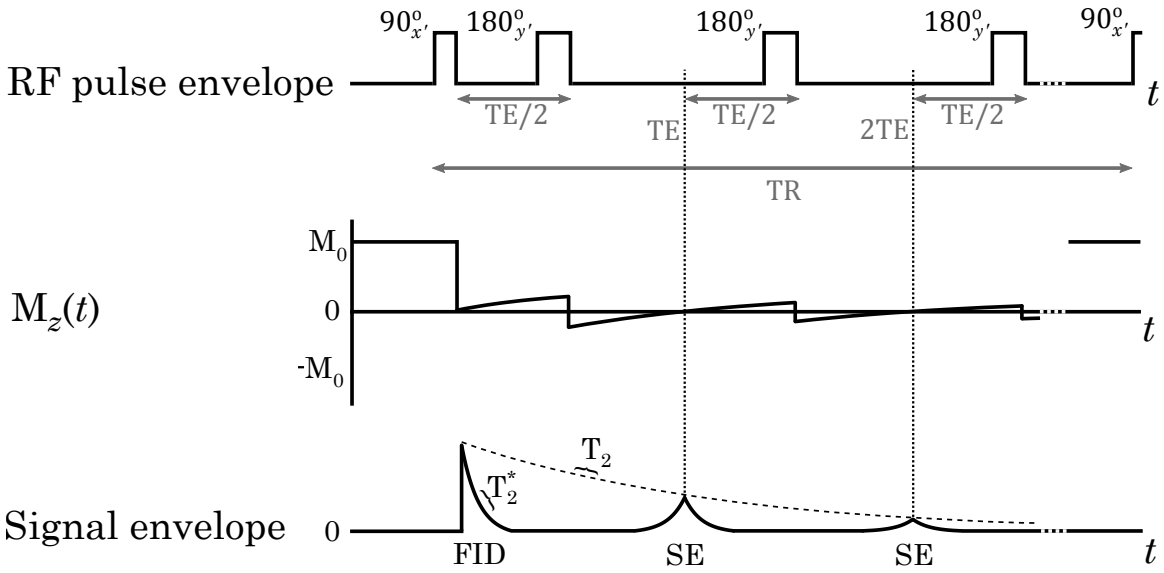

Figure 2.13: Spin echo NMR pulse sequence. Magnetisation is tipped onto the transverse plane using a 90° excitation pulse, whereat FID decay occurs with time constant T_2^*. A 180° refocusing pulse is applied TE/2 seconds later (along $\hat{\boldsymbol{y}}'$). At time TE, the nuclear spins become refocused, forming a spin echo. Subsequent spin echoes are formed by the application of additional 180° refocusing pulses. The amplitude of consecutive spin echoes decays according to T_2, allowing T_2 to be determined.

This, by extension of equation (2.5), leads to a spatially-dependent Larmor frequency:

$$\omega(\boldsymbol{r}) = \gamma B_z(\boldsymbol{r}) = \omega_0 + \gamma \mathbf{G} \cdot \boldsymbol{r} \tag{2.29}$$

Henceforth, the magnitude of transverse magnetisation at location $\boldsymbol{r}$ is denoted by $M_\perp(\boldsymbol{r},\ t)$, or $M_\perp$ for brevity, which is proportional to the image intensity of voxel $\boldsymbol{r}$. MRI seeks to image $M_\perp$. A general expression for the evolution of transverse magnetisation, in the presence of gradient fields, can be obtained by substituting equation (2.29) into equation (2.15):

$$M_{xy}(\boldsymbol{r},\ t) = M_\perp e^{-i\omega(\boldsymbol{r})t} = M_\perp e^{-i\omega_0 t} e^{-i\gamma \mathbf{G}\cdot\boldsymbol{r}\, t} \tag{2.30}$$

In the rotating frame, the off-resonance frequency is (by extension of equation 2.18) $\Delta\omega(\boldsymbol{r}) = \omega_{RF} - \omega(\boldsymbol{r})$, which, on resonance ($\omega_{RF} = \omega_0$) simplifies to $\Delta\omega(\boldsymbol{r}) = -\gamma \mathbf{G} \cdot \boldsymbol{r}$,

so that in this case equation (2.16) becomes:

$$\mathrm{M}_{x'y'}(\boldsymbol{r},\ t) = \mathrm{M}_{\perp} e^{-i\gamma \mathbf{G}\cdot\boldsymbol{r}\, t} \tag{2.31}$$

The observed MR signal, $\mathrm{S}(t)$, is a summation of the individual signals arising from each voxel that has transverse magnetisation:

$$\mathrm{S}(t) \propto \iiint_{object} \mathrm{M}_{\perp} e^{-i\gamma \mathbf{G}\cdot\boldsymbol{r}\, t} d\boldsymbol{r} \tag{2.32}$$

Equation (2.32) will be used to show how the MR signal S, obtained under the application of gradient fields, is used to achieve spatial localisation of a voxel.

2.2.2 Slice selection

In MRI, spatial localisation starts with defining the slice of the object (subject's body), perpendicular to $\hat{\boldsymbol{z}}$, that is to be excited. Once a given slice is excited, all subsequent signals detected can be attributed exclusively to that position along the z axis. Slice selection (SS) is achieved by first applying a gradient field G_z along $\hat{\boldsymbol{z}}$. The axial position, z, of a target slice is directly encoded by the Larmor frequency at that position, and the width or thickness of the slice (Δz) corresponds to a frequency bandwidth (BW) of BW_{slice}:

$$\begin{aligned} \omega(z) &= \omega_0 + \gamma \mathrm{G}_z z \\ \mathrm{BW}_{slice} &= \gamma \mathrm{G}_z \Delta z \end{aligned} \tag{2.33}$$

The slice at location z and with thickness Δz can then be excited using an RF pulse with frequency characteristics that match the range of precession frequencies in the slice according to equation (2.33), namely, a carrier frequency $\omega(z)$ and bandwidth BW_{slice}. This association between Larmor frequency and position is illustrated in Fig. 2.14a. Equation (2.33) defines a simple frequency-domain profile of the RF slice excitation pulse: a boxcar profile, centred at $\omega(z)$, with a width of BW_{slice}. The time-domain

equivalent of this, by the inverse Fourier transform (FT), is a sinc function modulating a carrier frequency of $\omega(z)$ (Fig. 2.14b) [26,48]. The RF pulse is of finite length, therefore the sinc function is truncated, but remains a good approximation to a boxcar in the frequency domain. Following slice selection, where the spins of a given slice are rotated onto the transverse plane (and assuming G_z is immediately turned off), the detected signal (equation 2.32) arises from the spins of that excited slice only; this localises the signal along $\hat{\boldsymbol{z}}$.

2.2.3 Bipolar gradients

In practice, there is a finite slew rate associated with switching of the gradient fields which means that they cannot be turned off instantaneously. After a slice has been excited, the continued presence of G_z causes the transverse spins to precess at a range of Larmor frequencies along the axis of the slice, leading to rapid gradient-induced dephasing between isochromats and loss of signal (Fig. 2.15a), on which spatial encoding in the xy plane cannot proceed. Gradient dephasing is reversed with the application of a 'rephasing lobe', where G_z is reversed in order to undo the gradient-induced phase dispersion between isochromats. In the case of slice selection, the gradient echo is formed owing to a reversal of gradient-induced dephasing effects immediately following excitation. In the case of spatial encoding in the xy plane, discussed next, gradient dephasing and rephasing is applied (Fig. 2.15b) as part of the acquisition sequence to form a gradient echo (GE).

2.2.4 k-space

In order to encode position along $\hat{\boldsymbol{x}}$ and $\hat{\boldsymbol{y}}$, G_x and G_y respectively are applied. In the presence of G_x and G_y, the observed signal is (assuming signal amplitude is proportional

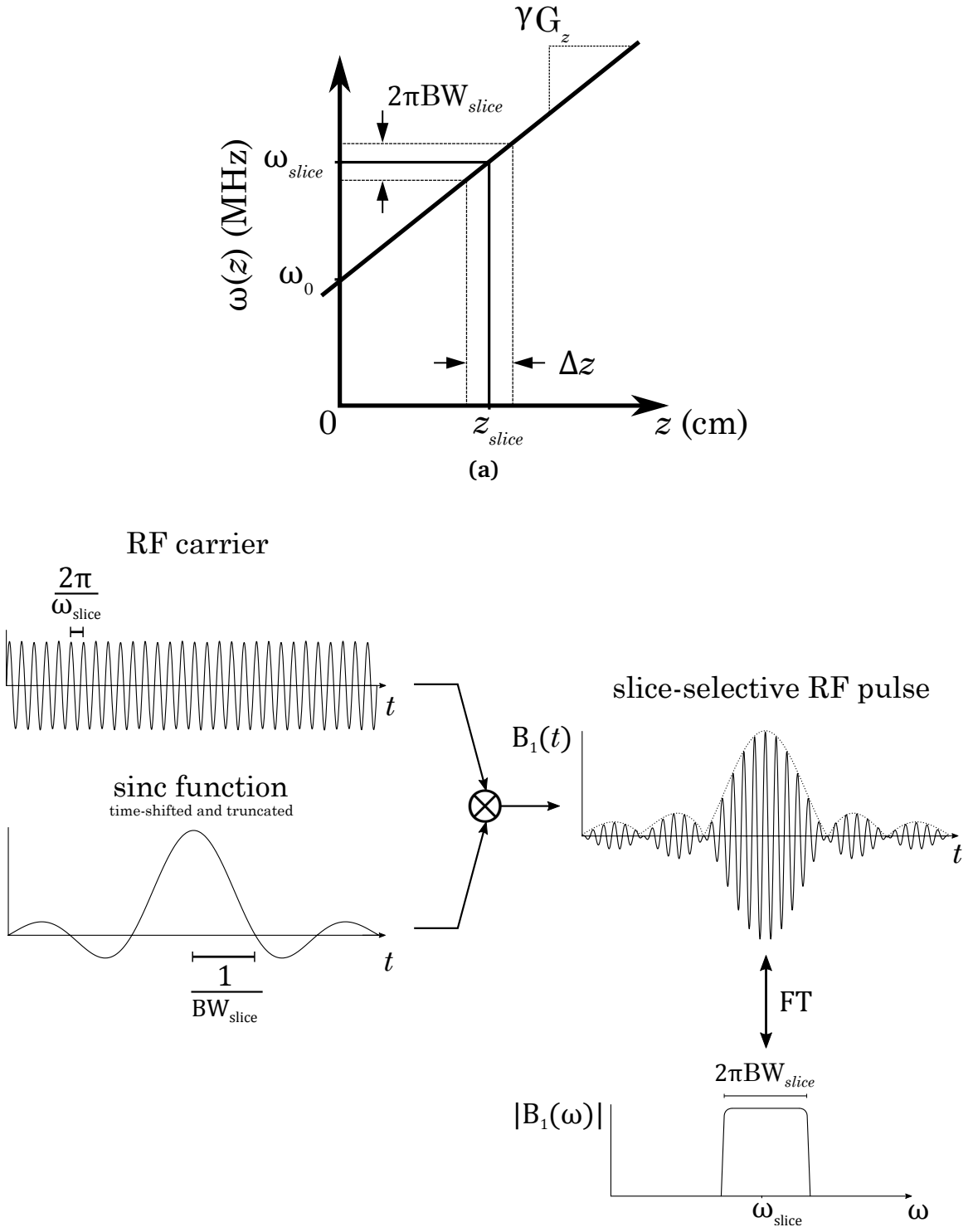

Figure 2.14: Frequency encoding of slice location and corresponding slice-selective RF pulse. **(a)** Spatial encoding along the z axis is achieved by applying a gradient field along $\hat{\mathbf{z}}$. The slice at location z_{slice} and with thickness Δz can then be excited using an RF pulse of frequency ω_{slice} and bandwidth BW_{slice}. **(b)** A slice-selective RF excitation pulse is obtained by multiplying a truncated sinc function, which has a lobe half-width of $1/\mathrm{BW}_{slice}$, with a carrier frequency ω_{slice} which corresponds to the Larmor frequency of the slice's z position [26,48]. The resulting modulated carrier has an approximately boxcar profile in the frequency domain. The bandwidth and carrier frequency correspond to the slice width and z position.

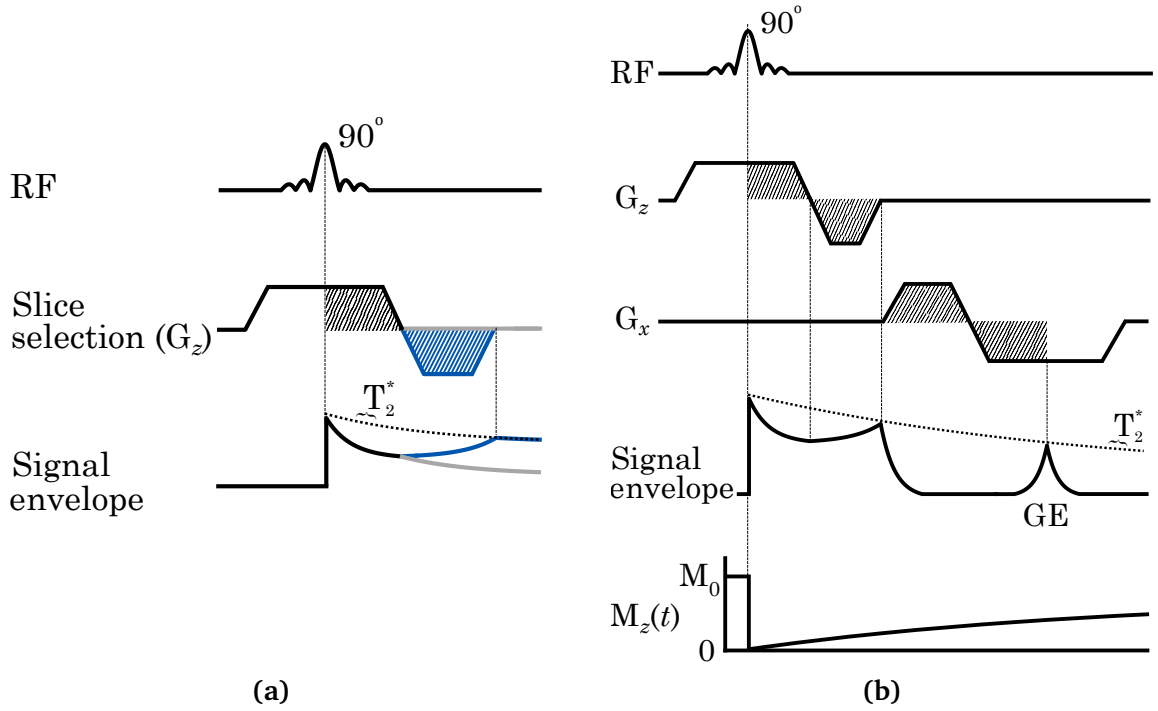

Figure 2.15: Using gradients to rephase the selected slice in **(a)**, and to form a gradient echo in **(b)**. **(a)** After slice excitation, continued presence of G_z (black area) causes rapid dephasing along the z axis, and a resulting loss of signal. To recover from the post-excitation dephasing effect of G_z, the polarity of G_z is reversed (rephasing lobe, blue trace), leading to a rephasing of the ischocromats when the shaded areas are equal. The signal then decays according to T_2^*. Without the rephasing lobe (grey trace), the signal amplitude is lower. **(b)** Other gradients, such as G_x, are used to intentionally dephase and then rephase the signal to selectively form a gradient echo (GE) at the point when the two areas are equal.

to slice thickness):

$$S(t) \propto \iint_{object} M_{\perp}(x,y) e^{-i\gamma(G_x x + G_y y)t} dx dy \Big|_{z=z_{slice}} \tag{2.34}$$

Since G_x and G_y are orthogonal, they can be applied independently and for different durations, assumed to be t for G_x and τ for G_y. This allows equation (2.34) to be written as:

$$S(t,\tau) \propto \iint_{slice} M_{\perp}(x,y) e^{-i\gamma G_x x t} e^{-i\gamma G_y y \tau} dx dy \tag{2.35}$$

By a change of variables, equation (2.35) reveals that the detected set of signals $S(t,\tau)$ are simply the Fourier transform of the voxel intensities (proportional to $M_{\perp}(x,y)$).

Equation (2.35) is written in terms of equivalent spatial frequencies k_x in $\hat{\boldsymbol{x}}$ and k_y in $\hat{\boldsymbol{y}}$[1]:

$$\begin{aligned} k_x &= \gamma \mathrm{G}_x t \\ k_y &= \gamma \mathrm{G}_y \tau \end{aligned} \tag{2.36}$$

Equation (2.35) can then be written as the two-dimensional (2D) Fourier transform of $\mathrm{M}_\perp(x, y)$:

$$\mathrm{S}(k_x, k_y) \propto \iint_{slice} \mathrm{M}_\perp(x, y) e^{-i2\pi(k_x x + k_y y)} dx dy \tag{2.37}$$

from which $\mathrm{M}_\perp(x, y)$ is obtained by the inverse Fourier transform:

$$\mathrm{M}_\perp(x, y) \propto \iint_{k\text{—space}} \mathrm{S}(k_x, k_y) e^{i2\pi(k_x x + k_y y)} dk_x dk_y \tag{2.38}$$

$\mathrm{S}(k_x, k_y)$ is the k-space representation of the image, and is what is acquired during an MRI scan. $\mathrm{S}(k_x, k_y)$ describes the composition of the image in terms of spatial frequencies along the x and y axes. During the acquisition, k-space therefore needs to be sampled according to the informational requirements of the desired image, such as voxel dimensions (image resolution) and the field of view (FOV). The FOV along the x axis is determined by the sample spacing:

$$\mathrm{FOV}_x = \frac{1}{\Delta k_x} \tag{2.39}$$

and the image resolution along x is determined by the frequency extent of k-space:

$$\Delta x = \frac{1}{2k_{x,max}} = \frac{\mathrm{FOV}_x}{\mathrm{N}_x} \tag{2.40}$$

The y axis and k_y and similarly related. The more central area of k-space corresponds to the lower frequency spatial components of the image, with spatial frequency increasing further away from the centre.

[1]The more general form of this is $k_{x,y}(t') = \gamma \int_0^{t'} \mathrm{G}_{x,y}(t) dt$ [26].

2.2.5 MRI pulse sequences

2.2.5.1 Gradient echo and fast gradient echo

A conventional GE pulse sequence scans k-space by acquiring one row of k-space per RF excitation pulse, after slice excitation with $\alpha \leq 90°$. In order to acquire row $n \in \{-N/2, ..., N/2\}$ of the total number of rows N, the amplitude of the G_y pulse is $n\Delta G_y$, where ΔG_y is the desired increment in G_y between rows (thereby setting the increment in k_y). When G_y is turned off, the phase accumulated by spins is dependent on their position along the y axis: $\phi(y) = 2\pi k_y(n)y$. G_y is also referred to as the phase encoding (PE) step. With this phase 'locked in' along the y axis, G_x is applied in a bipolar fashion to create a gradient echo which is sampled as it evolves in time t. Therefore, each sample corresponds to a different spatial frequency along $\hat{\boldsymbol{x}}$: $k_x(t) = \gamma G_x t$. Application of G_x is referred to as frequency encoding (FE), or the readout gradient. Thus for each n, all k_x are acquired for the corresponding $k_y(n)$. The initial dephasing lobe of the gradient echo is constructed such that the maximal signal occurs in the centre of k-space. Once magnetisation recovers during a period TR, this is repeated for the next row of k-space [49]. The acquisition time for an N × N matrix is N^2TR, making the conventional sequence relatively time-consuming. The GE signal is sensitive to T_2^* effects as there is no 180° refocusing pulse to cancel the effects of static dephasing.

A variation on conventional GE is Fast GE (FGE) (or Fast Field Echo, FFE), where a small flip angle is used (e.g. $\alpha = 15°$) so that less time is needed for longitudinal magnetisation to recover between row acquisitions, and therefore a shorter TR can be used. FGE also requires residual transverse magnetisation to be eliminated between repetitions, and this is achieved by gradient spoiling where rapid dephasing of the residual signal is induced using a strong G_z gradient (crusher gradient). GE and FGE pulse sequences, and k-space trajectories, are illustrated in Fig. 2.16.

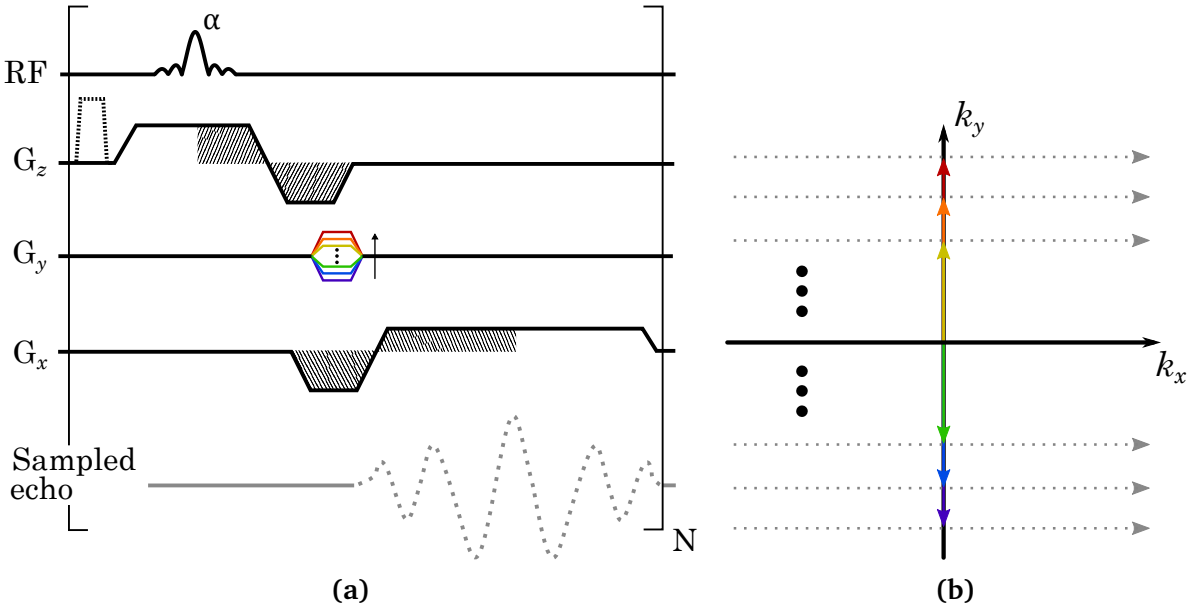

Figure 2.16: **(a)** Pulse sequence diagram and **(b)** *k*-space trajectory of a single-slice GE sequence. One row of *k*-space is acquired per TR. In a FGE sequence, α is small and each TR is also accompanied by a spoiler gradient (dotted G_z trace).

2.2.5.2 Single spin echo

A conventional SE pulse sequence comprises both a 90° excitation pulse and a 180° refocusing pulse which generates a single spin echo. This makes it sensitive to T_2 effects (Section 2.1.7) and has a higher in SNR, but the requirement of a second RF pulse makes it longer in duration than a GE sequence (Fig. 2.17) [49,50].

Manipulation of TR and TE leads to different recovery profiles of **M** and is used to achieve different modes of contrast. A short TE (< 40 ms) minimises the extent of transverse relaxation, such that the detected signal is largely T_1-weighted in the case of a short TR (< 750 ms) or weighted by proton density (PD) in the case of a long TR (> 1500 ms) [50]. On the other hand, a long TE (> 75 ms) and TR (> 1500 ms) produce an image that is weighted by T_2 relaxation [50].

2.2.5.3 Echo planar imaging

The image acquisition sequences presented thus far acquire one line of *k*-space per excitation pulse. SE echo planar imaging (SE-EPI) is able to sample the whole of *k*-space using a single spin echo, by rapidly creating a train of gradient echoes (typically 64

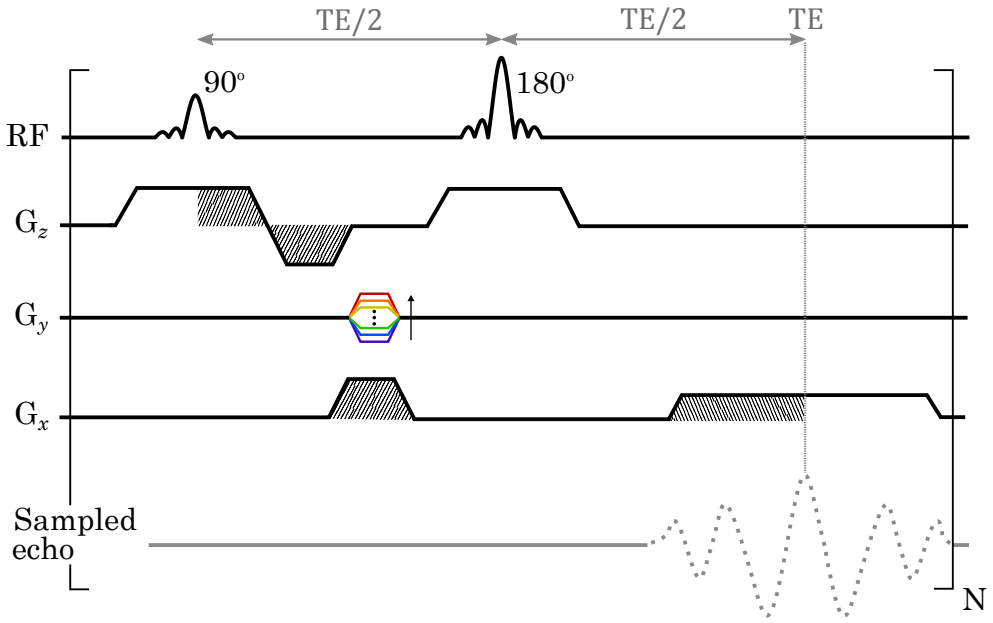

Figure 2.17: Conventional SE MRI pulse sequence. At TE/2 following slice excitation, a 180° refocusing pulse is applied to produce a spin echo at TE. The polarity of the readout gradient does not change, as an equivalent result is achieved by the refocusing pulse which inverts the plane of the spins.

to 128) following the refocusing pulse [50]. This produces an image with lower spatial resolution, but with higher temporal resolution as each slice can be obtained in less than 100 ms [44]. This is useful for minimising the effects of patient motion, reducing the time needed to acquire an image (longer sequences are less tolerable for patients), and is also used in dynamic imaging [26,49]. SE-EPI is the image acquisition technique used in this thesis for CEST MRI (discussed further in Section 2.3, with the specific MRI acquisition protocol described in Chapter 4). Following the 180° refocusing pulse, a preparatory phase-encoding pulse is applied corresponding to the most negative value of k_y. This is followed a bipolar G_x gradient to produce a gradient echo which is sampled, providing the lowest line of k-space. Subsequent lines are acquired by first applying a G_y 'blip' corresponding to Δk_y, followed again by a G_x gradient echo. This process is repeated during the course of the evolution of the spin echo. The accumulation of Δk_y scans k-space along the k_y axis, whilst the gradient echoes correspond to a sweep along the k_x axis. A SE-EPI pulse sequence and k-space trajectory is shown in Fig. 2.18.

The EPI scheme described above is single-shot EPI, where there is a full acquisition of *k*-space per TR. EPI can be multi-shot (segmented), where a subset of *k*-space lines are acquired per shot [26,49]. Partial Fourier EPI exploits the conjugate symmetry of *k*-space in order to skip the acquisition of redundant portions of *k*-space, instead reconstructing those portions using the symmetry property and thereby reducing acquisition time. Parallel imaging uses an array of receiver elements, each with a unique sensitivity profile which affords a form of spatial encoding, to reduce the number of *k*-space lines that need to be acquired [26].

EPI is vulnerable to a number of image artefacts. Nyquist ghosting is an artefact where, overlaid on the image, are low intensity copies of the image at an offset of half the FOV (FOV/2 or N/2) along the PE direction. After the *k*-space lines have been acquired, and before the 2D FT is taken, every second scan line must be reversed along the FE direction as the polarity of the readout gradient alternates between lines. The presence of background gradients has an additive effect which either slightly advances or delays echo formation depending on the polarity of G_x. After the scan lines are reversed, there remains an offset between each pair of adjacent lines, manifesting as a ghost image with an equivalent FOV of FOV/2. Aliasing or wrap-around occurs when anatomical regions outside of the FOV, with corresponding precession frequencies greater than the receiver bandwidth, are excited by the RF pulse and detected by the receiver coil. These regions outside of the FOV become aliased to the opposite edge of the image due to the cyclical repetition of phase accumulation outside the FOV, and the ambiguity this causes when localising the outside signals [26,51]. This can happen in both the FE and PE directions, but is relatively easily addressed along the readout direction by simply increasing the digitizer sampling rate or low-pass filtering the echo, neither of which have penalties for acquisition time [51]. Use of multiple gradient echoes makes EPI sequences very sensitive to T_2^* effects. In particular, magnetic susceptibility differences cause geometric distortion at soft tissue-bone and tissue-air interfaces [49]. In the FE direction, the ratio of background field offsets from water resonance (in Hz), to the

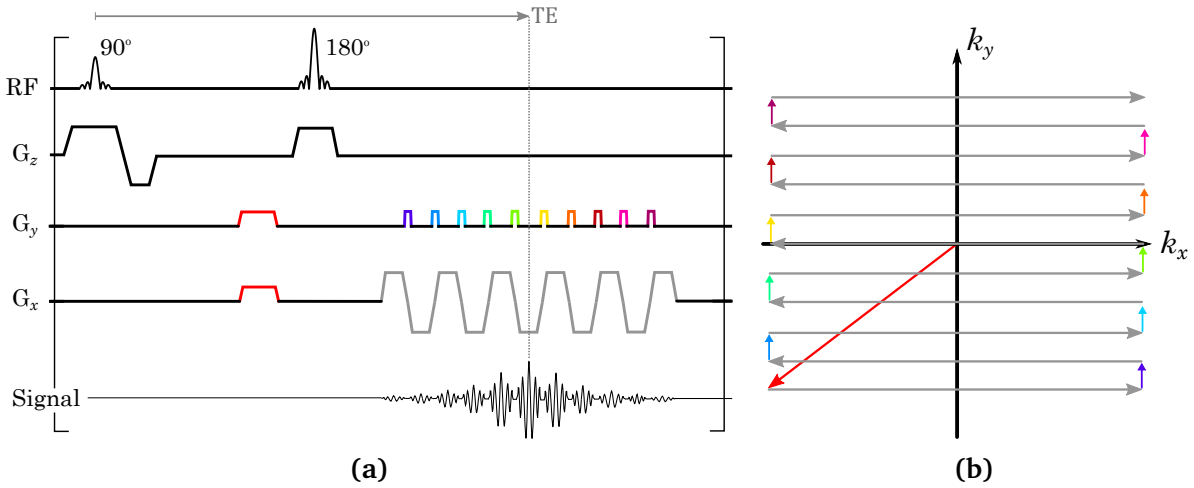

Figure 2.18: **(a)** SE-EPI pulse sequence used for sampling the whole of *k*-space during one TR period [52]. In practice the number of phase encoding pulses would be 64-128 [50]. **(b)** Corresponding *k*-space trajectory.

BW per voxel, are relatively small owing to the high sampling rate, such that distortion artefacts are often limited to being on a sub-voxel level. The PE direction is more vulnerable to distortion as the BW per voxel is relatively low (dictated by the period between PE blips).

2.2.5.4 Magnetisation-prepared rapid gradient echo

Whole-brain imaging of anatomical structures is commonly done using the 3D magnetisation-prepared rapid gradient echo (MP-RAGE) sequence, which is a rapid T_1-weighted acquisition method [26,53]. The sequence utilises a short TR and commences with a preparation pulse that inverts magnetisation in a given slice, serving to establish T_1-weighted contrast in a similar manner to IR. The 180° inversion pulse is followed by application of an excitation pulse and a spoiled gradient echo readout with a low flip angle (typically less than 8°) and a very short TR [26]. For 3D imaging, secondary phase encoding is applied along a third axis (e.g. slice selection) with respect to the frequency and phase encoding directions [26]. Structural T_1-weighted volumes acquired using MP-RAGE were used in the studies of this thesis for the purposes of image co-registration and for segmentation of images based on tissue type (grey matter, white matter, and cerebrospinal fluid or CSF) (discussed in Chapter 4).

2.2.5.5 Fluid-attenuated inversion recovery

Fluid-attenuated inversion recovery (FLAIR) is a variation of the IR method, used for obtaining images with T_2-weighted contrast whilst suppressing CSF contributions. In a FLAIR image, the signal from CSF is suppressed by using a long TI, adjusted such that CSF magnetisation transitions through a null point at the time of readout. Heavy T_2 weighting is imparted through the use of long TR and TE [54]. FLAIR images provide higher contrast between pathology and CSF than standard T_2-weighted acquisitions [54], and were used in the studies of this thesis for delineating the final stroke lesion (discussed in Chapter 4).

2.3 CEST mechanism

CEST MRI provides information on metabolites and metabolic processes by exploiting the chemical exchange of protons between metabolites and bulk water. Detecting the presence of metabolites directly is not possible as they exist in very low concentrations for which net magnetisation is close to zero. By using the large abundance of free (or bulk) water molecules in the body as a mediating mass for the metabolite of interest, CEST MRI achieves a large amplification of detection sensitivity. The detected signal is of the bulk water protons (the water 'pool'), but the CEST acquisition causes it to be modulated by chemical exchange effects of the metabolite species of interest (metabolite 'pool'). For instance, even though *in-vivo* concentration of amide groups is of the order of millimolars (estimated to be 71.9 mM [14]), detection sensitivity of several percent is achievable due to saturation build-up on the much larger water pool (112 M), which gives an enhancement of 100–1000 times.

2.3.1 Saturation transfer

Saturation of spins using an RF pulse is a process by which the distribution of spin energy levels is equalized, leading to a decrease in longitudinal magnetisation. If water

molecules are saturated with an RF pulse, efficient saturation necessitates that the pulse be well-tuned to the Larmor frequency of the ^{1}H protons bound to water (ω_0^w), and of sufficient amplitude and duration to reach equilibrium (Fig. 2.19a). Due to the abundance of water in the body, the Larmor frequency of bulk water is defined as 0 ppm (parts per million) denoting it to be the reference RF frequency in MRI:

$$\omega\ (\text{ppm}) = \frac{\omega - \omega_0^w}{\gamma \mathrm{B}_0} \times 10^6 \tag{2.41}$$

Thus, if a sweep of RF frequency is done across 0 ppm (e.g. -5 to 5 ppm), there would be a peak of saturation at water resonance and less saturation efficiency away from 0 ppm, as RF energy is absorbed less efficiently further out from water resonance. The saturation effect is symmetrical about 0 ppm and is illustrated in Fig. 2.19b on a so-called z-spectrum which plots M_z against an RF sweep.

CEST MRI exploits chemical exchange to indirectly measure protons attached to chemical groups apart from water. In a CEST experiment, rather than irradiating the water pool directly on resonance, the ^{1}H protons of the metabolite of interest are irradiated instead, having a slightly different Larmor frequency (a chemical shift) with respect to water. Positive chemical shifts (> 0 ppm) are referred to as being *downfield* of water. Downfield resonances are at a higher frequency than water resonance, as the protons are less shielded from the external magnetic field by neighbouring atoms (e.g. via the removal of electron spin density), exhibiting a stronger net magnetic field and therefore a higher Larmor frequency. Negative chemical shifts (< 0 ppm) are described as being *upfield* of water. Upfield resonances are at a lower frequency than water resonance as the protons exhibit a smaller effective external field owing to a greater degree of shielding from B_0. For amide molecules the chemical shift is 3.5 ppm downfield of water, or +3.5 ppm. When the metabolite pool is saturated, the decrease in metabolite pool M_z is not directly detectable. However, for a metabolite pool that is constantly exchanging ^{1}H protons with the water pool, the saturated metabolite protons begin to accumulate in the water pool for as long as the metabolite pool is being irradiated. If sat-

uration efficiency of the metabolite pool is good and persists for long enough, there will have been a sufficient proportion of unsaturated water protons exchanged for saturated metabolite protons, such that a detectable decrease in water M_z is occurs. This mechanism is illustrated in Fig. 2.20a. A large concentration of metabolites facilitates more throughput of exchanging protons, as does a high chemical exchange rate; therefore the amount of change in water M_z for a given excitation period can be reflective of the chemical composition (chemical shift, concentration) and metabolic activity (exchange

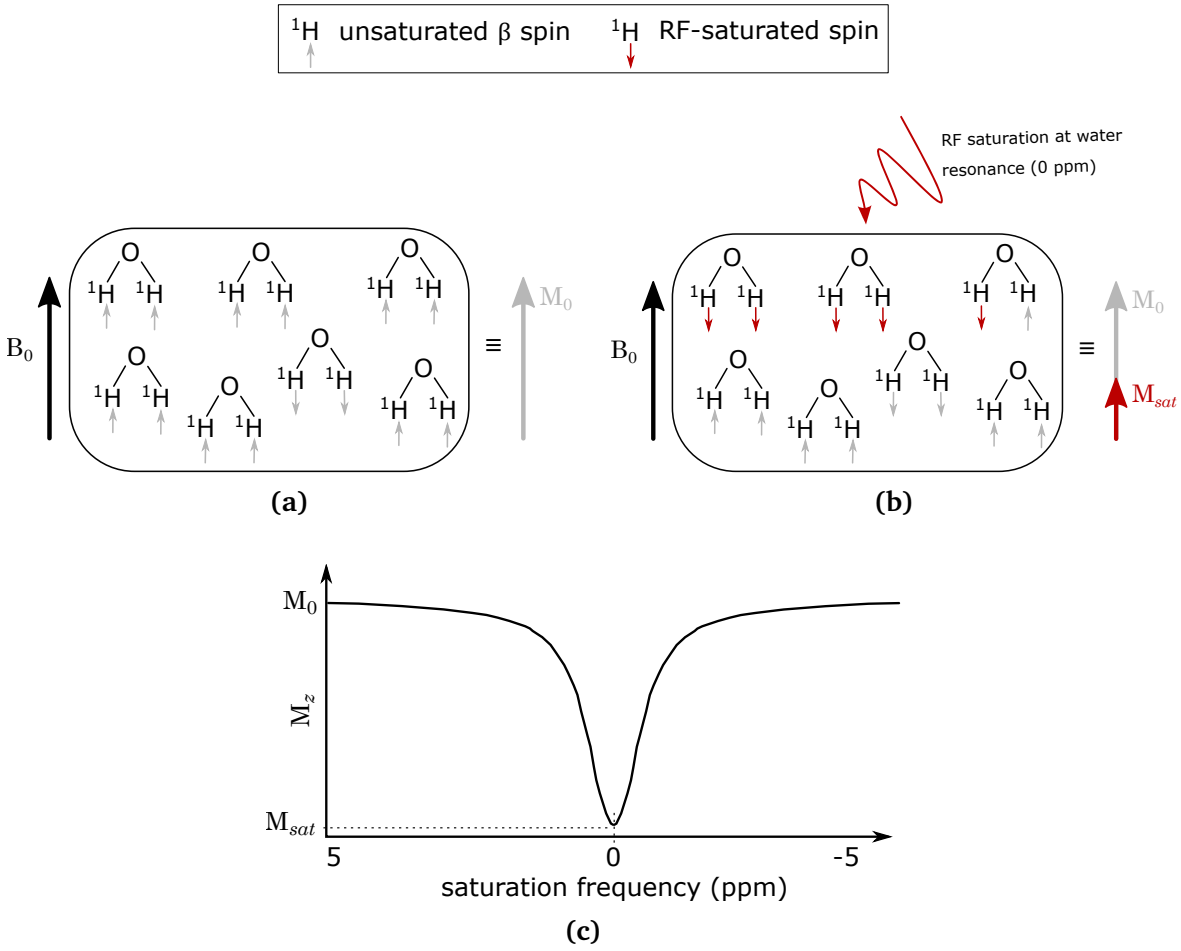

Figure 2.19: Illustration of the effect of RF saturation applied at the resonance frequency of water protons, shown for individual spins in **(a)**–**(b)**, and represented on a z-spectrum of water longitudinal magnetisation in **(c)**. **(a)** The water pool in the sample of tissue is initially at equilibrium, having equilibrium net magnetisation M_0 (grey M_0). **(b)** RF saturation is applied at the water resonance frequency 0 ppm in order to saturate most of the spins (red), leading to reduced net magnetisation, M_{sat}. **(c)** This is represented on the z-spectrum which graphs water M_z as a function of saturation frequency. There is a sharp resonance at 0 ppm and less efficient saturation off-resonance, forming the shoulders of the peak.

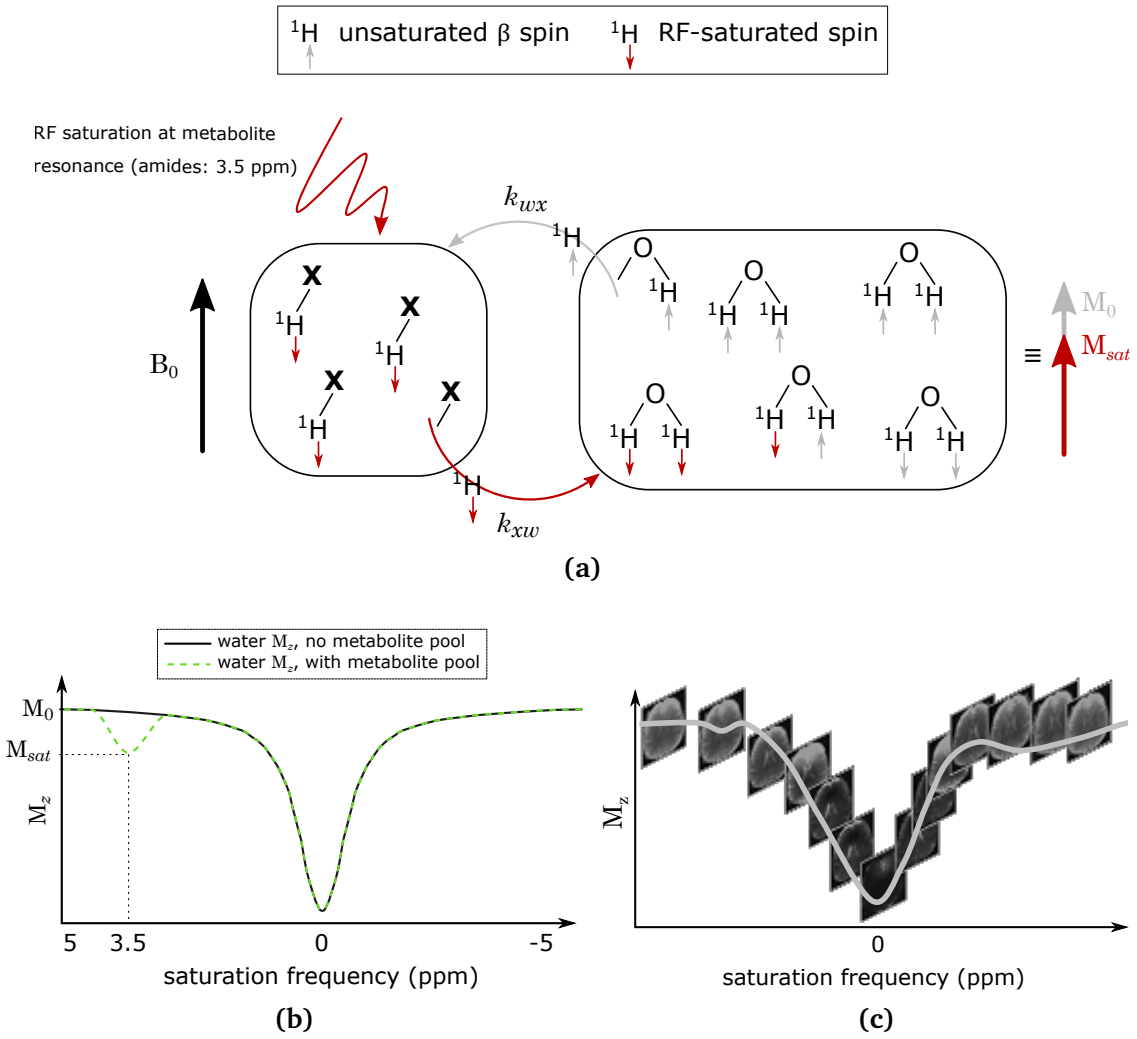

Figure 2.20: Illustration of saturation transfer via the CEST mechanism. **(a)** In a CEST experiment the metabolite pool of interest is saturated at its resonance frequency (in this example, amides at +3.5 ppm). By chemical exchange of the protons between the two pools (mediated by a forward exchange rate k_{xw}), the saturated metabolite spins accumulate on the pool. This reduces net water magnetisation. The corresponding reduction in M_z at this frequency is highlighted in **(b)**. **(c)** Single-slice CEST brain images. The grey trace represents the z-spectrum obtained from a single voxel as its intensity is traced across saturation frequency. There is a decrease in M_z at 0 ppm owing to saturation of the water pool.

rate) of metabolites in tissue. Amide molecules in particular, found along the backbone of proteins and peptides in cells, were one of the earliest endogenous contrast mechanisms used in CEST imaging of stroke as their chemical exchange interactions with water are pH-dependent.

Contrast associated with amides, for example, is achieved by selectively saturating proton spins at the pool's resonance frequency, which for the APT pool is at a chemical

shift of +3.5 ppm. The saturated amide protons then chemically exchange with bulk water, yielding a detectable loss of saturation on the water signal at +3.5 ppm (Fig. 2.20b).

Chemical exchange between a solute pool i and the water pool can be divided into three time-scales: slow ($k_{iw} \ll |\omega_0^i - \omega_0^w|$), medium ($k_{iw} \approx |\omega_0^i - \omega_0^w|$), and fast ($k_{iw} \gg |\omega_0^i - \omega_0^w|$) [55]. In the slow exchange regime, the resonance peak of solute pool i appears on the z-spectrum as a distinct peak from water resonance [56]. This is because each proton is on average within either the solute environment (pool) or the bulk water pool, resulting in sharp resonance peaks for both pools [56]. In the medium exchange regime, the protons move between the two pools during the experiment such that spectral broadening occurs and the peaks begin to merge [56]. In the fast exchange limit, the average proton moves rapidly between the two environments such that only the average value of the environments is observed, manifesting as a single resonance peak on the z-spectrum [56]. CEST effects are observed when the solute pool of interest is in the slow–intermediate regime. [35,57,58]. It is also necessary that k_{iw} is not much smaller than the longitudinal relaxation rate ($R_1 = 1/T_1$) for the exchanging pools, otherwise the accumulated saturation decays faster than the transfer of protons [59]. Therefore, the saturation of exchangeable protons must be fast enough to overcome relaxation, but slow on an NMR time-scale in order that it can be observed [10].

2.3.2 Bloch-McConnell formalism

The mathematical framework for describing CEST signal evolution is developed in this section, using, as a working example, the amide-water CEST mechanism illustrated in Fig. 2.20. An m-pool representation of the z-spectrum in the Bloch-McConnell formalism is illustrated in Fig. 2.21. Each pool i, where $i \in P, P = \{w, a, ..., m\}$, is characterised by its own T_1^i, T_2^i, Larmor frequency ω_0^i, and exchange rate. Referring to Fig. 2.21, the following relationships may be deduced. The model assumes no direct exchange between solute pools, or equivalently described by a zero exchange rate (denoting a

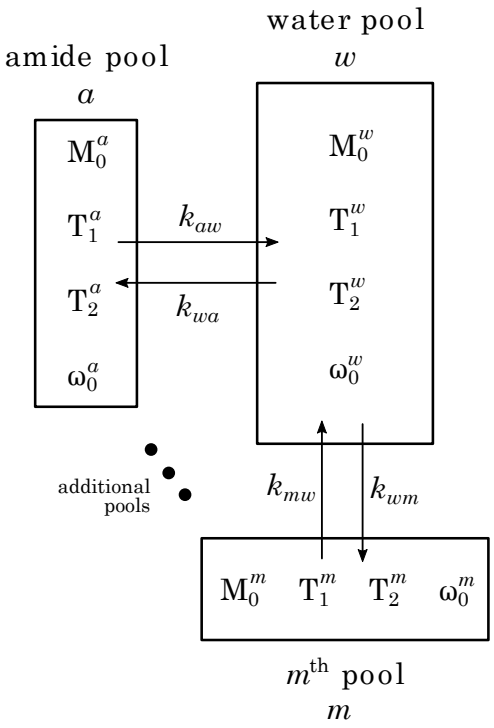

Figure 2.21: Diagram of an m-pool representation of the Bloch-McConnell equations, representing the interaction of small solute pools with the larger water pool: a bulk water pool, and pools a–m describing saturation effects from amides, and any further effects represented by additional pools. Each pool i is characterised by its own T_1^i, T_2^i, Larmor frequency ω_0^i, and exchange rates. There are no direct exchanges between the solute pools.

second pool as $j \in \mathrm{P}$): $k_{ij\ i\neq w, j\neq w} = 0$. Each pool is coupled to water via a forward and backward exchange rate. Each pool, in addition to losing magnetisation via forward exchange, is also losing magnetisation from internal relaxation processes with rates $R_1^i = 1/T_1^i$ and $R_2^i = 1/T_2^i$. The net longitudinal relaxation rate for pool i is a summation of its internal relaxation rate R_1^i and its forward exchange rate(s), similarly for pool i's transverse relaxation rate. A pool's net longitudinal and transverse decay rates may be written as [60,61]:

$$k_1^i = R_1^i + \sum_{j\in \mathrm{P}, j\neq i} k_{ij} \qquad k_2^i = R_2^i + \sum_{j\in \mathrm{P}, j\neq i} k_{ij} \tag{2.42}$$

The exchange terms defined above introduce coupling between the pools, each of which has a magnetisation vector $\mathbf{M}^i$. These modifications on the Bloch equations are known as the Bloch-McConnell (BM) equations. The system of coupled equations is first order

and linear. The x, y, and z components of pools i's magnetisation are [42]:

$$\begin{aligned}
\frac{d\mathrm{M}_x^i}{dt} &= -\Delta\omega_0^i \mathrm{M}_y^i - k_2^i \mathrm{M}_x^i + \sum_{j\in \mathrm{P}, j\neq i} k_{ji}\mathrm{M}_x^j \\
\frac{d\mathrm{M}_y^i}{dt} &= \Delta\omega_0^i \mathrm{M}_x^i - k_2^i \mathrm{M}_y^i + \sum_{j\in \mathrm{P}, j\neq i} k_{ji}\mathrm{M}_y^j + \omega_1 \mathrm{M}_z^i \\
\frac{d\mathrm{M}_z^i}{dt} &= \mathrm{M}_0^i \mathrm{R}_1^i - k_1^i \mathrm{M}_z^i + \sum_{j\in \mathrm{P}, j\neq i} k_{ji}\mathrm{M}_z^j - \omega_1 \mathrm{M}_y^i
\end{aligned} \tag{2.43}$$

These can be equivalently expressed in matrix form using the following definitions [42]:

$$\begin{aligned}
\mathbf{M}^i &= \begin{bmatrix} \mathrm{M}_x^i & \mathrm{M}_y^i & \mathrm{M}_z^i \end{bmatrix}^t & \mathbf{M} &= \begin{bmatrix} \mathbf{M}^w & \mathbf{M}^a & \cdots & \mathbf{M}^m \end{bmatrix}^t \\
\mathbf{B}^i &= \begin{bmatrix} 0 & 0 & \mathrm{M}_0^i \mathrm{R}_1^i \end{bmatrix}^t & \mathbf{B} &= \begin{bmatrix} \mathbf{B}^w & \mathbf{B}^a & \cdots & \mathbf{B}^m \end{bmatrix}^t \\
\mathbf{D}^i &= \begin{bmatrix} -k_2^i & -\Delta\omega_0^i & 0 \\ \Delta\omega_0^i & -k_2^i & \omega_1 \\ 0 & -\omega_1 & -k_1^i \end{bmatrix} & \mathbf{O}_{ij} &= \begin{bmatrix} 1 & 0 & 0 \\ 0 & 1 & 0 \\ 0 & 0 & 1 \end{bmatrix} k_{ji} \\
\mathbf{A} &= \begin{bmatrix} \mathbf{D}^w & \mathbf{O}_{wa} & \cdots & \mathbf{O}_{wm} \\ \mathbf{O}_{aw} & \mathbf{D}^a & \cdots & \mathbf{0} \\ \vdots & \vdots & \ddots & \vdots \\ \mathbf{O}_{mw} & \mathbf{0} & \cdots & \mathbf{D}^m \end{bmatrix}
\end{aligned} \tag{2.44}$$

where the matrix superscript t denotes the transpose. Using these definitions, the system has the form [52,62]:

$$\frac{d\mathbf{M}}{dt} = \mathbf{A}\cdot\mathbf{M} + \mathbf{B} \tag{2.45}$$

to which the analytical solution is:

$$\mathbf{M} = (\mathbf{M}_0 + \mathbf{A}^{-1}\mathbf{B})\boldsymbol{e}^{\mathbf{A}t} - \mathbf{A}^{-1}\mathbf{B} \tag{2.46}$$

$\boldsymbol{e}$ is the matrix exponential, and the initial condition, $\mathbf{M}(t=0)$, has been chosen to take the value of equilibrium magnetisation $\mathbf{M}_0$, i.e. $\mathbf{M}(t=0) = \mathbf{M}_0 = (0, 0, \mathrm{M}_0)$. The signal

detected in MRI is the water pool z magnetisation, M_z^w. Since a chemical exchange formalism is assumed, there is mass transfer (protons) which is conserved. This is expressed in the following relationship between the exchange rate and magnetisation vector of any two pools [60,61]:

$$k_{wi}M_0^w = k_{iw}M_0^i \qquad \rightarrow \qquad k_{wi} = k_{iw}\frac{M_0^i}{M_0^w} \tag{2.47}$$

The second term above indicates that for a known forward exchange rate and pool concentration, the back exchange rate k_{wi} is determined. The forward exchange rate is a physiological parameter of interest and generally 'exchange rate' is understood to be referring to this term.

2.3.3 Pulse sequences for CEST imaging

Pulse sequence schemes for saturation transfer imaging generally comprise two phases: RF irradiation to establish saturation transfer contrast, followed by a fast image readout scheme to minimise relaxation, such as EPI [52]. The two main CEST imaging schemes are continuous-wave (CW) RF saturation, and pulsed RF saturation, both of which have been employed in this thesis (see Chapter 4 for specific imaging parameters). An outline of these two schemes is presented in this section.

2.3.3.1 Continuous-wave saturation

Early CEST experiments employed CW saturation (Fig. 2.22), where a long rectangular RF pulse, of amplitude B_1 and saturation time $T_{sat} \gg T_1$, was applied at the desired off-resonance frequency before each excitation [42,52]. The saturation time is usually on the order of seconds, after which a crusher gradient is applied to suppress transverse magnetisation and the formation of unwanted echoes [10]. The saturation-excitation process is repeated every TR, with the repetitions ($N_{offsets}$) corresponding directly to a sweep of saturation frequencies across the z-spectrum (see Fig. 2.20c for an exploded

single-slice CEST imaging volume).

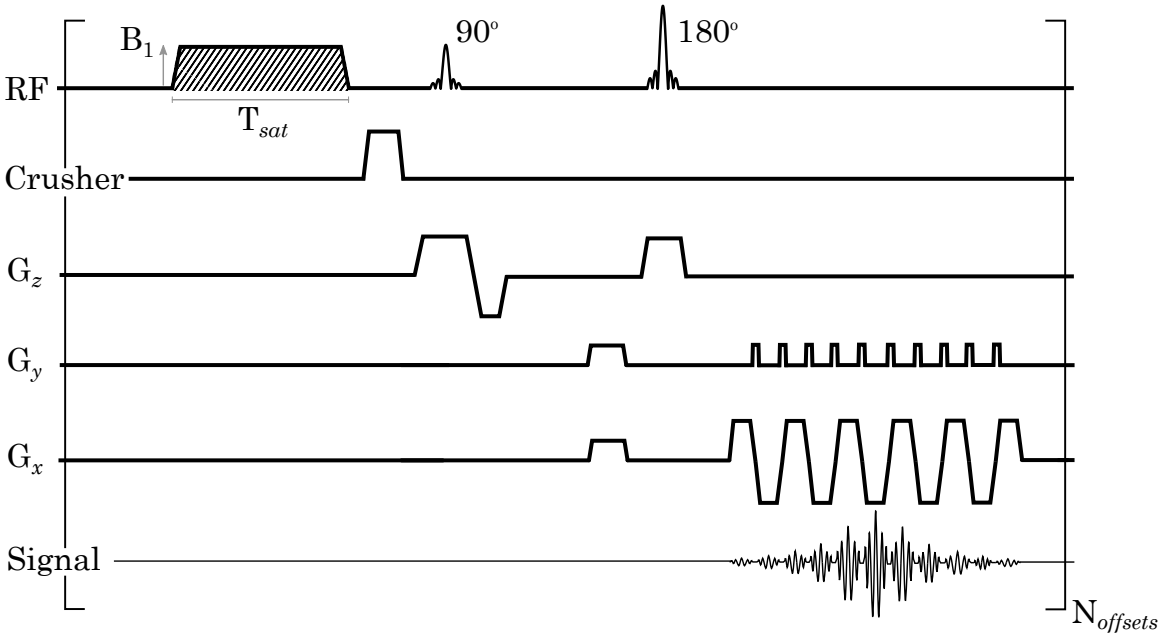

Figure 2.22: CW CEST MRI pulse sequence diagram. A long rectangular RF pulse of duration T_{sat} and amplitude B_1 prepares the CEST contrast by saturating spins at a given chemical shift. This is followed by image acquisition using a fast imaging sequence such as EPI. This is repeated every TR for each frequency offset on the z-spectrum that is to be acquired.

This simple CW saturation scheme has a number of benefits over a more complex pulsed scheme. Optimisation of saturation parameters for enhancing the CEST effect is more straightforward as the saturation phase depends only on B_1 and T_{sat}. In a CW scheme, steady state saturation and maximal CEST effects can be easily achieved using long saturation durations [10,30,52]. Another benefit is that long saturation times correspond to a narrow RF bandwidth, which allows for highly selective saturation of a given CEST resonance and narrower peaks on the z-spectrum [10,52]. CW saturation has two main drawbacks. In the context of clinical imaging, long saturation times can exceed specific absorption rate (SAR) safety limits (maximum RF power absorbed per unit mass of tissue), which would lead to unsafe levels of tissue heating and cannot be used for *in-vivo* imaging [10,52]. Most clinical scanners are also unable to generate long CW pulses (several seconds) owing to hardware limitations [10,52]. Therefore CW RF irradiation, when used in human imaging, must be done at a low power and for

shorter durations [52]. An alternative saturation scheme that overcomes some of these limitations is a pulsed scheme.

2.3.3.2 Pulsed saturation

A pulsed saturation scheme (Fig. 2.23) consists of a train of short RF pulses which are applied over a period of several seconds, leading to a gradual accrual of saturation transfer contrast. Each RF pulse is followed by a crusher gradient to nullify transverse magnetisation [10,52]. Pulsed saturation is more complex to optimise as the train of RF

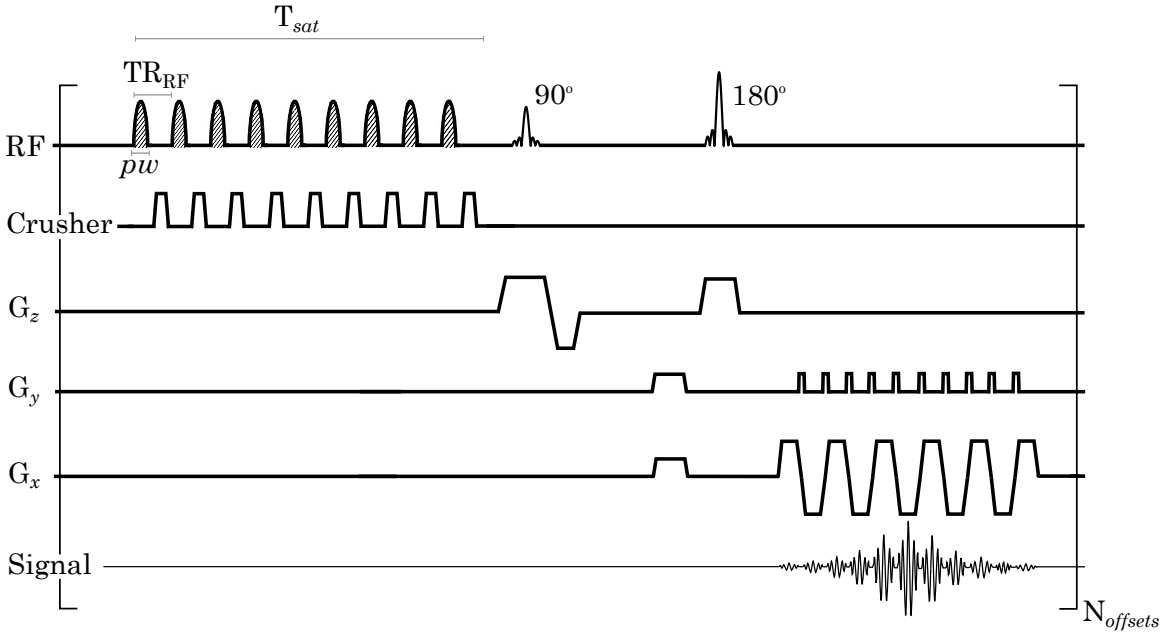

Figure 2.23: Pulsed saturation CEST MRI pulse sequence diagram. A train of RF pulses, of width pw and total period TR_{RF}, comprises the saturation phase of the CEST sequence which is of total duration T_{sat}. The parameters of the saturation phase, namely pulse shape, FA, pw, and TR_{RF}, can be optimised for maximal CEST contrast. Crusher gradients are used during the inter-pulse delay periods in order to nullify transverse magnetisation. The saturation phase is followed by image acquisition using a fast imaging sequence such as EPI. This is repeated every TR for each frequency offset on the z-spectrum that is to be acquired.

pulses is characterised by a number of tuneable parameters, including pulse shape, flip angle, pulse width (pw), pulse period (TR_{RF}), and the number of pulses per excitation. It is also less frequency-selective than CW saturation. The total saturation time, T_{sat}, is given by the product of the number of pulses and TR_{RF}. In a pulsed scheme the B_1 envelope is time-dependent, meaning that the analytical solution presented in equation

(2.46) is not valid and the BM equations must instead be solved by numeral integration which is computationally, expensive [52,63]. It has been shown that the equivalent RF power that maximises CEST contrast is approximately equal to the root mean square (RMS) of the pulse envelope B_{1e} [52,64]:

$$B_{1RMS} = \sqrt{\frac{1}{TR_{RF}} \int_0^{TR_{RF}} B_{1e}^2} \tag{2.48}$$

Studies on creatine phantoms have shown Gaussian-shaped pulses to exhibit higher frequency selectivity and contrast compared to sinc and rectangular pulses, and are commonly used [10,52].

A number of alternative saturation schemes have been proposed [10], but are not relevant to the imaging data in this thesis. They include spin locking [65], CEST phase mapping [66], saturation with frequency alternating RF irradiation [52], two-frequency RF saturation [67], chemical exchange rotation transfer [68], variable flip angle labelling [69], and variable-delay multi-pulse CEST [70].

2.4 Conclusion

In this chapter the quantum mechanical origins of tissue magnetisation were outlined and then expressed in terms of a classical description. The latter description provides a simplified and insightful way for understanding how macroscopic tissue magnetisation interacts with external magnetic fields, and how tissue properties can be measured through basic NMR experiments. The mathematical framework for this was extended to the CEST mechanism, describing how the presence of small concentrations of metabolites can be inferred through a CEST experiment. CEST imaging sequences relevant to this thesis were presented, and the particular experimental parameters in respect of them are detailed in Chapter 4. The z-spectrum was introduced as a representation for observing CEST interactions, and has been the subject of much research interest in

recent years owing its modulation by metabolic properties of tissue. The next chapter reviews the literature on CEST imaging in the context of tissue fate in ischaemic stroke, looking also at how information has been extracted from CEST data and the specific physiological changes that might underlie saturation transfer contrast.

Chapter 3

Literature review

3.1 Introduction

PROTEINS execute almost all cellular functions as well as being the building blocks of cells. They can be broadly classified by their mobility into two categories: semisolid (immobile) proteins, and labile (mobile) proteins [71]. The absorption of RF energy by mobile proteins, such as cytosolic and secreted proteins [71], can be further divided into two broad categories: RF energy absorbed by physically-exchangeable protons, and RF energy absorbed by non-exchangeable protons. Exchangeable, or labile, protons are those that are loosely bound to their resident molecule and can be physically swapped with protons of bulk water. Chemical exchange from labile protons is present in a number of places on the downfield part of the z-spectrum. Two such effects that are commonly studied are amides at 3.5 ppm (—NH protons) and amines at 1.8 ppm (—NH_2 protons) [72–77]. CEST signals from amide and amine proton transfer are of interest as the molecules are present in relative abundance *in-vivo*, offering an endogenous contrast mechanism, and they exhibit sensitivity to pH, which is a physiological parameter of interest in pathological conditions including ischaemic stroke. Amines, which are commonly used to quantify CEST effects in creatine phantoms, exhibit a peak width of approximately 0.8–3.0 ppm (field-dependent) [73–75,78] but their proximity to water resonance makes it difficult to

detect amine CEST signals in a clinical setting [58,79].

On mobile macromolecules, non-exchangeable protons are those that are tightly bound to their resident macromolecule through covalent C − H bonds and their effects manifest upfield of water. Lipids are largely composed of C − H and C = H bonds and the z-spectrum upfield of water may exhibit particular sensitivity to mobile lipid concentration. Magnetisation is transferred to bulk water from these bound protons via through-space coupling effects (dipole-dipole interaction) rather than by physical proton exchange. This dipolar coupling of saturation from non-exchangeable protons on mobile species is referred to as the nuclear Overhauser (NOE) effect, which is thought to be a compound effect from both through-space and chemical exchange pathways, appearing as multiple resonances between −2 to −5 ppm [72]. As a through-space dipolar coupling effect, NOEs are strongly dependent on the correlation time of coupled protons, which also determines the sign of the NOE; NOEs can either effect an increase in M_z (positive NOEs), or a decrease in M_z (negative NOEs) [80]. This thesis focuses on biological tissue, where the presence of large mobile macromolecules (LMMs), which are relatively restricted in motion (short T_2) and have long correlation times, gives rise to exclusively net negative NOEs [80,81]. In the NMR literature NOEs strictly describe through-space intramolecular coupling of magnetization, but in CEST studies they can also be referring to a compound of through-space coupling and intermolecular relay of magnetization [72,74].

Semisolid proteins in tissue, composed of immobile macromolecules, include membrane proteins, nuclear proteins, and lipids in myelin that are commonly believed to be in a solid phase [74,82]. Semisolid tissue exhibits broadband absorption of RF energy on the order of tens of ppm [57,72,74] which does not allow selective saturation of individual constituent resonances [74]. This pool has a short T_2 (around 10 μs [74]) as dipolar interactions between densely-packed neighbouring molecules in the semisolid lattice facilitate high efficiency energy transfer between spins, leading to rapid dephasing. This occurs at a rate that is too fast to observe directly in a CEST MRI experi-

ment [30]. Proton mobility, characterised by T_2, determines the efficiency with which magnetisation is transferred through dipolar coupling, with low mobility (short T_2) being more efficient at dipolar coupling due to the more restricted motion and increased spectral density of neighbouring spins [57]. This spin diffusion process, or fast through-space dipolar transfer, is followed by transfer of magnetisation to bulk water [30,57].

Direct saturation (DS) of bulk water protons by the RF field results in a narrow (< 1 ppm) notch-like saturation profile that is symmetric and centred about water resonance [72]. Cerebrospinal fluid (CSF) in the ventricles and around the periphery of the brain mostly exhibits a DS effect [72].

CEST studies generally identify four saturation transfer processes on a z-spectrum: DS at 0 ppm, APT saturation effects at +3.5 ppm, a composite of upfield saturation effects between -2 to -5 ppm originating from NOEs, and a broadband saturation profile originating from semisolid tissue. The appearance of these effects on the z-spectrum is illustrated in Fig. 3.1. The relatively few samples acquired in clinical scanning, limitations on transmit power and duration, and field strengths of 3 T or below, mean that additional effects beyond DS, APT, NOEs, and semisolid saturation have not been consistently observed in clinical imaging studies. Analysis techniques for quantifying these CEST effects are presented next, followed by a review of their applications in the stroke and oncological CEST literature.

3.2 Quantification techniques

The challenge to accurate quantification has been the heterogeneous *in-vivo* environment of human tissue, which exhibits several confounding magnetization effects including spillover of direct water saturation, broadband magnetization transfer from semisolid tissue, an overlapping of metabolite peaks due to their relatively broad spectra, nearness of metabolite peaks to the large water peak (< 10 ppm), asymmetry of the z-spectrum, as well as noise and artefact [32,72,74].

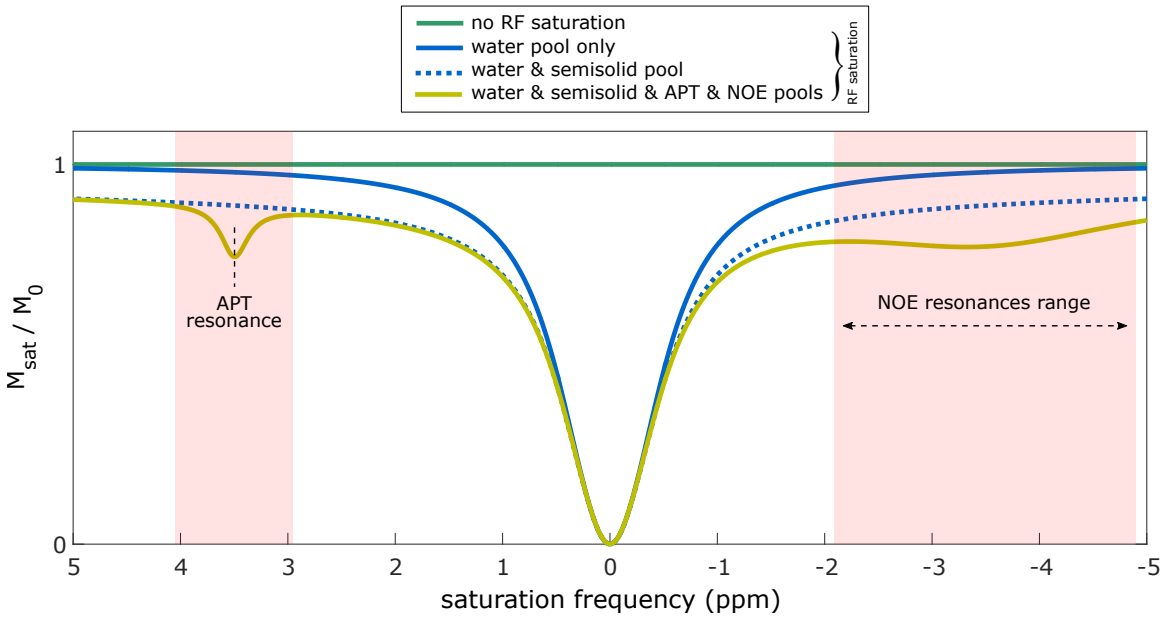

Figure 3.1: Normalised z-spectrum showing how the inclusion of different CEST resonances affects water magnetisation M_z. With no saturation, water M_z (normalised to M_0) (dark green) is at unity as it is unsaturated. When the water pool is directly irradiated (solid blue), energy absorption, hence the saturation of spins (and loss of M_z), is maximal at 0 ppm (DS line shape). When semisolid tissue is present (dotted blue) it overlays a broadband saturation effect on the spectrum. The presence of APT at +3.5 ppm saturates M_z further but only within a narrow resonance range. Upfield of water, NOEs introduce further saturation effects.

Early APT CEST studies tended to employ relatively simple measures of spectral asymmetry for quantification which assume a broad featureless spectrum upfield of water resonance as a fixed reference. This assumption has been undermined by the realisation that the upfield spectrum is not a good reference for asymmetry techniques due to the relatively prominent asymmetric NOEs. The recent literature has introduced various approaches to CEST analysis that seek to overcome the limitations of an asymmetry analysis when NOEs are present, of which both model-free and model-based solutions exist. A description of these techniques is presented below.

Table 3.1 and Table 3.2 respectively list model-free and model-based quantification techniques that have been reported in the CEST MRI literature. The model-free quantification techniques (Table 3.1) discussed are asymmetry analysis, local linear approximation, and spillover-corrected MTR. The model-based techniques (Table 3.2) are Lorentzian difference analysis and Bloch-McConnell model (BMM) analysis.

Table 3.1: Model-free APT quantification techniques. $S(\omega)$ is the acquired z-spectrum and S_0 is the unsaturated acquisition.

Model-free technique	General form	Parameters	References
$MT_{asym}(3.5\text{ ppm})$	$\frac{S(-\omega_1)-S(\omega_1)}{S_0}$	$\omega_1 = 3.5$ ppm	[72,74]
$MT^{enh}_{asym}(3.5\text{ ppm})$	$\frac{\int_{-\omega_2}^{-\omega_1} S(\omega)d\omega - \int_{\omega_1}^{\omega_2} S(\omega)d\omega}{\int_{-\omega_2}^{-\omega_1} 1 - S(\omega)d\omega}$	$\omega_1 = 2.9$ ppm $\omega_2 = 4.1$ ppm	[36,83]
$APTR_{LLA}$	$\left[\frac{S(\omega_1)+S(\omega_2)}{2} - S(\omega_3)\right]\cdot\frac{1}{S_0}$	$\omega_1 = 2.9$ ppm $\omega_2 = 4.1$ ppm $\omega_3 = 3.5$ ppm	[34]
$MTR_{Rex}(APT)$	$\left[\frac{1}{S(\omega_3)} - \frac{2}{S(\omega_1)+S(\omega_2)}\right]\cdot S_0$	$\omega_1 = 2.9$ ppm $\omega_2 = 4.1$ ppm $\omega_3 = 3.5$ ppm	[34,42,84–86]

Table 3.2: Model-based APT quantification techniques. $S^{acq}(\omega)$ is the acquired z-spectrum and S_0 is the unsaturated acquisition. $S^{BMM}_{[pools]}$ is the z-spectrum obtained through BM model fitting, the subscript $[pools]$ refers to the combination of CEST pools for which the simulated z-spectrum is obtained: w (water pool), a (APT pool), and s (semisolid pool).

Model-based technique	General form	Parameters	References
$APTR_{LDA}$	$\int_{\omega_1}^{\omega_2} \frac{S^{fit}(\omega) - S^{acq}(\omega)}{S_0^{acq}} d\omega$	$\omega_1 = 2.9$ ppm $\omega_2 = 4.1$ ppm $fit: water\ Lorentzian$	[57]
$APTR_{paLDA}$	$\int_{\omega_1}^{\omega_2} \frac{S^{BMM}_{w+s}(\omega) - S^{acq}(\omega)}{S_0^{BMM}} d\omega$	$\omega_1 = 2.9$ ppm $\omega_2 = 4.1$ ppm	Based on [57,87–89]
BM model (BMM) APTR*	$\frac{S^{BMM}_{w}(\omega_1) - S^{BMM}_{w+a}(\omega_1)}{S_0^{BMM}}$	$\omega_1 = 3.5$ ppm	[36,62,90]

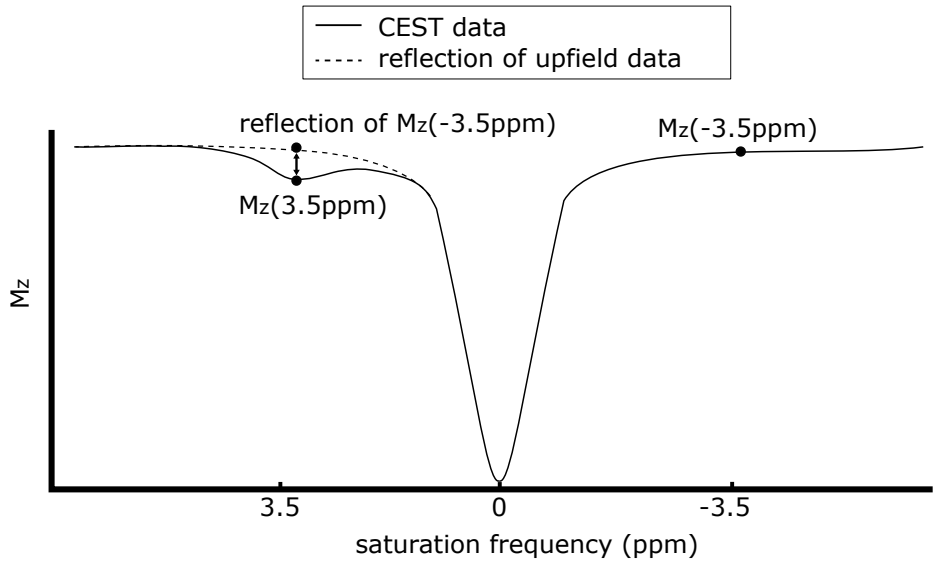

Figure 3.2: Illustration of the classical MT asymmetry technique for measuring APT effect size. The upfield portion of the acquired CEST data are mirrored and used as a baseline reference for measuring the size of the peak at 3.5 ppm. In this idealised case the upfield portion is shown as uniform, but in practice there are other CEST effects that influence this measurement, NOEs in particular due to the asymmetry they impart to the z-spectrum.

3.2.1 Model-free quantification

3.2.1.1 Asymmetry analysis ($\mathbf{MT_{asym}}$ and $\mathbf{MT^{enh}_{asym}}$)

The first studies that investigated APT effects did so using a simple measure of spectral asymmetry, MT_{asym}, which had previously been used for generating tumour tissue contrast and semisolid MT-weighted images. Semisolid MT has been associated with higher lipid content of white matter (WM) tissue, which facilitates rapid magnetisation transfer via spin diffusion owing to its much shorter T_2 compared to surrounding water [91–93]. For example, it has been used in identifying white matter disease, which is marked by demyelination of nerve axons in white matter, yielding lower magnetisation transfer ratios [91]. This technique is illustrated in Fig. 3.2.

Asymmetry analysis inherently captures changes on both sides of the z-spectrum together, and when used as a measure of APT, it relies on one side being constant in the face of any change in APT (such as pH effects). It has become evident that APT asymmetry can be strongly diluted in the presence of competing saturation effects in

pathology such as ischaemia [34], in particular non-specific semisolid MT, water T_1, spillover from direct water saturation, and most notably, spectral asymmetry [34]. The conceptual and computational simplicity of MT_{asym} means that it continues to be widely used for measuring CEST effects [74,94,95]. The presence of asymmetric NOEs in the upfield spectrum means that an asymmetry-based approach to quantification would not establish a good reference for simple relative measures of APT, making their use limited where specifically the APT effect is of interest and particularly in quantitative analysis. For instance, at low B_1 powers ($\sim 0.6\ \mu$T) NOEs typically dominate, giving $MT_{asym}(3.5\text{ ppm}) < 0$. At relatively high saturation powers ($\sim 1.0\ \mu$T) APT effects dominate, giving $MT_{asym}(3.5\text{ ppm}) > 0$ [72,74]. In-between these B_1 limits APT and NOEs may directly cancel out. Thus the sign of $MT_{asym}(3.5\text{ ppm})$ can reflect how dominant a particular saturation peak is and becomes more strongly APT-weighted or NOE-weighted depending on which end of the B_1 range saturation is applied.

A number of variations on MT_{asym} have been presented to suit different peak profiles, proximity to water resonance, and saturation efficiencies [83]. The study of ref. [83] found that averaging the spectra by integration rather than using point-based measures was more robust and had higher contrast *in-vivo* with paramagnetic CEST agents, referred to as enhanced MT asymmetry or MT^{enh}_{asym} [83].

3.2.1.2 Local linear approximation ($APTR_{LLA}$)

Larger B_0 fields result in larger-amplitude CEST effects due to proportionality with water T_1. Wider spectral separation associated with larger B_0 also allows more accurate delineation of the spectral boundaries of the APT peak. Jin et al. [72] developed a quantification technique, used at 9.4 T, that identified upper and lower frequency boundaries for the APT peak. A line segment connecting the two points gave a linear approximation to non-APT effects over that narrow spectral range (a local linear approximation, LLA), with the midpoint corresponding to the location of the APT peak maximum, against which the APT effect observed in the data at 3.5 ppm could be calculated. This tech-

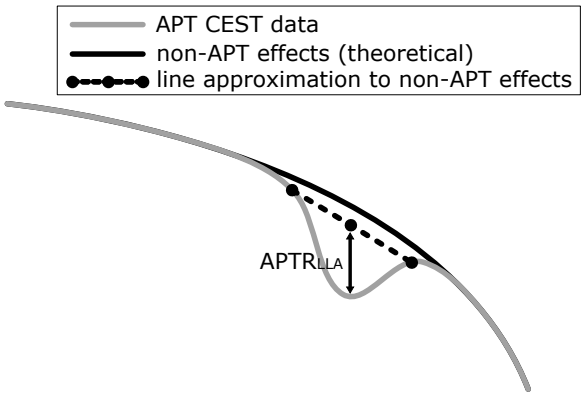

Figure 3.3: Illustration of the LLA technique for quantifying CEST effects, shown for APT. A line segment is used to locally approximate non-APT effects, such that the height of the acquired CEST data relative to the line is an approximation to APT-only effects. The line segment is defined using the observed upper and lower boundaries of the APT peak.

nique is illustrated in Fig. 3.3.

The LLA technique can be considered as an extreme simplification of z-spectrum fitting where all effects apart from APT are locally linearly approximated. It is advantageous over pixel-wise model fitting of the BM equations as the latter requires comprehensive sampling of the z-spectrum so that several parameters can be fitted using relatively small signal magnitudes [72]. The study reported a fitting error of less than 1% at the NOE peak. A possible improvement is to use a spline fit rather than linear interpolation for estimating the reference signal at ω_0 [34].

The accuracy of this technique depends on how precisely the peak boundaries can be delineated and how well the linear approximation, which inherently underestimates signal amplitude, resembles the convex spectral profile. At lower fields, such as 3 T used clinically, clear delineation of the APT peak is difficult. This is compounded by the use of pulsed, versus continuous-wave, CEST schemes which are necessary for limiting tissue heating within clinical safety bounds at the expense of being less frequency-selective. It is also necessary to have sufficient sampling points at the boundaries and at the peak in order that they can be accurately located. Higher saturation powers also broaden CEST peaks, which reduces the accuracy of quantification using this technique [34]. This technique has also been reported to be insensitive to changes in tissue pH when

used to quantify NOEs [57].

3.2.1.3 Spillover-corrected MTR (MTR_{Rex})

MTR_{Rex} is similar in form to the LLA measure, the difference being that it inverts the z-spectrum in order analytically eliminate relaxation terms arising from DS, and semisolid effects, yielding a less contaminated measure of APT [84].

This was further developed into a T_1-independent measure of exchange rate based on equivalence between spin-locking and CEST experiments; the apparent exchange-dependent relaxation measure, or AREX [42,84,85]. Quantitative T_1 maps are used that theoretically cancel out dependence on water T_1. AREX is obtained by multiplying MTR_{Rex} by the water relaxation rate to yield a quantitative T_1-corrected measure of chemical exchange effects [84]. This helps to correct for the effects of water relaxation, which is significantly enhanced in tumours. AREX(NOE) has been shown to significantly enhance tumour contrast compared to the LLA technique, which does not exhibit strong contrast [86]. AREX(APT) has also shown greater *in-vivo* ischaemic core contrast than the LLA technique, with a CNR in animal stroke models of of 3.21 versus 2.43 [34].

3.2.2 Model-based quantification

3.2.2.1 Lorentzian difference analysis ($APTR_{LDA}$)

The conventional Lorentzian difference analysis (LDA) technique proposed by Jones et al. is based on steady-state saturation of tissue with low-amplitude RF pulses such that broadband fast-exchanging semisolid effects are minimised, whilst maximising slow-exchanging APT and NOEs [57,87]. It is a semi-model-based technique in which model fitting is used to remove the water signal baseline from the acquired data. The resulting z-spectrum can be described as simply a combination of water DS (a Lorentzian line shape whose parameters are estimated from the data), and the slow-exchanging solute pools of interest [88]. This technique is illustrated in Fig. 3.4. At 7 T a range of different z-spectral effects have been observed, which could be associated with both

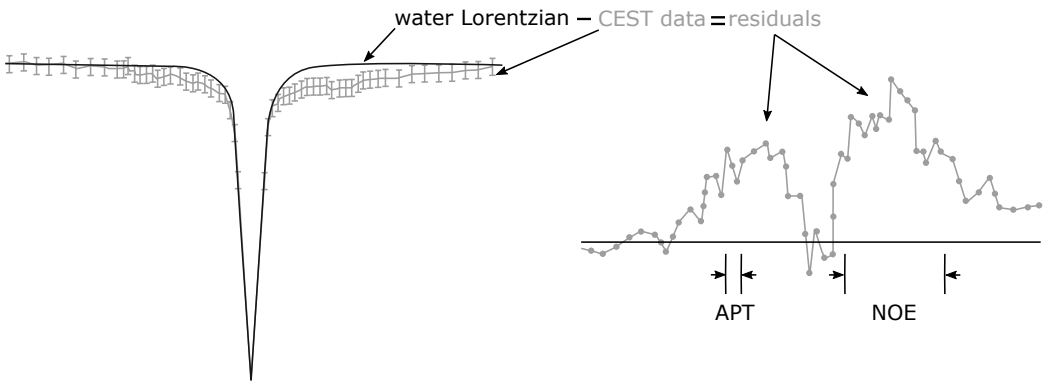

Figure 3.4: Illustration of the LDA technique. CEST data acquired using a low-power scheme (grey) are subtracted from a simulated water line shape (black), to give residuals that are minimally affected by higher-power broadband semisolid effects.

chemical exchange and NOE relayed transfer effects. Subtracting the z-spectrum from the fitted water line shape yields the independent contributions of APT and NOE. The fitted Lorentzian line shape is given by [57,87]:

$$\mathrm{L}\left(\mathrm{A}, b, \mathrm{LW}_{\frac{1}{2}}, f_0, f_{shift}\right) = 100 - \mathrm{A}\left(\frac{\left(\mathrm{LW}_{\frac{1}{2}}\right)^2}{\left(\mathrm{LW}_{\frac{1}{2}}\right)^2 + 4\left(f_0 - f_{shift}\right)^2}\right) + b \qquad (3.1)$$

where A is the amplitude, $\mathrm{LW}_{\frac{1}{2}}$ is the water full-width half-maximum (FWHM) linewidth, f_0 is the bulk water pool resonance frequency, f_{shift} is the frequency offset of the z-spectrum due to B_0 inhomogeneity, and b is a baseline offset [87]. The acquired signal is fitted to the water peak ($|\omega_{\mathrm{RF}}| < 0.7$ ppm) [88], and far away from the water peak ($|\omega_{\mathrm{RF}}| > 8$ ppm in ref. [96]) where any residual semisolid effects are further reduced [57,88,89].

3.2.2.2 Extrapolated semisolid MT reference (CEST$^{\#}$)

In the model fitting process of the LDA technique, both asymmetric and symmetric models of semisolid effects have been used, where the wide-offset data points used for fitting are from one or both sides of the z-spectrum [97]. The asymmetric model was reported to give erroneous results for NOEs, with the single-sided symmetric MT model yielding the highest contrast in a human glioma study [97]; this is more commonly

referred to as the extrapolated semisolid MT reference (EMR) technique [98]. A feature of this approach is that, like LDA, it permits utilisation of information in the raw data to a greater extent than fully model-based approaches, as, in the process of subtracting the raw data from the EMR baseline, the structure of the fine composite spectra are preserved.

3.2.2.3 Post-acquisition LDA ($APTR_{paLDA}$)

The post-acquisition LDA technique (paLDA), used in Chapter 5, is a semi-model-based technique which works by having the data acquired using a conventional CEST scheme rather than applying an ultra-low B_1 during the acquisition phase. Only the data points that are expected to exclude APT and NOEs are used for model fitting, such as the data points at ±300 ppm, ±50 ppm, ±30 ppm, ±0.6 ppm, ±0.3 ppm, and 0 ppm. These data points are fitted to a 2-pool BM model comprising water and semisolid effects. Subtraction of the acquired z-spectrum from the fitted spectrum yields a downfield APT residual in a similar way to conventional LDA.

3.2.2.4 Multi-Lorentzian line shape fitting

A fully model-based technique that bears some similarly with LDA is multi-Lorentzian line shape fitting. Using this technique, the fitting is done purely in terms of isolated Lorentzian line shapes discernible in the data [80]. It is therefore a non-physical model-based technique, as the line shapes are not generated from underlying physically-meaningful variables. This is in contrast to a fully model-based technique that is physical, discussed next.

3.2.2.5 Physical model ($APTR^{*}$)

Fitting CEST data to a BM model (BMM) is distinct from the aforementioned quantification techniques in that it is a physical model: the fitted z-spectra are generated from a set of model parameters that directly describe the underlying physical parameters, such

as exchange rates, relaxation times, and metabolite concentrations[1]. BM model-based analysis is also quantitative in its measure of CEST effects, attempting to extract an exact measure of CEST signals in non-arbitrary physical units [100]. This is as opposed to non-quantitative or semi-quantitative measures, where the images being generated are for visual interpretation, or are in arbitrary units that are converted into statistical measures for subsequent analysis [100]. Quantitative measures are, in principle, consistent and reproducible between repeat scans, different scanners, and imaging sites [100]. This is because they incorporate variables that directly account for different physical causes of variability, both physiological and artefactual (such as a non-uniform B_0 field which would otherwise introduce artefactual variability into the quantification).

Magnetisation exchange interactions between bulk water and different metabolites are described by separate exchange pools, with each pool transferring saturation to the main water pool on which a signal accumulates. Each pool is described by a set of BM equations coupled together through mass-conserving exchange rates (equation 2.43). The four CEST processes outlined in Section 3.1 can, as an approximation, be modelled by simply extending the 2-pool BMM example of Fig. 2.21, to four pools. A 4-pool BM model for modelling the z-spectrum is illustrated in Fig. 3.5. Each pool i, where $i \in \mathrm{P}$ and $\mathrm{P} = \{w, a, n, s\}$, is characterised by its own T_1^i, T_2^i, Larmor frequency ω_0^i, and exchange rates. Full expansion of equation (2.43) in matrix form, assuming 4 pools, gives matrix (3.2). Using the matrix definitions in equation (2.44), matrix (3.2) can be written in the form of equation (2.45), to which the analytical solution is equation (2.46) [62]. Whilst NOEs and semisolid pool saturation are not strictly chemical exchange effects, this same pool-based mathematical model has been shown to phenomenologically describe CEST data well [32,61].

[1]The BMM analysis technique for quantifying CEST signals is also known as the multi-pool analysis technique in the CEST literature [36,62,99]. In this thesis the BMM acronym is used to differentiate it as a physical model, in contrast to non-physical model-based approaches.

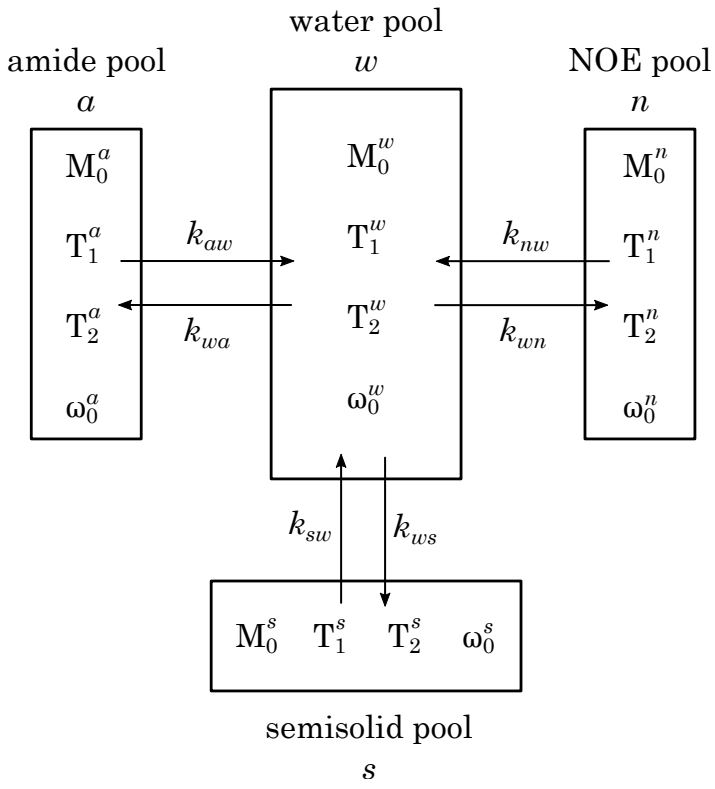

Figure 3.5: Diagram of a 4-pool BM model representing the interaction of small solute pools with the larger water pool: a bulk water pool, and a pool to describe the saturation effects from APT, NOEs, and semisolid tissue. Each pool i is characterised by its own T_1^i, T_2^i, Larmor frequency ω_0^i, and exchange rates. There are no direct exchanges between the solute pools.

$$\frac{d}{dt}\begin{bmatrix} M_x^w \\ M_y^w \\ M_z^w \\ M_x^a \\ M_y^a \\ M_z^a \\ M_x^n \\ M_y^n \\ M_z^n \\ M_x^s \\ M_y^s \\ M_z^s \end{bmatrix} = \begin{bmatrix} -k_2^w & -\Delta\omega_0^w & 0 & k_{aw} & 0 & 0 & k_{nw} & 0 & 0 & k_{sw} & 0 & 0 \\ \Delta\omega_0^w & -k_2^w & \omega_1 & 0 & k_{aw} & 0 & 0 & k_{nw} & 0 & 0 & k_{sw} & 0 \\ 0 & -\omega_1 & -k_1^w & 0 & 0 & k_{aw} & 0 & 0 & k_{nw} & 0 & 0 & k_{sw} \\ k_{wa} & 0 & 0 & -k_2^a & -\Delta\omega_0^a & 0 & & & & & & \\ 0 & k_{wa} & 0 & \Delta\omega_0^a & -k_2^a & \omega_1 & & & & & & \\ 0 & 0 & k_{wa} & 0 & -\omega_1 & -k_1^a & & & & \mathbf{0} & & \\ k_{wn} & 0 & 0 & & & & -k_2^n & -\Delta\omega_0^n & 0 & & & \\ 0 & k_{wn} & 0 & & & & \Delta\omega_0^n & -k_2^n & \omega_1 & & & \\ 0 & 0 & k_{wn} & & & & 0 & -\omega_1 & -k_1^n & & & \\ k_{ws} & 0 & 0 & & & \mathbf{0} & & & & -k_2^s & -\Delta\omega_0^s & 0 \\ 0 & k_{ws} & 0 & & & & & & & \Delta\omega_0^s & -k_2^s & \omega_1 \\ 0 & 0 & k_{ws} & & & & & & & 0 & -\omega_1 & -k_1^s \end{bmatrix} \begin{bmatrix} M_x^w \\ M_y^w \\ M_z^w \\ M_x^a \\ M_y^a \\ M_z^a \\ M_x^n \\ M_y^n \\ M_z^n \\ M_x^s \\ M_y^s \\ M_z^s \end{bmatrix} + \begin{bmatrix} 0 \\ 0 \\ M_0^w R_1^w \\ 0 \\ 0 \\ M_0^a R_1^a \\ 0 \\ 0 \\ M_0^n R_1^n \\ 0 \\ 0 \\ M_0^s R_1^s \end{bmatrix} \tag{3.2}$$

By model fitting of matrix (3.2) to the CEST data, spectral contributions of different species can be isolated from the CEST z-spectrum. This has been exploited previously to define the apparent APT ratio, APTR* [36,37,62,90], where a 3-pool model comprising water, APT, and combined semisolid and NOE contributions, was used to isolate APT effects. After fitting multiple pools to the spectral data, only a subset are simulated to predict the effect arising from a single pool, or a combination thereof. The apparent APT ratio, APTR*, is obtained by simulating the combined amide and bulk water pools, ignoring any other pools included in the fit to the original z-spectral data, and comparing this to a simulation of only the water pool. APTR* is then the difference between the two predictions at +3.5 ppm. A high-level outline of this process is shown in Fig. 3.6.

In the same way the apparent NOE ratio, NOER*, is obtained by simulating the combined NOE and bulk water pools, ignoring any other pools, and comparing this to a simulation of only the water pool. NOER* is then the difference between the two predictions at −3.5 ppm (Fig. 3.7). Similarly, the apparent semisolid effects ratio, semisolidR*, is obtained by simulating the combined semisolid and water pools, ignoring any other pools included in the fit, and semisolidR* is then the difference between the two predictions evaluated at 50 ppm[2]. In general, when using a BM model, the frequency at which the effect of a metabolite pool is quantified is the same as the pool's resonance frequency, as that is where the maximum signal change can be measured. In the case of a symmetric semisolid pool, whose resonance frequency (0 ppm) is identical to the water pool, it is not possible to make a meaningful measurement on resonance as the signal is dominated by water DS. For this reason, the offset of 50 ppm was chosen, similar to that used in classical semisolid MT experiments [101].

[2]In this thesis, CEST metrics suffixed 'R*' (e.g. APTR*, NOER*, semisolidR*) refer exclusively to the BMM technique, as do references to the number of pools, such as '3-pool' and '4-pool'.

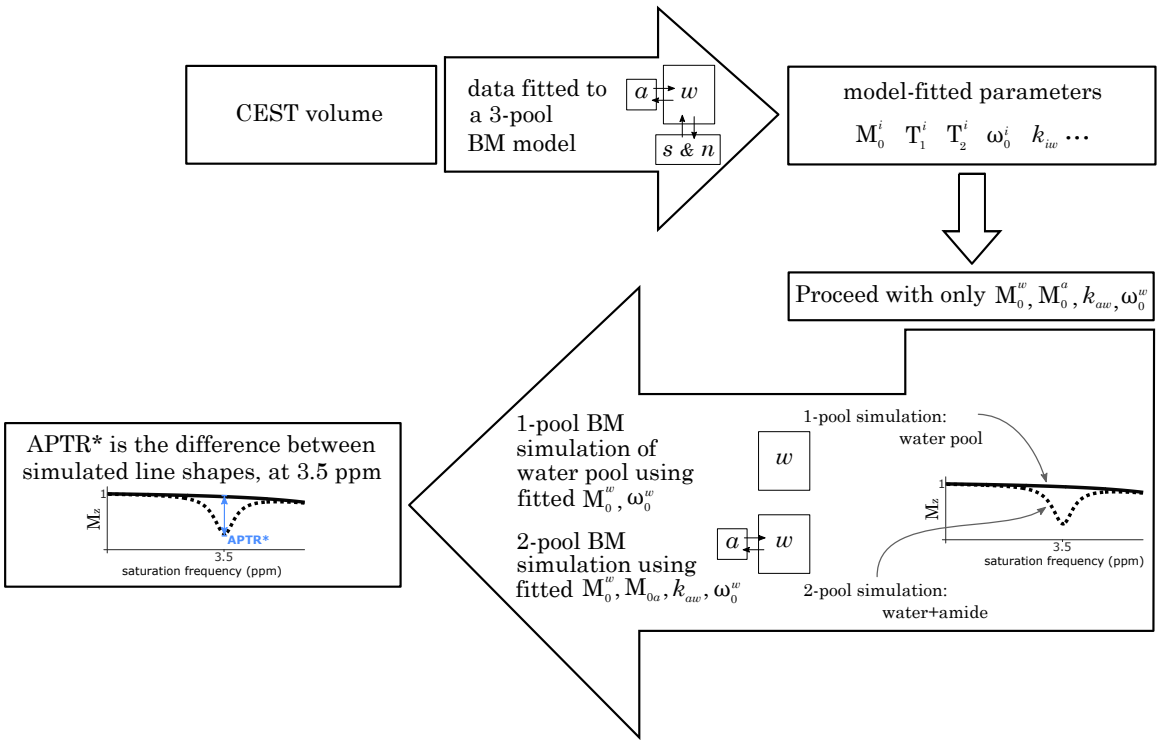

Figure 3.6: Flow diagram illustrating how ref. [62] defined APTR*. The CEST data were fitted to a 3-pool BM model which accounted for a water pool, amides, and a combined pool for NOEs and semisolid effects. The output of the model fitting process is a large number of model-fitted parameters corresponding to different variables in the physical model. In order to derive APTR*, which is an isolated quantitative measure of APT effects, only four model-fitted parameters are used: APT pool concentration, APT exchange rate, water resonance frequency, and water pool concentration. A 1-pool BM model simulates water-only saturation, and a 2-pool model simulates the CEST effects of the APT pool. APTR* is defined as the difference between the two simulated line shapes at the amide resonance frequency, 3.5 ppm.

3.2.3 Application of Bayesian inference techniques

With respect to quantification using a physical model, model fitting of the data to matrix (3.2) is an inference problem where the aim is to estimate meaningful physiological information from the data, represented using APTR*. A disadvantage of model fitting is that a large number of parameters need to be defined in advance, which may only be known with a low level of certainty whilst also exhibiting inter- and intra-subject variability [62]. Model fitting has the advantage of directly estimating the physical parameters of each pool from the data, but in the case of having multiple pools, there is an increased risk of over-fitting to limited data and thus inaccurate results [62]. In a typical non-linear fitting algorithm, the risk of over-fitting is increased if a large number

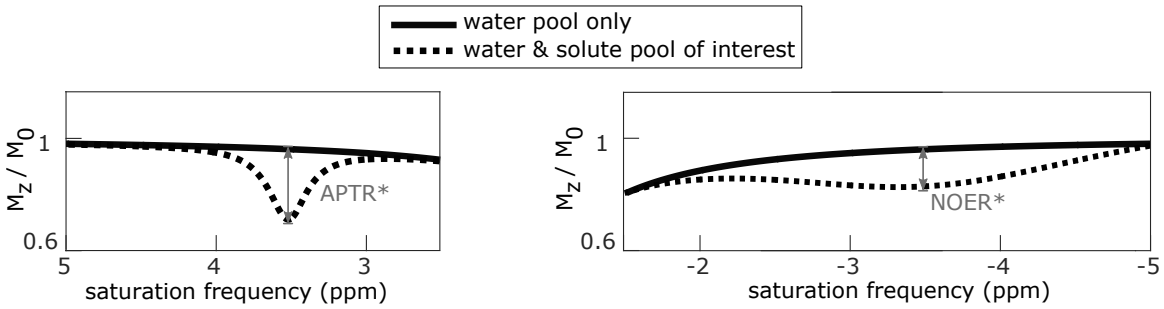

Figure 3.7: Illustration of the BMM analysis technique for quantifying CEST effects (shown for amide effects, APTR*, and NOEs, NOER*). After fitting multiple pools to the spectral data, only a subset are simulated to predict the effect arising from a single pool; the difference in saturation between these two simulations gives the apparent saturation effect arising from that solute pool independently of other pools.

of model parameters are allowed to freely vary, as the results may reflect variability from random noise more than they do the underlying signal [62]. To mitigate this risk strict assumptions could be made about some parameters, however, assumptions that are inaccurate may potentially bias the results [62]. In the case of quantifying CEST effects, particularly APT, many of the BM model parameters are known to be within a relatively restricted range of values, even if their precise value in a given subject is not known *a priori* [36,62].

A Bayesian approach to model fitting is an alternative to the conventional non-linear method which provides a framework for incorporating prior information about each parameter, reflecting uncertainty in the value or its expected variability, and mitigating over-fitting [62]. Bayesian methods have been applied in the similarly SNR-limited case of CBF estimation from arterial spin labelling (ASL) data, and are being increasingly applied in the analysis of MRI data [62]. The measured signal, S, is described as a combination of the model signal, f, plus additive noise ϵ:

$$S = f(\theta) + \epsilon \tag{3.3}$$

where θ is the set of model parameters that parameterise the signal [62]. If white Gaussian noise is assumed with a standard deviation (SD) of σ (or equivalently, a noise precision of $1/\sigma^2$), then the set of all model and noise parameters is $\Theta = \{\theta, \sigma\}$. The

likelihood of observing the n^{th} sample from S, given Θ, is [62]:

$$P(S_n|\Theta) = \frac{1}{\sqrt{2\pi}\sigma}\exp\left(-\frac{\left(S_n - f_n(\theta)\right)^2}{2\sigma^2}\right) \tag{3.4}$$

The objective of model fitting is to estimate the values of the model parameters that were responsible for generating the observed data. This can be expressed using Bayes' theorem:

$$P(\Theta|S) = \frac{P(S|\Theta)P(\Theta)}{P(S)} \propto P(S|\Theta)P(\Theta) \tag{3.5}$$

where $P(\Theta|S)$ is the posterior distribution of the parameters, and $P(\Theta)$ is the prior distribution [62]. $P(S)$ is the evidence term and can be omitted when correct normalisation of the posterior is not required [102]. For the purpose of quantification, expected parameter values can then be obtained from the mean of the posterior [62]. In general it might not be possible to evaluate equation (3.5) analytically, in which case the posterior can be approximated using a simpler form $q(\Theta)$ which itself is parameterised by a set of hyper-parameters [103]. The fit of the approximate distribution $q(\Theta)$ to the true posterior can be measured using the free energy [103]:

$$F = \int q(\Theta)\log\left(\frac{P(S|\Theta)P(\Theta)}{q(\Theta)}\right)d\Theta \tag{3.6}$$

Inferring $P(\Theta|S)$ is done by maximisation of F, which leads to the best approximation of $q(\Theta)$ to the true posterior [103]. To make the integrals tractable, a variational Bayesian (VB) approach is used, where $q(\Theta)$ is specified as a product of separate groups of parameters Θ_k, each with their own approximate posterior distribution $q_{\Theta_k}(\Theta_k)$ [103]:

$$q(\Theta) = \prod_k q_{\Theta_k}(\Theta_k) \tag{3.7}$$

This is known as the mean field approximation for $q(\Theta)$, which assumes that separate groups of parameters are independent, and is the key restriction of the VB ap-

proach [103]. It is generally not required to factorise over all model parameters, and a typical grouping of parameters is to separate them according to model parameters and noise parameters, namely that $q(\Theta) = q_\theta(\theta)q_\sigma(\sigma)$ [103]. The computation of $q_{\Theta_k}(\Theta_k)$ proceeds by maximising $q_{\Theta_k}(\Theta_k)$ over the free energy in equation (3.6) [103]. For any given $q_{\Theta_k}(\Theta_k)$, the form of F is a functional, whose maximum with respect to the subset of parameters Θ_k is obtained as a solution to the Euler-Lagrange equation [102]:

$$\log q_{\Theta_k}(\Theta_k) \propto \int q_{\Theta_{\not k}}\left(\Theta_{\not k}\right) \log\Big(\mathrm{P(S|\Theta)P(\Theta)}\Big) d\Theta_{\not k} \tag{3.8}$$

where $\Theta_{\not k}$ refers to parameters not in the k^{th} group. Computation of the factorised posteriors is simplified by choosing their form to be the same parametric form as the prior, which simplifies the VB method to a process of updating the hyper-parameters of the posteriors [103]. In the study of ref. [62], the form of the posterior used for the model parameters was a multivariate normal (MVN): $q_\theta(\theta) \sim \mathrm{MVN}(\theta; m, \Lambda^{-1})$, where m and Λ^{-1} are hyper-parameters defining the mean of the MVN and its covariance matrix, and a gamma distribution was chosen for the noise precision.

The VB algorithm follows an iterative update procedure, as each $q_{\Theta_k}(\Theta_k)$ in equation (3.8) depends on the other Θ_k [103]. To make the VB updates tractable for a non-linear model, an approximation to $f(\theta)$ is made by linearising it at each iteration using a first-order Taylor expansion about the mean of the posterior distribution [103]. Namely, $f(\theta) \approx f(m) + \mathrm{J}(\theta - m)$, where J is the Jacobian of f with respect to the model parameters [103]. This approximate VB method has been used with success in previous CEST studies (Section 3.2.2.5) on phantoms and on stroke patient data, where statistically significant patterns of change associated with tissue pathology were detected (Section 3.3) [36,37,62].

3.3 pH-weighted imaging of ischaemic stroke

The possibility of using the APT signal as a clinical imaging tool was explored in 2003 by Zhou et al. [14] in their *in-vivo* animal study on the pH dependence of the APT effect (Fig. 3.8), and was applied to tumour imaging in 2006 [31]. The APT exchange rate was previously established as base-catalysed for pH values above 5, from which a simplified exponential relationship between chemical exchange rate and pH was derived [14,104]:

$$k_{ex} = k_{base} \times 10^{\mathrm{pH}-\mathrm{pK}_w} = 5.57 \times 10^{\mathrm{pH}-\mathrm{pK}_w} \tag{3.9}$$

where k_{ex} is the amide proton chemical exchange rate, and $k_{base} = 5.57 \times 10^9$ Hz, obtained by fitting *in-vivo* and post-mortem exchange rate curves to pH (with $\mathrm{pK}_w = 15.4$ at 37° C) [14]. In the weak saturation approximation it is assumed that RF irradiation is applied directly on-resonance to the amide pool and that there is no spillover onto the bulk water pool [52]. Assuming that the amide pool reaches steady state immediately and that there is negligible back-exchange of protons, an approximation to the time-dependent amide proton transfer ratio (APTR) is given by [30,52]:

$$\mathrm{APTR} = \alpha_{sat} \frac{k_{ex}[amide]\mathrm{T}_1^w}{[\mathrm{H_2O}]} \left(1 - e^{-\mathrm{T}_{sat}/\mathrm{T}_1^w}\right) \tag{3.10}$$

where $[amide]$ and $[\mathrm{H_2O}]$ are respectively the concentration of exchanging amide protons and water, α_{sat} is saturation efficiency, R_{1w} is the water longitudinal relaxation rate ($\mathrm{R}_{1w} = 0.714$ s^{-1} at 4.7 T), and T_{sat} (4 s) is the duration for which the amide pool is irradiated [14,52]. The saturation efficiency α_{sat} takes a value of 0–1:

$$\alpha_{sat} \approx \frac{(\gamma \mathrm{B}_1)^2}{(\gamma \mathrm{B}_1)^2 + k_{iw}^2} \tag{3.11}$$

Zhou et al. [14] estimated the *in-vivo* amide proton concentration to be 71.9 mM, assuming complete saturation of the amide pool ($\alpha_{sat} = 100\%$) and a long CW saturation pulse. The relationship of APTR to pH with these assumptions is $\mathrm{APTR} = 5.73 \times 10^{pH-9.4}$.

During ischaemia a decrease in local tissue pH caused by tissue acidosis decreases the base-catalysed APT exchange rate, thus a decrease in the APT effect is observed locally, resulting in APT-weighted contrast [14,36,72] associated with intracellular protein [105]. However, proportionality of the APT signal to protein concentration, pH, and water T_1 (equation 3.10) means that it can be a confounded *in-vivo* measure if these parameters co-vary significantly. In stroke imaging it is accepted that APT effects within the hyperacute period (patients presenting within 6 hours of ischaemic onset) [106] can be attributed almost exclusively to pH changes in the ischaemic region, as amide concentration and water T_1 are assumed to exhibit negligible change during this period [14,34,72]. These may not be robust assumptions to make when quantifying CEST effects, as studies have reported early changes in both protein concentration (Section 3.5.6) and water T_1 (Section 3.5.9) following stroke [34,107].

In the study of ref. [14] the feasibility of using the APT signal for detecting ischaemia was assessed on animals who underwent middle cerebral artery occlusion (MCAO). Regions of APTR hypointensity corresponded with infarcted tissue that was identified through histological staining (Fig. 3.8e-f). A subsequent study suggested that pH-weighted imaging may be able to provide more accurate estimation of tissue at risk in the ischaemic penumbra [20], which could help in stratifying patients for early thrombolytic treatment [15]. Sun et al. [15] hypothesised that the reduction in pH that occurs before cellular depolarisation may provide a better indication of penumbral tissue that is at risk of infarction. In the MCAO study the authors found that pH-weighted deficit regions were smaller than the PWI deficit, and equal to, or larger than, the DWI deficit.

An MCAO study by Jin et al. [72] found significant APT-weighted contrast in the ischaemic core ($1.86\% \pm 0.27\%$, $p < 0.001$). The APT signal strongly correlated with the apparent diffusion coefficient (ADC) and exhibited regional heterogeneity within the lesion area, thought to be reflecting differences in pH between the infarct core and surrounding tissue (Fig. 3.9) [72].

More recently, APT CEST been used in clinical studies of ischaemic stroke by gener-

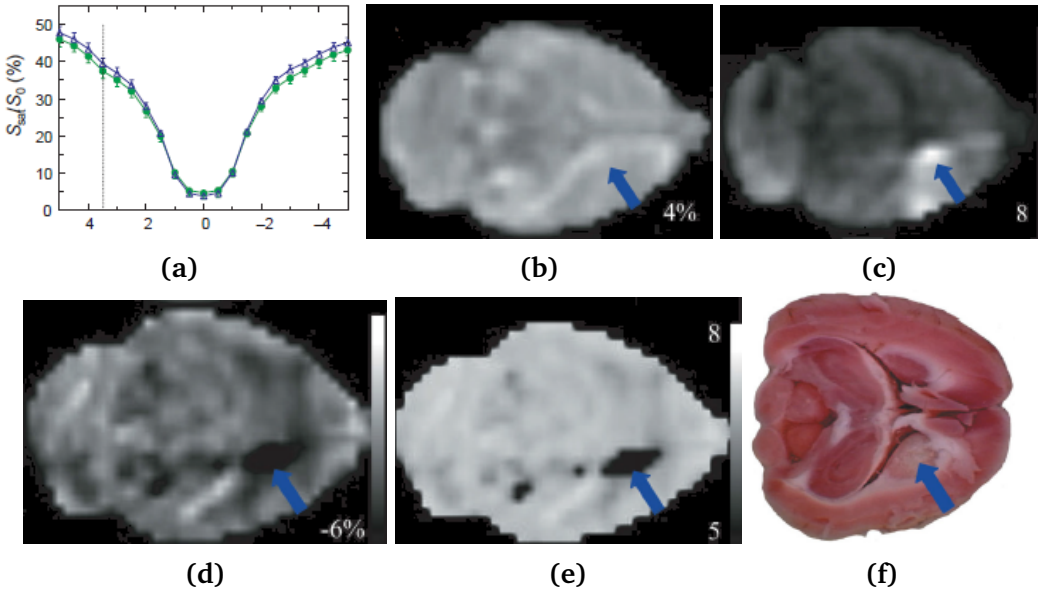

Figure 3.8: APT effects following ischaemia in an MCAO rat study by Zhou et al. [14]. z-spectrum **(a)** showed a decrease in the APT signal due to pH changes: 1.9% reduction in the pH-weighted signal for a pH decrease from 7.1 (normocapnia, green) to 6.7 (hypercapnia, blue) [15]. Images **(b)–(f)** are a comparison of T_2 **(b)**, DWI **(c)**, pH-weighted **(d)**, absolute pH images **(e)**, and histological staining **(f)**, in ischaemic rat brain. The DWI and histology images confirmed ischaemia and this corresponded to the strong hypointensity observed on the pH-weighted **(d)** and absolute pH **(e)** images. Figures reproduced from ref. [14] with permission from Springer Nature.

ating pH-weighted maps of brain tissue (Fig. 3.10) [36,37,90], with findings suggesting that this may have a role in improving imaging definition of penumbral tissue [37]. The study by Harston et al. in ref. [37] found that, at the tissue level, the pH-weighted APT signal was able to discriminate between the acidotic ischaemic core and mildly under-perfused benign oligaemic tissue [37]. In healthy brain tissue pH is maintained at a constant level (7.0–7.25 depending on the technique used) and this was reflected in the uniform pH-weighted maps of healthy subjects [37]. The small difference between grey matter (GM) and white matter (WM) was statistically significant and may be indicative of dependence on tissue type. Contrast between healthy grey matter and white matter has also been observed in a 9.4 T animal study by Jin et al. [72], who suggested APT to originate mainly from the higher concentration of mobile proteins found in grey matter (55% vs. 39% protein [108]), which is also more metabolically-active than white matter.

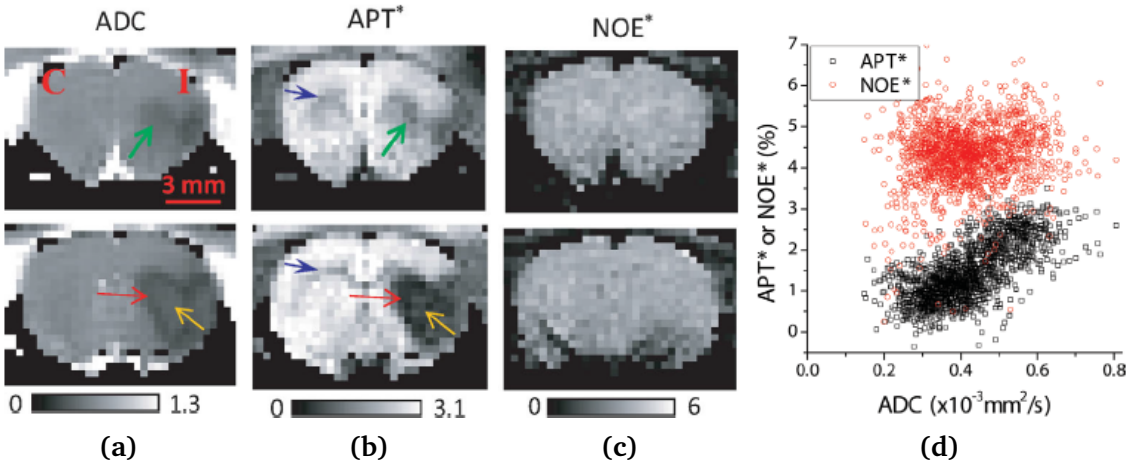

Figure 3.9: Two slices through a rat brain taken four hours after ischaemic onset following MCAO (LLA quantification technique was used). The ADC map **(a)** clearly showed the ischaemic lesion to correlate with APT maps **(b)** (red and green arrows) including in terms of regional heterogeneity (yellow arrow). The NOE map **(c)** exhibited almost no contrast between the ipsilateral and contralateral hemispheres. **(d)** A scatter plot from lesions of seven animals suggested that NOEs were almost independent of ADC. Figures reproduced from ref. [72] with permission from John Wiley & Sons.

In the study of ref. [36], it was observed that APT effects were decreased in regions around CSF, within tissue that was otherwise identified as normal-appearing. The cause of the decrease in APT was attributed to partial volume (PV) effects at tissue-CSF boundaries, as CSF has no substantial APT effect of its own. Thus, for any application, like stroke, where a reduction in APT is indicative of pathological tissue, the contribution of CSF is a potential confound [36,37,109].

In the clinical study of ref. [37], the hypointense pH-weighted signal in the ischaemic core was consistent with the understanding that ischaemic core tissue is highly acidotic and is expected to show reduced APT saturation effects compared to the contralateral hemisphere [37]. Oligaemic tissue is hypoperfused at presentation but does not subsequently infarct. The APT signal in the benign oligaemia region of interest (ROI) was consistent with this by having a value undifferentiated from the contralateral hemisphere, whilst being significantly higher than the ischaemic core signal. Infarct growth tissue is viable on presentation but subsequently infarcts, being perhaps metabolically stressed by mild acidosis and leading to the intermediate value of infarct growth APTR observed in the study of ref. [37].

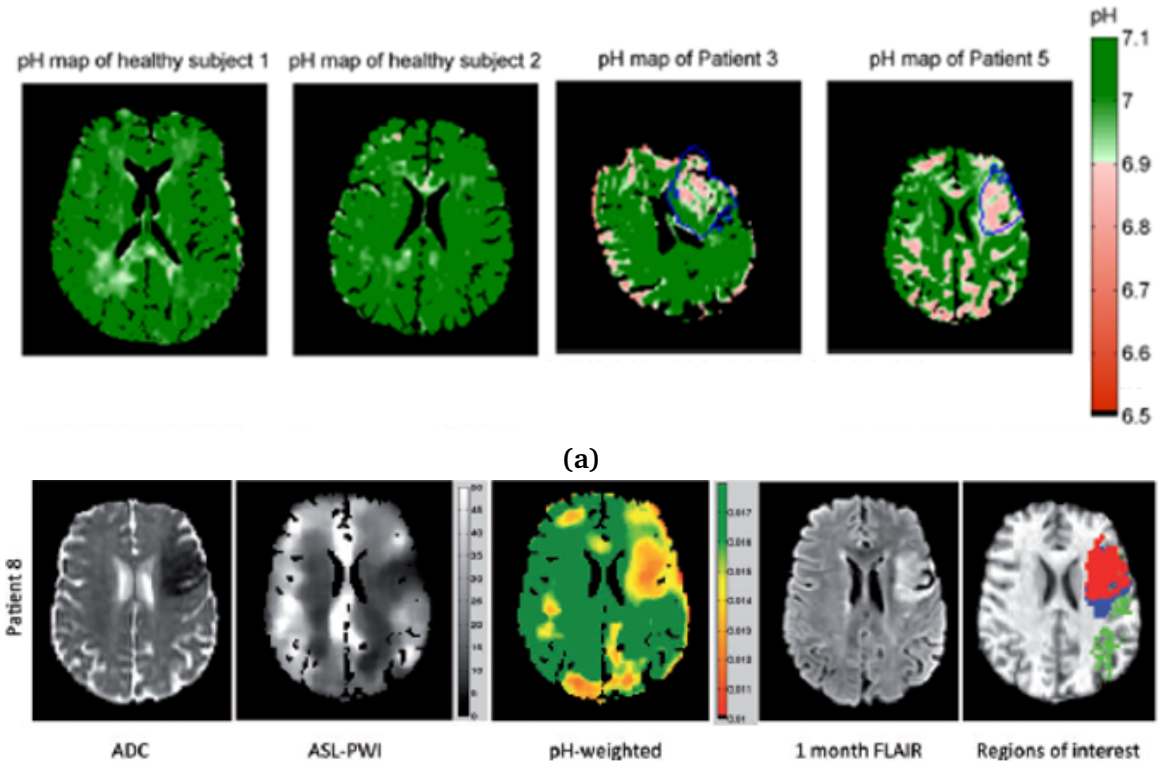

Figure 3.10: Clinical studies in stroke using quantitative pH-weighted maps. **(a)** Tee et al. [36], showing homogeneous estimated pH for healthy controls and APT hypointensity in the blue ischaemic core region, ascribed an absolute pH of 6.9 in the study. Figure reproduced from ref. [36] with permission from and John Wiley & Sons. **(b)** Study by Harston et al. [37] showing APT hypointensity in the ischaemic core (red region of interest). Figure reproduced from ref. [37] with permission from Oxford University Press.

3.4 NOE CEST in ischaemic stroke

Ischaemic core contrast using APT CEST is relatively well-studied both preclinically and in human stroke. Recent studies have found that NOEs exhibit contrast in tumours and in preclinical stroke models separately from downfield APT effects, particularly at lower RF saturation powers [32,57,72,74,86]. If NOEs are associated with cell metabolism then they may help in identification of the ischaemic penumbra in stroke patients [14–16].

Ischaemic stroke and oncological studies have sought to investigate the association of NOEs with final tissue outcome. The oncological literature in particular harbours active discussion on NOE signal origins and biophysical interpretations relevant to patho-

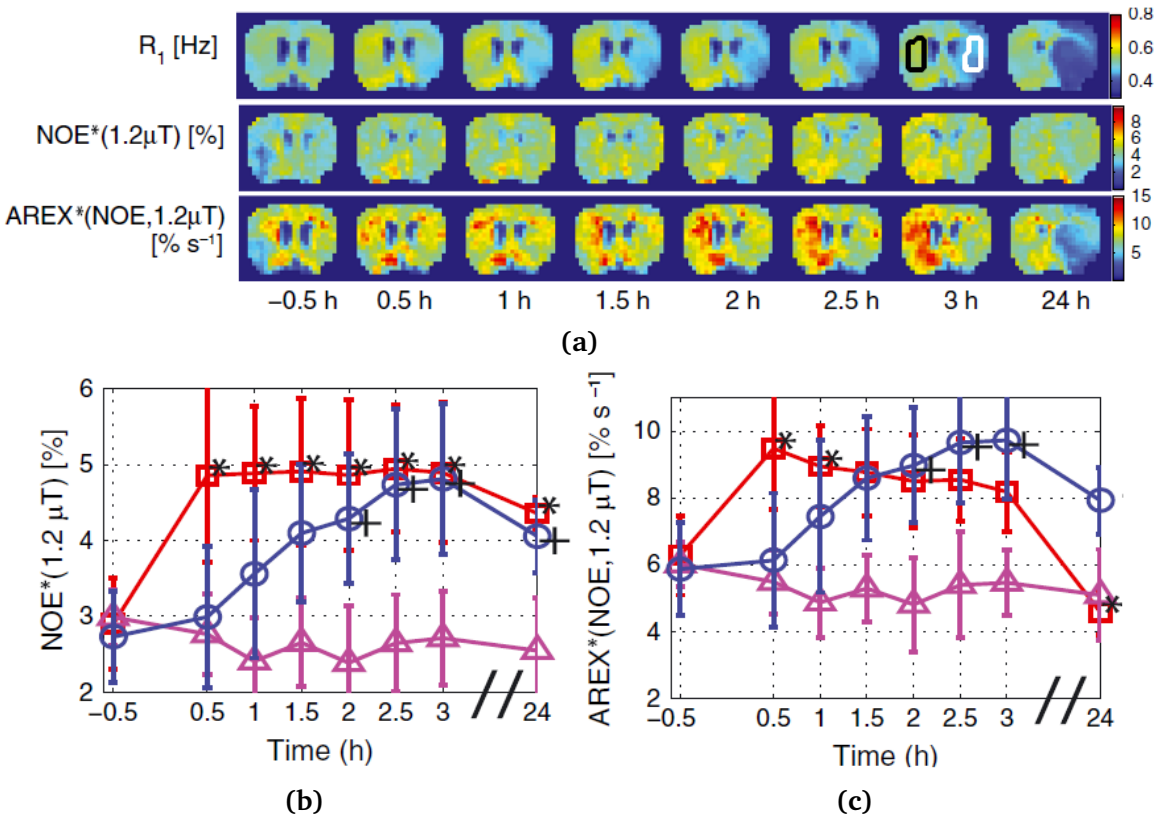

Figure 3.11: Serial study of NOE signal evolution pre- and post-MCAO. **(a)** NOE signal using the LLA technique (row 2) and NOE signal using the AREX technique (row 3) shown at different time points for a representative animal (white ROI: ischaemic hemisphere, black ROI: contralateral hemisphere). **(b)** Mean±standard deviation at different time points for the ischaemic hemisphere (red squares), contralateral hemisphere (blue circles), and healthy controls (magenta triangles). Superscripts $*$ and $+$ denote $p < 0.01$ with respect to pre-MCAO levels (for ischaemic and contralateral hemispheres respectively). The AREX technique for quantifying NOEs **(c)** showed a general decreasing trend relative to 0.5 h, whereas this trend was not observed using the LLA technique. Figures reproduced from ref. [34] with permission from John Wiley & Sons.

logical tissue. The present CEST literature is not conclusive on some of the fundamental characteristics of NOEs, such as their dependence on tissue pH and underlying mechanisms [57,72,94,95,110].

In the ischaemic core, an elevated NOE signal has generally been observed in preclinical studies, where NOEs increase 1 h post-MCAO and were elevated with respect to the contralateral hemisphere [34,81,111]. An MCAO study (ref. [72]) found that the NOE signal was homogeneous across the brain and did not exhibit contrast in the ischaemic core or in healthy grey matter and white matter, being almost independent of ADC (Fig. 3.9).

In another animal study NOEs increased immediately (imaged at 0.5 h) after onset of ischaemia, followed by a gradual decrease towards a baseline value at 24 h (Fig. 3.11) [34]. The contralateral hemisphere exhibited a gradual increase in NOE signal following MCAO, and *post-hoc* analysis of the results in ref. [72] suggested a similar trend [34]. At 2.5 h post-MCAO ref. [72] did not observe ischaemic core contrast, which could explain the lack of contrast reported in ref. [72] in which the animals were imaged at 4 h post-MCAO [34,72].

One of the earliest clinical demonstrations of NOE contrast in acute human stroke was by Tee et al. [90] who used a 3-pool model to quantify CEST effects, comprising a water pool, an APT pool, and a pool combining NOEs and semisolid effects. Two of the four patients exhibited a deficit of NOE signal in the ischaemic core, and these regions subsequently progressed to infarction based on follow-up FLAIR scans (Fig. 3.12). The remaining two patients in the study either saw a mild or no deficit in NOE signal; in the former case only part of the ADC ischaemic tissue progressed to infarction, and in the latter case no clear infarction was identifiable on the follow-up FLAIR scan (Fig. 3.12b). There was also a decrease in saturation effects at ±3.5 ppm in the ischaemic core compared to contralateral normal-appearing tissue (Fig. 3.12). All four patients had an apparent pH-weighted deficit in the ischaemic core, defined as ADC hypointensity at presentation.

In a recent study it has been shown that the ischaemic core exhibits not only a decrease in pH, but a concurrent decrease in cytoplasmic protein concentration, the latter of which has hitherto been assumed to remain constant immediately following ischaemic stroke in the CEST literature (Section 3.5.6) [107]. Both a reduction in protein concentration and of pH would effect a decrease in NOEs in the ischaemic core. Studies have also identified an NOE peak at −1.6 ppm (Section 3.5.4) which is distinct from the broader NOE at −3.5 ppm. The former NOE peak exhibited a significant decrease immediately after stroke [81,111].

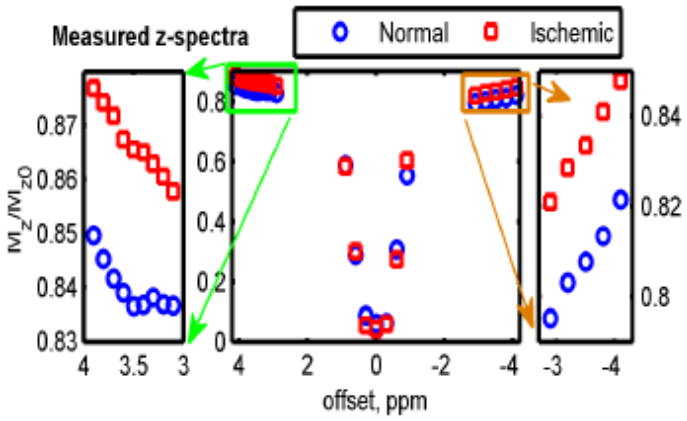

(a)

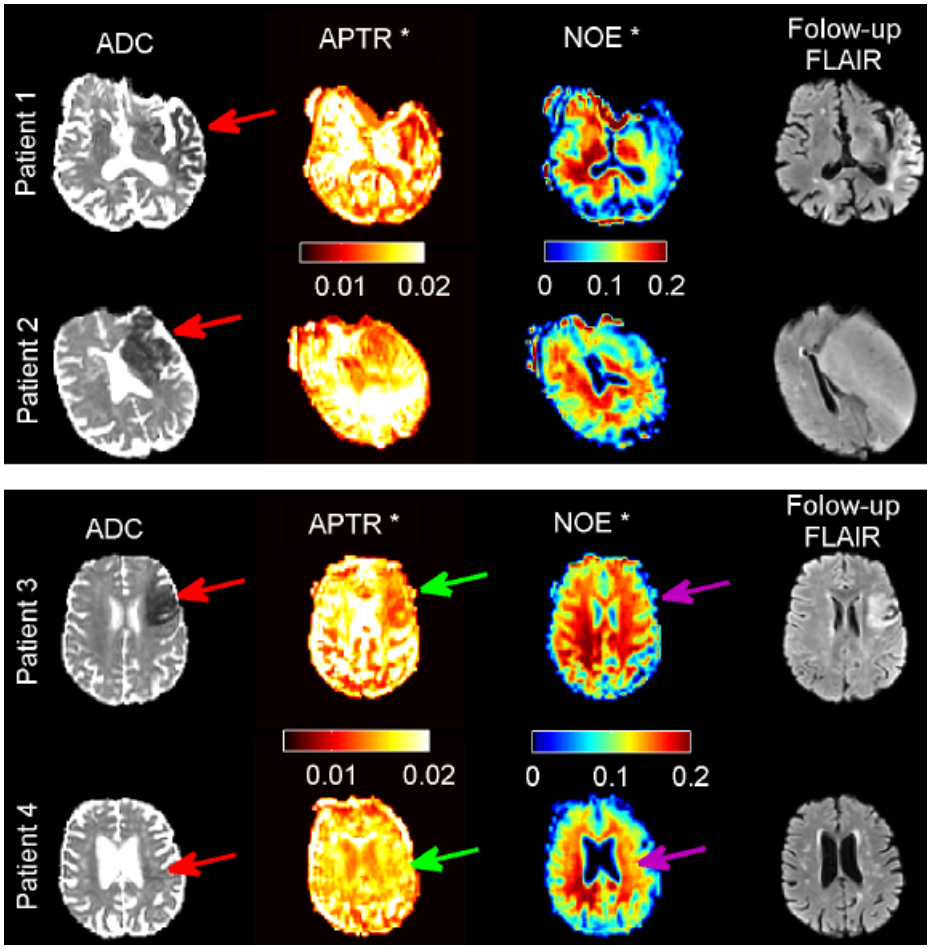

(b)

Figure 3.12: CEST study on patients presenting with hyperacute stroke, highlighting APT effects and NOEs. **(a)** z-spectra acquired in a representative acute stroke patient showing a decrease in APT and NOE saturation effects within a 6-hour hyperacute window. **(b)** Tissue regions that were not infarcted on presentation but that subsequently progressed to infarction appeared hypointense on the presenting BMM APT and NOE maps. When only part (patient 3) or none (patient 4) of the ADC lesion progressed to infarction in the follow-up FLAIR, the presenting NOE maps exhibited no apparent deficit in the lesion area. Figures reproduced from ref. [90].

3.5 Biophysical characteristics of NOEs

The spectral features of the NOE signal are relevant for determining how NOEs can be quantified whilst minimising contamination from competing effects. The salient features of z-spectra associated with NOEs are discussed below.

3.5.1 z-spectrum asymmetry

In early CEST studies it was thought that z-spectra were symmetrical about water resonance in the absence of metabolite exchanges, and a broad featureless spectrum upfield of water resonance was assumed, used as a reference. However, asymmetry of the z-spectrum slightly upfield from water (within -5 ppm), particularly at lower RF saturation powers, indicated the presence of strong saturation effects in the aliphatic region of the spectrum.

The cause of asymmetry was initially attributed to resonance mismatch between the bulk water and semisolid pools such that semisolid macromolecules could have a small negative chemical shift with respect to the water signal [52,74,112–114]. This is unlikely, however, as the broad line shape of semisolid effects, of the order of tens of ppm [72,74], suggests that they are symmetrical. Zhou et al. Some earlier studies have attributed upfield asymmetry to aliphatic protons of a mixture of mobile to relatively-mobile peptides, proteins, lipids, and metabolites, which have resonances located around -3.5 ppm, ranging from -2 to -5 ppm [74]. Upfield exchange processes related to mobile macromolecules [42,74], or NOEs, are now thought to be the cause of z-spectrum asymmetry [42,57,72,74,95,97].

Modelling these mobile components as a single pool with a T_2 of 0.1 to 30 ms (relatively-mobile to mobile protons), it was shown in theory that asymmetry caused by NOEs could be delineated at low B_1 powers ($\sim 0.6\ \mu$T), but not at higher B_1 powers ($\sim 2.1\ \mu$T) where the peak HWHM could be over 30 ppm, resulting in a broadband saturation effect similar to that from the semisolid phase. This notion corresponded

with *in-vivo* experiments where a peak at around −3.5 ppm could be delineated at low B_1, but almost all peak definition was lost at a higher B_1 [74].

3.5.2 Magnetisation transfer pathways

The mechanism of NOE-mediated magnetisation transfer to water has been suggested to occur through two main pathways. The first is dipolar coupling of the aliphatic spin to chemically-exchangeable amide protons along the protein backbone, facilitated by small distances between dipolar-coupled spins (proportional to $1/r^6$), which subsequently transfer magnetisation to bulk water ('exchange-relay mechanism'), potentially exhibiting sensitivity to pH due to the chemical exchange [57,74]. A water exchange (WEX) NMR experiment conducted by ref. [14] supports this description of an NOE mechanism [57]. For molecules in solution, the likelihood of magnetisation transfer to bulk water via dipole coupling (intermolecular transfer) is thought to be low, due to the relatively high mobilities involved [30,57]. Thus, studies generally suggest an exchange-relayed mechanism of NOEs.

Alternatively, non-chemically-exchangeable protons can transfer magnetisation to water through direct intermolecular dipole coupling, facilitated by long correlation times between interacting molecules. In the study of ref. [110] on protein-free mobile lipids, the build-up of NOE saturation on non-chemically-exchanging lipids was similar to that obtained using bovine serum albumin (BSA) protein phantoms which contained exchangeable protons. This supports the notion that NOEs manifest through pathways of both pH-dependent chemical exchange and of intermolecular dipolar coupling [57]. A third possible mechanism is through spectral overlap, where intramolecular NOEs are coupled to non-exchangeable protons whose signal overlaps with the CEST spectrum [82].

Two exchange pathways are illustrated in Fig. 3.13. Hydration water may also be involved in this process. Hydration water refers to trapped water molecules at the surface and within the core of proteins and is important to protein structure. Within

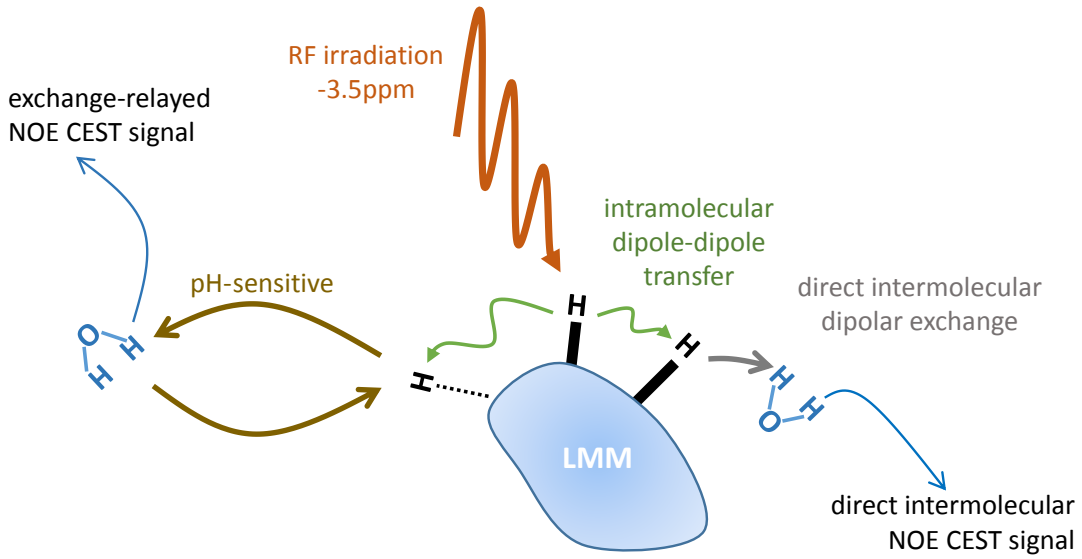

Figure 3.13: Illustration of two main NOE exchange pathways that are thought to be relevant. **H** denotes a hydrogen proton. Protons bonded by a thick line are aliphatic, that is, they do not physically exchange (resonance at −3.5 ppm), whereas the dotted bond denotes an exchangeable amide proton. Saturation is ultimately transferred to the bulk water pool (blue H_2O molecules). Green denotes the intramolecular dipolar exchange pathway to neighbouring protons including amide side groups, and is common to both mechanisms. Grey denotes direct dipolar coupling through hydration water. Gold denotes the pH-sensitive chemical exchange component of the exchange-relay mechanism.

a molecule, transfer of saturation to macromolecular-bound hydration water protons occurs through dipolar coupling, after which relay to bulk water can occur through chemical exchange. Present model-based approaches for quantifying NOEs employ a simplified description of NOEs where they are modelled as a pool in chemical exchange with water.

3.5.3 Absorption linewidth

The relatively narrow line widths of APT and NOEs, characteristic of species with short T_2, suggests that they originate from mobile species. This is because the RF absorption linewidth, or HWHM ($\nu_{1/2}$) is inversely proportional to T_2, which is long for mobile species [74]:

$$\nu_{1/2} = \frac{\gamma B_1}{2\pi}\sqrt{\frac{T_1}{T_2}} \tag{3.12}$$

APT effects are typically reported to be maximal at 3.5 ppm, with a (field-dependent) width of 1.2 ppm (corresponding to an APT range of 2.9 to 4.1 ppm) [14,72].

The signal from the semisolid phase originates from immobile lipids which facilitate rapid magnetisation transfer via spin diffusion, having a much shorter T_2 compared to the surrounding water and a correspondingly broad line width [91–93]. Semisolid effects have typically been used in identifying white matter disease that is marked by demyelination of nerve axons, yielding lower magnetisation transfer ratios [91] (Section 3.1).

For NOEs, a label frequency of −3.5 ppm is generally used and the observed linewidth is broader than that of amides, extending from −2 to −5 ppm [57,72,74]. LDA spectra over this range reveal several discrete peaks (Fig. 3.14), indicating a composite nature to NOE resonance. Compared to the broad and featureless semisolid spectrum, the detailed NOE spectra suggest an origin in mobile protein components [57]. NOEs have been said to originate mainly from the higher mobile lipid content found in the myelin sheath. The total lipid content in white matter of a healthy human brain is 36% to 65% higher than in grey matter, the remainder being mostly protein [108,115] as detailed in Table 3.3. Lipids have a high abundance of non-chemically-exchanging aliphatic bonds whose resonance frequency is centred at around −3.5 ppm, therefore saturation effects at this frequency have been assigned to lipids. The presence of an NOE mobile lipid signal has been supported by a recent experimental study into protein-free liposomised mouse brain tissue, reporting pronounced saturation effects confined to the frequency range of upfield protons [110].

3.5.4 NOE sub-resonance at −1.6 ppm

The aforementioned CEST literature has modelled NOEs as a relatively broad effect that ranges from around −2 to −5 ppm, being centred at around −3.5 ppm. This was based on observations in the data which have been consistently observed in the CEST literature. The discussion on the spectral characteristics of NOEs highlighted that

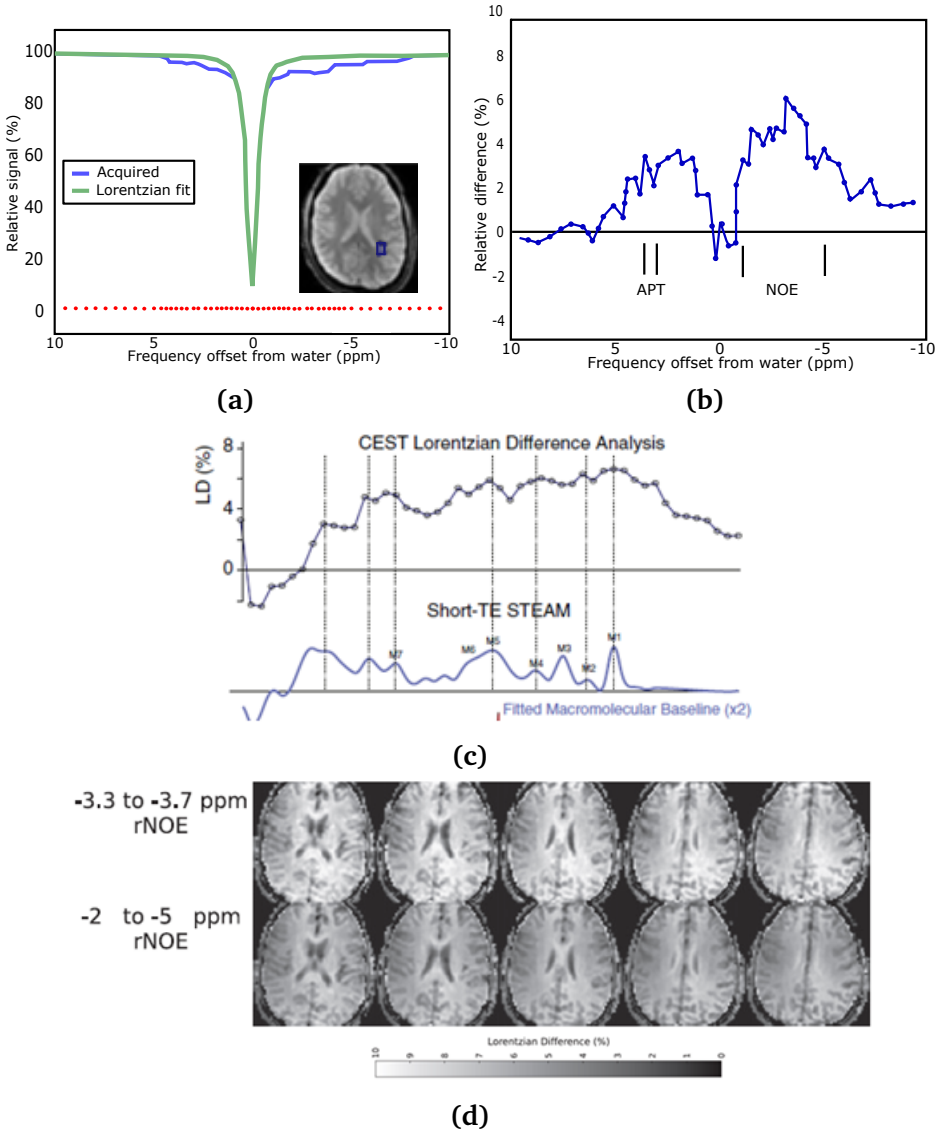

Figure 3.14: LDA of NOEs in a healthy subject. **(a)** A Lorentzian line shape (green) describing direct water saturation is fitted to the data acquired under low-B_1 steady-state conditions (blue). **(b)** Subtraction yields the APT and NOE peaks, highlighting the composite nature of the NOE spectra. Figures adapted from ref. [88]. **(c)** NOE spectra fitted to an MRS spectrum from the same area, allowing identification of different macromolecular components. **(d)** Integral of the Lorentzian difference spectrum suggest that NOEs are more abundant in white matter compared grey matter, with the highest intensity occurring over the NOE subrange from −3.7 to −3.3 ppm. Figures reproduced from ref. [57] with permission from Elsevier Inc.

Table 3.3: Human brain tissue composition expressed as a percentage of dry weight (except water). Myelin is the fatty sheath covering white matter nerve axons. White matter is characterized by its high lipid content. Lipids account for approximately 80% of the dry weight and protein 20%. White matter has a relatively high dry weight content of 25–30% compared to approximately 15% for grey matter. Taking into account that myelin constitutes 50% of white matter, myelin has a dry weight of approximately 60% [116].

[†]Based on four human subjects ranging from ten months to 55 years [108].
[‡]For a typical adult human brain [115].

substance	grey matter (%)	white matter (%)	myelin (%)
water	$82-85^{\dagger}$, $81.9^{\dagger}$	$75-80^{\dagger}$, $71.6^{\ddagger}$	–
total lipid	$36-40^{\dagger}$, $32.7^{\ddagger}$	$49-66^{\dagger}$, $54.9^{\ddagger}$	$78-81^{\dagger}$, 70.0^{**}
protein	$55.3^{\ddagger}$	$39.0^{\ddagger}$	$\sim 21^{\ddagger}$, $30.0^{\ddagger}$

NOEs are in a fact a composition of several narrower resonances. One of the first NOE sub-resonances[3] that was studied *in-vivo*, in isolation from the broader NOE centred at -3.5 ppm, was the resonance at -1.6 ppm identified in the recent study of ref. [117]. In fact, this resonance was apparent in the 7 T LDA spectra of healthy subjects in the study of ref. [57] (Fig. 3.14) but has not been discussed until recently [81]. The close proximity of this resonance to water is probably why it has not been observed in 3 T clinical studies [81]. In the preclinical study of ref. [117], NOEs at -1.6 ppm were reduced in tumour tissue, post-mortem normal tissue, and following an extended period of isoflurane-induced anaesthesia. A number of subsequent preclinical and clinical studies have corroborated these results, all of which attempted to isolate the NOE resonance at -1.6 ppm and reported a significant reduction of signal in tumour tissue compared to normal tissue [80,98,118].

As well as potentially being a biomarker for the detection of brain tumour, NOEs at -1.6 ppm have also been investigated in models of ischaemic stroke. Unlike NOEs at -3.5 ppm, which have been reported to increase following stroke onset, the signal at -1.6 ppm exhibited a significant decrease at $0.5-1$ h post-MCAO; an effect that was consistent for 2 h after onset and exhibited higher contrast compared to the APT signal and NOEs at -3.5 ppm [81,111]. Other characteristics of the NOE resonance

[3]An NOE peak apart from the broader NOE centred at -3.5 ppm.

at −1.6 ppm that differ from the APT and NOE CEST signals are, a lack of contrast between grey matter and white matter, and relatively high variability in resonance frequency offset and linewidth in both healthy tissue and pathological tissue, suggesting that complicated signal mechanisms are associated with this sub-resonance [80,81].

The NOE resonance at −1.6 ppm has been closely associated with interactions between choline head groups of membrane phospholipids, which have a resonance frequency at around −1.6 ppm, and water protons [80,81,117,118]. Choline phospholipids (phosphatidylcholine, or PC) are a major component of the phospholipid bilayer that forms cell membranes, accounting for 60% of membrane lipids [80,81]. In the MRS literature, dipole-dipole interactions at −1.6 ppm between PC membrane phospholipids and water protons have previously been identified at −1.6 ppm in tissue extracts, model lipids, and intact cell lines using 2D NOE spectroscopy (NOESY) and magic angle spinning [80,81,117]. In biological tissue there are other resonances close to −1.6 ppm (taurine at −1.8 ppm), but since choline head groups are motionally-restricted by their covalent bonding with rigid membrane lipids, they exhibit negative NOEs, whilst other metabolites are mobile and cannot contribute to negative NOEs. The same resonance at −1.6 ppm appears to also be present in more recent preclinical studies, which is why the origin of NOEs at −1.6 ppm has been associated with choline head groups [80]. This association has also been used to explain why the NOE signal decreases after animals are exposed to 3 h of isoflurane intake; isoflurane molecules are amphiphilic and are added on to bilayer cell membranes, affecting membrane conformation and the NOE signal [117]. As with the broader NOE centred around −3.5 ppm, there is more than one possible pathway through which NOEs at −1.6 ppm may propagate; either through direct dipole-dipole interactions, or through an exchange-relayed process [80].

3.5.5 Contrast between grey matter and white matter

Protons with relatively low exchange rates ($k_{ex} < 50$ to 100 Hz [87]) can be efficiently saturated at low B_1 powers according to the saturation efficiency approximation (equa-

tion 3.11) and equation (3.10) [30,87]. Amide protons have an *in-vivo* exchange rate of $\sim$ 29 Hz [87], giving a saturation efficiency of $\alpha_{sat} = 99.5\%$ at an applied B_1 of 1.5 μT. NOEs exhibit a lower net exchange rate of approximately 11 Hz and therefore can be saturated at a lower B_1 for a given saturation efficiency [57]. The use of a lower B_1 is advantageous as it allows semisolid effects, which have a large k_{ex} and a dominating broadband profile, to be minimised in a similar way to the low-B_1 human stroke studies of ref. [87] (Fig. 3.14a) and ref. [90].

B_1-dependence studies on animal brains have found that $B_1 = 0.6$ μT is optimal for enhancing NOEs [34,72,74]. At a B_1 of 0.55 μT, used for the data in this thesis, the saturation efficiencies are $\alpha_{sat} = 99.4\%$ for NOEs, and $\alpha_{sat} = 96.3\%$ for APT. Higher saturation powers broaden the APT and NOE peaks, which can make quantification of these effects more challenging [34].

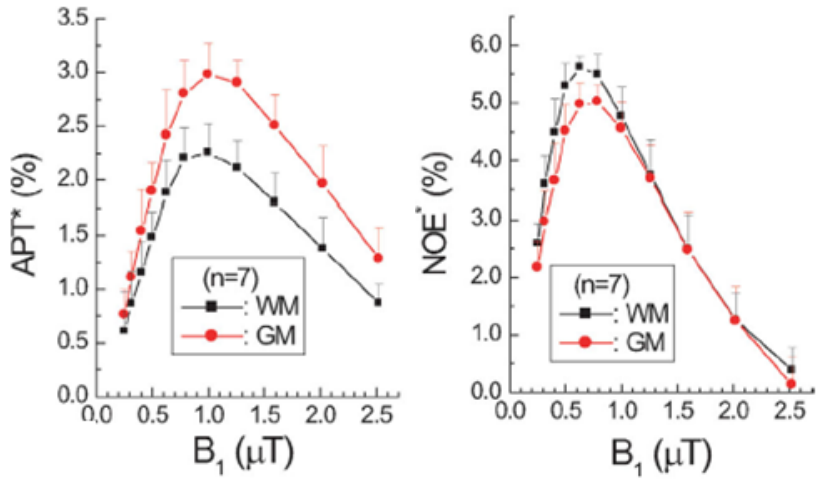

(a) **(b)**

Figure 3.15: Averaged B_1 dependence of **(a)** APT and **(b)** NOE (LLA technique) in seven animals. The APT contrast ratio remained approximately constant over a wide B_1 range whereas NOE contrast was present over a smaller range. The largest APT effect was observed at $B_1 = 1.0$ μT. For NOEs, the optimal B_1 was lower, at 0.6 μT. Figures reproduced from ref. [72] with permission from John Wiley & Sons.

Grey matter-white matter contrast is more pronounced with the APT signal (30% higher in grey matter), observed over a range of saturation powers up to 2.0 μT [72] (Fig. 3.15). The NOE signal is larger in white matter [57,72,88], with highest intensity occurring over the range from -3.3 to -3.7 ppm (Fig. 3.14d). However, the contrast

achieved (20%) appears to be lower than with APT, and is tightly confined to around a saturation power of 0.6 μT [72]. Paech et al. [95] imaged 12 glioblastoma patients at 7 T and reported a more pronounced NOE signal in normal white matter (−8.4%) compared to grey matter (−5.0%) (no effect in CSF). At a lower average B_1 of 0.45 μT, NOE-weighted maps clearly distinguished between white matter (5.1% ± 0.8%) and grey matter (3.4% ± 0.8%) [88].

3.5.6 Dependence on protein concentration

In the *in-vivo* environment it is not possible to attribute changes in NOEs solely to pH. A recent study has shown that the ischaemic core exhibits not only a decrease in pH, but also a concurrent decrease in cytoplasmic protein concentration [107]. In the CEST literature, the latter has hitherto been assumed to remain constant within the first 6 hours of ischaemic onset, thus APT-weighted contrast has been commonly attributed to pH changes with an assumption of constant protein concentration. In tumours the converse is assumed with respect to the cellular environment. Tumour studies can offer more detailed insight into the protein concentration dependence of NOEs, as tumour intracellular pH is thought to be almost the same as normal brain tissue (an increase in pH of less than 0.1). Contrast is thought to originate from differences in protein concentration, *vis-à-vis* tissue cellularity, where tumour cytoplasm has a high concentration of mobile proteins and peptides [31,95,119,120]. In the tumour core, particularly for malignant gliomas, mobile protein concentration is reported to be higher than contralateral tissue and this corresponds with higher tumour protein concentrations that have been confirmed by *in-vivo* MRS [120], although biochemical measurements in other studies have not observed a significant difference in protein concentration nor significant APT-weighted contrast after correcting for water T_1 [86].

Protein overexpression in tumours means that many proliferate rapidly and have a high cellular density compared to normal brain tissue. APT-weighted contrast has been shown to differentiate between tumour progression and radiation necrosis where

the latter is marked by a loss of cytoplasm and therefore an absence of mobile proteins [95,120]. *In-vitro* BSA phantom studies have shown that NOEs, as well as APT-weighted effects, to exhibit a proportional dependence on mobile macromolecule concentration [72]. Necrosed tissue also exhibits a weaker NOE signal, corresponding with the absence of proteins and peptides due to tissue necrosis.

A clinical study by Paech et al. (Fig. 3.16) reported glioma tissue to have a smaller NOE signal than normal white matter [95], as did the study of ref. [94] (Fig. 3.17). Zhou et al. [74] conducted a preclinical study on animal gliomas and also observed this. Lorentzian difference spectra corroborate these findings (Figs. 3.18 and 3.19). NOE signals were weaker in tumour regions [57], with tumour tissue showing less saturation effects compared to contralateral tissue. These clinical findings relating to NOEs, seem, at first, inconsistent with studies on isolated tumour cells which report larger APT-weighted effects in tumours [57], and also with the notion that increased cellularity, thus mobile protein density, should enhance NOEs. This discrepancy has been explained as follows. Tumours have elevated water content (oedema) due to increased vasculature, giving more water content per voxel despite the higher protein content from the elevated cellularity of tumour tissue [57]. Whilst the NOE signal is proportional to protein concentration, it may be disproportionately diluted by oedema [95]. Thus a reduced NOE signal does not necessarily indicate a reduction in cellular protein content [57,94]. Peritumoural oedema also exhibited a weaker NOE signal, which may be attributed to a lower concentration of cells (and therefore of mobile proteins) that is caused by tissue swelling. Higher protein mobility in the more liquid environment would also reduce the efficiency of dipolar magnetisation transfer by reducing correlation times and cross-relaxation efficiency [94].

3.5.7 Sensitivity to protein structure

Protein misfolding in tumours has also been suggested to result in a reduction of NOEs. Whilst in tumours the cellular environment is thought to be well-preserved in terms of

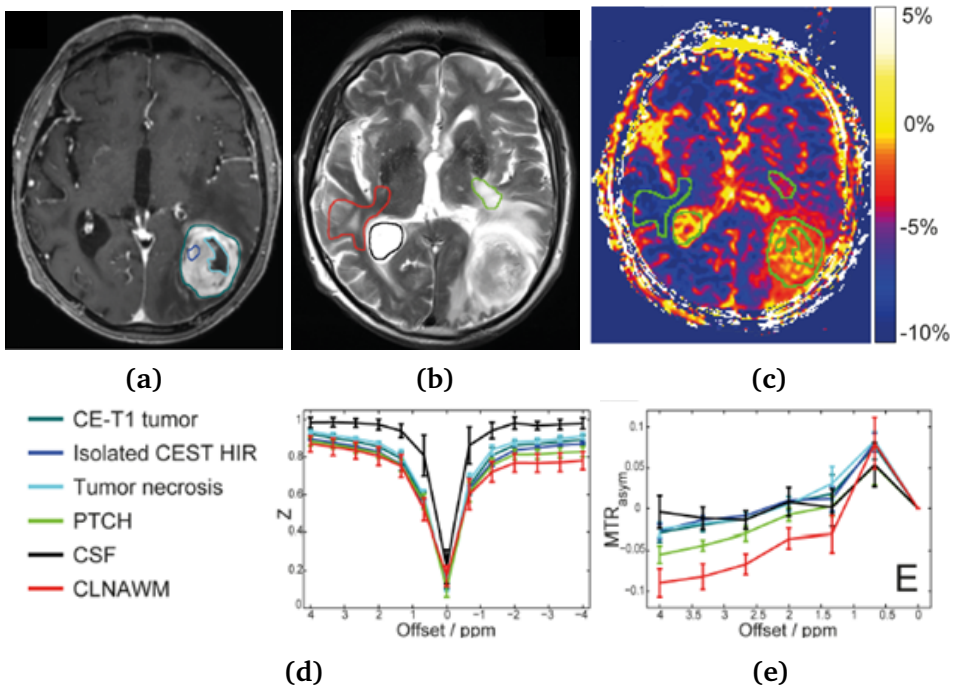

Figure 3.16: CEST effects in a study on patients with glioblastoma, by ref. [95]. Glioblastoma of a 79 year old patient. ROIs: gadolinium contrast-enhanced T_1 (CE-T_1), CEST hyperintense region (CEST HIR), tumour necrosis, peritumoural CEST hyperintensity (PTCH), cerebrospinal fluid (CSF), and contralateral normal-appearing white matter (CNAWM). **(a)** T_2 image, **(b)** gadolinium contrast-enhanced T_1 image. **(c)** MT asymmetry map at 3.3 ppm. **(d)** ROI Z-spectra, and **(e)** ROI asymmetry spectra. An APT peak was not observed in the data **(d)**, thus the results were more heavily-weighted by NOE exchanges. CNAWM was hypointense compared to the tumour, indicating stronger NOE saturation in the former. Less saturation within the necrotic region on the asymmetry map **(c)** is consistent with the contrast-enhanced T_1 scan. Figures reproduced from ref. [95] with permission from Paech et al.

preventing protein folding, necrotic tissue is characterised by a breakdown of cell membranes and is more likely to contain a mixture of native and denatured proteins as well as protein aggregates, suggesting that it could be a source of contrast between healthy and necrotic or highly damaged tissue [94]. This may also apply in the ischaemic core following stroke.

Zaiss et al. [94] investigated the dependence of NOEs on protein structure. Using BSA as a model phantom of mobile proteins and peptides in their native (folded) state, protein unfolding was induced by adding urea at different concentrations. The NOE signal as a function of urea concentration was strongly correlated with BSA denaturation curves obtained by fluorescence spectroscopy ($R^2 = 0.96$), with both curves having

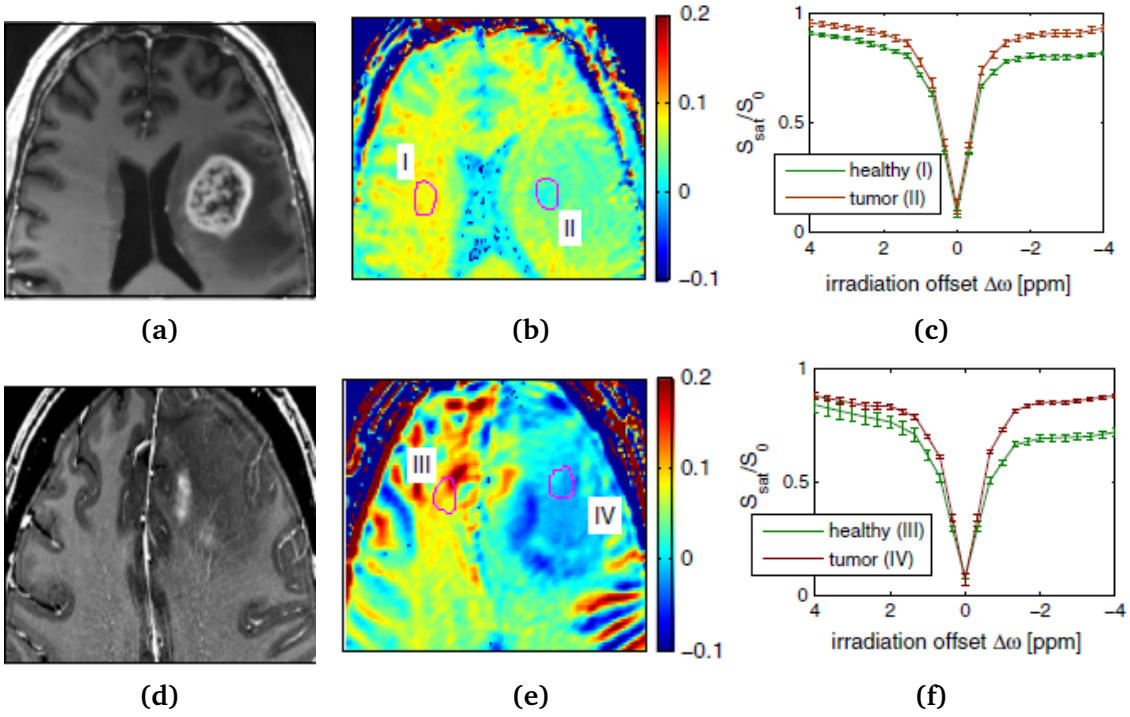

Figure 3.17: MT asymmetry maps and ROI-averaged z-spectra in two tumour patients with gadolinium-enhanced T_1 images. In patient 1 **(a)** the tumour ROI exhibited a reduction in NOE saturation **(b)**–**(c)** and may be necrotic tissue ($B_1 = 0.6\ \mu T$). Patient 2 **(d)** also exhibited a reduction in signal within the tumour ROI **(e)**–**(f)** ($B_1 = 0.8\ \mu T$). In normal tissue a clear saturation effect was observed in the aliphatic region. In both patients hypointensity was observed in the surrounding tumour tissue. Figures reproduced from ref. [94] with permission from John Wiley & Sons.

a sigmoidal profile and a well-defined transition midpoint at 5.5 M urea, where the drop in fluorescence intensity indicated protein denaturation (Fig. 3.20). Urea maintains denatured protein in a soluble state thus signal changes cannot be attributed to semisolid effects which would otherwise arise from the short T_2 of immobile proteins in aggregates [94]. This suggests that NOEs are dependent on protein conformation and may serve as a characteristic signal for proteins [94].

Zaiss et al. hypothesised that NOE magnetisation transfer pathways, whether direct or exchange-relayed, may depend on protein structure in the following ways. Protein denaturation would be accompanied by a dramatic rearrangement of hydration water. Coupling along the backbone between immobile and chemically-exchangeable protons could be affected in the same way, as well as the accessibility of chemically-exchangeable groups to water molecules [94]. There are three ways in which NOEs

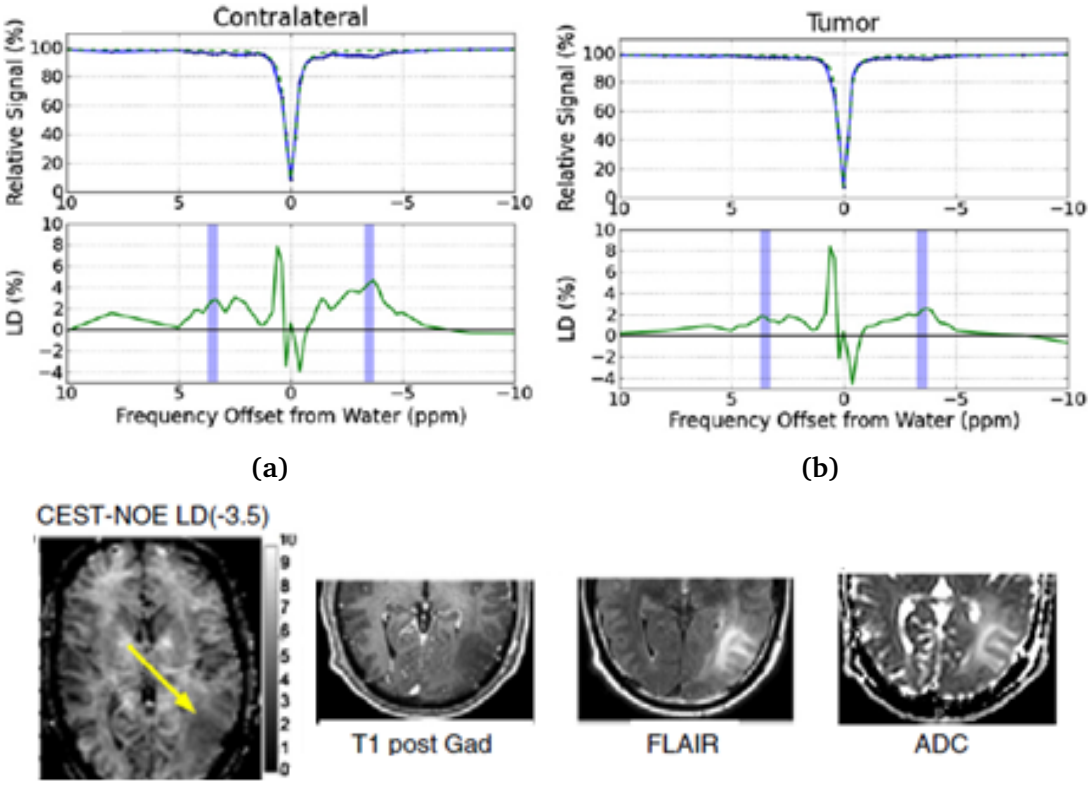

Figure 3.18: Astrocytoma patient where the z-spectra and residuals (from LDA) **(a)**–**(b)** show a reduction in the tumour region **(c)** (yellow arrow), compared to contralateral white matter. The NOE Lorentzian difference map in **(c)** shows an apparent deficit in the tumour region despite a non-enhancing T_1-weighted image of the high-grade tumour. FLAIR hyperintensity within the tumour region and an elevated ADC suggest a lower tumour cellular density, which would contribute to the reduction in observed saturation effects. Figures reproduced from ref. [57] with permission from Elsevier Inc.

originating from an exchange-relayed pathway can be affected by protein denaturation: (i) increased structural flexibility upon unfolding, changing the extent of interaction between the backbone and side-chains, (ii) changes in exchange rates due to the increased accessibility of exchangeable groups, and (iii) increased intermolecular interaction between water molecules contained within the protein core and those in the hydration shell on the surface of the protein. It is not possible to identify the separate contributions of each mechanism, although increased structural flexibility of unfolded proteins could be responsible for an initial increase in NOE signal observed in partially urea-destabilised BSA proteins [94].

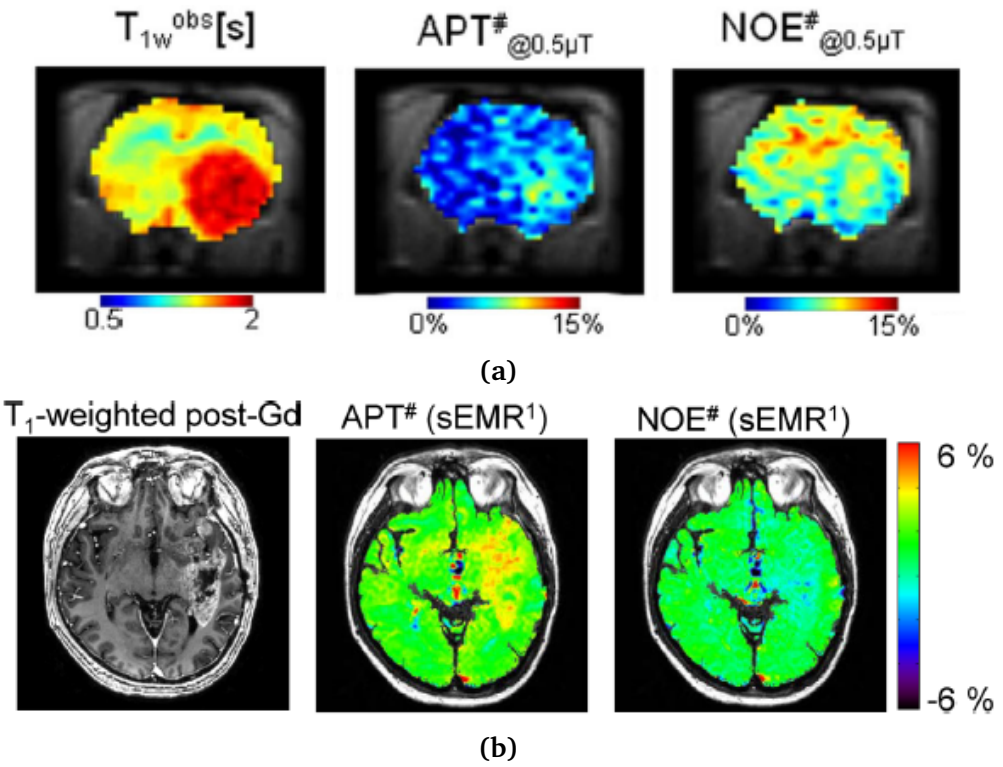

Figure 3.19: **(a)** A representative animal glioma model, reproduced from ref. [96] with permission from John Wiley & Sons. **(b)** A patient with glioblastoma from the clinical study of ref. [97], reproduced with permission from John Wiley & Sons. From left: quantitative T_1 image (T_1-weighted gadolinium-enhanced image in **(b)**), APT map using the EMR technique, and NOE map. Across the 11 patients in the study, the APT signal was significantly higher in glioma tissue (approximately 4%) compared to oedema and normal tissue. The NOE signal was significantly hypointense in the glioma and oedema ROIs compared to CNAWM.

3.5.8 pH dependence

Direct dependence of NOEs on pH could exist through an exchange-relayed mechanism of NOEs, where magnetisation of immobile protons is first dipolar-coupled to labile protons of amide side-groups on the same molecule (intramolecular transfer), before chemically-exchanging with bulk water protons [72]. Since chemical exchange of amides is base-catalysed, low pH of the ischaemic core would lead to a reduction in NOEs.

An absence of direct pH dependence would suggest a mechanism dominated by direct through-space intermolecular coupling between immobile protons and hydration water [57]. Given, however, the association between protein structure and NOEs dis-

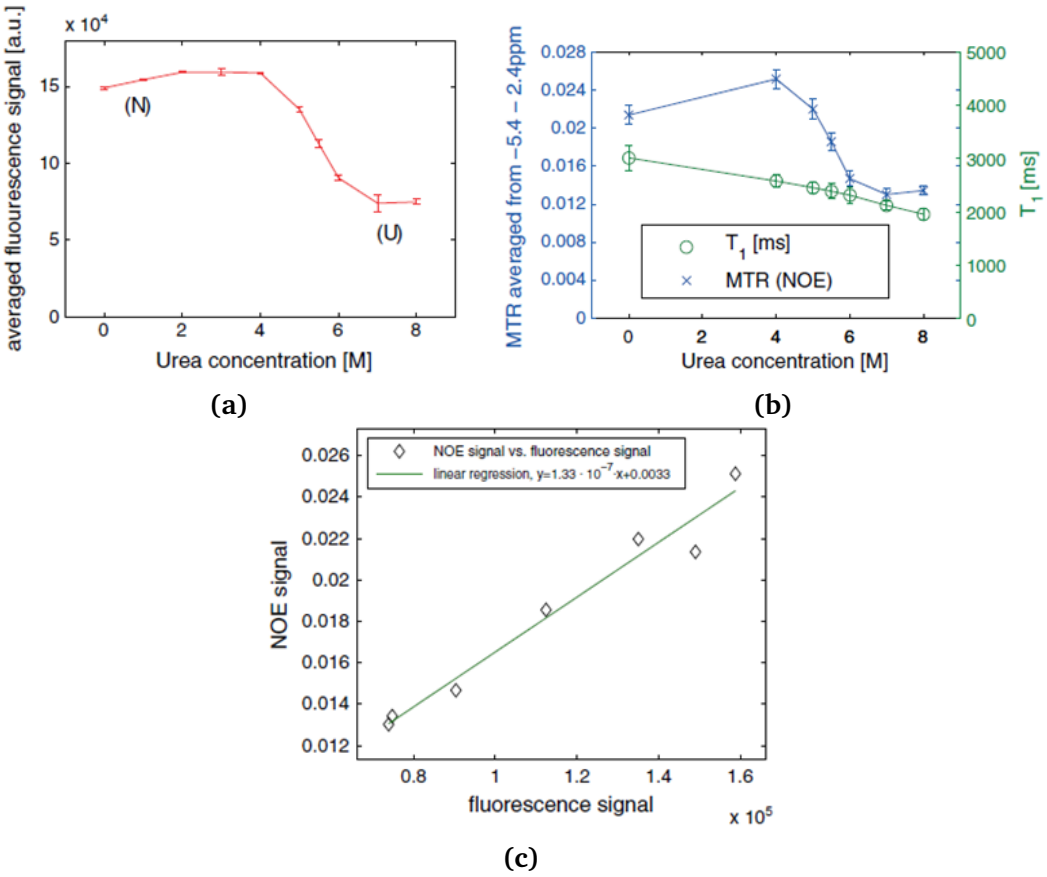

Figure 3.20: Results of a protein denaturation study explored through changes in the CEST signal, by Zaiss et al. [94]. **(a)** Fluorescence spectroscopy of BSA protein denaturation as a function of urea concentration. **(b)** Average NOE MT ratio as a function of urea concentration (blue), and change in T_1 (green). Both denaturation curves have a sigmoidal shape with the same 5.5M urea transition midpoint. **(c)** NOE MT ratio and the fluorescence signal were highly correlated ($R^2 = 0.96$), suggesting a strong dependence of NOEs on protein structure. Whilst T_1 also changed, its linear decrease did not explain the sigmoidal transition in the MT signal. Figures reproduced from ref. [94] with permission from John Wiley & Sons.

cussed in the previous section, an indirect dependence of NOEs on pH can be realised through this same pathway owing to changes in protein conformation caused by acidosis which reduce the number of dipolar coupling sites available, and lead to a reduction of direct intermolecular NOEs (also reducing exchange-relayed NOEs) [94,121]. There are thus two ways in which changes in NOE signal could be pH-driven, both of which would result in a reduction of signal under acidosis rather than an increase.

Experimentally there have been differing findings as to the pH sensitivity of NOEs [57,72], which may be a result of the different CEST analysis techniques used between studies. Jones et al. [57] studied the pH dependence of NOEs on phantoms of large mo-

bile proteins (10% BSA) using the LDA technique. APT effects and NOEs were observed without the presence of lipids or a semisolid phase [57]. The authors reported a pH dependence of NOEs from pH 5.7 to 8.0, specifically NOE $= 0.40 \times$ pH$+1.40$ ($R^2 > 0.3$). The study of ref. [122] reported a very weak dependence of NOEs on pH using the AREX technique. The pH-dependence study by Jin et al. [72] found that spectra over the NOE range were be almost identical from a pH of 5 to 7 using the LLA technique, suggesting insensitivity of NOEs to pH. The MCAO study reported strong APT lesion contrast, whilst NOE maps appeared homogeneous. The authors noted that their *in-vivo* assessment of pH dependence was not conclusive, as exchange rate and mobile macromolecule concentrations must be separately accounted for in tissue; both are proportional to NOE signal size (equation 3.10) and opposing changes could have led to a net cancellation of any measurable pH effect. The study concluded that the observed insensitivity of NOEs to ischaemia was consistent with the notion of mobile protein concentration not changing significantly during the initial hours of ischaemia [72], whereas the pronounced APT effect was largely attributed to the change in pH [72], suggesting that NOEs could be used as a complementary measure of protein concentration [72].

An explanation for the conflicting *in-vitro* results between Jones et al. and Jin et al. is the linear approximation technique used in the latter study which involved subtraction of the NOE peak from a local linear approximation of water and semisolid effects (LLA technique) [57]. Subtraction could have resulted in a cancellation of pH effects, especially given the similarity in pH dependence at the points used in the subtraction [57].

3.5.9 Effects of water T_1

Water content in the ischaemic hemisphere has been reported to be approximately constant during the first 3 h after onset of ischaemia, whilst at the 24 h time point water accumulation leads to an increase in T_1 [34]. Changes in T_1 have, however, also been reported during the initial minutes of ischaemia at 9.4 T, where the decrease in T_1 (ap-

proximately 7%) has been attributed to the cessation of blood flow [34]. This change in T_1 is irrelevant to chemical exchange, but can lead to an apparent decrease in CEST effects if not corrected for [34]. This is because the water pool mediates all CEST exchanges, such that a larger water T_1 scales CEST effects by affording more time for labelled states to accumulate in the water pool [42,84]. Thus local variations in T_1 directly modulate the size of the CEST signals. Biochemical measurements of gliomas in some studies have not observed significant APT-weighted contrast after correcting for water T_1 [86]. With respect to NOEs, quantitative T_1 maps have been used for correction, after which a reduction in dependence of the APT signal on water R_1 has been observed. The T_1-corrected NOE signal remained significantly correlated with water R_1, but also exhibited significant tumour contrast which was improved compared to the non-corrected equivalent. The BM model-based technique can in principle account for this confound by fitting for the water pool T_1.

3.6 Conclusion

The study of the NOE signal as a potential clinical biomarker in stroke and tumour imaging is relatively recent. Clinical studies suggest that NOE mechanisms operate differently to APT in ischaemic stroke. Unique contrast provided by NOEs compared to DWI and APT-weighted images may reveal information on alternative tissue injury pathways in stroke, in particular, pathways distinct from acidosis and which are associated with intracellular structural integrity of proteins.

The wide range of model-based and model-free quantification techniques introduced, as an alternative to asymmetry analysis, raises the question of which technique is optimal for separating the APT signal from competing CEST effects. This is explored in the methodological study of Chapter 5. The characterisation of NOEs and semisolid effects as largely distinct phenomena forms the basis of Chapter 6, where this understanding is used to improve signal separation.

In clinical studies, the large decrease in APT signal in otherwise normal-appearing tissue at tissue-CSF boundaries suggests that PV effects may be a confounding factor in CEST imaging, affecting quantification at the peripheries of brain tissue, near the ventricles, and at fissures [36,37,109]. In voxels at these tissue-CSF boundaries, correcting for large contributions of CSF might allow for more robust measurement of relatively small-scale CEST signals. This is explored in Chapter 7 with the introduction of a technique for PV correction of CEST data.

With respect to clinical CEST imaging of CEST effects in refs. [37,90], the use of a 3-pool BM model means that the NOE-weighted signal may be confounded by non-selective semisolid effects, as both saturation transfer phenomena are modelled using a single pool. More selective quantification is required in order to robustly explore the potential of quantitative NOE CEST imaging within acute ischaemic stroke. Chapter 8 seeks to do this by investigating NOEs and semisolid effects using the improved quantification technique developed in preceding chapters. Chapter 9 finally turns to one of the most recent developments in CEST imaging of stroke–NOE sub-resonances, and seeks to identify and quantify these effects in stroke models and clinical data.

Chapter 4

General methods

GENERAL methods employed in the subsequent chapters are detailed here, covering patient recruitment details, the image acquisition protocols, data processing, data extraction, and methods used in the analyses. Methods specific to a given chapter are presented therein.

4.1 Study details

This study used the same dataset in the clinical study in ref. [37] in which patients presenting with acute ischaemic stroke were recruited into a prospective observational imaging study according to research protocols agreed by the UK National Research Ethics Service committee references 12/SC/0292 and 13/SC/0362. After exclusions on the grounds of motion corruption and imaging artefacts this left 12 datasets for analysis in the original study, and which are used here. Patient demographics are detailed in Table 4.1. The median onset time was 2 h 45 min. In a separate study, six healthy individuals were recruited into a study of reproducibility of CEST imaging where they underwent four repeated CEST scans at three time points [37].

Patient number	Age	Gender	Hemisphere	NIHSS at presentation	Thrombolysed	Time to presenting scan (hr:min)
1	84	F	Left	3	N	03 : 25
2	92	M	Left	25	Y	02 : 50
3	64	M	Right	3	N	01 : 41
4	80	M	Left	3	N	11 : 06
5	86	F	Left	27	N	03 : 09
6	81	F	Left	21	N	03 : 25
7	95	M	Left	19	Y	04 : 14
8	53	F	Left	13	Y	02 : 48
9	57	M	Right	7	N	01 : 43
10	79	F	Right	14	Y	09 : 50
11	78	F	Left	9	Y	02 : 50
12	55	F	Left	7	Y	01 : 35

Table 4.1: Demographics of stroke patients whose datasets were used in this study. The acute datasets (time to presenting scan of less than 12 hours) were used. Larger NIHSS (National Institute for Health Stroke Scale) scores indicate more severe stroke and poorer prognosis. Adapted from ref. [37].

4.2 Image acquisition

4.2.1 Human imaging

All patient scans were performed on a 3 T Siemens Verio scanner using a 32-channel head coil at the Oxford Acute Vascular Imaging Centre (AVIC) located at the John Radcliffe Hospital. Each patient underwent a T_1-weighted structural scan (voxel dimensions $1.8 \times 1.8 \times 1.0$ mm^3, FOV = 228 mm, TR = 2040 ms, TE = 4.55 ms), DWI in three directions, multi-post labelling delay vessel-encoded pseudo-continuous arterial spin labelling (pCASL) PWI [123], and single-slice CEST imaging. A DWI (at 24 hours) and/or T_2-weighted FLAIR (at 1 week or 1 month) follow-up scan was taken to enable the definition of tissue outcome.

The single-slice CEST MRI parameters were as follows. The CEST imaging plane was selected by an expert clinician based on the DWI lesion. CEST preparation was done using a pulsed saturation scheme (Fig. 2.23), comprising a train of 50 Gaussian

pulses (FA = 184°, pw = 20 ms, TR_{RF} = 40 ms) over a total duration of T_{sat} = 2 s. Crusher gradients were applied between pulses to spoil transverse magnetisation. The corresponding average B_1 was B_{1RMS} = 0.55 μT. This was repeated at 32 saturation frequencies. For patients 1–4, an evenly distributed sampling (EDS) scheme was used, comprising 32 saturation frequencies from −4.5 ppm to 4.5 ppm in steps of 0.3 ppm, and 300 ppm. For patients 5–12, a semi-optimal sampling scheme (semi-OSS), which had a higher density of points around the amide resonance frequency, was used (−300, −50, −30, −4.1, −3.8, −3.5, −3.2, −2.9, −0.9, −0.6, −0.3, 0.0, 0.3, 0.6, 0.9, 2.9, 3.1, 3.2, 3.3, 3.4, 3.4, 3.5, 3.5, 3.6, 3.6, 3.7, 3.8, 3.9, 4.1, 30, 50, 300 ppm). The offsets at 3.4, 3.5, and 3.6 ppm were acquired twice in order to increase the SNR at these points during post-processing. [37,124]. The saturation phase was followed by SE-EPI readout (64 × 64 matrix, 6/8 partial Fourier). For patients 1–4 the SE-EPI parameters were: TR = 5000 ms, TE = 28 ms, with voxel dimensions 3.0 × 3.0 × 5.0 mm^3. For patients 5–12, the SE-EPI parameters were: TR = 5000 ms, TE = 23 ms, with voxel dimensions 3.4 × 3.4 × 5.0 mm^3. The total acquisition time for the CEST sequence was 2 minutes 45 seconds. The healthy subjects study had four repeat CEST scans at three time points; initial, 24 hours, and one week later, using the same semi-OSS CEST acquisition scheme as the patients. Fig. 4.1 shows an example of the unsaturated EPI CEST image, and the whole acquired z-spectrum, from both the EDS scheme and the semi-OSS scheme. Refer to Appendix A for an example of the whole slice raw CEST volume obtained using the EDS (Fig. A.1) and semi-OSS (Fig. A.2) schemes.

4.2.2 Preclinical imaging

The preclinical study included 6 male Wistar rats who had a stroke induced in the ipsilateral hemisphere by blocking the middle cerebral artery with a filament. MRI was performed on the animals using a 9.4 T Agilent spectrometer with a 72 mm inner diameter and 4-channel surface receiver array coils (RAPID Biomedical). Imaging was performed post-MCAO at two time points; 1 h and 2 h. Quantitative T_1 and T_2 maps

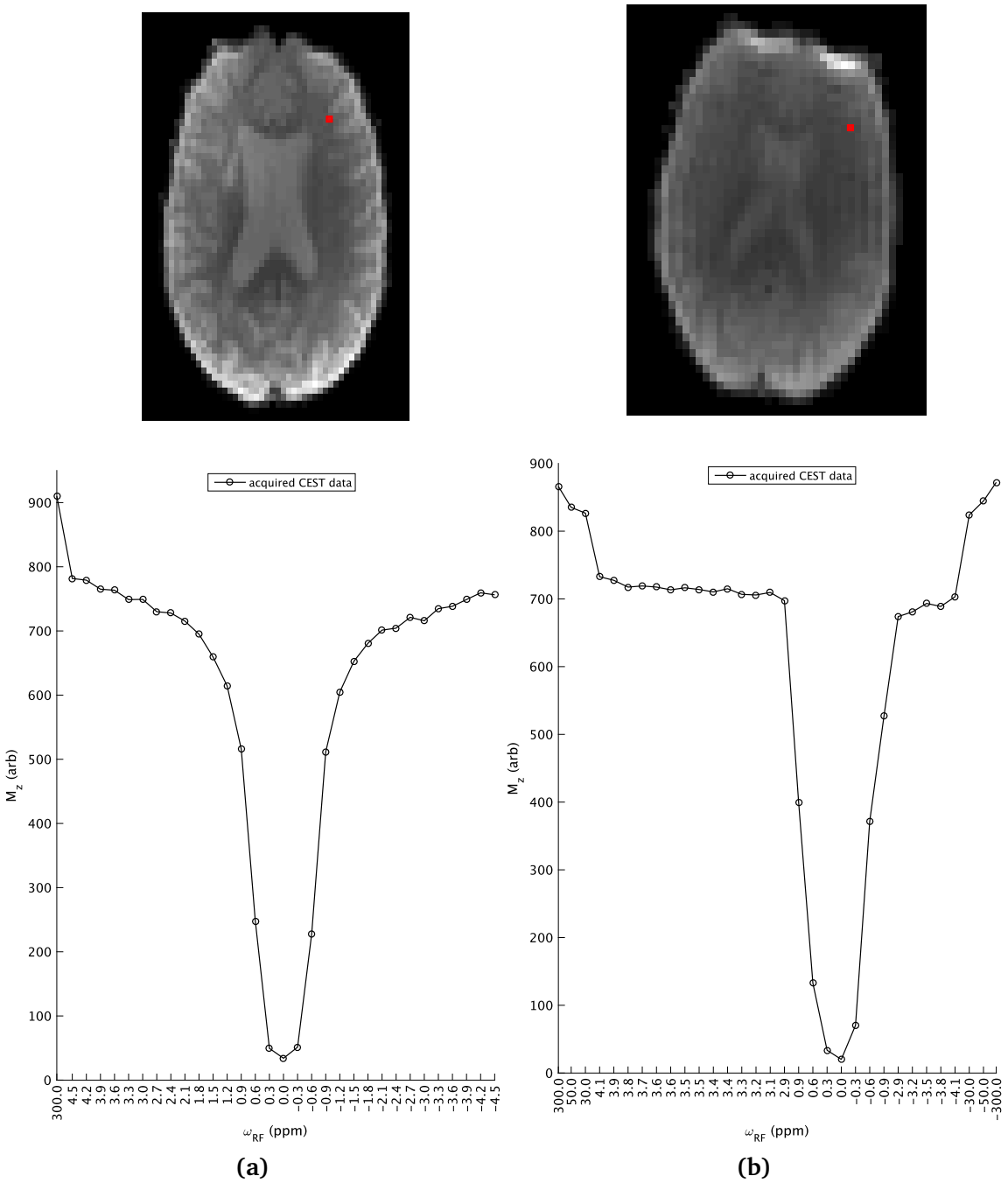

Figure 4.1: **(a)** Example of an acquired whole z-spectrum obtained from the EDS scheme where saturation frequencies are uniformly distributed between ±4.5 ppm. Shown for a single voxel (red square on the unsaturated EPI acquisition) from patient 1. **(b)** Example of an acquired whole z-spectrum obtained using the semi-OSS scheme, shown for a single voxel (red square on the unsaturated EPI acquisition) from patient 12. There is a higher density of sampling points near the amide resonance frequency, and the offsets at 3.4, 3.5, and 3.6 ppm have been acquired twice in order to increase the SNR at these points when quantifying CEST effects.

were obtained using inversion recovery (TR = 10 s, TE = 8.22 ms, TI = 13.14 ms-8 s) and spin echo experiments (TR = 10 s, TE = 30 ms to 160 ms in 10 steps). Cerebral blood flow was measured using multi-phase pCASL (8 phases between 0° and 315°, tag thickness 6.2 mm, post-label delay 550 ms), and ADC was measured from DWI in three directions with $b = 0$ s/mm^2 and $b = 1000$ s/mm^2.

The CEST acquisition was formed of a train of 50 Gaussian pulses ($pw = 20$ ms, FA = 180°) at a 50% duty cycle ($TR_{RF} = 40$ ms, equivalent to a CW B_1 power of 0.55 μT). Fifty-one offset frequencies were used (−300, −4.1, −3.8, −3.5, −3.2, −2.9, −2.6, −2.3, −2, −1.7, −1.5, −1.2, −0.9, −0.6, −0.3, 0, 0.3, 0.6, 0.9, 1.2, 1.5, 1.6, 1.7, 1.8, 1.9, 2, 2.1, 2.4, 2.7, 2.9, 3.1, 3.2, 3.3, 3.4, 3.5, 3.6, 3.7, 3.8, 3.9, 4.1, 5, 7, 9.7, 13.5, 19, 26, 37, 51, 72, 100, 300 ppm), each followed by a crusher gradient. Apart from the value of B_0 and the number of saturation frequencies, these parameters were identical to those used in the human imaging study. Image acquisition following the saturation period was done using a single-shot SE-EPI readout. Refer to Appendix A for an example an the animal raw CEST volume (Fig. A.3) and an acquired whole z-spectrum (Fig. A.4a).

4.2.3 Phantom imaging

Phantoms at different pH were prepared to mimic the intracellular environment of naïve mouse brain; refer to the study of ref. [78] for details of phantom preparation. Briefly, six female BALB/c mice aged 6–8 weeks were terminally anaesthetised; their brains were subsequently removed, homogenised, and formed into sample solutions which were titrated to six different pH values (6.3–7.7). The volume of solution in the phantoms was scaled to match *in-vivo* metabolite concentrations; BSA concentration was kept constant at 8% w/v, being representative of protein content values reported for rodent brain [78]. The BSA was not cross-linked in order to avoid introducing semisolid MT effects.

MRI was performed on all phantoms simultaneously using a horizontal bore 9.4 T

spectrometer (Agilent Technologies) with a volume receive coil (internal diameter 40 mm, RAPID Biomedical). Shimming was performed to minimise B_0 inhomogeneity. Quantitative T_1 and T_2 maps were obtained for each phantom, as follows. The T_1 relaxation time of each phantom was measured using an IR sequence (TR = 10 s, TE = 8.22 ms), where TI was varied in nine steps from 13.14 ms to 8 s, and the signals fitted to equation (2.22). The T_2 relaxation time of each phantom was measured using a spin echo sequence (TR = 10 s) where TE was varied in 10 steps from 30 ms to 160 ms, and the signals fitted to $M_z = M_0 \exp(-TE/T_2)$ (envelope of equation 2.23). In both cases eight-shot SE-EPI was used to acquire the images [78]. The CEST acquisition was formed of: 300 Gaussian pulses (pw = 26 ms, FA = 180) at a 50% duty cycle (equivalent to a CW B_1 power of 0.8 μT). Eighty-five saturation frequencies, evenly-spaced between ±10 ppm were used, and four further unsaturated acquisitions were obtained, two each at ±500 ppm. Image acquisition following the saturation period was done using an eight-shot SE-EPI readout (unsaturated acquisition and whole z-spectrum shown in Fig. A.4b). The scan parameters were: FOV = 38 mm × 38 mm, matrix size 32 × 32, slice thickness 2 mm, TE = 8.22 ms, and TR = 7.85 s. The total scan time was 3 h 6 min.

4.3 Processing

Image processing and analysis was performed using the FMRIB Software Library (FSL) [125–127] and MATLAB (Mathworks, Inc., Natick, MA).

4.3.1 Motion correction

The different CEST frequency offsets were motion-corrected relative to the unsaturated acquisition using the MATLAB function `imregister` which applied rigid-body registration accounting for rotation and translation.

4.3.2 Model fitting

The data were fitted to a CW approximation of the BM equations as implemented in the FSL tool BayCEST [62,64,103], which uses the `fabber` VB model fitting routine [62,103,128,129] to fit CEST data to a BM model [36]. Details of the specific model and constituent pools used are presented in each chapter. Example model-fitted z-spectra are presented in Appendix B for all of the model-based techniques used in this thesis.

4.3.3 ROI definitions in native space

The tissue outcomes defined this thesis were ischaemic core, infarct growth, and oligaemia. Stroke lesions were independently outlined by a neuroradiology fellow and a clinical research fellow using the masking tool in FSLView [25,126]. Where the mean overlap between the two assessors was less than 80%, a third rater, a consultant neuroradiologist, resolved discrepancies [25]. Ischaemic core tissue was defined as voxels with a presenting apparent diffusion coefficient (ADC) below a threshold of 620×10^{-6} mm^2/s, and included in the final infarct mask [37]. Final infarct was defined preferentially on the 1 week FLAIR image, or if not available, the DWI ($b = 1000$ s/mm^2 acquisition) at 24 hours. In the original study of ref. [37], final infarct was defined preferentially on the 1-month FLAIR image, or, if not available, on the 1-week FLAIR image. Oligaemic tissue was defined as voxels within a perfusion deficit but not within the final infarct [37]. The mask representing perfusion deficit was generated using a threshold approach where grey matter voxels with a CBF threshold of less than 20 ml/100g/min were identified and clustered, then used as a guide for manual delineation and subsequently closed by sequential dilation and erosion. This was a more objective approach than the method used in ref. [37], where manual delineation of the presenting perfusion deficit was guided using a perfusion threshold of 20 ml/100g/min. Infarct growth voxels are those not within the ischaemic core, but included in the final infarct [37]. Contralateral ROIs were obtained by non-linearly registering the pathological masks to standard MNI152 space, reflection in the sagittal plane, and transforming back to

CEST space. This differed from ref. [37], where a representative contralateral ROI was manually defined on the FLAIR image. Registration between time points was non-linear [130]. In ref. [37], registration between time points was done using a linear transformation with 6 degrees of freedom (DOF).

In the preclinical data, ROIs representing contralateral, infarct core, infarct growth, and oligaemic tissue, were defined from the ADC and CBF maps with the following thresholds. The infarct core mask was defined as ADC below a threshold of 620×10^{-6} mm^2/s and included in the final infarct mask [37]. Final infarct was defined on the 2 h DWI. Oligaemic tissue was defined as voxels within a perfusion deficit but not within the final infarct [37]. The mask representing perfusion deficit was generated using a threshold approach where grey matter voxels with a CBF threshold of less than 20 ml/100g/min were identified and then used as a guide for manual delineation. Infarct growth voxels were those not within the ischaemic core, but included in the final infarct [37]. The contralateral mask was the entire contralateral hemisphere excluding voxels that belong to a pathological ROI.

4.4 Data extraction

4.4.1 Transformation of images from native space and slice extraction

The CEST data were registered to the T_1-weighted scan using the FSL tool `flirt` [126, 131,132] with 6 DOF, and the resulting transformation matrix was inverted then used to transform the T_1-weighted scan to the resolution of the CEST images using the FSL tool `applywarp` [127] with two times super-sampling, after which the T_1-weighted slice corresponding to the CEST imaging plane could be extracted. Similar transformations were applied to transform masks derived on other imaging, such as grey and white matter definitions from the T_1-weighted image, as well as other imaging measures, such as DWI. The other imaging modalities were registered to CEST space and the slice

corresponding to the CEST lesion was identified by an expert clinician. All transformed images were subsequently masked to remove the cranium and other non-brain features, with the brain mask generated using the FSL tool `bet` [133] applied to the unsaturated CEST slice.

4.4.2 Generation of grey matter and white matter masks

Grey matter and white matter brain masks were generated from PV estimates (PVEs) using the FSL tool `fast` [134] on the presenting T_1-weighted scan, and the images were transformed to the resolution of the CEST images. Thresholds were applied to create masks in the data space as follows (summarised in Table 4.2). Primary analyses in Chapters 5–9 were conducted in voxels with a combined grey matter and white matter PVE of greater than 0.5. Secondary analyses were conducted within separate masks for grey matter and white matter. Grey matter masks were defined at a GM PVE threshold of 0.7, and white matter masks were defined at a WM PVE threshold of 0.9. The grey matter threshold was lower owing to fewer available voxels at the low resolution of the CEST data [37]. In healthy subjects, grey matter and white matter ROIs were defined in the same way.

4.4.3 B_0 inhomogeneity correction

The CEST data were compensated for B_0 inhomogeneity via a variable in the model fitting algorithm which attempted account for resonance shift of the main water peak. The B_0 map obtained from the 4-pool model was used to correct the model-free techniques listed in Table 3.1 by interpolating the acquired spectra voxel-wise onto a 0.1 ppm-resolution axis before applying any of the model-free techniques to the data.

The presence of other metabolite resonances, which, at 3 T, overlap with or are very close to the main water peak (such as myo-inositol at 0.2–1.6 ppm, or NOEs at −1.6 ppm) [10,135], presents a risk of biasing the fitting process at a slight offset from actual water resonance, thereby potentially introducing a systematic error into subse-

quent calculations. An approach that is not vulnerable to this is to separately acquire a direct water saturation map before or after the CEST acquisition, where a short-duration and low-amplitude saturation pulse minimises CEST effects whilst being sensitive to DS effects (referred to as a water saturation shift referencing map, or WASSR) [10,136]. This necessitates an additional 1–2 minutes of scan time, and was not acquired for the datasets used in this thesis. In creatine phantoms the model fitting approach has been shown to closely match the WASSR method, with a maximum difference of less than 0.03 ppm [124].

4.4.4 Calculation of means within an ROI

The patient measures derived in this study were exclusively voxel-weighted measures, used to investigate trends at the tissue level as opposed to at the patient level. Use of means at the tissue level, rather than at the patient level, helps account for heterogeneity within the lesion (ROI) which would otherwise be overlooked and lead to underestimation of any changes [25]. A voxel-weighted mean for each ROI was obtained from the patient data by performing a weighted sum of patient means, where the weight assigned to a patient was proportional to the number of contributing voxels for a given ROI. This was done separately for each quantification measure. Voxel-weighted measures were similarly derived from the animal data. The number of voxels and subjects used are listed in Table 4.2. Healthy subject and phantom means did not employ voxel weighting.

4.4.5 Calculation of relative mean values

Relative mean values were derived for each patient, where the mean in each pathological ROI (e.g. mean APTR*) was normalised to the mean value in the contralateral hemisphere, giving 'relative APTR*'. This further metric accounted for systematic variability between individuals not already controlled for by the quantification technique.

Table 4.2: Total number of patient datasets, animals, and corresponding voxels used in the studies in this thesis, categorised by the tissue outcome. Column 1 lists the type of voxel analysed, such as GM, WM, or GM+WM ('whole slice'). Column 2 lists the PVE map from which the mask was derived, and the PVE threshold that was applied to define the mask, is listed in column 3. In row 1, the whole slice mask is defined as a threshold of 0.5 on a GM+WM PVE map, used for primary analyses in Chapters 5–9. Rows 3 and 4 respectively define a GM-only mask and a WM-only mask, used for secondary analyses, where differences between GM and WM were explored.

			ischaemic core	infarct growth	oligaemia	contralateral
brain mask	PVE map	Mask PVE threshold				
stroke patients						
whole slice	GM+WM	0.5	445	919	843	1692
grey matter	GM	0.7	113	192	110	181
white matter	WM	0.9	114	206	165	478
animals (whole brain)	—	—	2076	1578	3583	11833
number of patients			11	11	8	12
number of animals					6	

4.5 Analysis

All analysis and quantification of CEST data was done in the native space of the data. The significance level used in this study was $\alpha_{crit} = 0.05$. Statistical tests involving patient or animal data incorporated voxel weighting.

4.5.1 Statistical testing

Differences between grey matter and white matter were assessed using a two-tailed paired t-test. Comparisons between multiple groups (ROIs and/or quantification techniques) were preceded with a one-way ANOVA test for significance. *Post-hoc* pairwise testing was done using a two-tailed Welch's unequal variances t-test which was corrected for multiple comparisons. Correction for multiple comparisons was done by adjusting the pairwise significance level ($\tilde{\alpha}_{crit}$) using the Bonferroni method, such that the family-wise error rate (FWER) was FWER $< \alpha_{crit}$. The number of DOF used in

the statistical tests was based on the number of patients rather than on the number of voxels, which reduced the DOF compared to the original study of ref. [37].

4.5.2 Repeatability

Two-way ANOVA was used for comparisons between healthy subjects and time points, and one-way ANOVA was used for comparisons between patient contralateral ROIs. Repeatability was further quantified using the coefficient of variation (CoV: standard deviation divided by the mean). This was used as it is a normalised measure of variation across subjects or time points, allowing comparisons between quantification measures which differ in their nominal or baseline values.

4.5.3 Spatial variability

Spatial variability, defined as the CoV within a given ROI, was used as a measure of spatial heterogeneity within the ROI, found in healthy subjects and in patient contralateral tissue.

4.5.4 Contrast-to-noise ratio

Contrast-to-noise ratio (CNR) was defined as follows for a given pathological ROI. Contrast was defined as the difference in mean signal between the ROI (m_{ROI}) and the contralateral ROI (m_{CO}), and noise was defined as the SD within the contralateral ROI ($\mathrm{SD}_{\mathrm{CO}}$):

$$\mathrm{CNR}_{\mathrm{ROI}} = \frac{m_{\mathrm{ROI}} - m_{\mathrm{CO}}}{\mathrm{SD}_{\mathrm{CO}}} \tag{4.1}$$

4.5.5 Correlation

Correlation between metrics was reported as the coefficient of determination (R^2) along with the corresponding p-value from an F-test on R^2. R^2 was interpreted according to an absolute criterion as follows: no correlation (0.00–0.19); low correlation (0.20–0.39);

moderate correlation (0.40–0.59); moderately high correlation (0.60–0.79); and high correlation ($\geq$ 0.80) [137].

Chapter 5

Comparative study of quantification techniques

5.1 Introduction

EARLY APT imaging studies tended to employ relatively simple measures of spectral asymmetry for quantification, which assume a broad featureless spectrum upfield of water resonance as a fixed reference. This assumption has been undermined by the realisation that the upfield spectrum is not a good reference for asymmetry techniques due to relatively prominent asymmetric saturation effects from NOEs [32,57,72,74,86].

The recent literature has introduced various approaches to CEST analysis that seek to overcome the limitations of an asymmetry analysis when NOEs are present. These include modifying the asymmetry approach, where instead of taking a reference from the upfield part of the z-spectrum, frequencies around the APT frequency in the downfield region are used [34,74,84]. More complex model-based approaches have also been developed using Bloch-McConnell and Lorentzian-based approaches [57,90], though such metrics have largely only been applied in non-human preclinical studies, or at high field strengths (7 T) that are, as yet, routinely unavailable in a clinical context. In the study

of ref. [37] where a BM model-based approach was tested on data derived from clinical acute stroke patients [36], the model developed to isolate the APT metric used 3 pools to model water, APT, and combined semisolid MT+NOE contributions. Given the potential of APT imaging to complement existing imaging techniques to provide clinically-relevant information, there is a need to develop analysis techniques that deliver a robust and repeatable APT metric. Both model-free and model-based solutions exist. Hence, the objective of this chapter was to compare model-based and model-free quantification techniques for CEST imaging that specifically separate APT and upfield effects for application in the clinical setting. Towards this end a methodological comparison of different CEST quantification techniques was undertaken around clinical endpoints in a cohort of acute stroke patients.

5.2 Methods

An outline of the methods used in this chapter is presented below; refer to Chapter 4 for further details.

5.2.1 Study details

This chapter employed the datasets from 12 patients presenting with acute ischaemic stroke and the datasets from 6 healthy subjects.

5.2.2 Processing

The model-free quantification techniques compared in this chapter are asymmetry analysis, LLA, and spillover-corrected MTR. The model-based techniques are 3-pool BM modelling and paLDA. The model-free and model-based quantification techniques are detailed in Tables 3.1 and 3.2.

The data were fitted to a CW approximation of the BM equations (Fig. B.1). The 3-pool BM model used in this chapter comprises a bulk water pool, an amide pool, and

Table 5.1: Three-pool BM model priors for clinical data, expressed as a mean and SD, reproduced from ref. [36].

Glossary – M_0: pool concentration relative to water pool (water pool M_0 is absolute), k_{ex}: pool→bulk water exchange rate, T_1: longitudinal relaxation time, T_2: transverse relaxation time, $\Delta\omega$: chemical shift with respect to water pool.

	water		APT		asymmetric semisolid	
Parameter	mean	SD	mean	SD	mean	SD
M_0 (norm.)	0	1×10^6	$\frac{90\text{ mM}}{112\text{ M}}$	$\frac{20\text{ mM}}{112\text{ M}}$	0	1×10^6
k_{ex} (Hz)	—	—	20	$e^{1.0}$	30	$e^{1.0}$
T_1 (s)	1.3	0.15	0.77	0.15	1.0	0.15
T_2 (ms)	70	14	10	2	0.2	0.04
$\Delta\omega$ (ppm)	0	$\sqrt{0.1}$	3.5	1×10^{-6}	−2.41	1×10^{-6}

a third pool which attempts to account for both semisolid effects and NOEs. The 3-pool parameter prior distributions are listed Table 5.1. The apparent APT ratio, APTR*, was defined in Section 3.2.2.5.

In this retrospective study it was not possible to follow the acquisition methodology from the original LDA approach. Instead, a post-acquisition LDA technique (Section 3.2.2.3) was used where, rather than applying an ultra-low B_1 during the acquisition phase, the data acquired using a conventional CEST scheme were used and only the data points which were expected to exclude APT and NOEs were used for model fitting [36]. The data points at ±300 ppm, ±50 ppm, ±30 ppm, ±0.9 ppm, ±0.6 ppm, ±0.3 ppm, and 0 ppm, were assumed to exhibit contributions from the bulk water and semisolid pools only and were fitted to a 2-pool BM model comprising water and a semisolid pool (Fig. B.1). Subtraction of the acquired z-spectrum (B_0-corrected) from the fitted spectra yielded a residual corresponding to the APT effect in a similar way to conventional LDA. The LDA measure at each voxel was obtained by integrating the residual between 3.0 to 4.0 ppm (in increments of 0.01 ppm) using trapezoidal integration.

5.2.3 Data extraction

The patient ROIs used in this study were the ischaemic core and a mirrored contralateral mask. In the analysis of patient results all measures were also normalised to their mean

in the contralateral hemisphere to produce a relative measure. The relative patient means were weighted by the number of contributing voxels and pooled to give a voxel-weighted group mean for each tissue outcome. Primary analyses of the clinical data were done in voxels with a combined grey matter and white matter PVE greater than 50%, defined as the whole slice mask. Secondary analyses were done in separate grey matter and white matter masks.

5.2.4 Analysis

Contrast between grey matter and white matter was assessed in healthy subjects. Repeatability in healthy subjects and in patient contralateral tissue was measured using ANOVA and the CoV. In patients the ischaemic core CNR was evaluated.

It was found that some metrics exhibited a near-zero mean but in a consistent manner, such that the CoV was large (low repeatability) despite the consistency of the metric. For this reason, an alternative measure of repeatability was also explored; the ratio of the SD to the interquartile range (IQR). This provided consistent normalisation across different metrics whilst obviating use of the mean and without being strongly influenced by outliers, which was found to be more of an issue for the model-free metrics.

5.3 Results

A box plot of healthy subject APTR is shown in Fig. 5.1 and provides a visual comparison of consistency in APTR quantification using different quantification techniques. Defining repeatability as the ratio of the SD to the IQR yielded a CoV of 1.35% using LLA, 1.65% using MTR_{Rex}, 2.47% and 3.94% for classical and enhanced asymmetry, with the two model-based measures being below 1.50%.

Contrast between grey matter and white matter in healthy subjects is shown in Fig. 5.2. BMM analysis exhibited the smallest difference between grey and white matter; 3-pool $APTR^*$ contrast was 2.7%. The remaining metrics exhibited contrast of at least

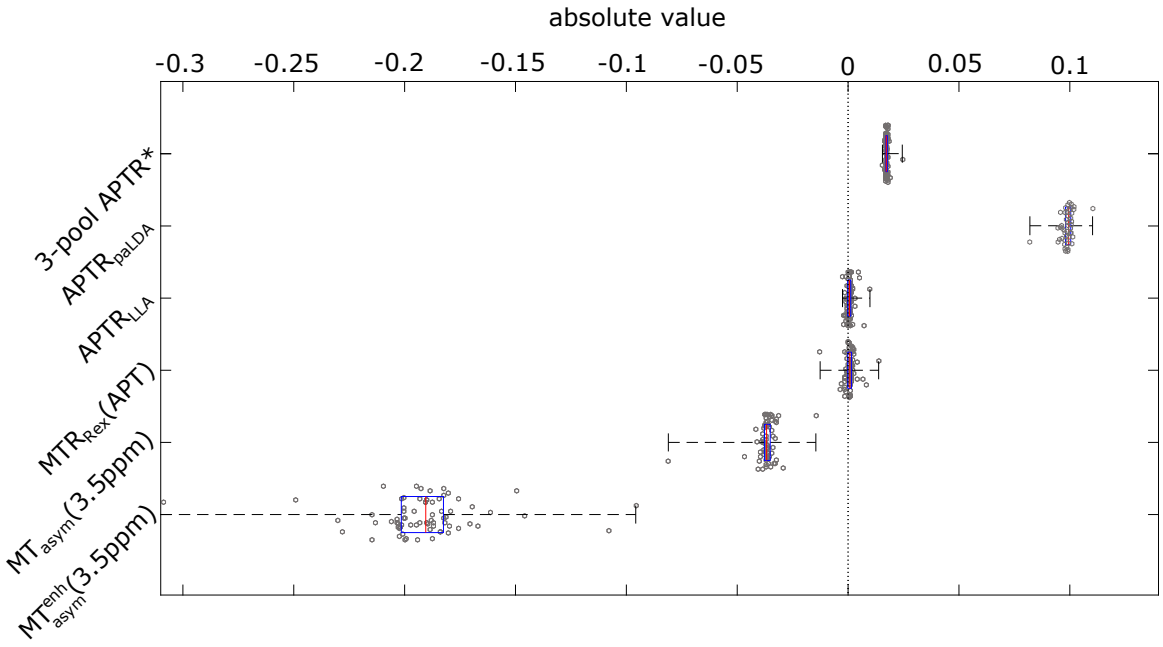

Figure 5.1: Box plot of mean APTR in healthy subjects for each quantification technique.

10%. Model-free metrics had the highest contrast between grey matter and white matter.

The measures did not exhibit significant variation across healthy subjects or between time points, except for the paLDA metric ($p = 0.08$ between subjects) and the LLA metric ($p = 0.03$ between subjects). Repeatability between subjects is shown in Fig. 5.3a. The model-based metrics had the lowest CoV. Three-pool APTR* had the lowest CoV in healthy tissue (3.93%). This was followed by paLDA (4.54%). Between the two asymmetry metrics, healthy subject CoV was lower using classical asymmetry (11.7% vs. 18.1%). Similar trends were present when repeatability between sessions was measured in healthy subjects, as follows. The lowest CoV was obtained using 3-pool APTR* (3.82%) and the paLDA metric (3.34%). Between the two asymmetry metrics, healthy subject CoV between time points was lower using classical asymmetry (8.95% vs. 20.5%).

The spatial variability of each metric in healthy subjects and patient contralateral tissue is shown in Fig. 5.3b. Model-based APT measures exhibited lower spatial variability than the model-free metrics. Three-pool APTR* had the lowest spatial variability

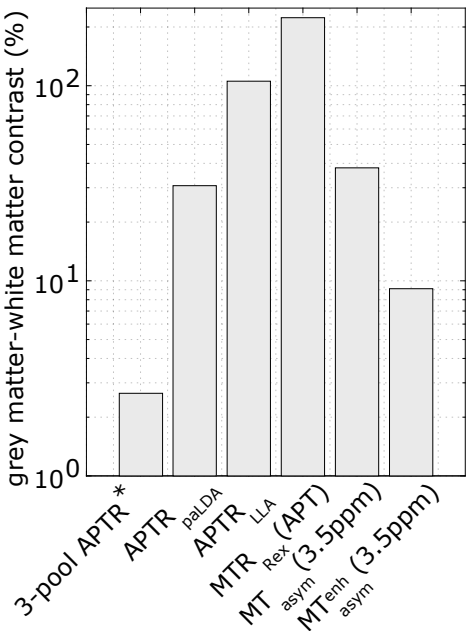

Figure 5.2: Contrast between grey matter and white matter in healthy subjects using different techniques for quantifying APT effects.

(19.4% in healthy subjects), followed by $APTR_{paLDA}$ (29.7%). Of the model-free metrics, classical asymmetry exhibited the least amount of spatial variability (53.2%).

Ischaemic core CNR is shown for the different metrics in Fig. 5.4. Three-pool $APTR^*$ exhibited the highest ischaemic core CNR (0.73). $APTR_{paLDA}$ had a CNR of 0.05. Three-pool $APTR^*$ had contrast of 0.0025 and a noise term of 0.0035. The paLDA metric exhibited a similar level of contrast (0.0017) to the 3-pool metric, but its low CNR was dominated by a noise term (0.031) that was approximately an order of magnitude larger than that of the 3-pool measure. The LLA metric and MTR_{Rex} had similar CNRs (0.47, 0.52), and classical asymmetry had a higher CNR (0.77) than enhanced asymmetry (0.29).

5.4 Discussion

Robustness analysis of the six quantification techniques indicated that the BM model-based metric had the smallest contrast between grey matter and white matter, whereas model-free metrics exhibited the highest contrast. Model-based metrics were the most

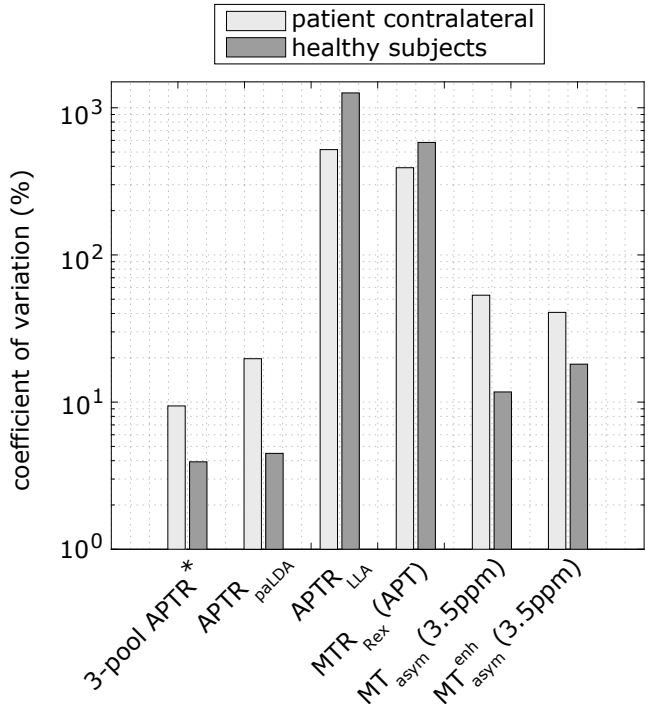

(a)

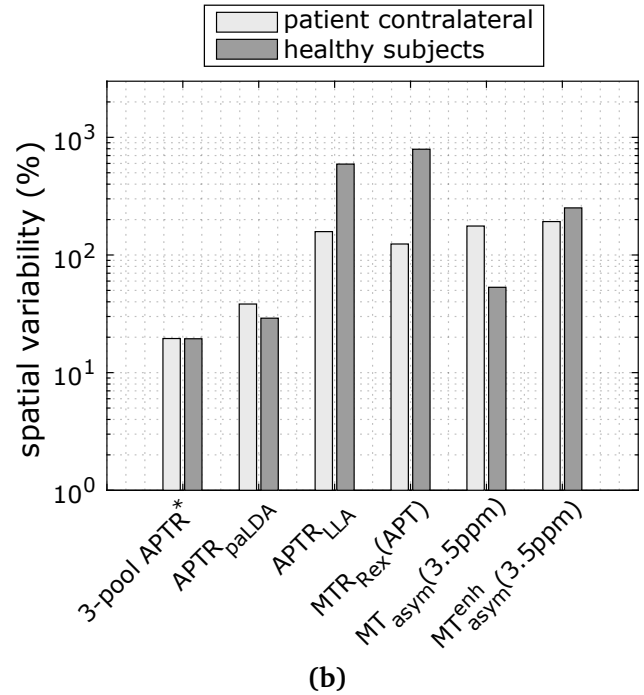

(b)

Figure 5.3: (a) Subject repeatability and **(b)** spatial variability of the APT signal in healthy subjects and in patient contralateral tissue using different quantification techniques.

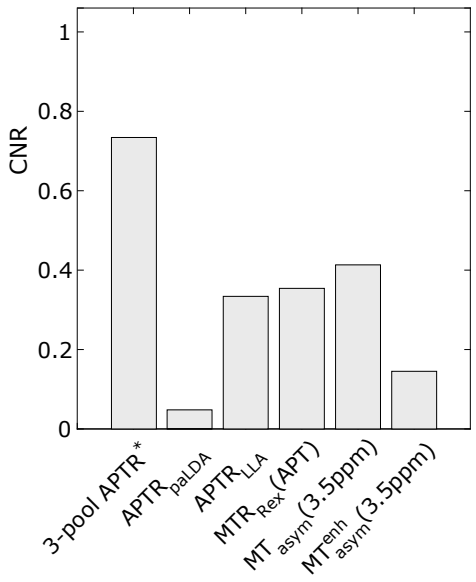

Figure 5.4: Ischaemic core CNR using different APTR quantification techniques.

repeatable across time points and between subjects, the lowest CoV being achieved using 3-pool APTR*. Model-based metrics also exhibited the lowest spatial variability, of which 3-pool APTR* was the most uniform. Three-pool analysis yielded the highest stroke lesion CNR. In these respects, classical asymmetry generally had improved measures compared to enhanced asymmetry.

Requirements of a metric in a clinical imaging context are that it is repeatable and maximises stroke lesion contrast. In these respects, 3-pool APTR* was the optimal metric. Model-based metrics, BMM analysis in particular, were more robust than model-free metrics. Similar APT measures in grey and white matter was expected on the basis of uniform brain tissue pH; however it is not known whether chemical properties of amides, such as concentration and exchange rate, ought to be the same in grey matter and white matter. Pragmatically, CEST imaging is more useful clinically if there is minimal contrast between grey matter and white matter. On this basis, in the context of clinical imaging of stroke, one of the advantages of a metric is that it minimises differences between grey matter and white matter. APTR* works well in this respect as not only has it shown minimal tissue contrast, but also similar patterns of change in response to ischaemia.

In this clinical study a relatively widely-available 3 T field was used, rather than an

ultra-high field strength, making it difficult to accurately identify the spectral boundaries of the solute pools. The performance of the LLA and MTR_{Rex} techniques is predicated on having well-defined boundaries (Section 3.2.1), and these metrics demonstrated good detection sensitivity in the 9.4 T studies where they have been used [34, 72]. With respect to the paLDA technique, the Lorentzian difference signal was small at 3 T compared to the study at 7 T using conventional LDA in ref. [87]. Thus the present study was limited to evaluating these metrics in sub-optimal conditions, and different results might have been found for an equivalent high-field preclinical CEST study.

A high CoV could be caused by a near-zero mean (small denominator) whilst the actual distribution of values across subjects (SD) is relatively consistent, making the CoV an inaccurate reflection of repeatability in cases where the mean value is close to zero. Model-based and classical asymmetry metrics exhibited a large mean compared to their spread of values and this yielded a relatively low coefficient of variation. Enhanced asymmetry and MTR_{Rex} had a high coefficient of variation and in both cases this was caused by a wide spread of values indicating that their repeatability was in fact low due to little robustness to small variations within largely homogeneous regions. Enhanced asymmetry differs from classical MT asymmetry by averaging over the spectrum, which would be thought to improve rather than decrease repeatability. However, it also bears a denominator that approaches zero in regions where APT effects are weak, and this non-linearly amplifies the asymmetry measure. This non-linear component of signal variation overwhelms the benefit afforded by averaging and is likely to be attributable to the presence of strongly asymmetric effects, which were not present in the context of the paramagnetic CEST agent for which this measure was first used. The high variability exhibited by the LLA metric and MTR_{Rex} was attributable to their small mean which inflated the CoV as defined earlier. A near-zero mean exhibited by these model-free methods indicates that they show almost no APT effect in the data, whereas other measures do. A more representative measure of repeatability in this case was the ratio of the SD to the IQR as the IQR provided consistent normalisation across differ-

ent metrics whilst obviating use of the mean and without being strongly influenced by outliers. Using this measure of repeatability, the model-based metrics still had lower variation than the model-free metrics.

5.5 Conclusion

In comparing the robustness of model-based and model-free quantification metrics, model-based metrics were found to be more repeatable and exhibited good contrast between normal and pathological tissue. The BM model-based metric performed better in these respects than the other metrics and might therefore be more suitable for use in clinical imaging of acute stroke. In the next chapter this technique is extended to a 4-pool model that more correctly describes upfield contributions to the z-spectrum based on observations in the literature, with the aim of achieving better separation of CEST signals in normal and pathological tissue.

Chapter 6

Extending Bloch-McConnell model analysis

6.1 Introduction

A range of CEST quantification techniques were compared in the previous chapter, and the 3-pool model-based metric was found to be the most robust for quantifying CEST signals in clinical data. The 3-pool model-based approach to APT quantification was introduced in the study of ref. [62] and subsequently used in the clinical study of ref. [36], and comprised a water pool, an APT pool, and a third pool that combined semisolid effects and NOEs in a single pool. However, the more recent literature [32,57,72,74,86] suggests that semisolid effects and NOEs are distinct and this might not be modelled well within a single pool. Separation of the semisolid and NOEs as two independent pools might be more accurate based on recent clinical literature [32,72,74]. This suggests using at least 4 pools for describing the z-spectrum: a water pool, an APT pool, and two further pools that separately account for semisolid effects and NOEs. Therefore, the existing implementation for APT in stroke might not be optimal and could feasibly have introduced bias into the measures of, or reduced the sensitivity to, changes in the APT effect.

Hence, the objective of this chapter was to determine whether substantial differences are observed between 3- and 4-pool model-based analysis of APT CEST in acute stroke. Towards this end, a comparison of these metrics was undertaken around clinical endpoints in a cohort of acute stroke patients.

6.2 Methods

An outline of the methods used in this chapter is presented below; refer to Chapter 4 for further details.

6.2.1 Study details

This chapter employed the datasets from 12 patients presenting with acute ischaemic stroke and the datasets from 6 healthy subjects.

6.2.2 Processing

The quantification metrics compared in this chapter, obtained through BMM analysis, were 3-pool APTR* and 4-pool APTR* (Section 3.2). The data were fitted to a CW approximation of the BM equations (Fig. B.2). The 3-pool BM model used in this study comprised a bulk water pool, an amide pool, and a third pool which attempted to account for both semisolid effects and NOEs. The third pool combined saturation effects from NOE and semisolid pool exchanges without distinguishing between these two signal sources. This may be sub-optimal given the observed differences in the linewidth of semisolid saturation and the region over which NOEs have been observed.

The 4-pool BM model, introduced in this chapter, is an extension of the 3-pool model such that semisolid effects and NOEs are described using two separate pools in order to achieve better separation of NOEs and semisolid effects. The parameter prior distributions are listed in Table 6.1 (3-pool priors are listed in Table 5.1). The semisolid pool modelled semisolid saturation as a classic Lorentzian effect centred at water reso-

Table 6.1: Four-pool BM model priors for clinical data, expressed as a mean and SD.

Glossary – M_0: pool concentration relative to water pool (water pool M_0 is absolute), k_{ex}: pool→bulk water exchange rate, T_1: longitudinal relaxation time, T_2: transverse relaxation time, $\Delta\omega$: chemical shift with respect to water pool.

*Same value as 3-pool model was used [36].
**Based on the 4-pool model used in ref. [32].
†Same value as APT pool was used, as suggested in ref. [32].

	water [36]		APT [36]		symmetric semisolid		NOE	
Parameter	mean	SD	mean	SD	mean	SD*	mean	SD*
M_0 (norm.)	0	1×10^6	$\frac{90\text{ mM}}{112\text{ M}}$	$\frac{20\text{ mM}}{112\text{ M}}$	0*	1×10^6	0*	1×10^6
k_{ex} (Hz)	—	—	20	$e^{1.0}$	60**	$e^{1.0}$	20†	$e^{1.0}$
T_1 (s)‡	1.3	0.15	0.77	0.15	1.0 [32,36]	0.15	0.77†	0.15
T_2 (ms)	70	14	10	2	0.1**	0.02	0.3 [32]	0.06
$\Delta\omega$ (ppm)	0	$\sqrt{0.1}$	3.5	1×10^{-6}	0 [32]	1×10^{-6}	−3.5 [32]	1×10^{-6}

nance, and NOEs were modelled separately as a single pool upfield of water based on observations in the literature.

6.2.3 Data extraction

The patient ROIs used in this study were ischaemic core, infarct growth, oligaemia, and a mirrored contralateral mask. Primary analyses of the clinical data were done in voxels with a combined grey matter and white matter PVE greater than 50%, defined as the whole slice mask. Secondary analyses were done in separate grey matter and white matter masks. In the analysis of patient results all measures were also normalised to the contralateral hemisphere to produce a relative measure. The relative mean values were weighted by the number of contributing voxels and pooled to give a voxel-weighted group mean for each tissue outcome.

6.2.4 Analysis

Group mean absolute APTR* was found in healthy subjects for the whole slice, grey matter and white matter, and values were compared between the 3- and 4-pool models. In patients, the voxel-weighted ischaemic core absolute APTR* was compared against

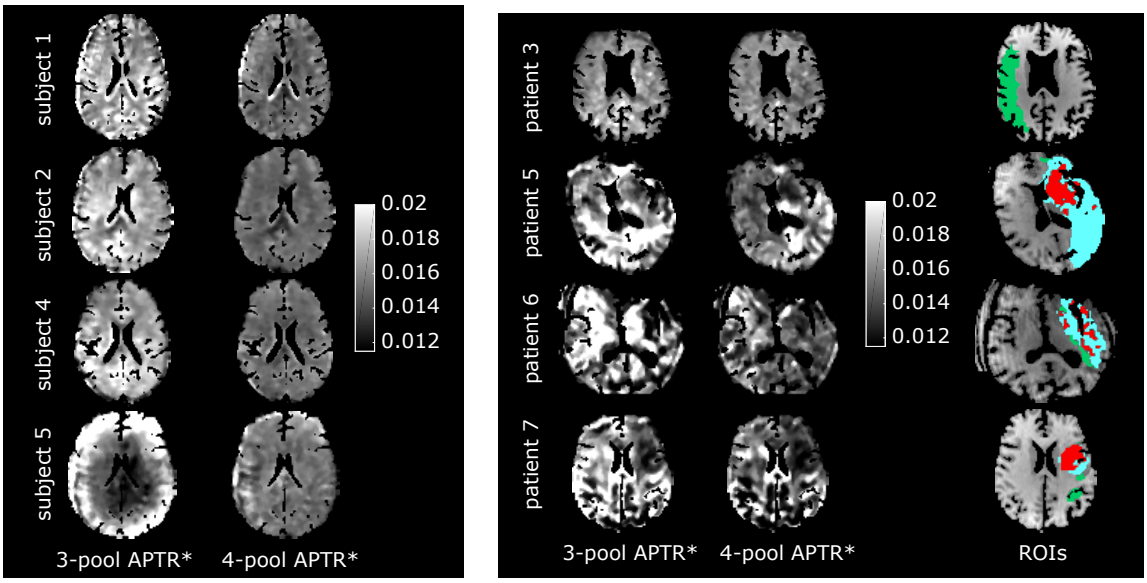

(a) **(b)**

Figure 6.1: Comparison of 3- and 4-pool maps of **(a)** healthy subjects, and **(b)** representative patients. Red: ischaemic core; green: oligaemia; cyan: infarct growth.

healthy subjects for each model. Repeatability in healthy subjects and patient contralateral tissue was measured using ANOVA and the CoV. The spatial variability within healthy subjects and patient contralateral tissue was compared between models. In patients, relative APTR* was compared between pathological ROIs, and the CNR was found for both the 3-pool and 4-pool models in the ischaemic core and infarct growth ROIs.

6.3 Results

Representative maps of the healthy subjects and six stroke patients are presented in Fig. 6.1. Whole slice mean 3- and 4-pool APTR* in healthy subjects and in patient ROIs are presented in Fig. 6.2. Group mean 3-pool APTR* was 0.0174 ± 0.0003, and group mean 4-pool APTR* was 0.0156 ± 0.0002; 3-pool APTR* was thus larger by 11.3% ($p < 0.001$). APTR* did not vary significantly between subjects or across time points.

Mean APTR* in grey matter and white matter is shown in Fig. 6.2b. Grey matter APTR* was significantly larger than white matter; by 2.7% (4.7×10^{-4}, $p = 0.002$) using

3-pool analysis, and by 2.0% (3.1×10^{-4}, $p < 0.001$) using 4-pool analysis. Three-pool APTR* exhibited lower spatial variability in grey matter compared to white matter (CoV of 14.1% vs. 20.6%), whereas 4-pool APTR* had similar spatial variability in both grey and white matter (CoV of 9.5% and 7.6%).

Patient mean APTR* values in the different ROIs are shown in Fig. 6.2c. Differences between the ROIs were significant in both 3-pool ($p < 0.001$) and 4-pool ($p = 0.001$) analysis. Both 3- and 4-pool APTR* yielded a statistically significant decreased ischaemic core signal compared to the mean in healthy subjects (3 pools: $p = 0.001$, 4 pools: $p < 0.001$) and the mean in patient contralateral tissue (3 pools: $p < 0.001$, 4 pools: $p = 0.002$). In the ischaemic core, 3-pool APTR* (0.0156 ± 0.0009) was larger than 4-pool APTR* (0.0143 ± 0.0008) in a similar proportion (8.8%) to that found in healthy subjects (11.3%).

The relative (to contralateral tissue) mean APTR* in patients is presented in Fig. 6.3. When the whole slice was analysed using 3-pool APTR*, ischaemic core relative APTR* (0.86 ± 0.07) was lower than in oligaemia (0.97 ± 0.07). Although an ANOVA test indicated significant variation between pathological ROIs ($p = 0.047$), *post-hoc* testing did not detect a significant difference ($p = 0.020$). Four-pool analysis, on the other hand, exhibited a significant difference between the ischaemic core signal and oligaemic tissue ($p = 0.014$). In the ischaemic core 4-pool APTR* was 0.91 ± 0.05. In oligaemic tissue 4-pool APTR* (0.99 ± 0.05) was slightly closer to unity than 3-pool analysis. In secondary analysis of grey matter voxels (Fig. 6.3b), 3-pool APTR* exhibited a significant difference ($p = 0.016$) between the ischaemic core (0.87 ± 0.08) and oligaemia (1.0 ± 0.1), as did 4-pool APTR* ($p = 0.007$). In white matter voxels (Fig. 6.3c), neither of the two measures exhibited significant variation between pathological ROIs (3 pools: $p = 0.20$, 4 pools: $p = 0.31$), although 3-pool analysis retained decreased values in the ischaemic core (0.86 ± 0.08) and in infarct growth (0.93 ± 0.06). In white matter, 4-pool analysis of the ischaemic core signal was closer to unity (0.95 ± 0.08) than the grey matter or whole slice means, whereas the 3-pool measure remained at a lower level.

Infarct growth tissue exhibited an intermediate value using 3-pool analysis (whole slice relative mean: 0.93 ± 0.05) that put it approximately mid-way between the ischaemic core and oligaemia values, having a CNR of 0.38 with respect to patient contralateral tissue. This contrast of the infarct growth signal was diminished, CNR= 0.07, using 4-pool analysis, as the relative mean in infarct growth was approximately unity (0.99 ± 0.06) .

A two-way ANOVA test indicated that 4-pool APTR* varied significantly between subjects ($p = 0.04$). Repeatability between subjects is shown in Fig. 6.4. Four-pool APTR* had the lowest CoV in healthy subjects and patient contralateral tissue (2.35%, 6.61%). The CoV using 3-pool APTR* was 3.93% in healthy subjects and 10.4% in patient contralateral tissue. These trends were also present when repeatability between sessions was measured in healthy subjects. Four-pool APTR* CoV was the lowest (2.01%), followed by 3-pool APTR* (3.82%).

The spatial variability of each metric in healthy subjects and patient contralateral tissue is shown in Fig. 6.4b. Four-pool APTR* exhibited lower spatial variability in healthy subjects and patient contralateral tissue (10.2%, 13.0%) than 3-pool APTR* (19.4%, 19.5%). Ischaemic core CNR is shown for the different metrics in Fig. 6.5. Four-pool APTR* had a CNR of 0.70, and the CNR was 0.73 using 3-pool APTR*. Four-pool APTR* exhibited smaller contrast (0.0014 vs. 0.0025), but had a similar CNR owing to a smaller SD in patient contralateral tissue (a contralateral SD of 0.0021 vs. 0.0035).

6.4 Discussion

In assessing the effects of adding a fourth pool to BMM analysis of APT, neither 3- nor 4-pool APTR* varied significantly between time points, and both exhibited a significantly decreased ischaemic core signal with respect to healthy subjects and patient contralateral tissue. In the case of 4-pool analysis, the differentiation between the ischaemic

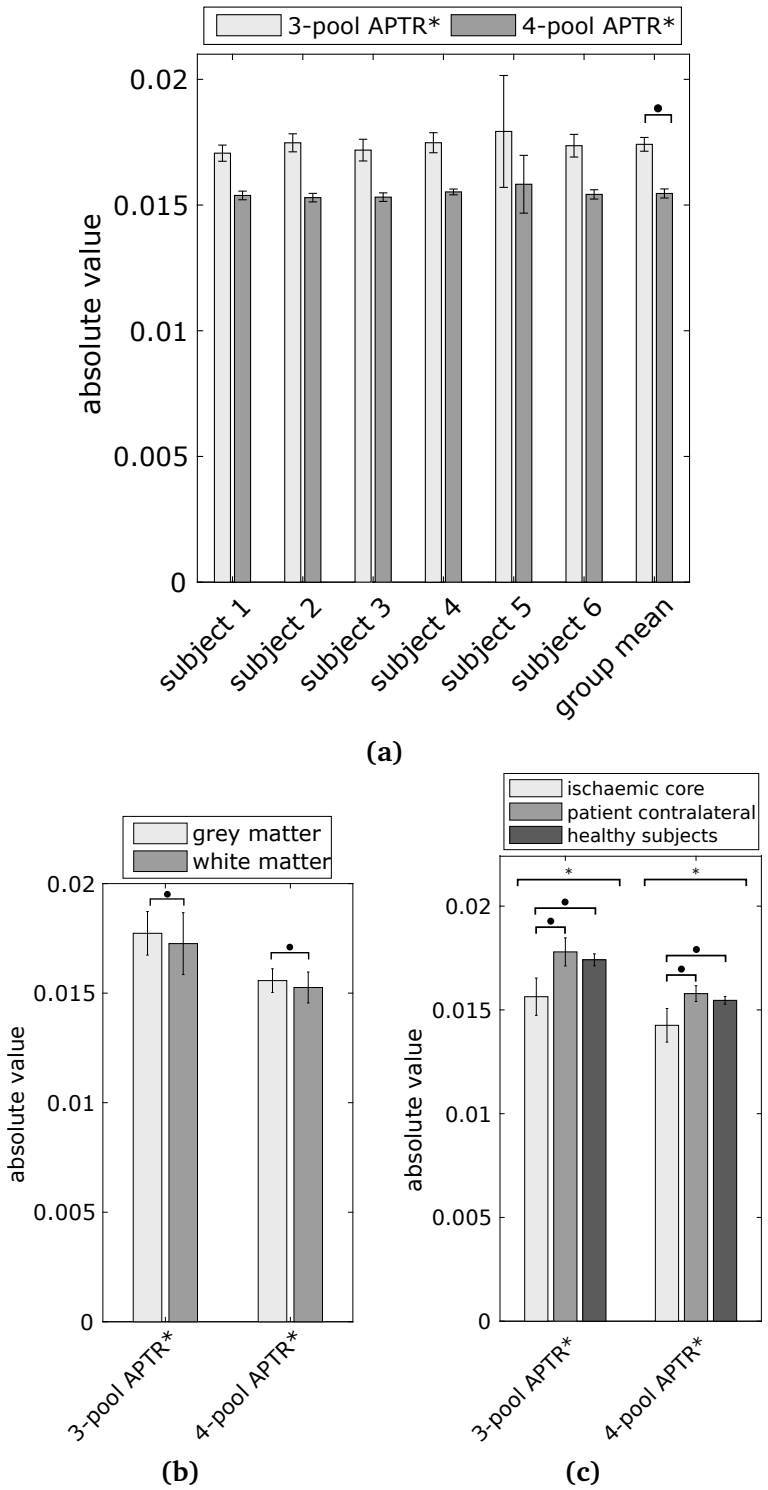

Figure 6.2: **(a)** APTR* in healthy subjects averaged across time points, shown for the 3-pool and 4-pool models. Error bars are the SD across the brain (• denotes Welch's t-test $p < 0.05$). **(b)** Absolute values of APTR* in healthy subjects shown for grey matter and white matter voxels using 3- and 4-pool analysis. Error bars are the SD across subjects (• denotes paired t-test $p < 0.05$). **(c)** Mean APTR* in healthy subjects and in stroke patients, shown for 3- and 4-pool models. Error bars are the 95% CI ($*$ denotes ANOVA $p < 0.05$; • denotes significant Welch's t-test result where $\tilde{\alpha}_{crit} = 0.017$).

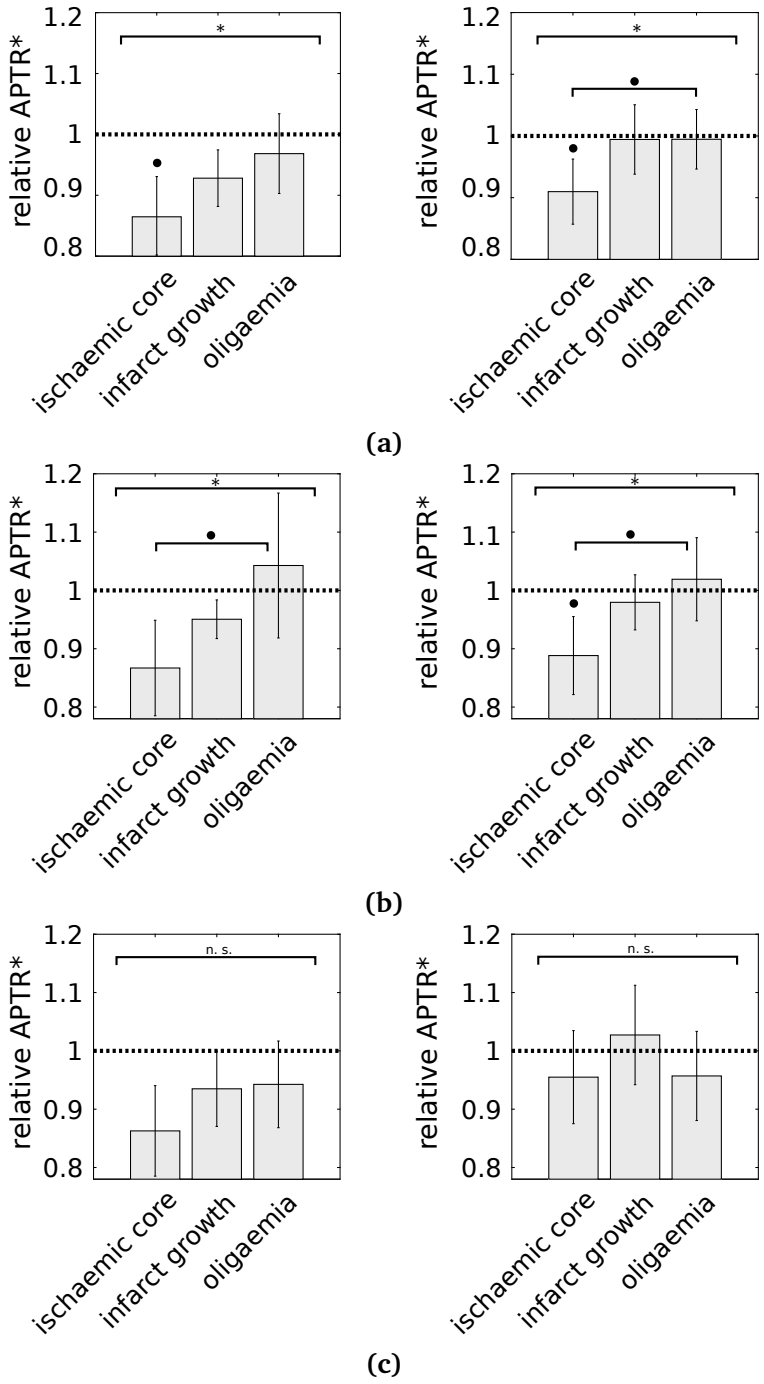

Figure 6.3: BMM relative APTR* within different patient ROIs using 3-pool (left column) and 4-pool (right column) analysis in **(a)** the whole slice, **(b)** grey matter voxels, and **(c)** white matter voxels. Error bars are the 95% CI. For the relative mean values shown, $*$ denotes ANOVA $p < 0.05$. Significance between ROIs is denoted by a horizontal bar with • (Welch's t-test $\tilde{\alpha}_{crit} = 0.017$). Significance with respect to the contralateral hemisphere is denoted by • (ANOVA of absolute means followed by Welch's t-test with $\tilde{\alpha}_{crit} = 0.0083$).

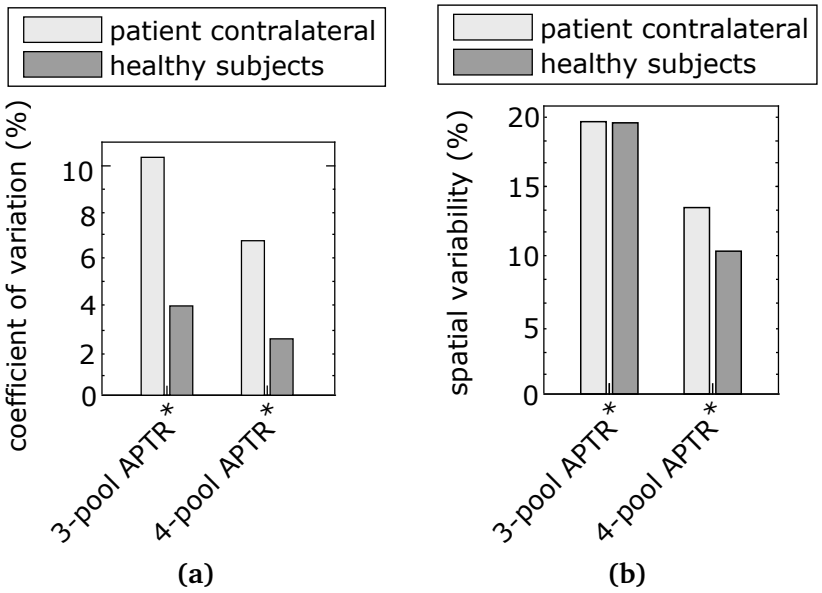

Figure 6.4: **(a)** Subject repeatability of APTR* in healthy subjects and patient contralateral tissue using different metrics, **(b)** spatial variability of APT measures in healthy subjects and patient contralateral tissue using different quantification techniques.

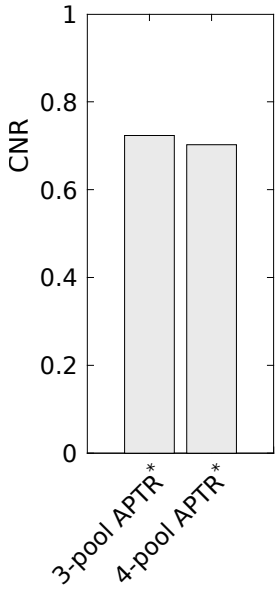

Figure 6.5: CNR in the ischaemic core tissue using 3- and 4-pool BM models.

core and oligaemic relative mean values was statistically significant, and when only grey matter voxels were considered, both 3- and 4-pool measures detected a significant difference. White matter did not exhibit significant differentiation. In healthy subjects, the 4-pool model had lower contrast between grey matter and white matter, and was the most repeatable metric between subjects and across time points. Four-pool analysis also exhibited lower spatial variability and yielded a comparable stroke lesion CNR.

The improvements offered by the 4-pool model appear be accompanied by reduced contrast between infarct growth tissue and normal tissue. Three-pool analysis yielded an intermediate infarct growth APTR*, appearing to exhibit gradation in APTR* as a function of tissue outcome, offering the potential to use the metric to identify 'tissue at risk', i.e. tissue that is viable according to diffusion measures on presentation, but that does go on to infarct. This pattern was not observed using 4-pool analysis where contrast was largely confined to the ischaemic core. Since this reduction in contrast was the result of separately modelling NOEs and semisolid effects (hence decoupling the effects of NOEs from other metabolite peaks), it suggests that the origin of infarct growth contrast might be associated with NOEs, and therefore the changes in NOEs in acute stroke need to be examined further.

In white matter voxels, neither 3-pool nor 4-pool analysis significantly differentiated pathological ROIs, although 3-pool analysis retained decreased values in the ischaemic core and in infarct growth, whereas the 4-pool measures were closer to unity. Spatial variability of the ischaemic core signal in white matter was also higher using 3-pool analysis compared to 4 pools. NOEs have previously been shown to exhibit statistically significant change in stroke (Section 3.4) and to be more strongly associated with white matter compared to grey matter [72,88]; these associations are explored further in Chapters 8 and 9. This all implies that the reduction in infarct growth contrast using 4 pools represents a trade-off between identifying tissue to target for treatment and biophysically more accurate modelling of CEST effects. The 3-pool model-based analysis, whilst less biophysically accurate, may still be useful for identifying penumbra, not

purely because of gradation in APT effects, for example associated with changes in pH, but also by incorporating a degree of changes associated with NOEs. At the same time, a simpler model might present less scope for understanding the underlying mechanisms as it is less able to isolate interacting effects and explore their unique modes of contrast. A more complex model is more exploratory and may be better-disposed as a tool for understanding the multifaceted interactions associated with the disease.

The downfield APT signal obtained from BM model fitting using the 4-pool model was lower in amplitude compared to that of the 3-pool model, even though the additional pool primarily separated upfield effects. In BM models, exchange pools are distinct from one another in that direct transfer of magnetisation only occurs with the bulk water pool. However, broad spectral phenomena such as semisolid effects can overlap with peaks from other pools and may therefore indirectly influence the distribution of saturation between pools. Asymmetry in the z-spectrum upfield of water has been attributed to NOEs [74]. Since NOEs can account for spectral asymmetry, it allows semisolid effects to be described as a symmetric phenomenon centred at water resonance [42].

In order to explore the way in which addition of the NOE pool affected quantification of the downfield APT signal, the 3- and 4-pool spectra were averaged over healthy subjects. The model-fitted spectra averaged over healthy subjects are presented in Fig. 6.6. In the 3-pool model, the line shapes downfield of water are 3-pool NOER* (dotted blue), representing combined NOEs and an asymmetric semisolid pool, and 3-pool APTR* (dotted green). A fourth pool is added to separately model NOEs (4-pool NOER*, orange) and a symmetric semisolid pool (semisolidR*, solid blue). SemisolidR* described a similar profile to 3-pool NOER* (solid blue vs. dotted blue). The main difference was that 4-pool NOER* had a narrower line shape owing to a larger T_2, and exhibited a lower-amplitude tail of saturation (0.02) overlapping with amide resonance compared to the 3-pool approximation (0.06). This led to a lesser degree of coupling between upfield and downfield spectra. The downfield NOE tail phenomenon has also

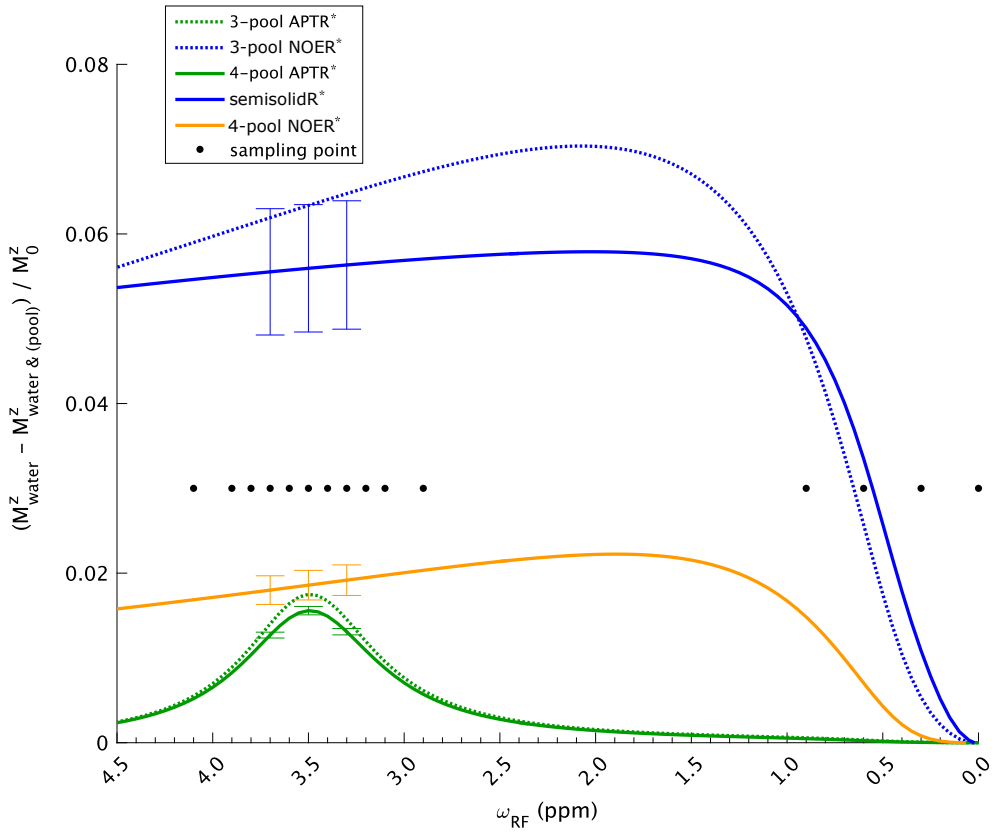

Figure 6.6: Simulated z-spectrum based on healthy subject model-fitted data. Dotted lines are the 3-pool spectra and solid lines are the 4-pool spectra. Sample points used in model fitting are indicated by black dots. Error bars indicate the SD across fits at representative points.

been recently observed though water exchange (WEX) spectroscopy of BSA phantoms as well as higher-field healthy subject studies [32,122].

Increasing the number pools, and therefore the number of model parameters, can lead to over-fitting or fitting to noise which would result in higher spatial variation. However, in this case, adding a fourth pool yielded more repeatable APTR* in healthy subjects, which also exhibited lower spatial variability compared to 3-pool APTR*. This is more consistent with the expectation that APT would be uniform across subjects and within a given subject, and supports the appropriateness of using a 4-pool model for the analysis of APT CEST data at 3 T. Requirements of a metric in a clinical imaging context are that it is repeatable and maximises stroke lesion contrast. In these respects, 4-pool APTR* was the optimal metric.

Using 4 pools is still very much an approximation to the many processes going on in

the spectrum [87]. For example, pH-dependent amine resonances are reported around 1.8–1.9 ppm [76,77] but their close proximity to water resonance makes them difficult to detect in a clinical setting. In light of this, adding further pools increases the risk of over-fitting and is hard to justify on clinical data, considering field strength, the number of samples, and patient motion.

In healthy subjects, the 4-pool model yielded a smaller signal than the 3-pool model, while in ischaemic core tissue both models had similar APTR*. This convergence could be due to the diminishment of APT effects under acidosis, resulting in a measure dominated by common priors that both models share. In grey matter and white matter, similar APTR* was expected on the basis of uniform brain tissue pH; however, it is not known whether chemical properties of amides, such as concentration and exchange rate, ought to be the same in grey matter and white matter. The small difference observed between grey matter and white matter was statistically significant. Grey matter APTR* also contributed more to the signal's spatial variability, which may be indicative of dependence on tissue type. Contrast between grey matter and white matter has been observed in a 9.4 T rat study by Jin et al. [72], who suggested APT effects to originate mainly from the higher concentration of mobile proteins found in grey matter (55% vs. 39% protein [108]), which is also more metabolically-active than white matter. Pragmatically, CEST imaging is more useful clinically if there is minimal contrast between grey matter and white matter. On this basis, in the context of clinical imaging of stroke, one of the advantages of a metric is that it minimises differences between grey matter and white matter. APTR* works well in this respect as not only has it shown minimal tissue contrast, but also similar patterns of change in response to ischaemia.

Repeatability of APTR* was higher in healthy subjects compared to patient contralateral tissue. This is expected due to ongoing changes in brain tissue physiology which adapt to the stroke injury following stroke, causing lower repeatability across time points. A stroke cohort would inherently exhibit more diversity in baseline physiology compared to healthy subjects, leading to lower repeatability across patients. There

will also be more motion in patients (particularly through-plane) which cannot be fully corrected for, leading to higher apparent variability.

The decreased ischaemic core relative APTR* is consistent with the understanding that ischaemic core tissue is highly acidotic, thus would be expected to show reduced amide saturation effects compared to contralateral tissue, and had a correspondingly smaller APT signal [37]. Oligaemic tissue is hypoperfused on presentation and appears at risk but does not subsequently infarct, indicating that it does not undergo acidosis. This is consistent with the oligaemic relative APTR* which was not significantly different from the contralateral hemisphere, and significantly larger than the ischaemic core signal. Infarct growth tissue is viable at presentation but subsequently infarcts. It has been hypothesised that infarct growth tissue could be metabolically stressed at presentation by mild acidosis but not to the extent of necrosed ischaemic core tissue [37]. This description of tissue state is consistent with the intermediate relative APTR* in the 3-pool model, but is not seen using 4 pools. This might imply that this tissue is not experiencing mild acidosis, but that there are other changes in the z-spectrum that are appearing in APT quantification using 3 pools.

In the representative maps, APT effects were decreased in regions around CSF, within tissue that was otherwise identified as normal-appearing. This might be attributable to signal dilution from partial volume effects at tissue-CSF boundaries, as CSF has a low concentration of amides. Possible contributions from CSF are explored in the next chapter through the development of a method that attempts to correct for PV effects.

6.5 Conclusion

Addition of a fourth pool that separates NOEs and semisolid effects appeared to be more biophysically accurate and provided better separation of the APT signal compared to the 3-pool equivalent, but this improvement appeared be accompanied by reduced contrast

between infarct growth tissue and normal tissue. As such, the 3-pool model may have more clinical utility in delineating the ischaemic penumbra precisely because it retained some NOE-based contribution. The reduction in contrast between infarct growth tissue and contralateral tissue using 4 pools represents a trade-off between identifying tissue to target for treatment and biophysically more accurate modelling of CEST effects.

APT effects were decreased in regions around CSF, within tissue that was otherwise identified as normal-appearing, and this might be attributable to signal dilution from partial volume effects at tissue-CSF boundaries. The next chapter addresses quantification in the presence of PV effects by adapting the existing structure of a 4-pool model rather than explicitly introducing an additional pool. In voxels at tissue-CSF boundaries, such as near ventricles and fissures, contributions of CSF have not previously been taken into account in CEST image analysis, and may be contaminating the relatively small-amplitude CEST signals explored thus far.

Chapter 7

Correcting for partial volume effects

7.1 Introduction

STROKE imaging using APT CEST has shown that tissue within the ischaemic core exhibits a significant decrease in APT value, as observed in the previous chapter and in other studies [14,37]. The decrease in signal associated with pathology is similar to the reduction of APT effects that would be observed due to a dilution of CEST effects in a voxel owing to the presence of CSF that has no substantial APT effect of its own. Thus, for any application, like stroke, where a reduction in APT is indicative of pathological tissue, the contribution of CSF is a potential confound [36,37, 109]. In the previous chapter, it was observed that APT effects were decreased in regions around CSF, within tissue that was otherwise identified as normal-appearing. This was also observed in the study of ref. [36], where the cause of the decrease in APT was attributed to PV effects at tissue-CSF boundaries. In voxels at tissue-CSF boundaries, such as at the peripheries of brain tissue, near the ventricles, and at fissures, possible contributions of CSF have not previously been taken into account in the analysis of CEST images. PV correction (PVc) for CSF might allow for more robust measurement of relatively small-scale CEST signals through a more informed model-fitting procedure that takes the distribution of CSF across the brain into account.

The objective of this chapter was to develop a technique for PV correction APT CEST

data based on the 4-pool BM model used in Chapter 6, and to see if there was a resulting change in quantification of APT effects compared to the standard multi-pool technique.

7.2 Theory

The PV correction BM model is schematically illustrated in Fig. 7.2, it is an extension of the BM model-based analysis technique developed in Chapter 6, where a 4-pool BM model of exchange was used to interpret sampled z-spectra via model fitting. The PV correction model fits the data to a tissue-weighted sum of a CSF component and a tissue component. Each of the two components generates a z-spectrum; $\mathrm{S}^{\mathrm{CSF}}(\omega)$ from the CSF model and $\mathrm{S}^{tissue}(\omega)$ from the tissue model. The weighting factor is derived from an independent estimate of tissue PV, which describes the proportion of tissue in each voxel, denoted as $[tissue]$. The weighted sum of the CSF and tissue components is fitted to the data:

$$\mathrm{S}^{total}(\omega) = (1 - [tissue]) \times \mathrm{S}^{\mathrm{CSF}}(\omega) + [tissue] \times \mathrm{S}^{tissue}(\omega) \tag{7.1}$$

In Chapter 6 it was found that grey matter-white matter contrast of the 4-pool APT signal was small. For the purpose of PV correction in this study, approximating grey matter and white matter tissue properties using a generic 'tissue' description might be a suitable way to correct for CSF effects whilst minimising model complexity. Model complexity is of particular consideration in this clinical imaging context, as spectral features are relatively broad and data points are limited.

7.3 Methods

An outline of the methods used in this chapter is presented below; refer to Chapter 4 for further details.

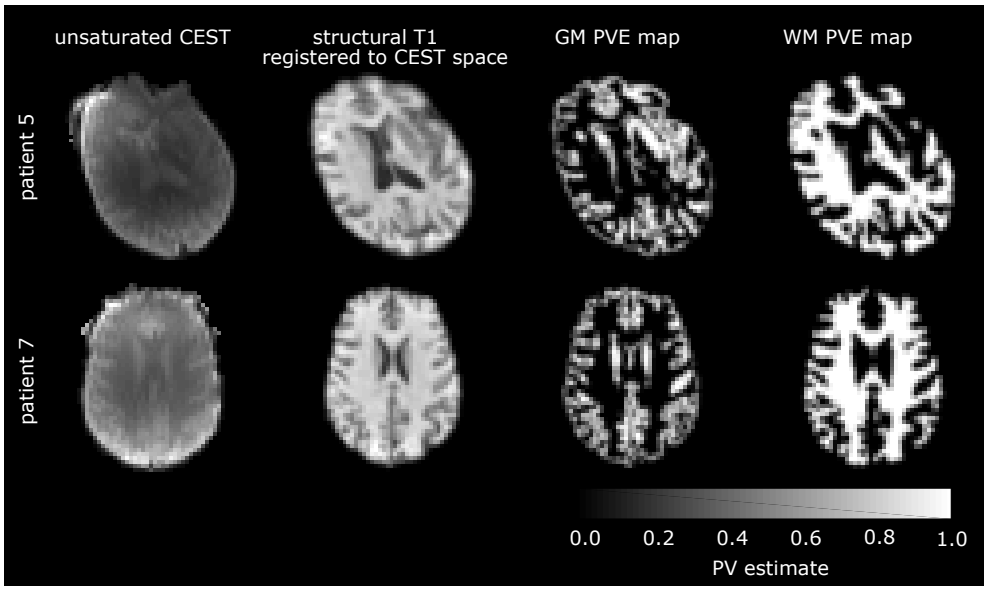

Figure 7.1: PVE maps registered to CEST space, shown for two patients. The structural T_1 image was first rigidly registered to the unsaturated CEST acquisition, from which an inverse transform was derived. This was applied to the PVE maps to transform them from T_1 space to CEST space. The transformed maps were subsequently thresholded for mask generation. A tissue PVE map was obtained from GM+WM, used directly in the PV correction model fitting process.

7.3.1 Study details

This chapter employed the datasets from 12 patients presenting with acute ischaemic stroke and the datasets from 6 healthy subjects.

7.3.2 Generation of PVE maps

Tissue PVE, $[tissue]$ (a fraction in the range $0-1$), was obtained using the FSL brain segmentation tool `fast` operating on a structural T_1-weighted scan (Fig. 7.1) [134]. This generated tissue PVEs of grey matter, white matter, and CSF. For the tissue PVE map used in model fitting, grey matter and white matter PVEs were combined to give a tissue PVE map. The images were transformed to the resolution of the CEST images by first transforming CEST data to the T_1-weighted structural scan using the FSL tool `flirt` [126,131,133], inverting the transformation matrix, and using that to transform the PVE maps to the resolution of the CEST images using the FSL tool `applywarp`.

7.3.3 Model fitting

The BMM quantification techniques compared in this study were 4-pool APTR*, and 4-pool APTR* incorporating PV correction (PVc APTR*) (Table 7.1). The 4-pool model used in this chapter was shown shown to exhibit higher repeatability when quantifying APT effects in clinical data (Chapter 6), compared to a more approximate 3-pool model, hence 4-pool metrics were used [99,138]. The 4-pool model comprised a pool for water, APT effects at 3.5 ppm, symmetric semisolid effects, and nuclear Overhauser effects (an extension of the 3-pool model in ref. [36]). Parameter prior distributions are listed in Table 6.1. For PVc APTR*, tissue was modelled by 4 pools, and CSF was modelled by a single pool (parameter priors listed in Table 7.2).

For the PV correction model, voxels with a tissue PVE of less than 50% were deemed non-interpretable. Therefore, for voxels where tissue PVE was less than 50%, only a CSF pool was fitted and the voxels were not included in the further analyses (corresponding to exclusion of 13.7% healthy subject voxels from a total of 1721 voxels). CSF pool concentration M_0^{CSF} was fixed in relation to tissue concentration M_0^{tissue}: $M_0^{CSF} = \overline{M_0^{CSF}/M_0^{tissue}} \times M_0^{tissue}$ where $\overline{M_0^{CSF}/M_0^{tissue}}$ is a constant representing the mean ratio of CSF M_0 to tissue M_0; a proton density ratio modulated by T_1. This was done as otherwise the fitting process simply reduced to the tissue model, as it alone was capable of achieving a good fit to the data. The ratio $\overline{M_0^{CSF}/M_0^{tissue}}$ was estimated using the unsaturated acquisitions from the healthy subjects. For each scan, the respective tissue PVE was used to generate a CSF-only mask (tissue PVE < 0.1) and a tissue-only mask (grey matter PVE $> 0.7 \cup$ white matter PVE > 0.9), from which the ratio of CSF-to-tissue M_0 was calculated as (mean±SD) $0.5269 \pm 12.2\%$.

7.3.4 Data extraction

The patient ROIs used in this study were ischaemic core, infarct growth, oligaemia, and a mirrored contralateral mask. Analysis was performed within three masks defined by the following tissue PVE ranges: voxels comprising more than 75% PVE (i.e. less

Table 7.1: BM model 4-pool and PV correction quantification techniques. $S^{BMM}_{[pools]}$ is the z-spectrum obtained from the BM model, where the subscript $[pools]$ refers to the combination of CEST pools for which the simulated z-spectrum is obtained: w (water pool), a (APT pool), n (NOE pool), and s (semisolid pool).

† Glossary of parameters values — (i) APTR*: $\omega_1 = 3.5$ ppm, $[pools] = w + a$; (ii) NOER*: $\omega_1 = -3.5$ ppm, $[pools] = w + n$; (iii) semisolidR*: $\omega_1 = 50$ ppm, $[pools] = w + s$.

Quantification technique	General form†	References
Four-pool BM model	$\frac{S^{BMM}_{w}(\omega_1) - S^{BMM}_{[pools]}(\omega_1)}{S^{BMM}_{0}}$	Based on [36,62]
PV-corrected BM model	$\frac{S^{tissue\ BMM}_{w}(\omega_1) - S^{tissue\ BMM}_{[pools]}(\omega_1)}{S^{tissue\ BMM}_{0}}$	Based on [139]

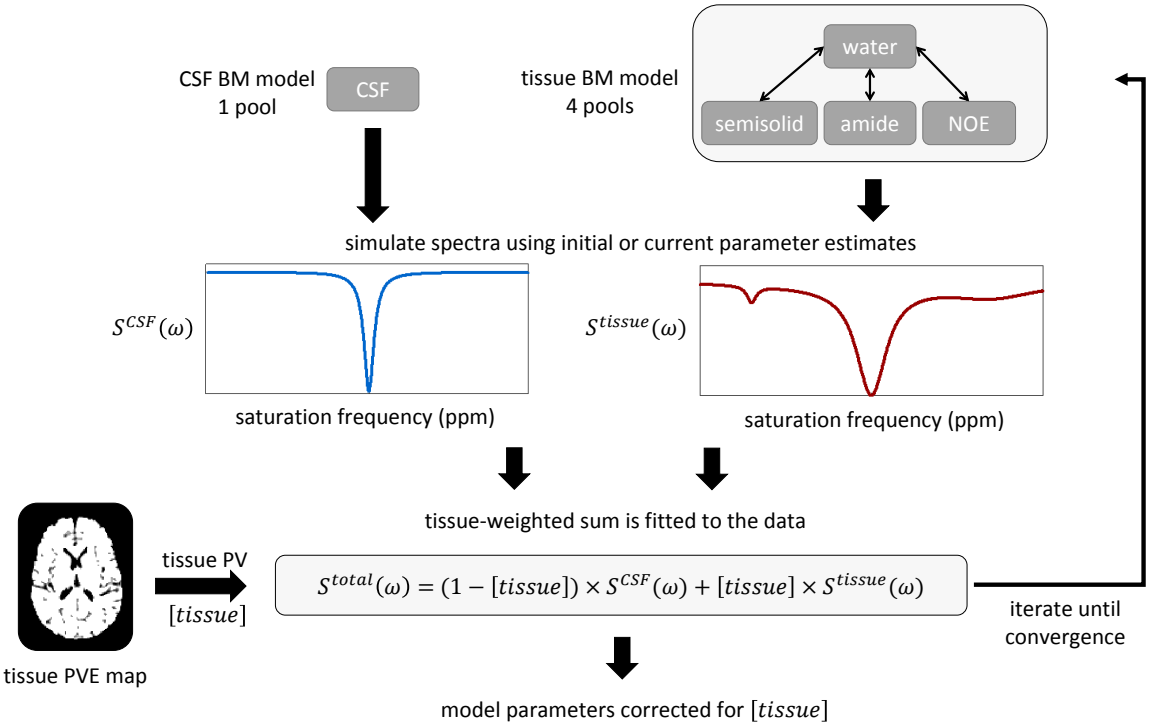

Figure 7.2: Outline of the PV correction model fitting process. The CSF and tissue model components each generate a spectrum (S^{CSF}, S^{tissue}), and the data are fitted to a weighted sum based on tissue PV $[tissue]$ which is derived from a tissue PVE map.

Table 7.2: CSF pool BMM priors expressed as a mean and SD. For 4-pool model priors, used in the tissue BM model and the standard 4-pool model, refer to Table 6.1.

Glossary – M_0: pool concentration relative to water pool (water pool M_0 is absolute), k_{ex}: pool→bulk water exchange rate, T_1: longitudinal relaxation time, T_2: transverse relaxation time, $\Delta\omega$: chemical shift with respect to water pool.

† Based on ref. [140]
‡ Based on ref. [141]

	CSF pool of the PV correction BM model	
	water	
Parameter	mean	SD
M_0 (norm.)	$0.5269 \times M_0^{tissue}$	1×10^{-6}
k_{ex} (Hz)	–	–
T_1 (s)	1.9†	0.15
T_2 (ms)	250‡	50
$\Delta\omega$ (ppm)	0	1×10^{-6}

than 25% CSF), voxels containing 50–75% tissue, and on the union of these two masks (i.e. 50–100% PVE). In the former subset of voxels, the two models were expected to converge, thus serving as a reference for comparison. In the latter subset, voxels are more prone to contamination by CSF and were therefore expected to exhibit an improvement in quantification when the PV correction model was used. Finally, the net effect of PV correction was assessed by combining both sets of voxels.

7.3.5 Analysis

The number of voxels and subjects used to inform the analyses are listed in Table 7.3. Analyses of the PV correction and 4-pool models were done on the same voxels. Group mean absolute APTR* in voxels with $>$ 75% PVE was found in healthy subjects and values were compared between the 4-pool and PV correction models. In patients, the voxel-weighted ischaemic core absolute APTR* was compared against healthy subjects for each model. Repeatability in healthy subject and patient contralateral tissue was measured using ANOVA and the CoV. The spatial variability within healthy subjects and patient contralateral tissue was compared between models. These comparisons were done for voxels with a tissue PVE of 50–75%, $>$ 75%, and for the whole slice.

In patients, relative APTR* was compared between pathological ROIs, and the ischaemic core CNR was found for both models. This was done for voxels with a tissue PVE of 50–75%, $>$ 75%, and for the whole slice. The dependence of BMM signals on tissue PVE was assessed by finding the CoV across 10 equally-spaced CSF PVE ranges from 0–5% to 45–50%.

7.4 Results

Healthy subject and patient APTR* maps are shown in Fig. 7.3. Areas of APTR* hyperintensity at the periphery of the brain on the 4-pool maps were diminished on the PVc maps. In stroke patients the PVc maps generally had a lower spread of hyperintense

Table 7.3: Total number of voxels used in this study for the different tissue outcome ROIs.

		ischaemic core	infarct growth	oligaemia	contralateral
brain mask	tissue PVE range				
whole slice	0.50–1.00	445	919	843	1692
high tissue PV voxels	0.75–1.00	429	779	730	1484
low tissue PV voxels	0.50–0.75	16	140	113	208

regions at tissue-CSF boundaries compared to 4-pool APTR* (patients 5–7).

7.4.1 APTR* in voxels with >75% tissue

The mean value of APTR* in subjects, using the 4-pool and PV correction models, is shown in Fig. 7.4. Healthy subject APTR* differed statistically significantly between the two models ($p < 0.001$). The values were (mean±95% CI) 0.0154 ± 0.0002 using 4-pool APTR*, and 0.0150 ± 0.0001 using PVc APTR*; a difference of −3.15%. The patient ROI means did not differ significantly between the two models (ischaemic core: $p = 0.68$, patient contralateral: $p = 0.16$). Both models significantly differentiated the ischaemic core signal from the patient contralateral (4 pools: $p = 0.002$, PVc: $p = 0.005$).

The relative (to contralateral tissue) mean APTR* in voxels with > 75% tissue is shown in Fig. 7.5a. The values were, as expected, almost identical for both models. The ischaemic core signal was significantly decreased with respect to the patient contralateral (4 pools: $p = 0.002$, PVc: $p < 0.005$). The relative mean values were significantly different between the ischaemic core and the oligaemia ROI (4 pools: $p = 0.01$, PVc: $p = 0.01$). The 4-pool ischaemic core relative mean was 0.91 ± 0.05, and the PVc relative mean was 0.92 ± 0.05. The PVc measure further significantly differentiated the relative mean values in the ischaemic core and in the infarct growth ROI (1.01 ± 0.06,

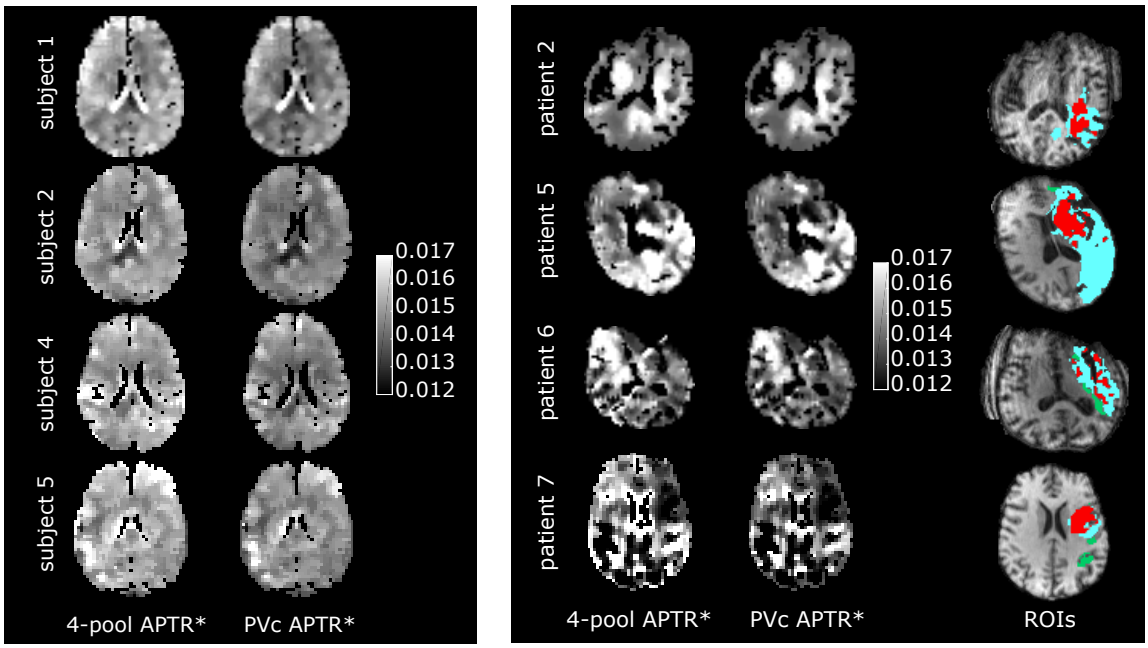

(a) **(b)**

Figure 7.3: (a) Healthy subject APTR* maps, and **(b)** representative patient maps using 4-pool and PV correction models. Red: ischaemic core; green: oligaemia; cyan: infarct growth.

$p = 0.015$), although the 4-pool measure exhibited a very similar infarct growth relative APTR* (1.00 ± 0.06).

7.4.2 APTR* in voxels with 50–75% tissue

In healthy subjects and patient contralateral tissue, voxels with 50–75% tissue were more spatially homogeneous using the PV correction model compared to the 4-pool model (healthy subject CoV of 9.92% vs. 14.2%, and patient contralateral tissue CoV of 9.03% vs. 12.4%). In voxels with 50–75% tissue, subject repeatability was higher using the PV correction model (Fig. 7.6a). In healthy subjects, the CoV across time points was 3.13% using the 4-pool model and 1.97% using the PV correction model. The CoV across healthy subjects was 3.50% using the 4-pool model and 2.31% using the PV correction model (6.50% and 3.50% across patient contralateral tissue). In this PVE range, the differences between the ROI relative mean values were not statistically significant (4 pools: $p = 0.24$, PVc: $p = 0.20$). The PVc measure exhibited a small

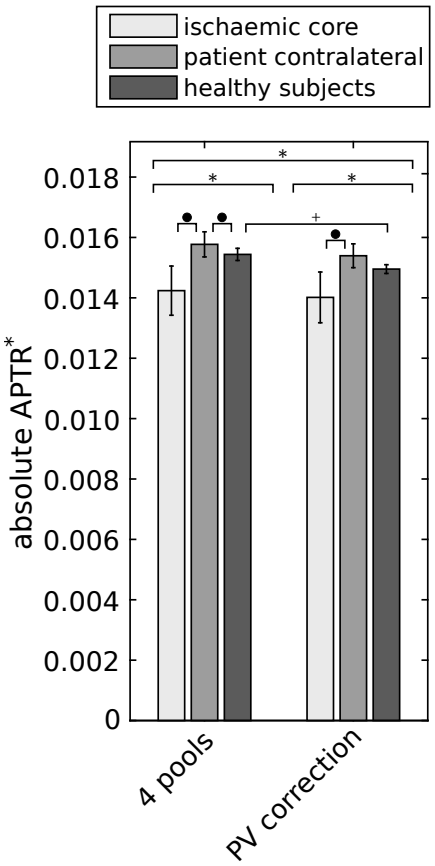

Figure 7.4: Group mean of absolute APTR* in voxels with > 75% tissue using the 4-pool and PV correction models. Shown for the ischaemic core, patient contralateral tissue, and healthy subjects. Error bars are the 95% CI ($*$ denotes ANOVA $p < 0.05$; • denotes significant Welch's t-test result where $\tilde{\alpha}_{crit} = 0.016$; + denotes significant Welch's t-test result where $\tilde{\alpha}_{crit} = 0.0033$).

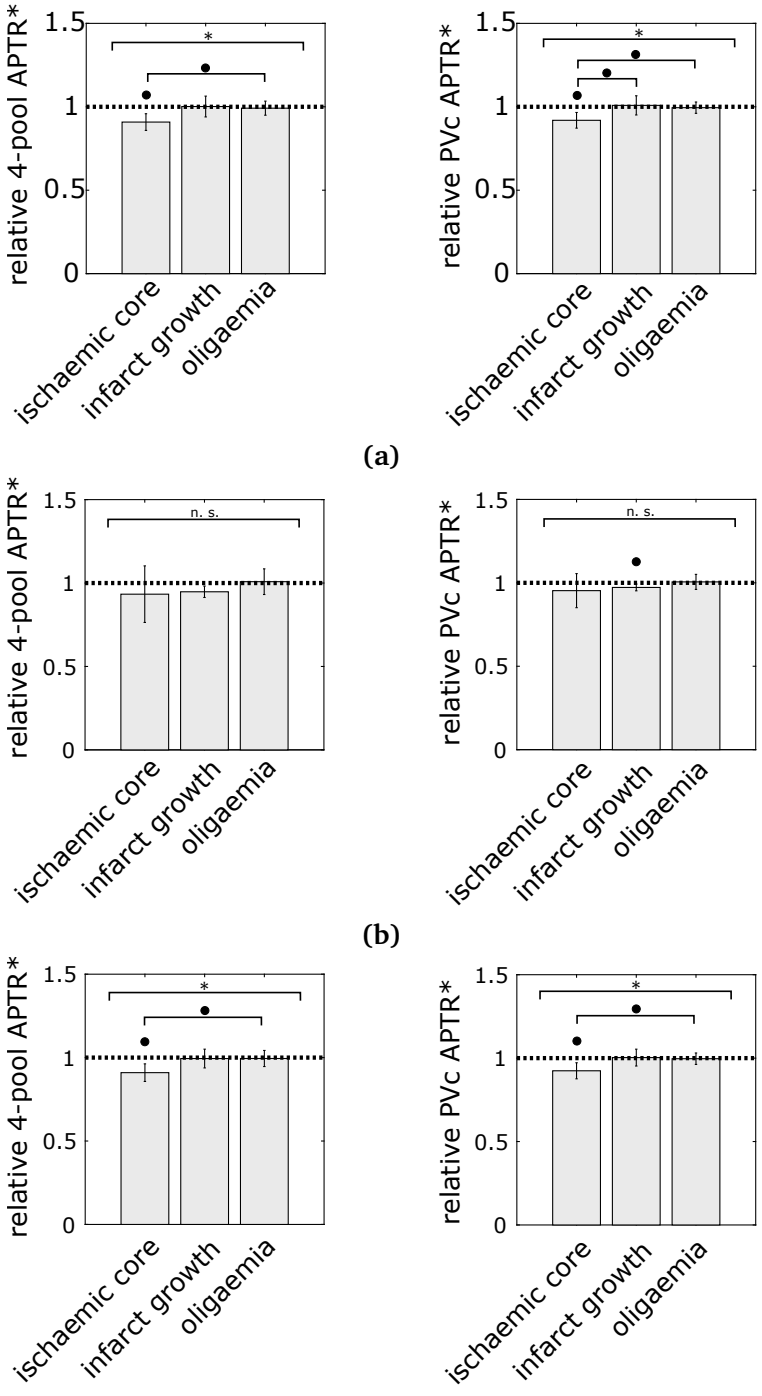

Figure 7.5: Relative APTR* in **(a)** voxels with > 75% tissue, **(b)** voxels with 50–75% tissue, and **(c)** the whole slice, using the 4-pool and PV correction models. Error bars are the 95% CI. For the relative mean values shown, $*$ denotes ANOVA $p < 0.05$. Significance between ROIs is denoted by a horizontal bar with • (Welch's t-test $\tilde{\alpha}_{crit} = 0.017$). Significance with respect to the contralateral hemisphere is denoted by • (ANOVA of absolute means followed by Welch's t-test with $\tilde{\alpha}_{crit} = 0.0083$).

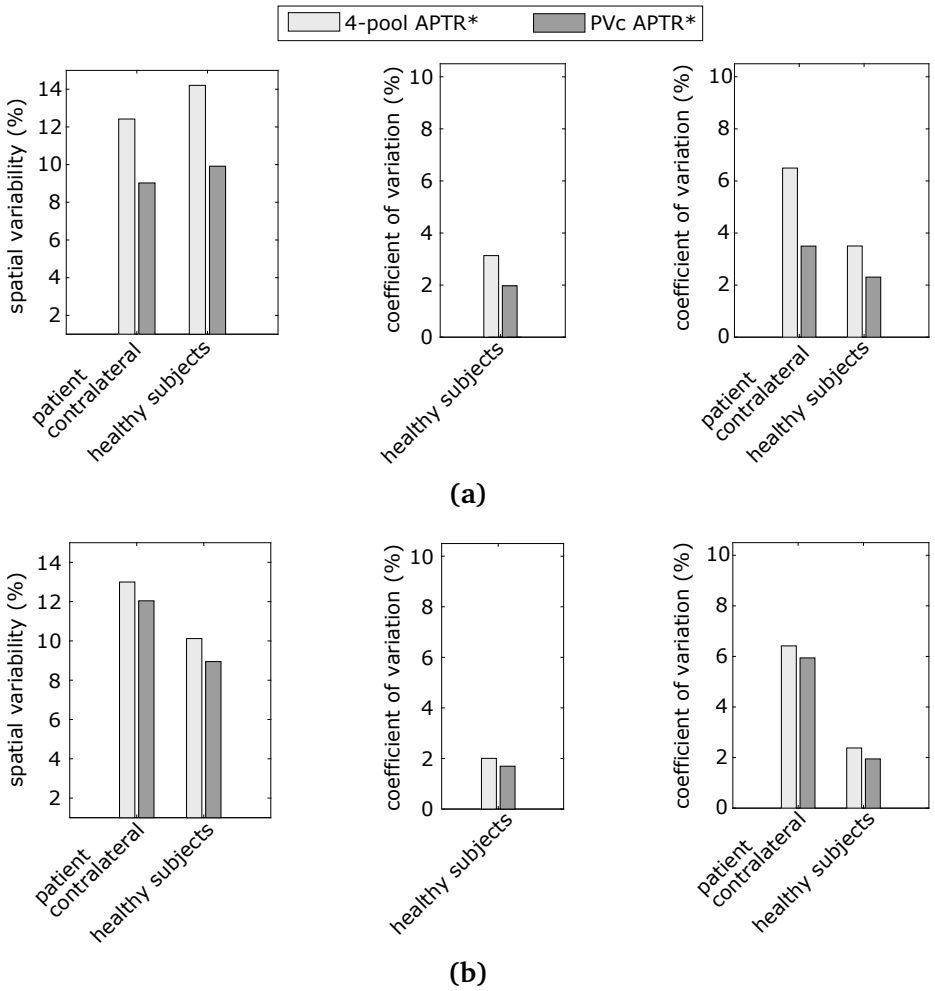

Figure 7.6: Spatial variability (left), time point repeatability (centre), and subject repeatability (right). **(a)** In voxels with 50–75% tissue, and **(b)** in the whole slice, using 4-pool and PV correction models.

and statistically significant difference (-3.97%, $p = 0.005$) between infarct growth tissue (0.0145 ± 0.0003) and patient contralateral tissue (0.0151 ± 0.0003). PVc APTR* exhibited a similar ischaemic core CNR (0.52) to 4-pool APTR* (0.55).

7.4.3 Whole slice APTR*

PVc APTR* did not vary significantly between healthy subjects or time points, while 4-pool APTR* varied significantly between subjects ($p = 0.04$). Both models exhibited small but significant contrast between grey matter and white matter in healthy subjects (4 pools: 2.01%, PVc: 2.20%, $p < 0.005$). In healthy subjects, spatial variability was 10.1% using the 4-pool model and 8.95% using the PV correction model (13.0% and

12.0% in patient contralateral tissue) (Fig. 7.6b). Repeatability in healthy subjects and patient contralateral tissue was also similar between the two models. For example, repeatability between patient contralateral tissue using 4-pool APTR* was 5.38%, and 5.27% using PVc APTR*. Ischaemic core APTR* was significantly decreased in both models (4 pools: $p = 0.005$, PVc: $p = 0.005$), and relative APTR* (4 pools: 0.91 ± 0.05, PVc: 0.92 ± 0.05) was statistically significantly differentiated (4 pools: $p = 0.015$, PVc: $p = 0.013$) from the oligaemia ROI (Fig. 7.5c). Oligaemic tissue exhibited a signal value of unity in both models (4 pools: 1.00 ± 0.05, PVc: 1.00 ± 0.03), as did infarct growth tissue (4 pools: 0.99 ± 0.06, PVc: 1.0 ± 0.05). Ischaemic core CNR was 0.70 using the 4-pool model and 0.62 using the PV correction model.

7.4.4 Whole slice NOER* and semisolidR*

In healthy subjects, the 4-pool and PVc measures of NOER* did not differ significantly from each other ($p = 0.52$) (4 pools: 0.069 ± 0.004, PVc: 0.070 ± 0.004). SemisolidR* was also not significantly different between the two models (4 pools: 0.0049 ± 0.0003, PVc: 0.0053 ± 0.0003).

7.4.5 Dependence of BMM signals on CSF percentile

The change in BMM signals with respect to CSF percentile is shown in Fig. 7.7a. Four-pool APTR* was relatively invariant to the CSF percentile (CoV of 0.84%, Fig. 7.7b). After PV correction, the signal exhibited lower variance across CSF percentiles (CoV of 0.75%; 10.7% less, expressed in terms of the 4-pool APTR* CoV). Four-pool NOER* and semisolidR* generally increased in value as CSF percentile increased, particularly over the 5–45% CSF percentiles where the trend was broadly linear, whereas the PVc signals changed less over this range of tissue PV (4-pool and PVc CoVs of: 13.1% vs. 9.92% for NOER*, and 18.5% vs. 14.8% for semisolidR*).

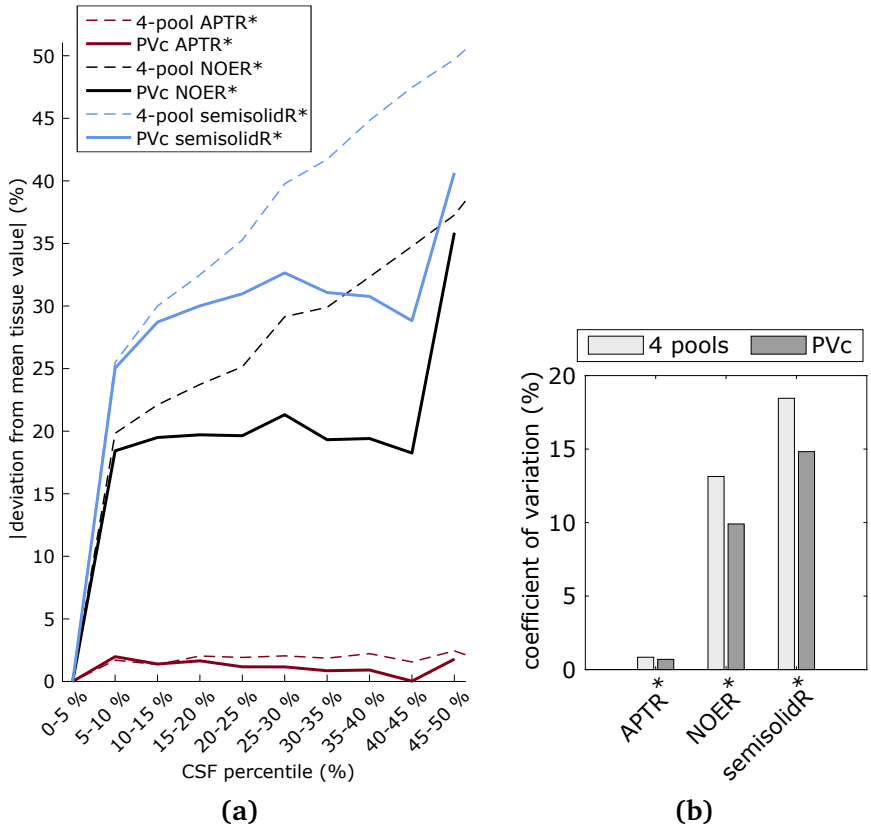

Figure 7.7: Dependence of 4-pool and PVc signals on tissue PV in healthy subjects, **(a)** as a function of CSF percentile, and **(b)** expressed as a CoV.

7.5 Discussion

In voxels with a tissue PVE > 75% both models exhibited an ischaemic core relative APTR* that was significantly decreased. In voxels that contained 50–75% tissue, the pathological ROIs did not exhibit significantly different values. In these voxels (50–75% tissue), ischaemic core CNR was similar using the PVc model and the signal exhibited higher repeatability than 4-pool analysis. In healthy subjects this was also the case; PVc yielded higher repeatability and lower spatial variability. In whole slice analysis, PV correction yielded a small and consistent decrease in spatial variability. Four-pool APTR* did not exhibit high variability as a function of tissue PVE, and this was lower still after PV correction was applied. NOER* and semisolidR* were more strongly dependent on tissue PV using the 4-pool than the PV correction model.

In voxels with a tissue PVE > 75% the 4-pool and PV correction models were broadly consistent, indicating that voxels with a high tissue PVE did not benefit significantly

from PV correction, and that the two models converged in such a case. Voxels with a tissue PVE of 50–75% are, on the other hand, more vulnerable to a dilution of CEST effects by CSF. This was observed in the ischaemic core relative APTR*; voxels with 50–75% tissue detected no significant difference to patient contralateral tissue, whilst voxels with $> 75\%$ had a significantly reduced signal. After PV correction, a significant difference was still not apparent in voxels with 50–75% tissue. However, the effect of PV correction on voxels with 50–75% tissue was observed as an increase in the measures of subject and time point repeatability, and spatial homogeneity, compared to those of the 4-pool model, whilst maintaining similar pathological contrast. Based on these measures, PVc APTR* was more consistent with clinical knowledge of tissue condition, as, in healthy brain tissue, normal intracelluar pH is known to be maintained at a constant level in healthy subjects (7.0–7.25 depending on the technique used) [37]. This suggests that a PV correction model can extract CEST signals with greater precision in voxels that have a low tissue PVE. This is of particular relevance in stroke imaging using APTR*, where nominal signal amplitudes, and physiological changes in signal, are small. The improved measures were achieved using PVc without significantly affecting ischaemic core CNR. PV correction therefore appeared more able to deal with PV-based heterogeneities in stroke data whilst at the same time preserving pathological tissue contrast, and may therefore be more amenable to clinical interpretation.

The PV-corrected signals exhibited a weaker dependence on tissue PV than those of the 4-pool model, whilst maintaining a similar CNR in pathological tissue. At high tissue PVEs both models were similar in their quantification. At lower tissue PVEs, the PV correction model yielded more uniform APTR*, higher repeatability, and a similar CNR in pathological tissue, suggesting that of the two models, its analysis was more robust at low tissue PVEs. Whole slice analysis indicated that, on balance, the models exhibited similar performance. This may be because at the CEST imaging resolution used here, a majority of voxels had a tissue PVE of $> 90\%$, so whilst an improvement in repeatability was observed in voxels with 50–75% tissue, they only constituted a small

proportion of the entire image and the net impact was small.

The stroke population is physiologically more heterogeneous in brain composition than in healthy subjects, making differentiation between physiological features and artefacts less clear. It also more difficult to derive PVE maps from stroke patient data, as pathological tissue might not exhibit the same voxel intensity characteristics that distinguish the different tissue classes, leading to potential inaccuracy of the segmentation method in the affected regions. Applying PV correction yielded APTR* maps that were more uniform around tissue-CSF boundaries, such as the ventricles, fissures, and the brain periphery. This was achieved without diminishing the contrast of the ischaemic core. PV correction therefore appeared more able to deal with PV-based heterogeneities in stroke data whilst at the same time preserving the more clinically-relevant causes of heterogeneity.

Beyond the 0–5% CSF percentile (100–95% tissue percentile), NOER* and semisolidR* exhibited a large deviation in value. A majority of voxels (72%) were contained in the 95–100% tissue PVE range, which is mostly described by white matter voxels. Previous studies have identified a dependence of semisolid effects and NOEs on white matter concentration [72], which explains why a sudden change (a decrease) in signal was observed across this range and not across subsequent ranges where grey and white matter proportions were more balanced.

7.6 Conclusion

The PV-corrected signals exhibited a weaker dependence on tissue PV than those of the 4-pool model. At lower values of tissue PV, the PV-corrected model yielded more homogeneous APTR* and higher repeatability, suggesting that of the two models, its analysis was more robust at low tissue PVs. These improvements did not yield a significant difference when the whole slice was considered, as voxels with a low tissue PVE comprised only a small subset of the volume. This method of correction is recommended

for the purpose of more accurate quantification where physiological changes in signal amplitude are on a small scale, although it might not be required in a clinical context where a simpler model, which does not correct for tissue partial volume effects, yields comparable results.

A 4-pool BM model presents the opportunity to explore upfield effects more robustly. The nascent literature on NOEs suggests that they may play a complementary role to APT as an imaging biomarker in acute stroke. The next chapter therefore focuses on NOEs and semisolid effects in order to better-understand their biophysical characteristics and potential as indicators of tissue fate in acute ischaemic stroke.

Chapter 8

Investigating upfield effects

8.1 Introduction

NUCLEAR Overhauser effects, if associated with cell metabolism, may help to identify the ischaemic penumbra in stroke patients, the classical definition of which is a region of tissue around the ischaemic core which is hypoperfused and metabolically stressed [14–16]. The existing CEST literature is not conclusive on some of the fundamental characteristics of NOEs, such as their dependence on tissue pH and exchange mechanisms [57,72,94,95,110].

A 3-pool BM model has been used in previous clinical studies of CEST spectra to examine APT effects by including a water and an amide pool, while also attempting to correct for spectral asymmetry using a third pool which combines upfield effects with broader MT effects [36,37]. A clinical demonstration of changes in NOEs using 3-pool BMM analysis in acute human stroke was reported by Tee et al. [90] on the data from the study in ref. [37], finding a decrease in saturation effects at −2.41 ppm in the ischaemic core. In the 3-pool model, the combination of semisolid and NOE effects might feasibly have introduced bias into the measures of, or reduced the sensitivity to, changes in upfield signals. The more recent literature suggests that semisolid effects and NOEs are distinct and this would not be modelled well as a combined effect. It is apparent, therefore, that if NOEs are to be explored as a phenomenon in their own right in stroke,

it will be necessary to use a metric that isolates them from contaminating exchange processes associated with semisolid effects. This suggests that at least 4 pools may be necessary in order to separately quantify NOEs, semisolid effects, and APT effects. The findings from Chapter 5 suggest that a model-based approach is more robust for quantifying CEST signals than other non-model-based methods that seek to separate both upfield and downfield CEST effects. In Chapter 6 it was found that a 4-pool BM model was more robust than 3-pool BMM analysis, but the inclusion of an extra pool did not substantially affect the APT effects observed.

The aim of this chapter was specifically to explore what information 4-pool BMM analysis provides about upfield CEST phenomena in ischaemic stroke, contrasting that with the intentionally approximate 3-pool model. The first objective was to determine whether substantial differences are observed between 3- and 4-pool model-based analysis of upfield signals in acute stroke and whether these differences are repeatable in higher-field preclinical data. The second objective was to gain a better understanding of signal origins using a preclinical model of ischaemic stroke in order to help to inform physiological interpretation of the clinical data. Towards this end a methodological comparison of BMM quantification techniques was undertaken around clinical endpoints in a cohort of acute stroke patients, and in animals that underwent MCAO.

8.2 Theory

The principles underlying quantification using BM model fitting were laid out in Section 3.2.2.5; z-spectra are generated from a set of model parameters which directly describe the underlying physical parameters, such as exchange rate, relaxation times, and metabolite concentrations. Magnetisation exchange interactions between bulk water and different metabolites are described by separate exchange pools, with each pool transferring saturation to the main water pool on which a signal accumulates. Each pool is described by a set of Bloch equations coupled together through mass-conserving

exchange rates (the BM model). Model fitting allows the spectral contributions of different species to be isolated by subtracting unwanted saturation components from the pools of interest. This has been exploited previously [36,37,62,90]. After fitting multiple pools to the spectral data, only a subset are simulated to predict the effect arising from a single pool, or a combination thereof.

Previously for acute clinical stroke a 3-pool model has been used, comprising a bulk water pool, an amide pool, and a third pool which attempts to account for both semisolid effects and NOEs [36,37,90], the findings of which were related in Section 3.4. The third pool groups together saturation effects from NOE and semisolid pool exchanges without distinguishing between these two signal sources and was implemented to reduce the confounding contamination of these effects on the APT signal. This may be sub-optimal given the observed differences in the linewidth of the semisolid pool signal and the region over which NOEs have been observed, particularly when seeking to examine changes in these effects in stroke. The 4-pool model used in this study extends the model such that semisolid effects and NOE exchanges are described using two separate pools in order to achieve better separation of NOEs and semisolid effects. The NOE pool models a classic Lorentzian effect centred at −3.5 ppm based on observations in the literature [57,74]. The semisolid pool approximates semisolid effects using a Lorentzian line shape centred at water resonance [72,142].

Previously the apparent APT ratio, APTR*, has been defined (Section 3.2.2.5); in the same way the apparent NOE ratio, NOER*, was obtained by simulating the combined NOE and bulk water pools, ignoring any other pools included in the fit to the original z-spectrum data, and comparing this to a simulation of only the water pool. NOER* was the difference between the two predictions at −3.5 ppm. Similarly, the apparent semisolid effects ratio, semisolidR* (Table 8.1), was obtained by simulating the combined semisolid and bulk water pools, ignoring any other pools included in the fit, and semisolidR* was the difference between the two predictions evaluated at 50 ppm. In general, when using a BM model, the frequency at which the effect of a metabolite pool

is quantified is the same as the pool's resonance frequency, as that is where the maximum signal change can be measured. In the case of a symmetric semisolid pool, whose resonance frequency (0 ppm) is identical to the water pool, it is not possible to make a meaningful measurement on resonance as the signal is dominated by water DS. For this reason, the offset of 50 ppm was chosen, similar to that used in classical semisolid MT experiments [101].

8.3 Methods

An outline of the methods used in this chapter is presented below; refer to Chapter 4 for further details.

8.3.1 Study details

This chapter employed the datasets from 12 patients presenting with acute ischaemic stroke, the datasets from 6 healthy subjects, a preclinical dataset, and naïve mouse brain phantom data.

8.3.2 Processing

The BMM measures compared in this study are 3-pool NOER*, 4-pool NOER*, semisolidR*, and the conventional MT measure. The conventional MT model-free measure used in this study is defined as in ref. [101]:

$$\text{conventional MT} = \frac{S_0 - S(50\text{ ppm})}{S_0} \tag{8.1}$$

The data were fitted to a CW approximation of the BM equations (Figs. B.2, B.3, and B.4a, show examples of human, animal, and phantom model-fitted data, respectively). The 3-pool BM model used in this study comprised a bulk water pool, an amide pool, and a third pool which attempted to account for both semisolid effects and NOEs. The

Table 8.1: BMM quantification technique for NOEs and semisolid effects. $S^{BMM}_{[pools]}$ is the z-spectrum obtained through BM model fitting, the subscript $[pools]$ refers to the combination of CEST pools for which the simulated z-spectrum is obtained: w (water pool), a (APT pool), and s (semisolid pool).

†General form of a BMM measure is $\left[S^{BMM}_{w}(\omega_1) - S^{BMM}_{[pools]}(\omega_1)\right]/S^{BMM}_{0}$

BMM metric	Parameters†	Description
$3-$pool NOER*	$\omega_1 = -2.41$ ppm $[pools] = w + s\ (asymmetric)$	Three-pool approximation treating NOEs and semisolid effects as a single asymmetric semisolid pool
$4-$pool NOER*	$\omega_1 = -3.5$ ppm $[pools] = w + n$	Four-pool measure of a separated NOE pool
semisolidR*	$\omega_1 = 50$ ppm $[pools] = w + s\ (symmetric)$	Four-pool measure of a separated symmetric semisolid pool

Table 8.2: Four-pool BM model priors for animal data, expressed as a mean and SD. The tabled values are derived from those used for the clinical data in Table 6.1, with an adjusted APT pool concentration, and T_1 was adjusted for the 9.4 T field assuming T_1 was approximately proportional to $B_0^{1/3}$. For brevity the annotations from Table 6.1 are not reproduced.

Glossary – M_0: pool concentration relative to water pool (water pool M_0 is absolute), k_{ex}: pool→bulk water exchange rate, T_1: longitudinal relaxation time, T_2: transverse relaxation time, $\Delta\omega$: chemical shift with respect to water pool.

	water		APT		symmetric semisolid		NOE	
Parameter	mean	SD	mean	SD	mean	SD	mean	SD
M_0 (norm.)	0	1×10^6	$\frac{100\text{ mM}}{112\text{ M}}$	$\frac{200\text{ mM}}{112\text{ M}}$	0	1×10^6	0	1×10^6
k_{ex} (Hz)	—	—	20	$e^{1.0}$	60	$e^{1.0}$	20	$e^{1.0}$
T_1 (s)	1.9	0.15	1.1	0.15	1.5	0.15	1.1	0.15
T_2 (ms)	70	14	10	2	0.1	0.02	0.3	0.06
$\Delta\omega$ (ppm)	0	$\sqrt{0.1}$	3.5	1×10^{-6}	0	1×10^{-6}	−3.5	1×10^{-6}

third pool combined saturation effects from NOE and semisolid pool exchanges without distinguishing between these two signal sources. This may be sub-optimal given the observed differences in the linewidth of semisolid saturation and the region over which NOEs have been observed.

The 4-pool BM model used in this study extended the model such that semisolid MT and NOE exchanges were described using two separate pools in order to achieve better separation of NOEs and semisolid effects. The parameter prior distributions are listed in Table 6.1 for the clinical data, and in Table 8.2 for the preclinical data. In Table 8.2, T_1 was adjusted for the 9.4 T field assuming T_1 was approximately proportional to $B_0^{1/3}$ [143,144], and the amide pool M_0 prior mean and SD were also changed. The semisolid pool models semisolid saturation as a classic Lorentzian effect centred at water resonance, and NOEs are modelled separately as a single pool upfield of water based on observations in the literature.

The pH phantom data, for which semisolid effects have been minimised during the phantom preparation stage, were fitted to a 3-pool BM model comprising a water pool, an amine pool at 2.8 ppm, and an NOE pool at −3.5 ppm. The BM model was fitted to each phantom in sequence, and T_1 and T_2 priors used for each phantom were ob-

tained by finding the mean relaxation time from the respective quantitative T_1 and T_2 maps, thereby helping to correct for variations in relaxation time [78]. The paLDA technique was also applied to the phantom data by fitting the data points within ±1 ppm to a 1-pool BM model (water pool) in order to extract a water line shape from which the acquired data were then subtracted. A 1-pool model was sufficient in this case as the phantoms were prepared such that they did not contain a semisolid phase [78]. NOE(LDA) was found by integrating the mean residual of each phantom between −3.0 to −4.0 ppm (using trapezoidal numerical integration), from which the pH dependence of NOEs, as quantified using the paLDA technique, was found (Fig. B.4b).

8.3.3 Data extraction

The patient ROIs used in this study were ischaemic core, infarct growth, oligaemia, and a mirrored contralateral mask. The same tissue outcome ROIs were used for analysing the preclinical data but defined automatically based on the threshold values in ref. [37]. Primary analyses of the clinical data were done in voxels with a combined grey matter and white matter PVE greater than 50%, defined as the whole slice mask. Secondary analyses were done in separate grey matter and white matter masks. All brain voxels in the animal data (whole brain) were used (no PVE threshold defined). In the analysis of patient and animal results, all measures were also normalised to the contralateral hemisphere to produce a relative measure.

8.3.4 Analysis

Group mean absolute 3-pool NOER*, 4-pool NOER*, semisolidR*, and conventional MT were found in healthy subjects for the whole slice, grey matter, and white matter, and values were compared between metrics. Contrast between grey matter and white matter in healthy subjects was also found. Repeatability in healthy subjects and patient contralateral tissue was measured using ANOVA and the CoV. The spatial variability within healthy subjects was compared between metrics. The correlation between met-

rics was reported as R^2 along with the p-value of an F-test on R^2. Correlation was the primary means for comparing the different metrics, establishing whether (and to what extent) they provided similar (i.e. correlated) information.

In patients, relative APTR* was compared between pathological ROIs using each metric. This was done for the whole slice, grey matter, and white matter. The infarct growth CNR was found. In animals, relative APTR* was compared between pathological ROIs using 3- and 4-pool analysis, found for data acquired at 1 h and 2 h post-MCAO. The pH phantom data were fitted to vial pH using least squares linear regression, and the p-value for the F-test on the regression model was reported.

8.4 Results

8.4.1 Healthy subjects

Healthy subject BMM maps are shown in Fig. 8.1. The group mean absolute value for each metric in the healthy subjects is shown in Fig. 8.2a, for the whole slice and separately for grey and white matter. Mean 3-pool NOER* was (mean±SD) 0.124 ± 4.1%, mean 4-pool NOER* was 0.069 ± 5.1%, mean semisolidR* was 0.005 ± 5.3%, and mean conventional MT was 0.019 ± 5.2%. Each metric exhibited a larger value in white matter compared to grey matter ($p < 0.001$, shown as a percentage in Fig. 8.2b). Spatial variability of the 3-pool and 4-pool NOER* metrics was 30.0% (Fig. 8.2c), 39.7% using semisolidR*, and 42.0% using conventional MT.

There was no correlation between the 4-pool metrics (4-pool NOER* and semisolidR*) ($R^2 = 0.09$, $p = 0.012$). Three-pool NOER* exhibited low correlation with semisolidR* ($R^2 = 0.37$, $p < 0.001$) and with 4-pool NOER* ($R^2 = 0.32$, $p < 0.001$). SemisolidR* was moderately correlated with conventional MT ($R^2 = 0.50$, $p < 0.001$).

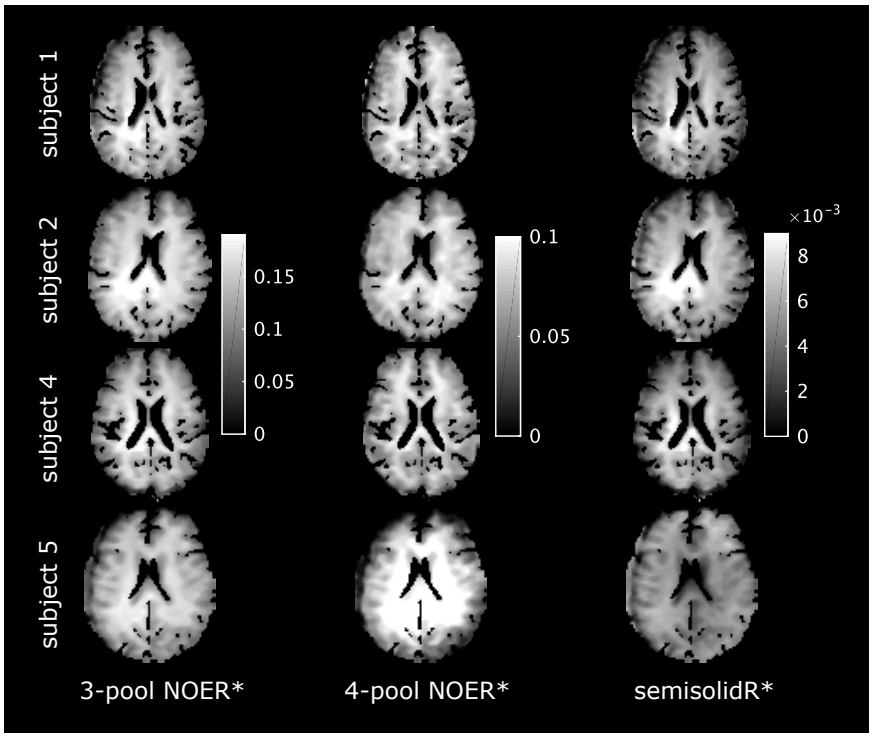

(a)

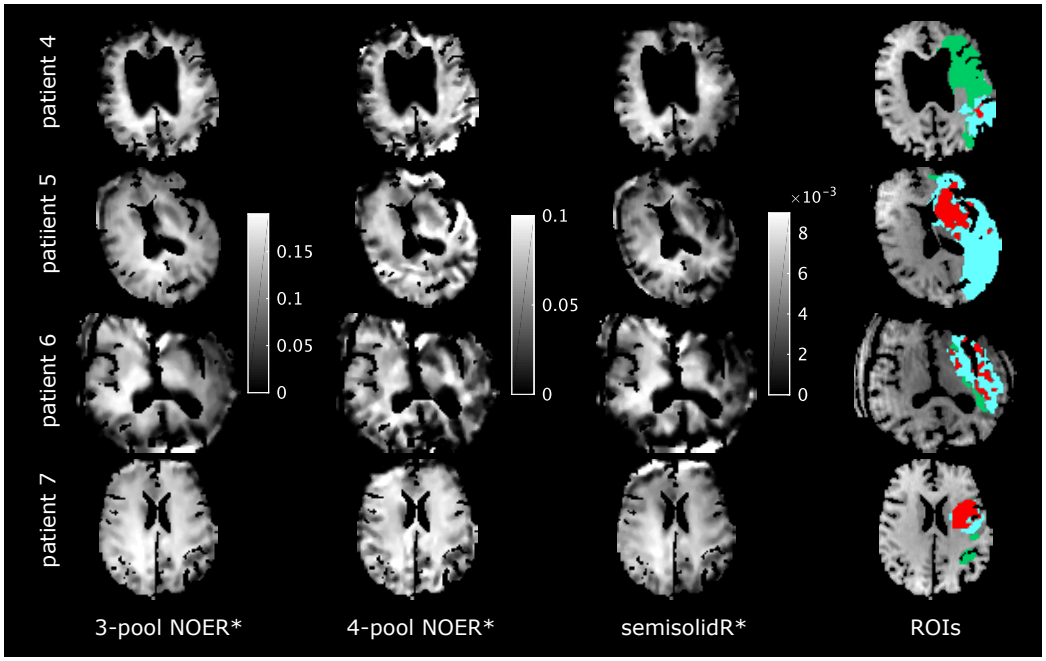

(b)

Figure 8.1: Maps from the BM model in **(a)** healthy subjects, and **(b)** representative stroke patients. Red: ischaemic core; green: oligaemia; cyan: infarct growth.

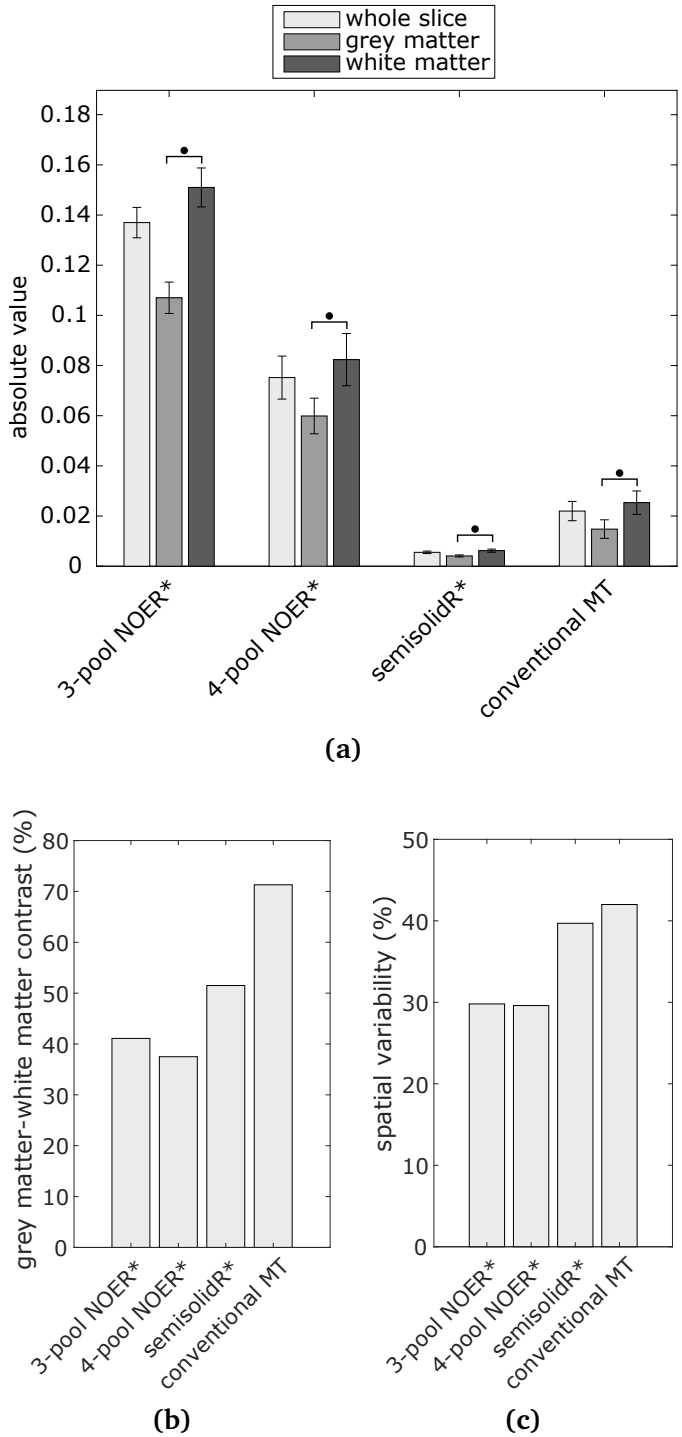

Figure 8.2: **(a)** Group mean BMM and conventional MT metrics in healthy subjects (whole slice, grey matter, and white matter). Error bars are the SD across subjects, and • denotes paired t-test $p < 0.05$. **(b)** Grey matter-white matter contrast expressed as a percentage, and **(c)** spatial variability within healthy subjects.

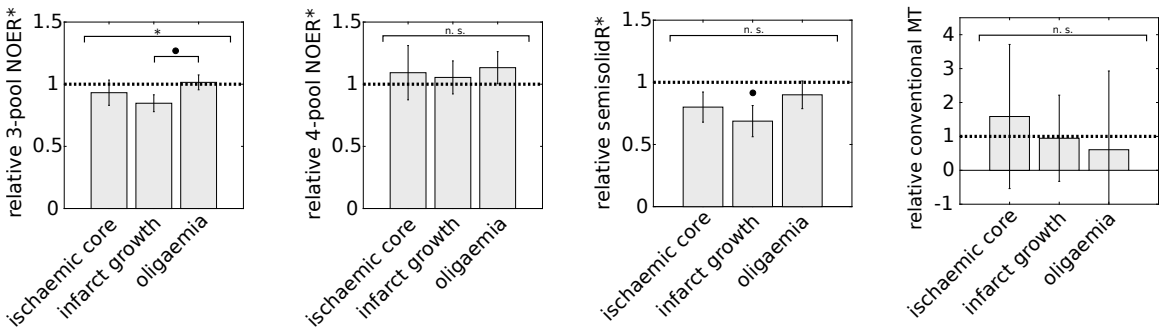

(a)

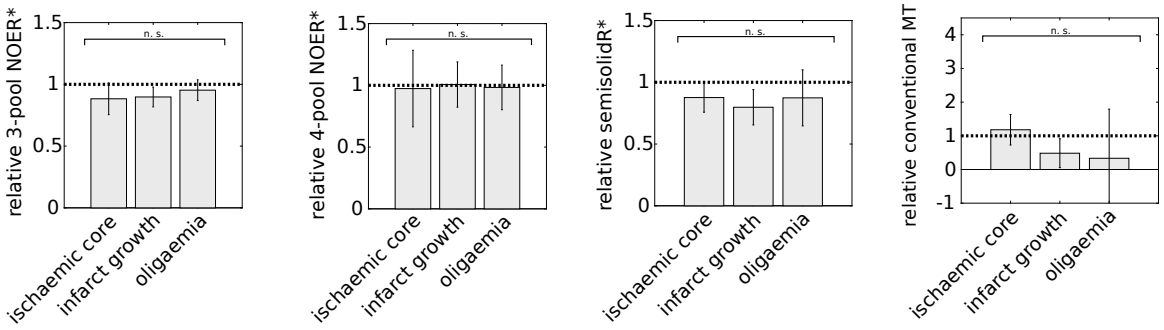

(b)

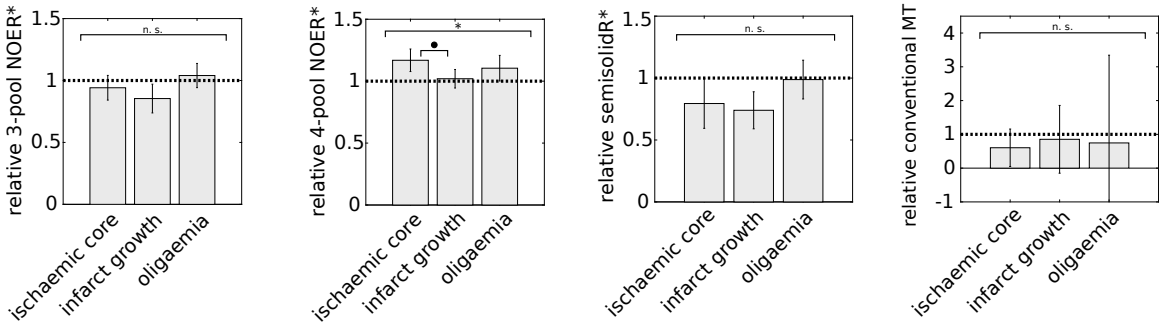

(c)

Figure 8.3: Stroke patient pooled voxel measures relative to the contralateral hemisphere: **(a)** whole slice, **(b)** grey matter voxels, and **(c)** white matter voxels. Shown for 3-pool NOER*, 4-pool NOER*, semisolidR*, and conventional MT (note the different scale). Error bars are the 95% CI. For the relative mean values shown, $*$ denotes ANOVA $p < 0.05$. Significance between ROIs is denoted by a horizontal bar with • (Welch's t-test $\tilde{\alpha}_{crit} = 0.017$). Significance with respect to the contralateral hemisphere is denoted by • (ANOVA of absolute means followed by Welch's t-test with $\tilde{\alpha}_{crit} = 0.0083$).

8.4.2 Patients

Representative patient BMM maps are shown in Fig. 8.1. The relative (to contralateral tissue) means of each metric are shown in Fig. 8.3 for the different tissue outcome ROIs (mean±95% CI) in the whole slice (Fig. 8.3a), grey matter (Fig. 8.3b), and white matter (Fig. 8.3c). In grey matter voxels, the BM model metrics did not exhibit significant differences between pathological ROIs. In all analyses the conventional MT metric did not exhibit significant differences between pathological ROIs. In white matter voxels, 3-pool NOER* and semisolidR* did not exhibit statistically significant differences between pathological ROIs, whereas 4-pool relative NOER* was significantly elevated in the ischaemic core (1.17 ± 0.09, $p = 0.010$) compared to the infarct growth ROI (1.02 ± 0.07).

In whole slice analysis, 3-pool relative NOER* was significantly decreased in the infarct growth ROI (0.85 ± 0.07) compared to the oligaemia ROI (1.01 ± 0.06) ($p < 0.001$). Relative semisolidR* was also decreased (0.7 ± 0.1), and the absolute mean was significantly lower than the contralateral tissue mean ($p < 0.001$). The 3-pool NOER* metric appeared to be strongly weighted by the semisolidR* values. Infarct growth CNR was 0.34 using 3-pool NOER* and 0.47 using semisolidR*.

8.4.3 Preclinical results

Fig. 8.4 shows example slices from all of the animals in the preclinical study at 1 h post-MCAO. Differences in the z-spectrum at 1 h post-MCAO in the cohort are illustrated in Fig. 8.5 that shows the average of the spectrum across all animals in both the ischaemic core and contralateral tissue. Relative mean values in the pathological ROIs from the preclinical data are shown in Fig. 8.6. Relative 4-pool NOER* was elevated in the ischaemic core (1.4 ± 0.3) at 1 h post-MCAO. At 2 h post-MCAO, the infarct growth signal increased to a similar level (1.3 ± 0.1) and was significantly different from oligaemic tissue (1.1 ± 0.1, $p = 0.009$). Three-pool relative NOER* and semisolidR* were both decreased in pathological ROIs at 1 h and 2 h post-MCAO. There was no significant

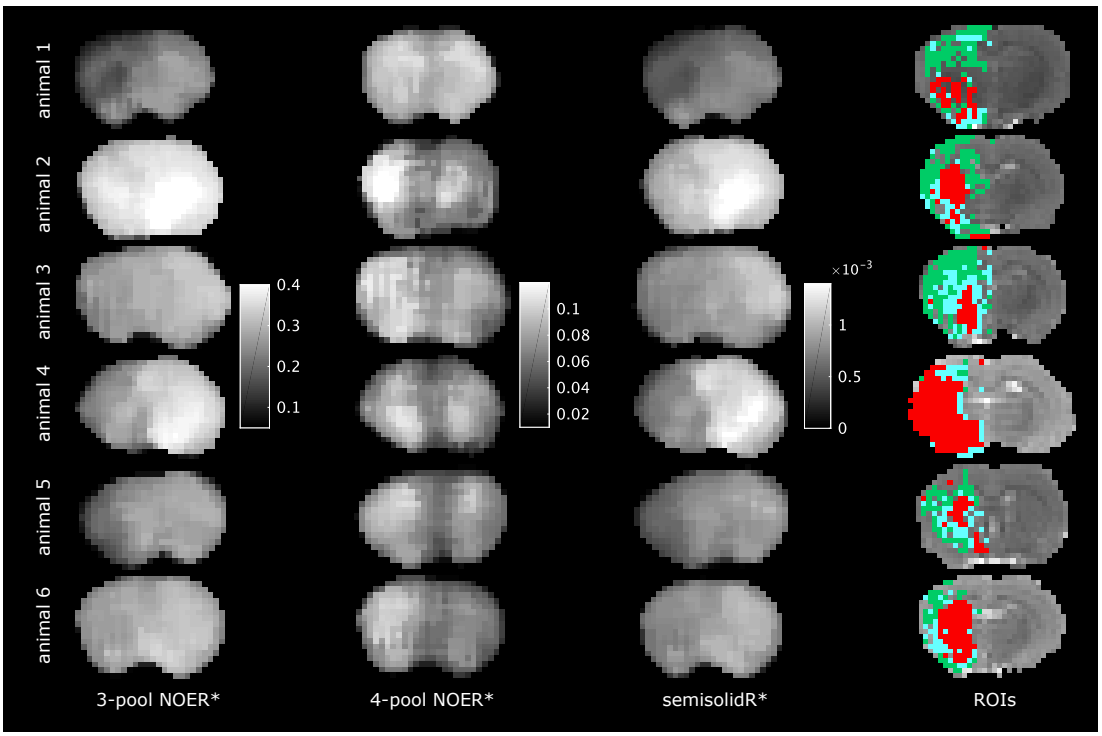

Figure 8.4: Example slices from all of the animals in the preclinical study at 1 h post-MCAO. Red: ischaemic core; green: oligaemia; cyan: infarct growth.

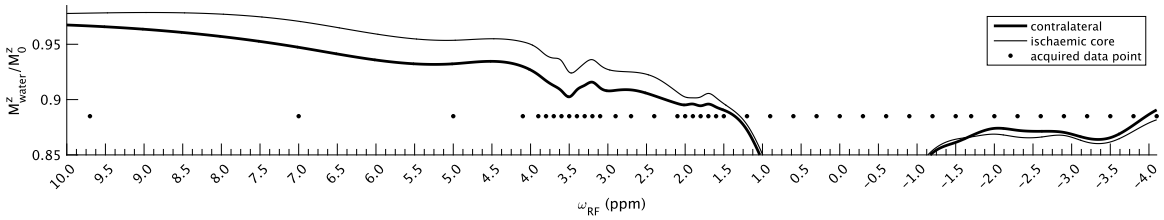

Figure 8.5: Average of the acquired z-spectrum across all animals in both the ischaemic core and contralateral tissue, at 1 h post-MCAO (B_0 correction and spline interpolation applied).

variation in 4-pool NOER* or semisolidR* between animals or the two time points.

8.4.4 Naïve brain pH phantoms

In the naïve brain pH phantoms, a significant and moderately high positive association between NOER* and pH was observed ($R^2 = 0.75$, $p = 0.027$), as shown in Fig. 8.7. Using the LDA technique, the regression relationship was NOE LDA $= 1.97 \times \text{pH} - 6.00$ (phantom LDA data shown in Fig. B.4).

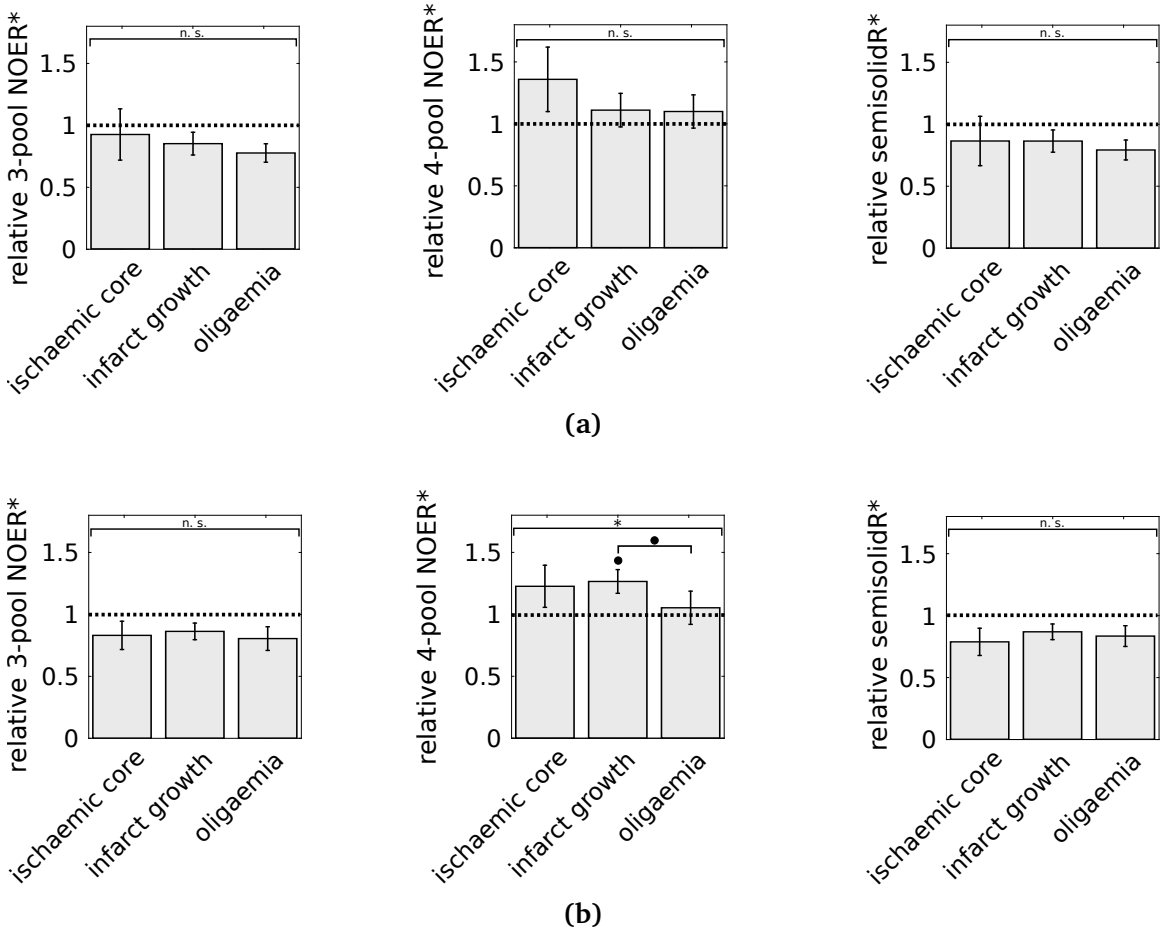

Figure 8.6: Animal relative means for each of the tissue outcomes, shown for 3-pool NOER*, 4-pool NOER*, and semisolidR*: **(a)** 1 h post-MCAO, **(b)** 2 h post-MCAO. Error bars are the 95% CI. For the relative mean values shown, $*$ denotes ANOVA $p < 0.05$. Significance between ROIs is denoted by a horizontal bar with • (Welch's t-test $\tilde{\alpha}_{crit} = 0.017$). Significance with respect to the contralateral hemisphere is denoted by • (ANOVA of absolute means followed by Welch's t-test with $\tilde{\alpha}_{crit} = 0.0083$).

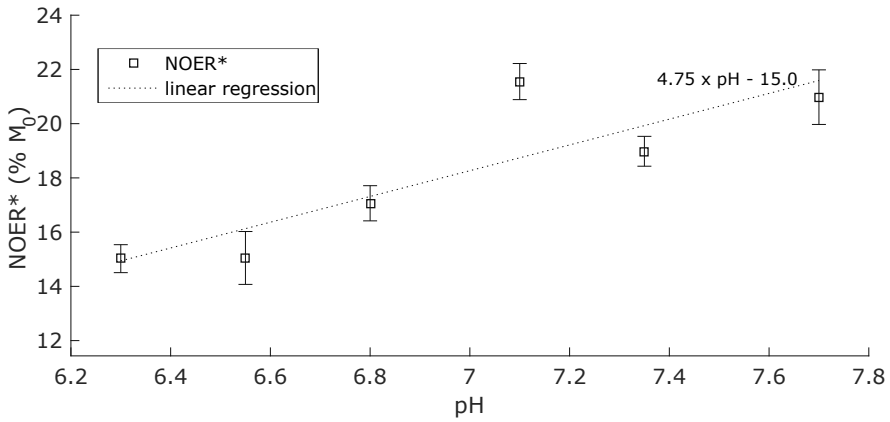

Figure 8.7: pH dependence of 4-pool NOER* (open squares) in naïve brain phantoms titrated to different pH. Error bars are the 95% CI. Black dotted line is the fitted linear regression relationship ($R^2 = 0.75$, $p = 0.027$).

8.5 Discussion

The main objective of this study was to explore what information a 4-pool model provides in ischaemic stroke, which was thought to be a more biophysically accurate model of NOEs, contrasting that with the intentionally approximate 3-pool model. The 4-pool measure of NOEs provided information on tissue outcome that was different from the 3-pool approximation, and from the 4-pool measure of semisolid effects. This information on NOEs, that was unobservable via the 3-pool approximation, was obtained by using a more complex model without apparent over-fitting of the data since it exhibited similar spatial variability to the 3-pool measure. For these reasons it seems reasonable to interpret 4-pool NOER* as being a metric that more closely reflects *in-vivo* changes in NOEs compared the 3-pool approximation.

In the ischaemic core ROI, 4-pool NOER* was elevated in patients and in animals; a change that appeared to be driven by values in white matter voxels. NOEs remained elevated in the ischaemic core at 2 h post-MCAO. Relative semisolidR* was decreased in patients and in animals. In the infarct growth ROI, the 4-pool measure of NOEs was slightly elevated at presentation in patients and in animals, and once this tissue was recruited into the infarct core at 2 h post-MCAO, it exhibited an elevated value identical to that of the presenting lesion. In the oligaemia ROI, 4-pool NOER* was el-

evated in patients and in animals, and in animals it approached a normal value at 2 h post-MCAO. Quantification of NOEs using 3 pools appeared to be strongly weighted by semisolid effects while the 4-pool measure of NOEs did not exhibit any substantial correlation; 3-pool NOER* exhibited similar, but less pronounced, changes in pathological ROIs compared to semisolidR*, suggesting that the latter metric obscures some of the variability associated with pathology. This supports the supposition that 3-pool NOER* is a weighted average of NOEs and semisolid effects, but appears to be biased towards the latter.

8.5.1 Association of NOER* with pH

In the present study an elevated NOER* signal was observed in the ischaemic core, consistent with some previous preclinical studies in the CEST literature [34,81,111]. This is concurrent with the decrease of APT effect in the ischaemic core (Chapter 6). This raises the question of whether NOEs are sensitive to pH, as the APT effect is generally assumed to be. Changes in NOEs could be pH-driven via two pH-dependent pathways. For exchange-relayed NOEs, a direct dependence on pH would exist where magnetisation of aliphatic protons is first dipolar-coupled to labile protons of amide sidegroups on the same molecule, before finally undergoing chemical exchange with free water protons [72]. In the study of ref. [110] the build-up of NOEs on non-chemically-exchanging lipids was similar to that obtained using BSA protein phantoms that do permit chemical exchange. This supports the notion that NOEs manifest through pathways of both intermolecular dipolar coupling and pH-dependent chemical exchange [57]. For NOEs that are not exchange-relayed, an indirect dependence of NOEs on pH can be realised through intermolecular coupling which, owing to changes in protein conformation caused by acidosis (reducing the number of dipolar coupling sites available), leads to a reduction of intermolecular-coupled NOEs [94,121]. For both pathways, a decrease in pH would effect a decrease in NOEs.

As discussed in the literature review (Section 3.5.8), there have, however, been dif-

fering experimental results as to whether NOEs are pH-sensitive [57,72]. In this study, NOER* exhibited moderately high correlation with pH and the trend was statistically significant. A comparable study to the one conducted herein is the study of ref. [57] which analysed the pH dependence of NOEs in 10% BSA phantoms at 7 T using the LDA technique, reporting a positive pH dependence of NOEs (NOE LDA $= 0.40 \times \text{pH} + 1.40$, $R^2 > 0.3$). The LDA technique was also applied to the data in this study and yielded a positive trend, consistent with that reported in ref. [57]. Therefore, when metabolite concentration is controlled for and pH is decreased, NOEs appear to change in the same direction as base-catalysed amides. The pH phantom study of ref. [72] found that NOEs were insensitive to pH, however this apparent insensitivity might have been an artefact of the model-free subtraction technique used to quantify NOEs which could have resulted in a cancellation of pH effects, especially given the similarity in pH dependence at the points used in the subtraction [57] (Section 3.5.8).

In the present study it was observed that NOEs were elevated in the ischaemic core. In the *in-vivo* environment it is not possible to attribute changes in NOEs solely to pH, as both pH and concentration changes have been observed in the ischaemic core. A recent study has shown that the ischaemic core exhibits a decrease in pH, and a concurrent decrease in cytoplasmic protein concentration, the latter of which has hitherto been assumed to remain constant immediately following ischaemic stroke in the CEST literature [107]. That both pH and protein concentration decrease, rather than increase, would lead to a reduction in the mechanisms currently known of for NOEs. In contrast to this is the significant increase of NOEs, observed in the present study and other studies [34,81,111], hence the observations still cannot be fully explained. NOEs in the ischaemic core appear to be affected by competing processes that have yet to be identified, and alludes to a complex array of mechanisms at play in the early stages of ischaemic stroke.

An elevated 4-pool NOER* value was observed in infarcted tissue, whether that was the region at 1 h post-MCAO, or the larger region that includes infarct growth at 2 h

post-MCAO. This was consistent with the clinical data in that raised 4-pool NOER* is indicative of tissue death, but the 4-pool model did not provide much further differentiation between the infarct growth and oligaemia ROIs. In terms of physiological changes occurring within the infarct growth ROI, the preclinical study of ref. [107] isolated the cytoplasmic protein concentration and found no significant difference in protein concentration with respect to contralateral tissue. The same region subsequently underwent a significant decrease in APT effects at 2 h post-MCAO.

8.5.2 Association of metrics with white matter

In healthy subjects the larger white matter NOER* value compared to grey matter was consistent with previous studies on NOEs [57,72,81,88]. Lipids have a high abundance of non-chemically-exchanging aliphatic bonds whose resonance frequency is centred at around −3.5 ppm, therefore saturation effects at this frequency have been associated with lipids [72]. Coupled with the relatively narrow line width, characteristic of mobile species with short T_2, this has led to the suggestion that NOEs may originate from the higher mobile lipid content found in the white matter myelin sheath [110]. The total lipid content in white matter of a human brain is 36 to 65% higher than in grey matter, which would be consistent with the lower white matter signal observed here [108,115]. The presence of an NOE mobile lipid signal has been supported by a recent experimental study into protein-free liposomised mouse brain tissue, which exhibited pronounced saturation effects confined to the frequency range of aliphatic protons [110].

Semisolid effects originate from immobile lipids which facilitate rapid magnetisation transfer via spin diffusion, having a much shorter T_2 compared to the surrounding water and a correspondingly broad line width [91–93]. Semisolid effects have typically been used in identifying white matter disease which is marked by demyelination of nerve axons in white matter, yielding lower magnetisation transfer ratios [91]. In ischaemic stroke, significant white matter injury can occur [145–147]. SemisolidR* was decreased in all pathological ROIs relative to the contralateral normal tissue. Given

that this was observed in the entirety of the stroke hemisphere, it may suggest a global cause of signal change rather than specific sensitivity to a secondary, delayed cell-death pathway. The decrease of semisolidR^* in the ischaemic core might also reflect a decrease in the concentration of cell membrane-bound proteins, which is a consequence of the rapid cell death and membrane degradation which occurs following ischaemic stroke. This has been observed in semisolid MT studies of stroke [101], where saturation is much decreased in the ischaemic core imaged at 1 month. In comparison, conventional MT did not exhibit significant variation between pathological ROIs in this study. Conventional MT is widely used in studies on demyelination where an acquisition sequence with a low FA and long TR is employed to yield proton density-weighted images [148,149]. In this study a larger FA was used, optimised for APT CEST effects, and this may explain why it was not sensitive to the processes that the BMM analysis technique captured [150].

8.5.3 Evaluation of modelling assumptions

In this study semisolid effects were modelled as a symmetric phenomenon, with NOEs giving the spectrum its upfield asymmetry. This construction was based on observations in the literature. In early CEST studies is was thought that z-spectra were symmetrical about water resonance in the absence of metabolite exchanges, and a broad featureless spectrum upfield of water resonance was assumed, used as a reference. However, asymmetry of the upfield spectra, particularly at lower RF saturation powers, indicated the presence of strong saturation effects in the aliphatic region of the spectrum. The cause of asymmetry was initially attributed to resonance mismatch between the bulk water and semisolid pools such that semisolid macromolecules had a positive chemical shift with respect to the water signal [52,74,112–114]. This is unlikely as the broad spectral distribution of semisolid effects, on the order of tens of ppm [72,74], suggests that the spectrum should be symmetric. Some earlier studies have attributed this asymmetry to the aliphatic protons of a mixture of mobile to relatively-mobile peptides,

proteins, lipids, and metabolites, which have resonances located around −3.5 ppm, ranging from −2 to −5 ppm [74]. Upfield exchange processes related to mobile macromolecules [42,74], or NOEs, are now thought to be the cause of z-spectrum asymmetry, and this assumption has been made in the model fitting process of the present study [42,57,72,74,95].

Despite the distinction made between the semisolid pool and the NOE pool, broad spectral phenomena such as semisolid effects can overlap with different exchange peaks and may influence the distribution of saturation between pools due to indirect coupling between them via the mediating water pool. In Chapter 6 (Section 6.4) the model-fitted spectra, averaged over the healthy subjects, showed that 4-pool NOER* exhibited a tail of saturation extending downfield of water from −3.5 ppm, overlapping with the APT resonance [32,122]. Increasing the number of pools, and therefore the number of model parameters, can lead to over-fitting which would result in higher spatial variation. In this case, adding a fourth pool yielded similar spatial variability between 3- and 4- pool NOE signals, and there was no substantial correlation between the two metrics, which suggests that the signals are associated with different effects. These factors may be indicative of better signal separation using 4-pool analysis of NOEs.

The BM formalism describes each pool using a single transverse relaxation time, which analytically yields a Lorentzian absorption line shape [151]. This is more accurate for mobile populations which can be described using a single T_2. The semisolid pool, however, is composed of immobilised proteins and large lipids that are restricted in motion, for which this assumption might not be a good approximation [152,153]. Super-Lorentzian and Gaussian line shapes have been found to provide a better fit for tissue, with the former giving optimum results *in-vivo* and is used in model-based MT studies [60,91,142,154]. In this study the semisolid pool was modelled using a classic Lorentzian line shape. For the purposes of quantifying NOEs, this simplification may be acceptable as NOEs are evaluated within a small frequency range (< 5 ppm) [60,155] over which the differences between a Lorentzian line shape and a more accurate super-

Lorentzian line shape are negligible owing to the semisolid pool's short T_2 and very wide NMR signal [32,60]. This does, however, introduce uncertainty when quantifying semisolid effects using semisolidR^*, as the super-Lorentzian is wider than the classic Lorentzian, resulting in an inflated estimate of T_2, and differences between the two line shapes at large offset frequencies [32]. This does not account for the decreased value of relative semisolidR^* in all of the pathological ROIs, as the decreased values are with respect to the contralateral tissue ROI. The approximation appears to be valid here as the results obtained in this study were consistent with the literature in describing semisolid effects as being significantly elevated in white matter, and decreased in the ischaemic core.

8.6 Conclusion

The 4-pool measure of NOEs provided information on tissue outcome that was different from the 3-pool approximation, and from the 4-pool measure of semisolid effects. This information on NOEs, that was unobservable via the 3-pool approximation, suggests that the 4-pool NOE metric is better at capturing *in-vivo* changes in NOEs. NOEs were elevated in the ischaemic core, but given that both pH and protein concentration have previously been reported to decrease in infarcted tissue, the observations still cannot be fully explained in terms of known NOE mechanisms. An elevated 4-pool NOE value was also observed in the larger infarcted region that includes infarct growth at 2 h post-MCAO. This was consistent with the clinical data in that a raised value is indicative of tissue death, but the 4-pool model did not provide much further differentiation between the infarct growth and oligaemia ROIs. NOEs appear to be affected by competing processes that have yet to be identified, and alludes to a complex array of mechanisms at play in the early stages of the disease. Further investigation of NOEs is needed in order to better-understand the physiological origins of these observations and their potential as complementary imaging biomarkers in acute stroke.

Whilst NOEs have been modelled as a relatively broad effect, high-field studies have identified NOEs as a composite of several resonances, one such being a sub-resonance at −1.6 ppm which may be associated with tissue pathology in stroke (Section 3.5.4). The next and final chapter thus seeks to identify NOE sub-resonances and explores their association with tissue outcome following stroke.

Chapter 9

Quantifying NOE sub-resonances

9.1 Introduction

THE study of upfield effects in Chapter 8 modelled NOEs as a relatively broad effect centred at −3.5 ppm based on observations of CEST spectra in the literature. The discussion on the spectral characteristics of NOEs in Section 3.5.3 highlighted that NOEs are in a fact a composition of several narrower resonances. Recent studies have identified an NOE sub-resonance[1] at −1.6 ppm (Section 3.5.4) which exhibits a significant decrease immediately after ischaemic stroke [81,111] and is hypointense in tumour tissue [80,98,117,118]. The objectives of this chapter were (i) to identify and isolate NOE sub-resonances in preclinical stroke models, and (ii) thereby explore their association with tissue outcome, with the final objective of (iii) quantifying these effects in a cohort of patients with acute ischaemic stroke.

9.2 Methods

An outline of the methods used in this chapter is presented below; refer to Chapter 4 for further details.

[1] An NOE peak apart from the broader NOE centred at −3.5 ppm.

9.2.1 Study details

This chapter employed the datasets from 12 patients presenting with acute ischaemic stroke and a preclinical dataset.

9.2.2 Processing

In the animal data, the Lorentzian difference spectrum, which is the raw spectrum after removal of the water+semisolid effects baseline, was obtained as follows. Individual animal Lorentzian difference spectra and ROI-averaged Lorentzian difference spectra were used for the purpose of visually identifying the NOE sub-resonance at −1.6 ppm in the animal dataset, as well as any other identifiable sub-resonances. The Lorentzian difference spectra were also used for estimating parameter priors of the sub-resonances for use in subsequent BMM analysis of these effects.

The rationale for adopting this 'LDA-directed' approach is as follows. LDA is a useful tool for 'model-free' exploration of CEST spectra, but since it is not as robust as a fully model-based approach (based on the methodological comparisons in Chapter 5), it is not expected that very consistent effects from animal to animal will be observed using LDA, particularly in the context of noise and overlapping sources that LDA cannot fully resolve. Hence the strategy of identifying potential sub-resonances using LDA, as a precursory step to BMM analysis, which is more robust, allows quantification of these effects in the context of noise and overlapping sources that LDA cannot fully resolve.

The Lorentzian difference spectrum of the preclinical data was first obtained for the purpose of observing NOE spectra without the water and semisolid baseline. The data from each animal were fitted to a 2-pool model of the Bloch equations comprising a water pool and a semisolid pool (an example fit is shown in Fig. B.3a). The parameter priors used for these two pools are listed in Table 9.1. The following offset frequencies, assumed to be representative of direct water saturation and semisolid effects, were used in the fitting process: ±0.9, ±0.6, ±0.3, 0.0, 51, 72, 100, and ±300 ppm. The Lorentzian difference spectrum of each animal was obtained by subtracting the

acquired spectrum from the model fitted 2-pool spectrum. Before the subtraction was performed, the acquired data were corrected for B_0 and linearly interpolated onto a higher-resolution (0.02 ppm) axis. A voxel-weighted mean across the animals was obtained for each tissue outcome.

In this study two NOE sub-resonances were identified in the animal data (see results); at −1.6 ppm and at −2.4 ppm. The 4-pool model used in Chapter 8 (pools: water, amide, semisolid, and NOEs at −3.5 ppm) with preclinical priors was extended to two separate 5-pool models; in the first 5-pool BM model, the fifth pool accounted for effects at −1.6 ppm, and in the second 5-pool BM model, the fifth pool accounted for effects at −2.4 ppm (Fig. B.5). Parameter priors for the animal data are listed in Table 9.1. A 5-pool model was fitted to the clinical data, comprising the four pools used in Chapter 6, and a fifth pool representing an NOE sub-resonance at −2.4 ppm (parameter priors for clinical data are listed in Table 9.2).

9.2.3 Data extraction

The patient ROIs used in this study were ischaemic core, infarct growth, oligaemia, and a mirrored contralateral mask. Analysis was conducted in voxels with a tissue PVE greater than 0.5. The same tissue outcome ROIs were used for the preclinical data but defined automatically based on the threshold values in ref. [37].

A reduced animal dataset was used as follows[2]. Of the 10 longitudinal slices acquired for each animal, all brain voxels in contiguous slices 3–6 were used (no PVE threshold defined) and the remainder were excluded from analysis. The fractions of ROI voxels from the whole dataset that also appear in the subset used in this study are: ischaemic core 63% (1304 voxels included), infarct growth 56% (877 voxels), oligaemia 38% (1365 voxels), and contralateral 44% (5180 voxels).

In the analysis of patient and animal results, all measures were also normalised to the contralateral tissue mean to produce a relative measure. The relative mean val-

[2]This was done in order to reduce the processing time required whilst optimising coverage of pathological ROIs.

Table 9.1: Parameter priors used for 5-pool BMM analysis of the animal data. Model priors are expressed as a mean and SD.

Glossary – M_0: pool concentration relative to water pool (water pool M_0 is absolute), k_{ex}: pool→bulk water exchange rate, T_1: longitudinal relaxation time, T_2: transverse relaxation time, $\Delta\omega$: chemical shift with respect to water pool. For brevity, annotations of the parameter priors that were listed in Table 6.1 are not reproduced in this table.

[†]T_1 for pools 1–4 is from Table 8.2.

	water		APT		symmetric semisolid	
Parameter	mean	SD	mean	SD	mean	SD
M_0 (norm.)	0	1×10^6	$\frac{100\text{ mM}}{112\text{ M}}$	$\frac{200\text{ mM}}{112\text{ M}}$	0	1×10^6
k_{ex} (Hz)	—	—	20	$e^{1.0}$	60	$e^{1.0}$
T_1 (s)[†]	1.9	0.15	1.1	0.15	1.5	0.15
T_2 (ms)	70	14	10	2	0.1	0.02
$\Delta\omega$ (ppm)	0	$\sqrt{0.1}$	3.5	1×10^{-6}	0	1×10^{-6}

	NOE(−3.5 ppm)		NOE(−1.6 ppm)		NOE(−2.4 ppm)	
	mean	SD	mean	SD	mean	SD
M_0 (norm.)	0	0.01	0	0.01	0	1×10^6
k_{ex} (Hz)	20	$e^{1.0}$	20	$e^{1.0}$	20	$e^{1.0}$
T_1 (s)[†]	1.1	0.15	1.1	0.15	1.1	0.15
T_2 (ms)	0.3	0.06	3.0	0.6	3.0	0.6
$\Delta\omega$ (ppm)	−3.5	1×10^{-6}	−1.6	1×10^{-6}	−2.4	1×10^{-6}

ues were weighted by the number of contributing voxels and pooled to give a voxel-weighted group mean for each tissue outcome.

9.2.4 Analysis

In the animal data, NOER*(−1.6 ppm) and NOER*(−2.4 ppm) (henceforth referred to as $NOER^*_{-1.6}$ and $NOER^*_{-2.4}$ for brevity) were found for each pathological ROI at 1 h post-MCAO. In the clinical data, $NOER^*_{-2.4}$ was found for the presenting scan. In both datasets $NOER^*_{-3.5}$ was also obtained. Absolute group mean NOER* measures were compared to the contralateral tissue ROI, and relative NOER* was used for comparisons between pathological ROIs.

Table 9.2: Parameter priors used for 5-pool BMM analysis of the clinical data. Model priors are expressed as a mean and SD.

Glossary – M_0: pool concentration relative to water pool (water pool M_0 is absolute), k_{ex}: pool→bulk water exchange rate, T_1: longitudinal relaxation time, T_2: transverse relaxation time, $\Delta\omega$: chemical shift with respect to water pool. For brevity, annotations of the parameter priors that were listed in Table 6.1 are not reproduced in this table.

	water		APT		symmetric semisolid	
Parameter	mean	SD	mean	SD	mean	SD
M_0 (norm.)	0	1×10^6	$\frac{90\text{ mM}}{112\text{ M}}$	$\frac{20\text{ mM}}{112\text{ M}}$	0	1×10^6
k_{ex} (Hz)	—	—	20	$e^{1.0}$	60	$e^{1.0}$
T_1 (s)	1.3	0.15	0.77	0.15	1.0	0.15
T_2 (ms)	70	14	10	2	0.1	0.02
$\Delta\omega$ (ppm)	0	$\sqrt{0.1}$	3.5	1×10^{-6}	0	1×10^{-6}

	NOE(−3.5 ppm)		NOE(−2.4 ppm)	
	mean	SD	mean	SD
M_0 (norm.)	0	1×10^6	0	1×10^6
k_{ex} (Hz)	20	$e^{1.0}$	20	$e^{1.0}$
T_1 (s)	0.77	0.15	0.77	0.15
T_2 (ms)	0.3	0.06	3.0	0.60
$\Delta\omega$ (ppm)	−3.5	1×10^{-6}	−2.4	1×10^{-6}

9.3 Results

The Lorentzian difference spectra of the animals are shown in Fig. 9.1a for each tissue outcome. A peak at −1.6 ppm appeared pronounced in the contralateral tissue and oligaemia ROIs. At this offset, the signal also appeared to be elevated in ischaemic core tissue (1.2 ± 0.6), although in this case it was not clear how much of the elevated signal was due to overlapping sources that were also increased, and which LDA cannot fully resolve. The the infarct growth ROI value at this offset was similar to that of the contralateral tissue. By visual inspection, the HWHM of the peak in contralateral tissue was approximately $\nu_{1/2} = 0.18$ ppm, which, using equation (3.12), corresponds to an estimated T_2 of 2.9 ms.

It was possible to visually differentiate the infarct growth ROI from the contralateral tissue ROI at −2.4 ppm, where the infarct growth ROI exhibited a graded intermediate value between normal and infarcted tissue (contralateral: 3.0%, oligaemia: 3.2%,

infarct growth: 3.8%, and ischaemic core: 4.4%). Further investigation of saturation effects near −2.4 ppm in Fig. 9.1b revealed a distinct narrowing of confidence intervals that occurred for each tissue outcome, which suggests that saturation effects at this frequency may be more consistent between animals and tissue pathology compared to other frequencies. The confidence intervals were such that the ischaemic core ROI and infarct growth ROI could be distinguished on the basis of their spectra at this frequency. These spectral features warranted further investigation as they indicated an association with tissue at risk, at an offset that may be readily observed on a lower-field clinical scanner, and where saturation effects in the Lorentzian difference data (i.e. minimally processed) were visually distinct. The HWHM of the apparent peak at −2.4 ppm was approximately 0.2 ppm, corresponding to an estimated T_2 of 2.4 ms. A value of $T_2 = 3$ ms was used as the T_2 prior for both sub-resonances (Table 9.1), and $\Delta\omega$ for each of the two pools was set to a constant, with a value based on the ROI-averaged animal spectra.

The animal BMM maps are shown in Fig. 9.2. The relative (to contralateral tissue) mean NOER* in animals is shown in Fig. 9.3. In both 5-pool models, relative NOER$^*_{-3.5}$ was, as in Chapter 8, elevated in the ischaemic core, with the oligaemia ROI and infarct growth ROI values close to unity. The mean trends of relative NOER$^*_{-3.5}$ in pathological tissue were consistent between the two 5-pool models and the 4-pool results of the previous chapter, and are not explored further in this chapter (refer to Chapter 8 for analyses of NOER$^*_{-3.5}$).

In the ischaemic core, relative NOER$^*_{-1.6}$ (mean±95% CI) (1.6 ± 0.6) was, despite a significant ANOVA result ($p = 0.03$), not statistically significantly different from the contralateral tissue mean ($p = 0.08$). There was no significant variation between ROIs using relative NOER$^*_{-2.4}$ ($p = 0.7$). The infarct growth ROI relative mean appeared to be elevated using NOER$^*_{-2.4}$ (1.2 ± 0.2) compared to the ischaemic core (1.1 ± 0.5) and the oligaemia ROI (1.2 ± 0.3).

The absolute value of NOER$^*_{-1.6}$ and NOER$^*_{-2.4}$ in the contralateral hemisphere exhibited a relatively high level of variation compared to NOER$^*_{-3.5}$. The absolute values in

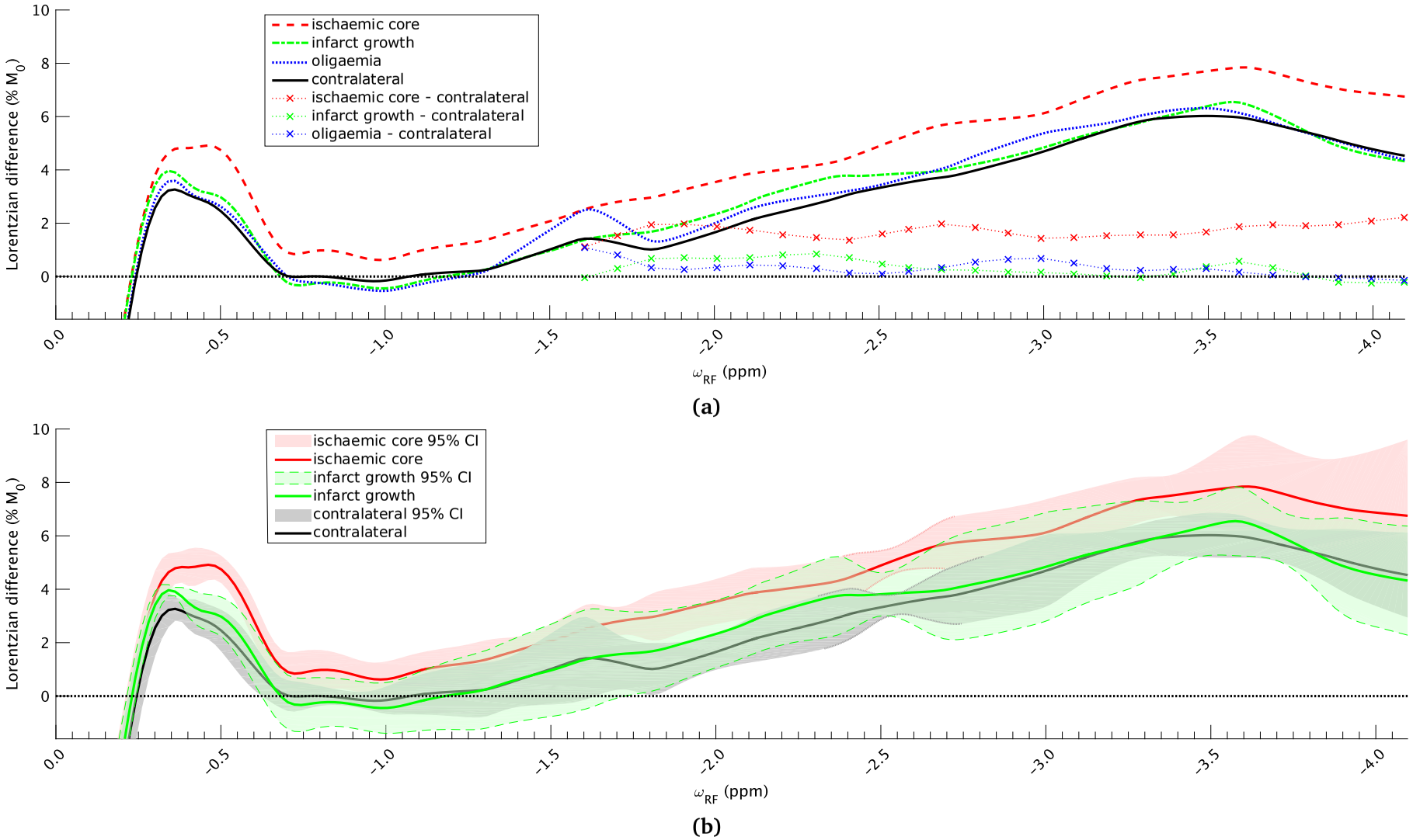

Figure 9.1: Lorentzian difference spectra of MCAO animals **(a)** for each tissue outcome, and **(b)** shown with 95% CIs for the ischaemic core, infarct growth, and contralateral ROIs.

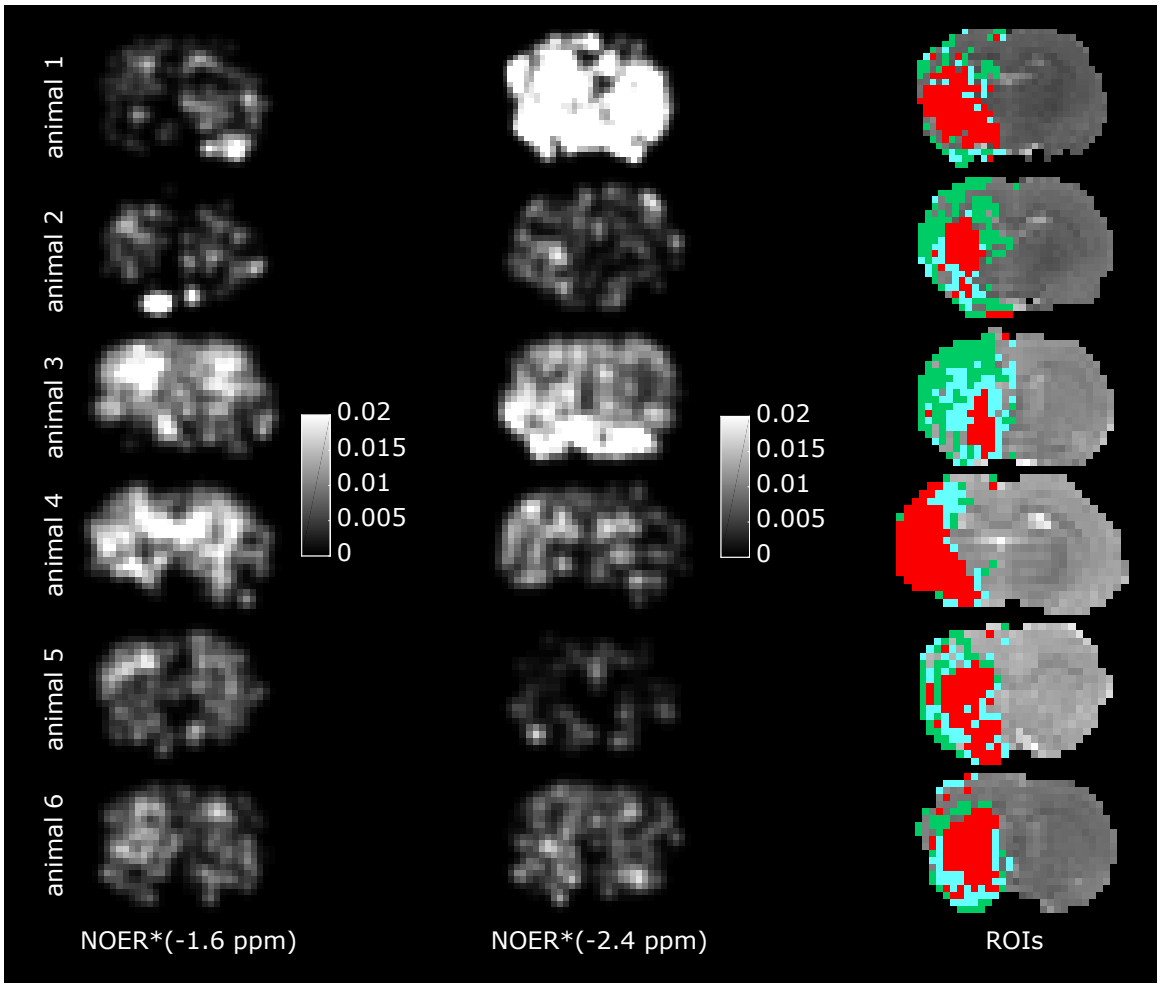

Figure 9.2: 5-pool BMM maps of animals at 1 h post-MCAO. Red: ischaemic core; green: oligaemia; cyan: infarct growth.

the contralateral hemisphere were (mean± %SD) $NOER^*_{-1.6}$: 0.012±88.0%, $NOER^*_{-2.4}$: 0.097 ± 55.4%, and $NOER^*_{-3.5}$: 0.074 ± 8.38%.

The relative $NOER^*$ results in patients are shown in Fig. 9.4. Relative $NOER^*_{-3.5}$ exhibited a similar trend to the 4-pool whole slice value derived in Chapter 8. The elevated ischaemic core mean in 5-pool analysis was (mean±95% CI) 1.1 ± 0.2. Relative $NOER^*_{-2.4}$ was decreased in the ischaemic core (0.5 ± 0.2, $p = 0.01$), and also in the infarct growth ROI (0.8 ± 0.3). Relative $NOER^*_{-2.4}$ was approximately unity in the oligaemia ROI (1.1 ± 0.8). The variation in the absolute value of $NOER^*_{-2.4}$ in the contralateral hemisphere was larger than that of $NOER^*_{-3.5}$. In the contralateral hemisphere, absolute $NOER^*_{-3.5}$ was (mean± %SD) 0.056 ± 8.4%, and $NOER^*_{-2.4}$ was 0.0149 ± 45.5%.

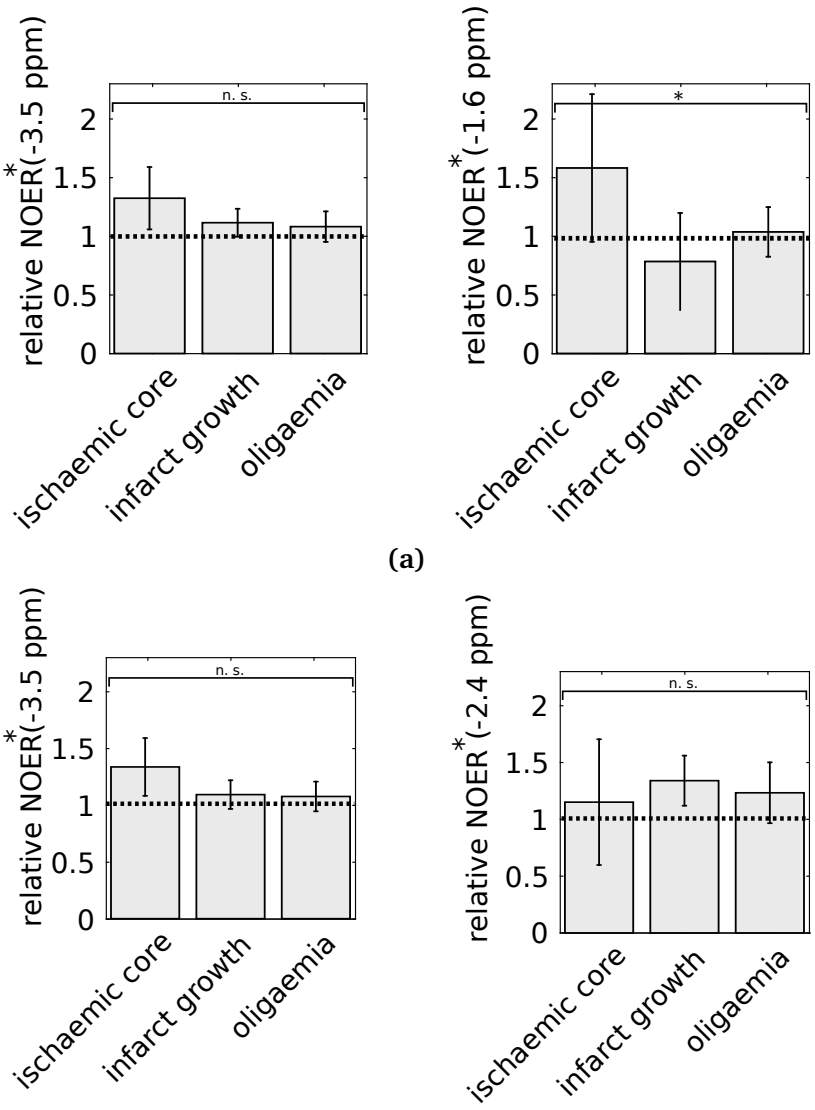

Figure 9.3: Relative 5-pool NOER* in animals at 1 h post-MCAO in different pathological ROIs. Results were obtained from two separate 5-pool models: **(a)** relative NOER*(−3.5 ppm) and relative NOER*(−1.6 ppm) using the first 5-pool model, and **(b)** relative NOER*(−3.5 ppm) and relative NOER*(−2.4 ppm) using the second 5-pool model. Error bars are the 95% CI. For the relative mean values shown, $*$ denotes ANOVA $p < 0.05$. Significance between ROIs is denoted by a horizontal bar with • (Welch's t-test $\tilde{\alpha}_{crit} = 0.017$). Significance with respect to the contralateral hemisphere is denoted by • (ANOVA of absolute means followed by Welch's t-test with $\tilde{\alpha}_{crit} = 0.0083$).

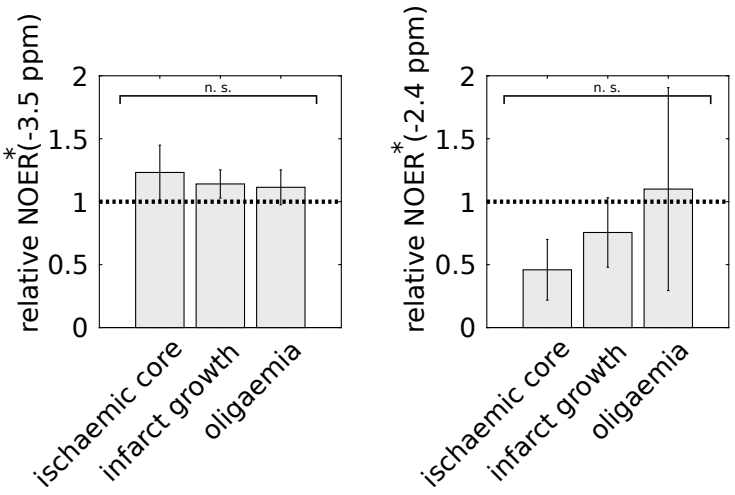

Figure 9.4: Whole slice relative NOER*(-3.5 ppm) and relative NOER*(-2.4 ppm) in patients shown for the different pathological ROIs. Error bars are the 95% CI. For the relative mean values shown, $*$ denotes ANOVA $p < 0.05$. Significance between ROIs is denoted by a horizontal bar with $\bullet$ (Welch's t-test $\tilde{\alpha}_{crit} = 0.017$). Significance with respect to the contralateral hemisphere is denoted by $\bullet$ (ANOVA of absolute means followed by Welch's t-test with $\tilde{\alpha}_{crit} = 0.0083$).

9.4 Discussion

In the preclinical data, the elevated value of $\text{NOER}^*_{-1.6}$ in the ischaemic core appeared to be consistent with that observed through LDA, as did the infarct growth ROI signal which was not significantly different from the contralateral tissue. However, the elevated signal level in oligaemic tissue that was observed in the Lorentzian difference spectra, was not observed in the model-fitted results, where the mean relative value was approximately unity. $\text{NOER}^*_{-1.6}$ did not describe the same pattern of a decreased ischaemic core signal that has been reported in other stroke studies [81,111]. One reason for this might be the relatively low B_1 power employed in this study, 0.55 μT, which is not optimal for observing saturation effects at -1.6 ppm. B_1 dependence studies suggest using a power of 1 μT at 9.4 T [80,117], and other studies of NOEs at -1.6 ppm have also used this power [81,118].

The relatively few sampling points in the vicinity of -1.6 ppm could have also contributed to the lack of differentiation of $\text{NOER}^*_{-1.6}$ in oligaemic tissue, where the Lorentzian difference spectra indicated that the peak becomes visibly more pronounced. In the animal dataset, one sampling point was located within the FWHM range of the

peak (−1.78 to −1.42 ppm), whereas studies that have detected a significant difference in pathological tissue (ischaemic core) have generally used 3 sampling points [80,81,98]. NOEs at −1.6 ppm are particularly vulnerable to under-fitting owing to their proximity to the water peak, and this may explain why such a peak has not been reported in lower-field clinical studies [81]. This means it is likely that there were not enough data to adequately fit for the multiple parameters used to describe subtle features of the sub-resonance at −1.6 ppm. The NOE peak at −1.6 ppm has been closely associated with NOE-mediated interactions between choline head groups of membrane phospholipids, which have a resonance frequency around −1.6 ppm, and water protons [118].

The elevated value of $NOER^{*}_{-2.4}$ in infarct growth tissue of the animal data appeared to correspond with the peak identified through LDA, and might suggest sensitivity to a secondary, delayed cell-death pathway precipitating infarct growth. However, it should be noted that there were large differences between the preclinical and clinical results in this respect, and that in the preclinical analyses there was a relatively large fluctuation in the contralateral tissue signal (also observable in the animal BMM maps). These observations most probably imply that it was difficult to extract an effect consistently in this study. Quantification of NOEs at −2.4 ppm might improve with more comprehensive sampling of the spectrum; in the present clinical data there was one sample point in the vicinity of −2.4 ppm. Redistributing the 32 sample points more uniformly upfield (e.g. by using an EDS scheme) is one way of achieving more even sampling of clinical data without prolonging acquisition time, but this would be at the expense of coarser sampling of APT effects.

9.5 Conclusion

The NOE sub-resonances at −1.6 ppm and −2.4 ppm identified and explored in the animal data suggest that there may be an association of NOEs with tissue outcome in

a manner that appears to be distinct from the broader NOE centred at −3.5 ppm. The results also partially highlight the limitations of the data used in this study. There is potential to explore the association of NOE sub-resonances with tissue outcome at a different saturation power and with more comprehensive spectral sampling, in order that their potential as imaging biomarkers in stroke can be better understood.

Chapter 10

Conclusion

The aim of this thesis was to develop analysis techniques for CEST MRI data in order to quantify metabolic signals associated tissue fate in patients with acute ischaemic stroke. This included the development of robust analysis techniques for use in a clinical setting, and the development of quantitative tools that exploit, and allow exploration of, the *in-vivo* complexity.

10.1 Summary

The development of robust analysis techniques commenced in Chapter 5, where quantification techniques from across the *in-vitro*, preclinical, oncological, and stroke literature were collated and compared for robustness. The aim was to establish the optimal way of quantifying CEST signals from existing techniques. The outcome of Chapter 5 was that improved robustness and pathological contrast of model-based analysis, BM model fitting in particular, was shown, indicating the potential clinical utility of model-based analysis for quantifying CEST signals. In Chapter 6 the BMM analysis technique was extended to 4 pools in light of the CEST literature which described NOEs and semisolid effects as being distinct phenomena. The 4-pool model corroborated that of 3 pools and also demonstrated an improved ability in isolating the APT signal. The reduction in contrast between infarct growth tissue and normal tissue represented a

trade-off between identifying tissue to target for treatment and biophysically more accurate modelling of CEST processes.

Chapter 7 turned more towards the challenge of improving quantification within the constraints of clinical data. The accuracy of the analysis techniques depends on two factors: correctness of the underlying modelling assumptions as far as how accurately they reflect the underlying biophysics, and secondly, the quality of the acquired data in terms of SNR, spectral resolution, and freedom from through-plane motion artefacts. The former is an effort to explain data in terms of what is understood of signal origins, whilst the latter leads to diminishing returns as the risk of over-fitting grows with model complexity. Chapter 7 developed an analysis technique for minimising PV effects which can contaminate signals of interest. This yielded a quantification technique that was more robust against partial volume effects. Whilst there was no overall improvement in pathological tissue contrast, the method of partial volume correction presented an improvement in repeatability and showed how quantification may be further improved within the constraints of clinical data.

Chapter 8 used 4-pool analysis to investigate NOEs and semisolid effects as distinct phenomena, and how they may be associated with tissue fate following ischaemic stroke. Analyses of NOEs from a clinical data perspective were offered and were corroborated by those conducted on the preclinical data, contributing to an ongoing discussion on the physical origins of NOEs and in particular providing answers as to the spectral symmetry or otherwise of semisolid effects, and the suggested pH dependence of NOEs. NOEs were enhanced in the ischaemic core, contrary to notion that the acidotic environment would denature proteins and result in a net decrease in NOEs. This alludes to the complex composition of the *in-vivo* environment and underscores the necessity of using quantitative imaging to isolate the effect being measured from competing phenomena. In this case, for example, using 4 pools to quantify NOEs appeared to provide better quantification than what seemed to be a contaminated 3-pool measure. Chapter 9 identified NOE sub-resonances where the preclinical results indicated an association

with tissue outcome that was distinct from the broader NOE. The results also partially highlighted the limitations of the data used in this study. There is potential to explore NOE sub-resonances further at a more optimal saturation power and with more comprehensive spectral sampling, in order that their potential as novel imaging biomarkers in stroke can be better-understood.

10.2 General considerations

10.2.1 Analysis of clinical CEST data

10.2.1.1 Quantifying CEST effects

The model-free techniques explored in this thesis have previously been shown to perform well with higher field data and under more controlled conditions, such as in a preclinical setting, where they exhibited good pathological contrast. When applied to the clinical data, the measures exhibited low repeatability compared to model-based techniques. The utility of model-free techniques in a clinical stroke imaging context therefore appears to be limited.

LDA is a semi-model-based approach that was used in this thesis when analysing the preclinical data. LDA was shown to be useful as an exploratory tool when looking at the finer structure of raw data. As a semi-model-based approach, it appeared to share some robustness with the fully model-based technique (BMM analysis), whilst sharing a lack of precision (an inability to account for overlapping peaks), and susceptibility to noise, with the model-free techniques. When analysing clinical data, the latter aspect appeared to dominate its performance, as it failed to exhibit consistent pathological contrast.

Not explored in this thesis were non-physical fully model-based techniques, such as multi-Lorentzian line fitting. Based on the comparisons made between different types of quantification techniques in this thesis, it would be expected that multi-Lorentzian line fitting, as a fully model-based technique, is more robust than model-free and LDA

approaches, but perhaps not as able to isolate CEST signals as well as the physical BM model, as the fitting is done purely in terms of isolated line shapes discernible in the data, rather than the interacting variables that collectively generate those line shapes.

Pragmatically, CEST imaging is more useful clinically if there is minimal contrast between grey matter and white matter. On this basis, in the context of clinical imaging of stroke, one of the advantages of a technique is that it minimises differences between grey matter and white matter. Model-free quantification techniques exhibited markedly different values in grey matter and white matter, and in this respect flat contrast is advantageous. The model-based measures worked well in this respect as not only did they show minimal tissue contrast, but also similar patterns of change in response to ischaemia.

The physical model-based approach, BMM analysis, was found to be advantageous for a number of reasons. BMM analysis was more repeatable between repeat scans and subjects, and provided quantitative imaging measures of CEST effects, making it more reproducible. However, quantitative values cannot necessarily be interpreted as absolute measures in their own right [100]. APTR* is a case-in-point, as the studies in this thesis revealed it to be less of a pH (or pH-weighted) measure than initially thought. The modulation of APTR* by CEST processes on the opposite side of the spectrum underlined how this quantitative measure is likely a reflection of a range of biological and physiological changes, and without further information it cannot be directly linked to a specific change in physiology.

10.2.1.2 Model complexity and clinical utility

Having established BM models as being useful for analysing clinical data, it can be helpful to view them in terms of their potential for use in routine clinical practice in stroke (patient-centred), versus their use for scientific purposes in providing insight into tissue physiology (disease-centred) [25]. In the former, the biological accuracy of the model is less important than its clinical validation if it is to be used in helping stratify

patients for treatment [25]. The measures obtained from such a model do not need to be intrinsically biologically meaningful, if they have been validated as reflecting tissue fate [25]. An example of a model that may have the potential to be used in this sense is the 3-pool BM model. The 3-pool model made less accurate assumptions with respect to the biology compared to the 4-pool model, and its measure of APT effects was also more ambiguous in terms of its links with physiological processes. However, the 3-pool model exhibited uniquely high contrast with respect to tissue that is sought for clinical intervention, and therefore may have more potential for use in clinical practice than the other models.

The level of model complexity at which quantification may have become more disease-centred and investigative, is upon the addition of a fourth pool. This better-reflected the underlying biophysical processes, providing insights into NOEs and their associations with tissue pathology that were otherwise obscured when observed through simpler models. The strength of this more accurate model was that it enabled better isolation of different CEST effects to be achieved, thus enabling more precise characterisation of signal patterns. This came at the cost of diminishing the contrast that highlighted tissue at risk, but was more exploratory as a tool.

Having considered quantification measures as being more well-suited for clinical practice versus as investigative tools, a categorical distinction cannot be made in the context of this thesis, for the following reasons. The PVc model was architecturally more complex than the 4-pool model, but the additional complexity was utilised to make quantification more clinically meaningful. The 4-pool model helped to explain the observations made using simpler 3-pool analysis. Also, the 4-pool model was used more readily to exploit, rather than to explain, underlying physiological complexity, in order to reveal novel modes of contrast that a simpler model could not. Further investigation of these new patterns, particularly their unexplored dynamic traits, could mean that the more complex models have utility in both roles.

10.2.1.3 Bias of modelling assumptions versus limitations of the data

The same general trends that were seen in the clinical data were also observed preclinically. This was despite the marked advantage that the preclinical data had in terms of data quality, such as a high B_0 field, higher sampling density and more brain volume, and the absence of motion artefact. The similarity in results also indicates that the small number of upfield data points in the clinical data was nevertheless sufficient for deriving representative measures of NOEs and semisolid effects. The BMM analysis techniques used in this thesis were able to consistently extract signals associated with different CEST mechanisms in MR imaging of human stroke. This highlights their utility as quantitative tools for investigating the disease.

A limiting factor in terms of measuring CEST effects was found to primarily be the modelling assumptions made, rather than limitations of the data. An example of this is that the 3-pool measure of NOEs in fact masked NOEs behind dominant semisolid effects, whereas a simple refinement of modelling assumptions was able to reflect the presence of NOEs in the clinical data much more clearly, and bring to bear their distinct mode of contrast. The distinction was more subtle when quantifying APT effects, as both 3- and 4-pool analysis reflected the same gross features of the data, but had more subtle variations between tissue fates. It is therefore important to interpret the results of BMM analysis in the context of the assumptions made. The bias that modelling assumptions imparted to the results was in some cases strong, as in the case of NOEs being masked, or subtle yet important, as in the case of observing infarct growth contrast. In as far as limitations of the data, they became more apparent in the investigation of NOE sub-resonances where it was difficult to extract an effect consistently. This may have been attributable to both the sub-optimal B_1 power that was used for analysing those resonances, and a lack of acquisitions near the relevant frequency offsets.

10.2.1.4 Investigation of NOEs

This thesis commenced with the study of APT effects in clinical data, whereat NOEs came under consideration when attempting to better-quantify APTR*. This later allowed NOEs to be explored as an effect in their own right, where it was first established that the 4-pool metric may be a more accurate reflection of changes in NOEs *in-vivo* compared the 3-pool approximation, providing information on tissue outcome that was otherwise unobservable. Thereupon, it was observed that: (i) NOEs appeared to be predominantly associated with white matter; (ii) that they were independent of pathological ROI in grey matter; and (iii) that they were elevated in the ischaemic core. The association of NOEs with tissue fate motivated their observation in a preclinical setting, in which dynamic changes in the early hours after stroke were apparent, and the elevated ischaemic core signal, first observed in the clinical data, was corroborated. NOEs were finally analysed in realistic phantoms to permit more controlled exploration of their pH dependence, where a positive association with pH, contrary to that expected, was observed. The pattern of NOEs in pathological tissue was well-described using physical model-based quantification, but could not be fully explained in terms of the current understanding of the biophysical mechanisms. The results provide motivation for exploring NOEs using serial imaging, and for analysing their association with regions of the brain remote from the DWI lesion.

10.2.2 Technical considerations

10.2.2.1 Statistical testing

The statistical testing employed in this thesis applied a relatively conservative correction to the critical level, the Bonferroni adjustment, in cases where multiple comparisons were being made [156]. This increased the likelihood of type II errors, thus important differences between pathological ROIs might have been deemed statistically non-significant [156]. The deflation of α_{crit} might not have been a significant problem

for the analyses in this thesis, however, as in most cases a non-significant ANOVA result ruled out further comparisons, and in cases where there was significant variation between groups, at least one significant pattern was detected in *post-hoc* testing. There were a small number of instances (Figs. 6.3a and 9.3a) where a group comparison suggested significant differences between pathological ROIs, whilst *post-hoc* testing did not identify any significant pairs.

Chapters 6–8 each compared a simpler model versus a more complex one. The more complex models achieved statistical significance a greater number of times when assessing differences between tissue outcomes, which could be seen as a relative strength of using those measures. This has helped to highlight differences between quantification measures that are related, but which are derived from different BM models.

10.2.2.2 Study size limitations

The broader research context to this thesis is the improvement of individual patient outcomes in stroke by identifying patients who will benefit from intervention. At the patient level CEST data do not clearly discriminate between tissue fate [37]. In this tissue-level study, analyses were performed by pooling voxels across 12 patients. The stroke population is physiologically very heterogeneous and the small sample size means that the pooled results in this study, an average over all patients, makes the results susceptible to bias and might not be reflective of the wider stroke population. The influence of bias can be reduced by analysing a larger dataset. Validating the results of this thesis in an independent stroke cohort would test repeatability of analyses techniques against the presence of such bias.

10.3 Areas of future work

10.3.1 Serial trends

The analyses represented one snapshot in time, the presentation scan, and the main trends observed were an elevated NOE signal in the ischaemic core and oligaemic tissue, a decreased infarct growth signal when quantifying semisolid effects, and, when using 3-pool analysis, a graduated decrease in APT effects in accordance with tissue outcome. Recent serial analyses of 3-pool data have demonstrated distinct APT and NOE profiles for each tissue outcome [157]. This is a promising development for post-acute management of stroke, as injury initially occurs over minutes to hours and is followed by secondary injury from hours to days, followed by subsequent complications. The serial profiles of CEST signals may therefore be mirroring different compensatory mechanisms of the brain, such as alkalosis which is associated with delayed cellular injury. In this respect CEST signals could potentially be used to monitor and inform treatment decisions for patients in the post-acute phase. The serial trends of CEST signals warrant investigation using the quantification measures advanced in this thesis that afford separation of competing effects.

10.3.2 Whole-brain CEST imaging

The CEST sequence used in this study excited tissue in a single imaging plane which was selected by a clinician to correspond with the plane of the diffusion lesion. This allowed analysis of the ischaemic core tissue and of tissue at the interface with penumbral or normal regions. However, inferences could only be made within the tissue region highly local to the lesion. A multi-slice (3D) CEST sequence providing interpretable whole-brain acquisitions would allow extensive investigation of tissue remote from the ischaemic core. It would also improve image registration with the 3D modalities routinely used in clinical practice, and would improve the ability to correct for motion artefacts (particularly through-plane) [37,87]. A pulsed CEST scheme capable of ac-

quiring a whole 3D brain volume has been demonstrated by Jones et al. [87]. However the acquisition time of this scheme was not practical for use with stroke patients, at 14 minutes 24 seconds (11 seconds per frequency offset) compared to the sub-three-minutes time (2 minutes 45 seconds) attainable with single-slice CEST. Long acquisition times are unusable with stroke patients in particular, who due to their physiological condition, are unlikely to remain still for more than three to five minutes during a scan. The development and validation of whole-brain CEST imaging is a necessary prerequisite for establishing CEST in the clinical sphere as a routine imaging tool for acute stroke [37,87].

10.3.3 NOE sub-resonances

The NOE peak at -1.6 ppm has been reported to exhibit a significant decrease immediately after stroke [81,111]. Quantifying this effect in addition to those already present in the 4-pool model would necessitate adding a fifth pool. Whilst using 4 pools is still very much an approximation to the many processes going on in the spectrum [87], adding further pools would increase the risk of over-fitting, particularly because this resonance is close to the water peak and Chapter 9 highlighted the limitations of adding further pools. Further analysis is therefore hard to justify on the present clinical data considering field strength, number of samples, patient motion, and the sub-optimal B_1 power for detecting effects at -1.6 ppm. There is scope to explore NOE sub-resonances at a higher B_1, but at the expense of diminishing the signal from NOEs at -3.5 ppm which are maximised at a lower B_1. Optimising the distribution of sampling points would ameliorate the risk of over-fitting without prolonging acquisition time, achieving a better trade-off when these effects are being explored within clinical imaging constraints.

10.3.4 Semisolid effects

In this study the semisolid effects pool was modelled using a classic Lorentzian line shape. This is more accurate for mobile populations which can be described using a single T_2. The semisolid pool is composed of immobilised proteins and large lipids that are restricted in motion, for which this assumption might not be a good approximation, and instead super-Lorentzian and Gaussian line shapes have been found to provide a better fit for tissue [91,142,152]. The approximation has little effect on the quantification of NOEs and APT effects as they are evaluated within a small frequency range, over which the differences between a Lorentzian line shape and a more accurate super-Lorentzian line shape are negligible [32]. It does, however, introduce uncertainty when quantifying semisolid effects as the differences between the two line shapes are more pronounced at large offset frequencies [32]. The approximation appears to be valid here as the results obtained were consistent with the literature in describing semisolid effects as being significantly elevated in white matter, and being decreased in the ischaemic core. Semisolid effects were also decreased in infarct growth tissue. Further exploration of these patterns could attempt more precise extraction using a model that incorporates a super-Lorentzian line shape.

10.3.5 Correction for water relaxation

Representative BMM patient maps were often highly heterogeneous, which reduced pathological contrast. This could be due to poor individual fitting of parameters, such as T_1, whilst fitting well for the set of parameters that affect the z-spectrum in similar ways (T_1 and T_2 combined), to give an accurate overall shape [64]. The water pool mediates all CEST exchanges, and a larger water T_1 scales CEST effects by affording more time for labelled states to accumulate in the water pool [42,84], thus local variations in T_1 directly modulate the size of the CEST signals. The relative measures were less prone to this sort of variation as signal values were normalised to the contralateral mean, which reduced dependence on local T_1. Incorporating quantitative T_1 maps in

the model fitting process, such as via prior maps, would help to correct for this confounding effect. Quantitative T_1 maps have been used for correction in the study in ref. [84], where they led to a reduction in the dependence of the APT signal on water R_1. The T_1-corrected NOE measure remained significantly correlated with water R_1, but also exhibited significant tumour contrast which was improved compared to the non-corrected equivalent.

10.3.6 Exchange-relayed NOEs

There is scope to improve the present model of NOEs at −3.5 ppm without adding many new parameters. Existing model-based approaches for quantifying NOEs describe the NOE pool as one in chemical exchange with bulk water. This yields a good fit to clinical data ($R^2 > 98.8\%$) [63], but makes a simplistic assumption about the underlying exchange mechanism that gives rise to the NOE signal. This is in contrast to the exchange-relayed mechanism of NOEs which is supported by the literature [57,74]. Implementing an exchange-relayed model could be done by re-arranging the structure of the BM model in Fig. 7.2 such that the NOE pool is concatenated to the amide pool. This does not increase model complexity, as no new parameters are introduced, and is also a more accurate representation of the exchange-relayed NOE pathway.

10.4 Closing remarks

Improved quantification techniques were demonstrated which were sufficiently robust to be used on clinical data, but also provided insight into the different biological processes at work in ischaemic tissue in the early stages of the disease. The complex array of competing processes in pathological tissue has underscored a need for analysis tools for investigating these effects in the context of human imaging. The trends herein identified at the tissue level support the use of quantitative CEST MRI analysis as a clinical metabolic imaging tool in the investigation of acute ischaemic stroke.

Appendix A

Examples of SE-EPI CEST volumes used in this thesis

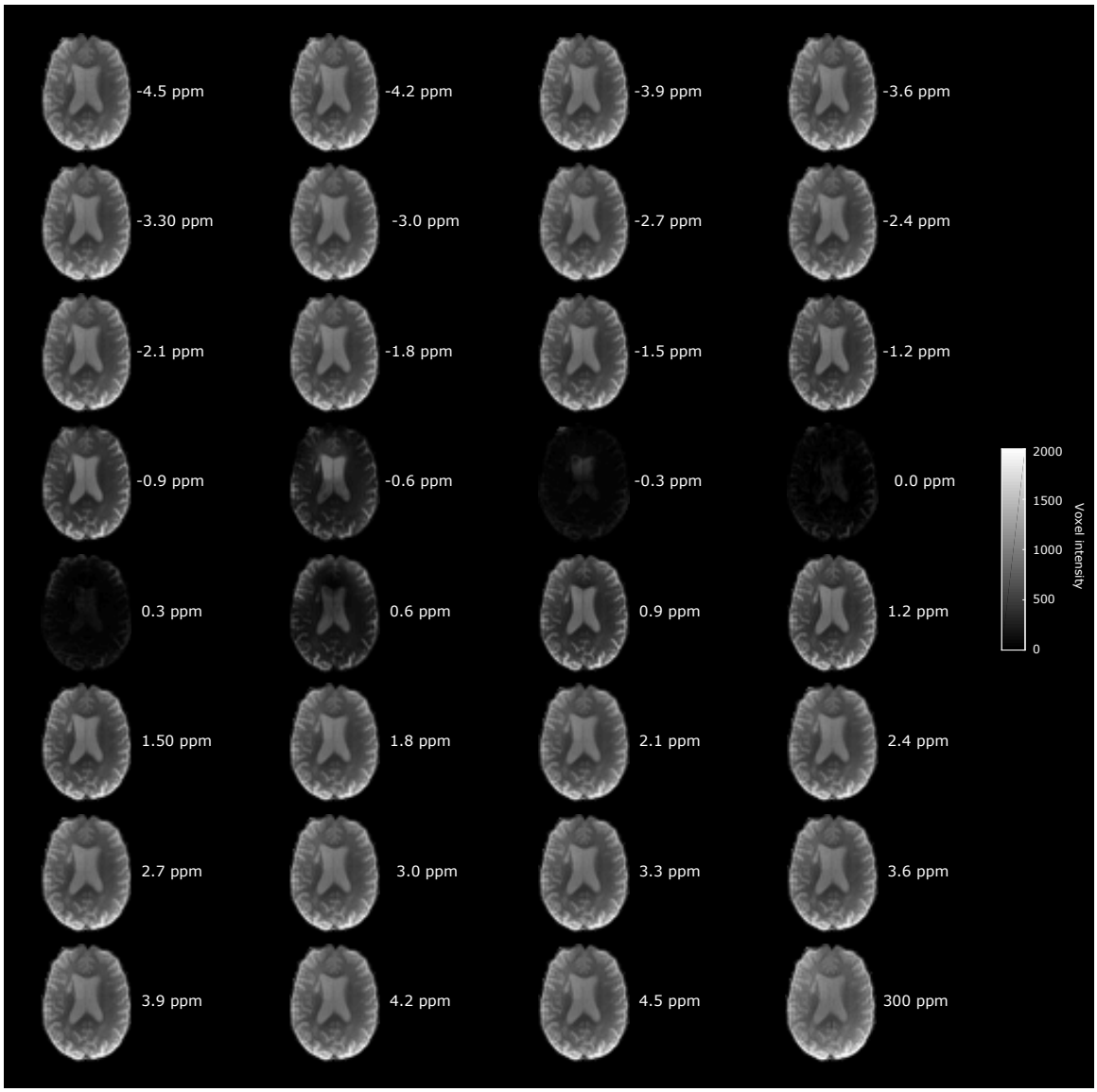

Figure A.1: Example of a patient EPI CEST volume obtained using the EDS scheme, where saturation frequencies are uniformly distributed between ±4.5 ppm (used for patients 1–4). Shown is that of patient 1 after motion correction and brain extraction.

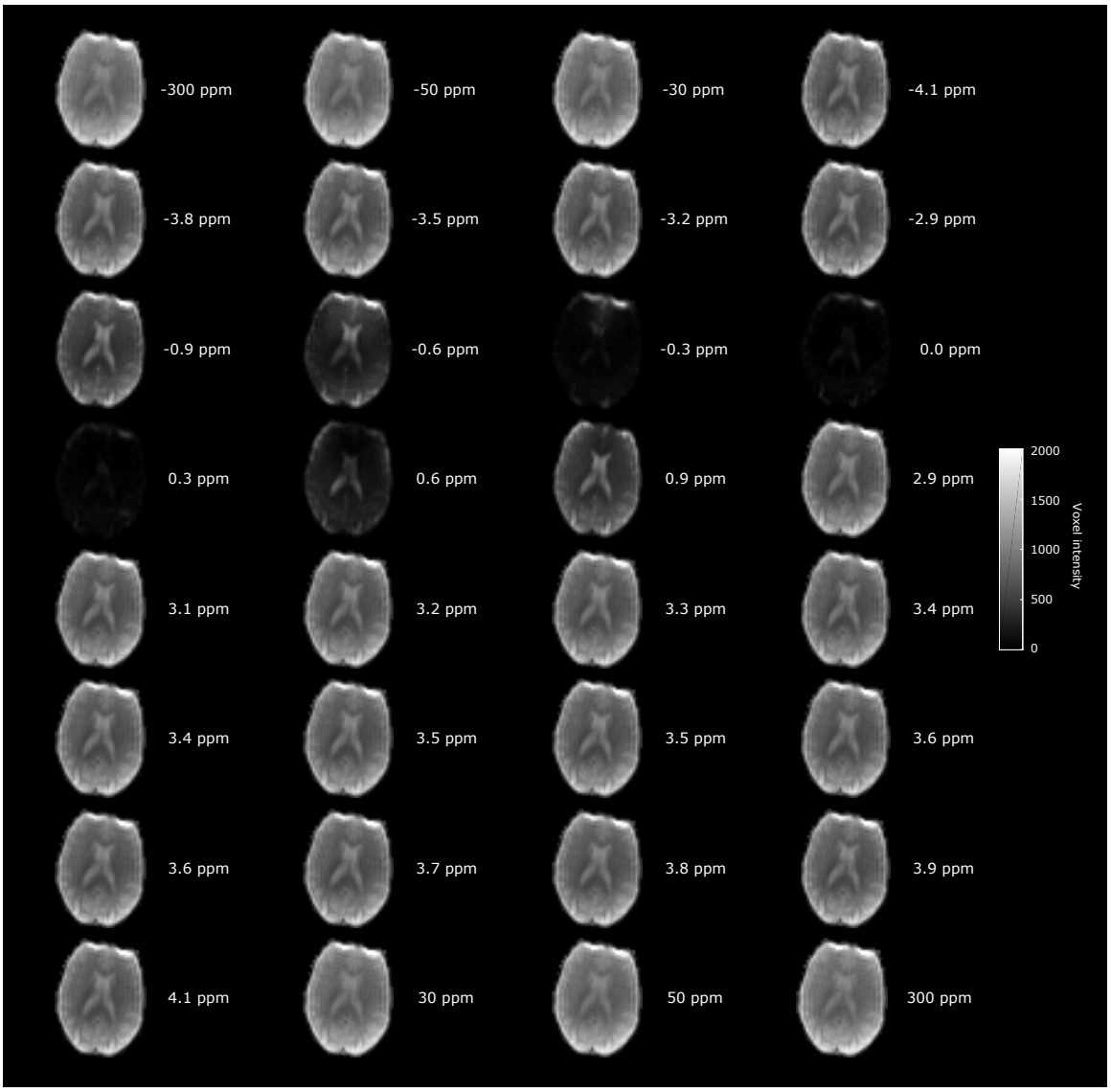

Figure A.2: Example of a patient EPI CEST volume obtained using the semi-OSS scheme (used for patients 5–12). Shown is that of patient 12 after motion correction and brain extraction. There is a higher density of sampling points near the amide resonance frequency, and the offsets at 3.4, 3.5, and 3.6 ppm have been acquired twice in order to increase the SNR at these points during post-processing.

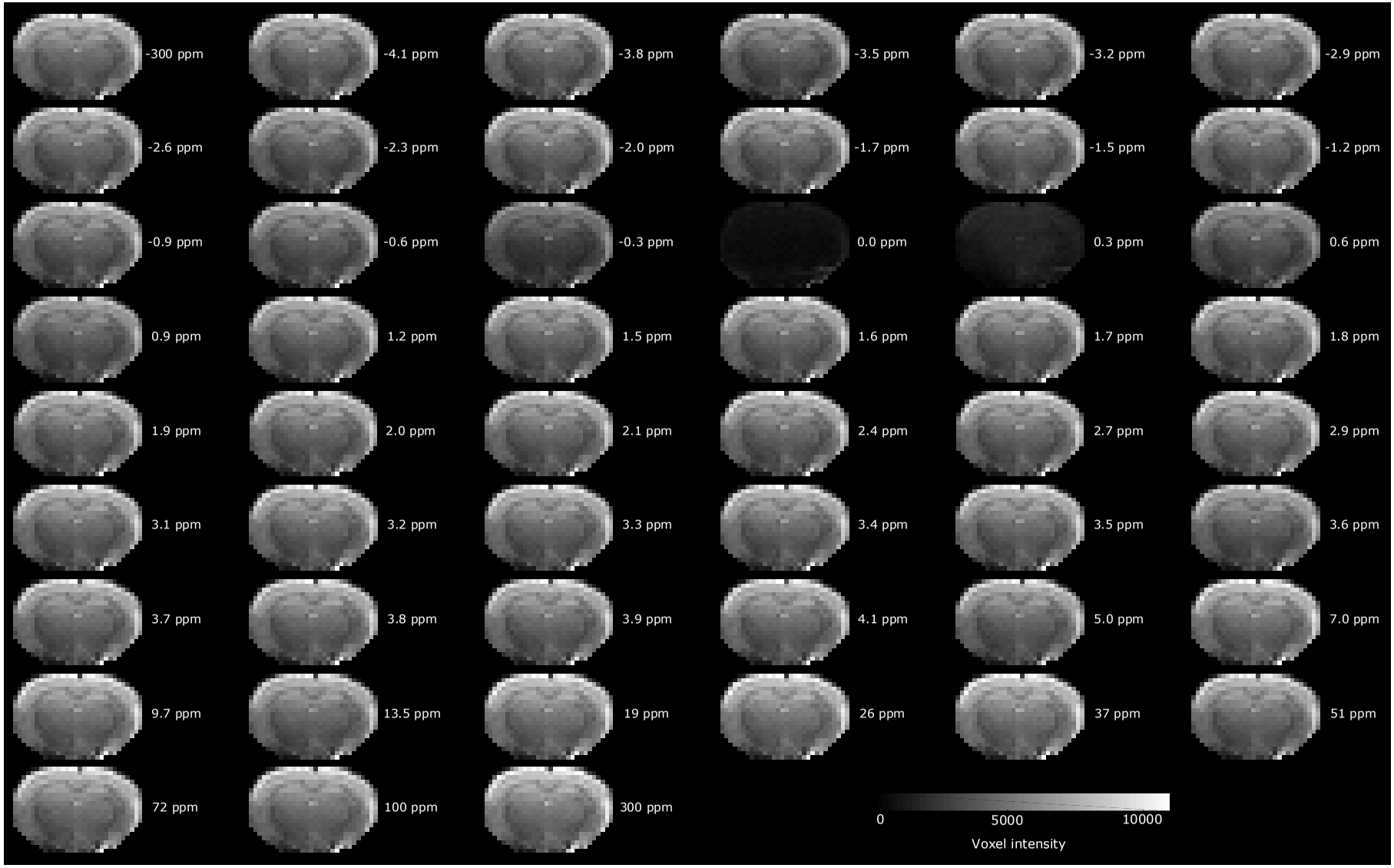

Figure A.3: Example of an animal EPI CEST volume (animal 1, slice 5 of 10) after the brain has been masked in. There is a visibly sharper transition across water resonance compared to a patient CEST dataset, owing to the higher field used in the animal study.

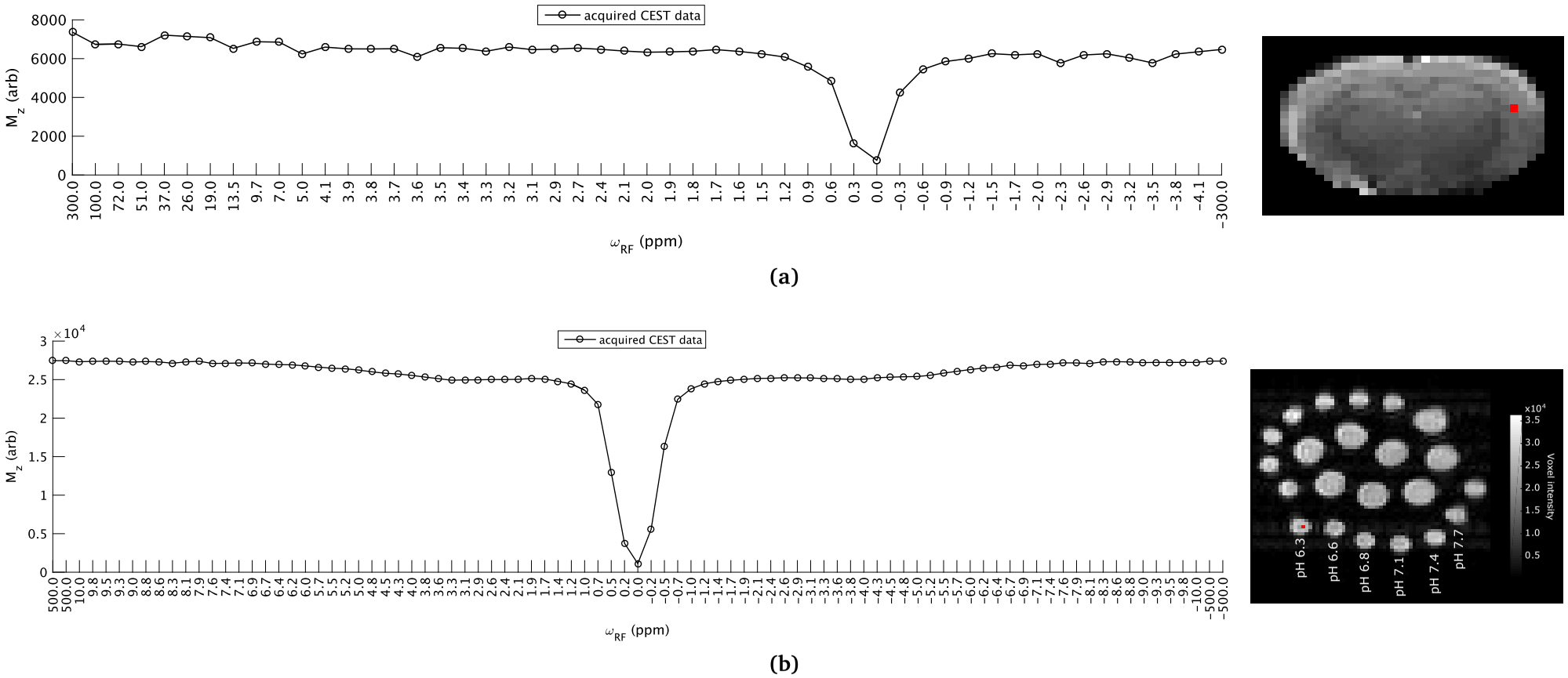

Figure A.4: **(a)** Example of an acquired whole z-spectrum shown for a single voxel (red square on the unsaturated EPI acquisition) from animal 1 (shown is slice 5 of 10). **(b)** pH phantoms unsaturated EPI acquisition, showing the layout of the pH phantoms (labelled) used in this thesis. Example of an acquired whole z-spectrum shown for a single voxel (red square on the unsaturated EPI acquisition) from the pH 6.3 phantom.

Appendix B

Bloch-McConnell models fitted to CEST data

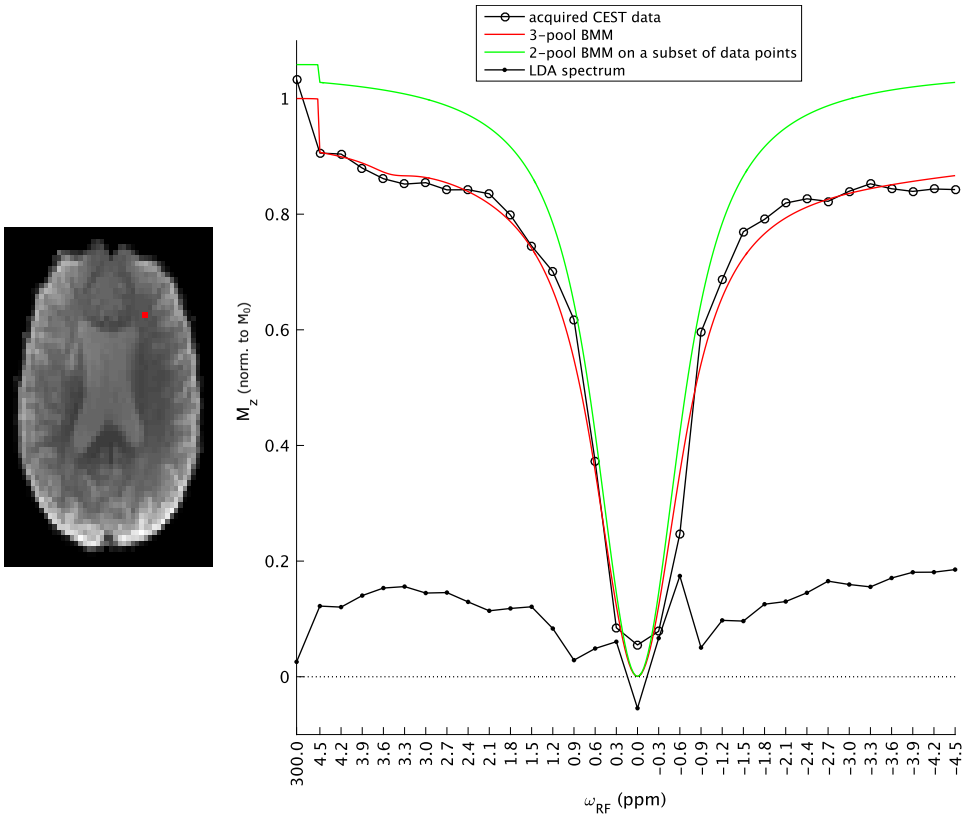

Figure B.1: Results of 3-pool BM model fitting and paLDA of patient data, shown for a single voxel (red square) from patient 1. The 3-pool BM model (red trace) comprised a water pool (0 ppm), an APT pool (3.5 ppm), and an asymmetric semisolid effects pool (−2.41 ppm). The 2-pool BMM (green trace), which comprised a water pool and a semisolid effects pool, was only fitted to data points within ±0.9 ppm and beyond ±30 ppm. The LDA spectrum (black dotted trace) was then obtained by subtracting the acquired CEST data from the 2-pool fit.

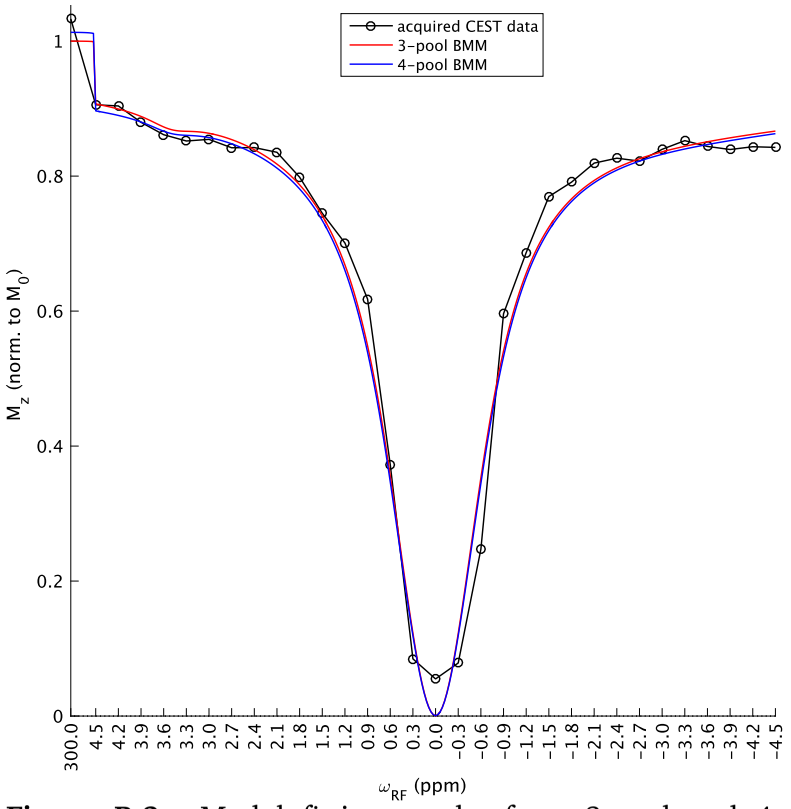

Figure B.2: Model fitting results from 3-pool and 4-pool BM model fitting of patient data, shown for a single voxel (red square) from patient 1. The 3-pool BM model (red trace) comprised a water pool (0 ppm), an APT pool (3.5 ppm), and an asymmetric semisolid effects pool (−2.41 ppm). The 4-pool BMM (blue trace) comprised a water pool (0 ppm), an APT pool (3.5 ppm), a symmetric semisolid effects pool (0 ppm), and an NOE pool (−3.5 ppm).

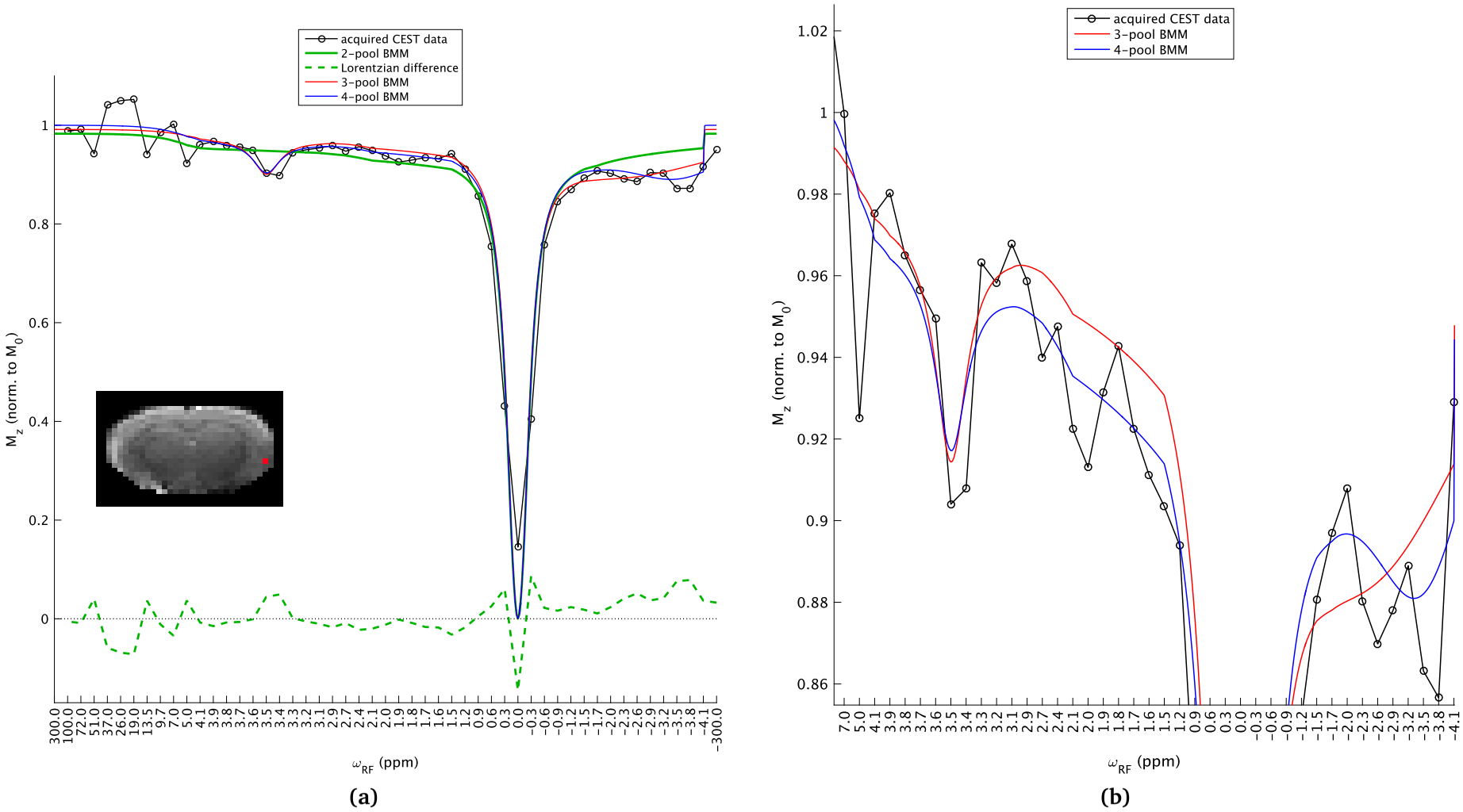

Figure B.3: Results from 2-pool (used in Chapter 9), 3-pool and 4-pool BM model fitting of animal data, shown for a single voxel (red square) from animal 1. The whole z-spectrum is shown in **(a)**, and the data points within ±10 ppm are shown in **(b)**. The 2-pool BMM (green trace) comprised a water pool and a semisolid effects pool, and was only fitted to data points within 1 ppm and beyond ±50 ppm. The LDA spectrum (green dashed trace) was then obtained by subtracting the acquired CEST data from the 2-pool fit. The 3-pool BM model (red trace) comprised a water pool (0 ppm), an APT pool (3.5 ppm), and an asymmetric semisolid effects pool (−2.41 ppm). The 4-pool BM model (blue trace) comprised a water pool (0 ppm), an APT pool (3.5 ppm), a symmetric semisolid effects pool (0 ppm), and an NOE pool (−3.5 ppm).

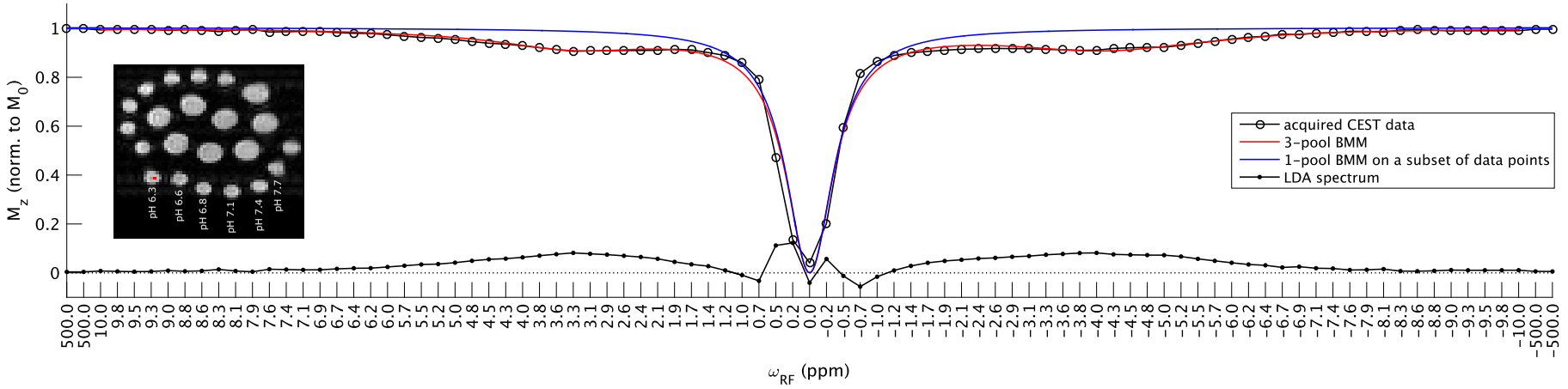

(a)

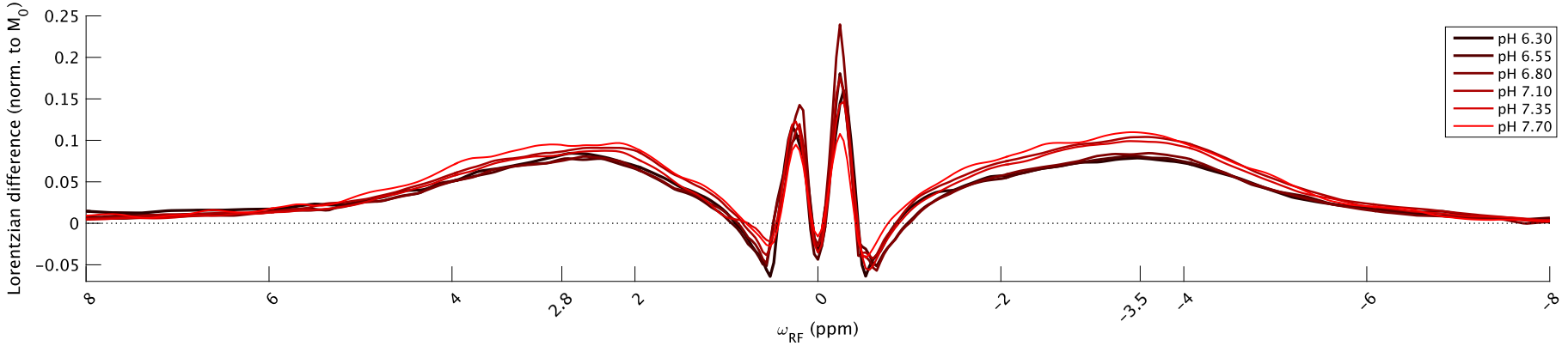

(b)

Figure B.4: Results from 3-pool BM model fitting and LDA of pH phantoms. **(a)** Whole z-spectrum shown for a single voxel from the pH 6.3 phantom. The 3-pool model (red trace) comprised a water pool, an amine pool (2.8 ppm), and an NOE pool (−3.5 ppm). The 1-pool BMM was fitted to data points within ±1 ppm in order to extract a water line shape from which the data were then subtracted (dotted black trace). **(b)** Lorentzian difference spectra averaged over each pH phantom.

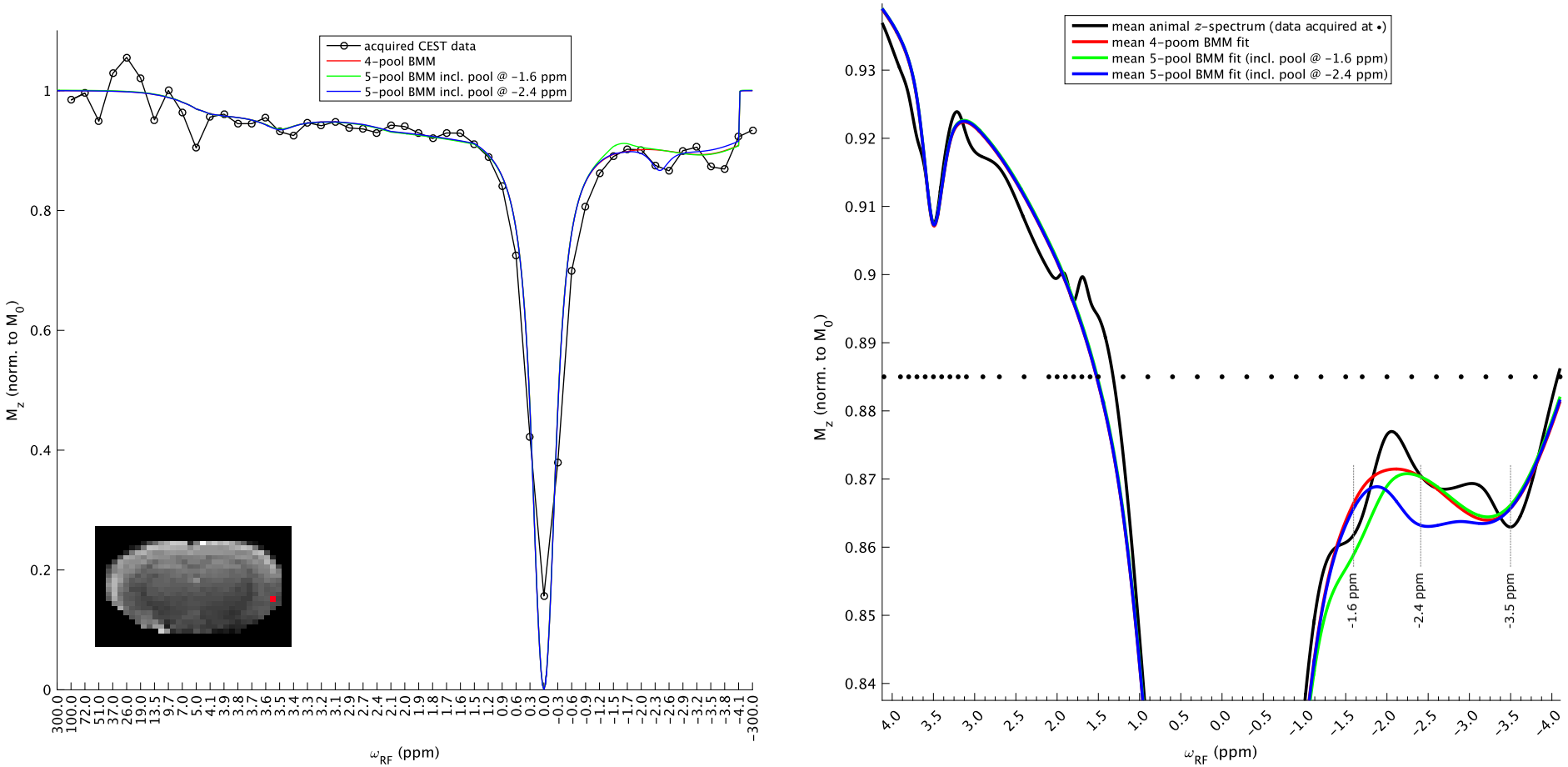

Figure B.5: Results from 4-pool and 5-pool BM model fitting of animal data, shown for a single voxel in **(a)**, and averaged over all animals in **(b)**. **(a)** Whole z-spectrum fit shown for a single voxel from animal 1. **(b)** Mean animal z-spectrum shown for the range ±10 ppm. The 4-pool BM model (red trace) comprised a water pool (0 ppm), an APT pool (3.5 ppm), a symmetric semisolid effects pool (0 ppm), and an NOE pool (−3.5 ppm). The first 5-pool model (green trace) included an additional pool at −1.6 ppm to represent the NOE sub-resonance observed at that frequency. The second 5-pool model (blue trace) instead included a pool at −2.4 ppm to represent the NOE sub-resonance observed at that frequency. Notice how in **(b)** the 5-pool models describe these respective features of the raw data which the 4-pool model cannot, whilst reasonably matching the 4-pool model in terms of the main NOE at −3.5 ppm.

References

[1] R. Perna and J. Temple, "Rehabilitation Outcomes: Ischemic versus Hemorrhagic Strokes," *Behav Neurol*, vol. 2015, p. 891651, 2015.

[2] P. M. Bath and K. R. Lees, "Acute stroke," *West. J. Med.*, vol. 173, no. 3, pp. 209–212, Sep 2000.

[3] P. Bhatnagar, K. Wickramasinghe, J. Williams, M. Rayner, and N. Townsend, "The epidemiology of cardiovascular disease in the UK 2014," *Heart*, vol. 101, no. 15, pp. 1182–1189, Aug 2015.

[4] Y. Zhang, A. M. Chapman, M. Plested, D. Jackson, and F. Purroy, "The Incidence, Prevalence, and Mortality of Stroke in France, Germany, Italy, Spain, the UK, and the US: A Literature Review," *Stroke Res Treat*, vol. 2012, p. 436125, 2012.

[5] P. M. Rothwell, A. J. Coull, M. F. Giles, S. C. Howard, L. E. Silver, L. M. Bull, S. A. Gutnikov, P. Edwards, D. Mant, C. M. Sackley, A. Farmer, P. A. Sandercock, M. S. Dennis, C. P. Warlow, J. M. Bamford, and P. Anslow, "Change in stroke incidence, mortality, case-fatality, severity, and risk factors in Oxfordshire, UK from 1981 to 2004 (Oxford Vascular Study)," *Lancet*, vol. 363, no. 9425, pp. 1925–1933, Jun 2004.

[6] B. J. Lutz, M. E. Young, K. J. Cox, C. Martz, and K. R. Creasy, "The crisis of stroke: experiences of patients and their family caregivers," *Top Stroke Rehabil*, vol. 18, no. 6, pp. 786–797, 2011.

[7] O. Saka, A. McGuire, and C. Wolfe, "Cost of stroke in the united kingdom," *Age and Ageing*, vol. 38, no. 1, pp. 27–32, 2009.

[8] K. A. Hossmann, "Pathophysiological basis of translational stroke research," *Folia Neuropathol*, vol. 47, no. 3, pp. 213–227, 2009.

[9] P. Deb, S. Sharma, and K. M. Hassan, "Pathophysiologic mechanisms of acute ischemic stroke: An overview with emphasis on therapeutic significance beyond thrombolysis," *Pathophysiology*, vol. 17, no. 3, pp. 197–218, 2018.

[10] Y. K. Tee, "Quantitative measurement of pH in stroke using chemical exchange saturation transfer magnetic resonance imaging," Ph.D. dissertation, Department of Engineering Science, University of Oxford, May 2013.

[11] N. T. Cheng and A. S. Kim, "Intravenous Thrombolysis for Acute Ischemic Stroke Within 3 Hours Versus Between 3 and 4.5 Hours of Symptom Onset," *Neurohospitalist*, vol. 5, no. 3, pp. 101–109, Jul 2015.

[12] J. M. Roth, "Recombinant tissue plasminogen activator for the treatment of acute ischemic stroke," *Proc Bayl Univ Med Cent*, vol. 24, no. 3, pp. 257–259, Jul 2011.

[13] T. Robinson, Z. Zaheer, and A. K. Mistri, "Thrombolysis in acute ischaemic stroke: an update," *Ther Adv Chronic Dis*, vol. 2, no. 2, pp. 119–131, Mar 2011.

[14] J. Zhou, J. F. Payen, D. A. Wilson, R. J. Traystman, and P. C. van Zijl, "Using the amide proton signals of intracellular proteins and peptides to detect pH effects in MRI," *Nat. Med.*, vol. 9, no. 8, pp. 1085–1090, Aug 2003.

[15] P. Z. Sun, J. Zhou, W. Sun, J. Huang, and P. C. van Zijl, "Detection of the ischemic penumbra using pH-weighted MRI," *J. Cereb. Blood Flow Metab.*, vol. 27, no. 6, pp. 1129–1136, Jun 2007.

[16] J. Astrup, B. K. Siesjo, and L. Symon, "Thresholds in cerebral ischemia - the ischemic penumbra," *Stroke*, vol. 12, no. 6, pp. 723–725, 1981.

[17] C. L. Paul, A. Ryan, S. Rose, J. R. Attia, E. Kerr, C. Koller, and C. R. Levi, "How can we improve stroke thrombolysis rates? A review of health system factors and approaches associated with thrombolysis administration rates in acute stroke care," *Implement Sci*, vol. 11, p. 51, Apr 2016.

[18] D. J. Clarke and A. Forster, "Improving post-stroke recovery: the role of the multidisciplinary health care team," *J Multidiscip Healthc*, vol. 8, pp. 433–442, 2015.

[19] J. L. Saver, "Time is brain-quantified," *Stroke*, vol. 37, no. 1, pp. 263–266, 2006.

[20] F. Chen and Y. C. Ni, "Magnetic resonance diffusion-perfusion mismatch in acute ischemic stroke: An update," *World J Radiol*, vol. 4, no. 3, pp. 63–74, Mar 2012.

[21] C. Rosso, A. Drier, D. Lacroix, G. Mutlu, C. Pires, S. Lehericy, Y. Samson, and D. Dormont, "Diffusion-weighted MRI in acute stroke within the first 6 hours: 1.5 or 3.0 Tesla?" *Neurology*, vol. 74, no. 24, pp. 1946–1953, Jun 2010.

[22] K. van Everdingen, J. van der Grond, L. Kappelle, L. Ramos, and W. Mali, "Diffusion-weighted magnetic resonance imaging in acute stroke," *Stroke*, vol. 29, no. 9, pp. 1783–1790, 1998.

[23] E. Reid, D. Graham, M. R. Lopez-Gonzalez, W. M. Holmes, I. M. Macrae, and C. McCabe, "Penumbra detection using PWI/DWI mismatch MRI in a rat stroke model with and without comorbidity: comparison of methods," *J. Cereb. Blood Flow Metab.*, vol. 32, no. 9, pp. 1765–1777, Sep 2012.

[24] P. Orlowski, M. Chappell, C. S. Park, V. Grau, and S. Payne, "Modelling of pH dynamics in brain cells after stroke," *Interface Focus*, vol. 1, no. 3, pp. 408–416, Jun 2011.

[25] G. W. J. Harston, "Investigating the pathophysiology of acute ischaemic stroke using magnetic resonance imaging," Ph.D. dissertation, University of Oxford, Oxford, UK, 2015.

[26] P. L. Croal, "Quantification of the BOLD response via blood gas modulations," Ph.D. dissertation, University of Nottingham, 2014. [Online]. Available: http://eprints.nottingham.ac.uk/14382/1/Merged_thesis_HARDCOPY.pdf

[27] E. E. Kim and E. F. Jackson, *Molecular Imaging in Oncology: PET, MRI, and MRS*. Berlin, Germany: Springer-Verlag, 1999.

[28] D. E. Saunders, "MR spectroscopy in stroke," *Br. Med. Bull.*, vol. 56, no. 2, pp. 334–345, 2000.

[29] K. M. Ward, A. H. Aletras, and R. S. Balaban, "A new class of contrast agents for MRI based on proton chemical exchange dependent saturation transfer (CEST)," *J. Magn. Reson.*, vol. 143, no. 1, pp. 79–87, Mar 2000.

[30] P. C. van Zijl and N. N. Yadav, "Chemical exchange saturation transfer (CEST): what is in a name and what isn't?" *Magn Reson Med*, vol. 65, no. 4, pp. 927–948, Apr 2011.

[31] J. Zhou, H. Zhu, M. Lim, L. Blair, A. Quinones-Hinojosa, S. A. Messina, C. G. Eberhart, M. G. Pomper, J. Laterra, P. B. Barker, P. C. van Zijl, and J. O. Blakeley, "Three-dimensional amide proton transfer MR imaging of gliomas: Initial experience and comparison with gadolinium enhancement," *J Magn Reson Imaging*, vol. 38, no. 5, pp. 1119–1128, Nov 2013.

[32] D. Liu, J. Zhou, R. Xue, Z. Zuo, J. An, and D. J. Wang, "Quantitative characterization of nuclear overhauser enhancement and amide proton transfer effects in the human brain at 7 Tesla," *Magn Reson Med*, vol. 70, no. 4, pp. 1070–1081, Oct 2013.

[33] C. K. Jones, M. J. Schlosser, P. C. van Zijl, M. G. Pomper, X. Golay, and J. Zhou, "Amide proton transfer imaging of human brain tumors at 3T," *Magn Reson Med*, vol. 56, no. 3, pp. 585–592, Sep 2006.

[34] H. Li, Z. Zu, M. Zaiss, I. S. Khan, R. J. Singer, D. F. Gochberg, P. Bachert, J. C. Gore, and J. Xu, "Imaging of amide proton transfer and nuclear Overhauser enhancement in ischemic stroke with corrections for competing effects," *NMR Biomed*, vol. 28, no. 2, pp. 200–209, Feb 2015.

[35] E. Vinogradov, A. D. Sherry, and R. E. Lenkinski, "CEST: from basic principles to applications, challenges and opportunities," *J. Magn. Reson.*, vol. 229, pp. 155–172, Apr 2013.

[36] Y. K. Tee, G. W. Harston, N. Blockley, T. W. Okell, J. Levman, F. Sheerin, M. Cellerini, P. Jezzard, J. Kennedy, S. J. Payne, and M. A. Chappell, "Comparing different analysis methods for quantifying the MRI amide proton transfer (APT) effect in hyperacute stroke patients," *NMR Biomed*, vol. 27, no. 9, pp. 1019–1029, Sep 2014.

[37] G. W. J. Harston, Y. K. Tee, N. Blockley, T. W. Okell, S. Thandeswaran, G. Shaya, F. Sheerin, M. Cellerini, S. Payne, P. Jezzard, M. Chappell, and J. Kennedy, "Identifying the ischaemic penumbra using pH-weighted magnetic resonance imaging," *Brain*, vol. 138, no. Pt 1, pp. 36–42, Jan 2015.

[38] G. W. J. Harston, Y. K. Tee, N. Blockley, Y. Msayib, F. Sheerin, P. Mathieson, I. Reckless, K. Shah, U. Schulz, S. Payne, P. Jezzard, M. Chappell, and J. Kennedy, "Novel imaging of protein integrity to better define ischemic injury after stroke," *Stroke*, vol. 47, no. 63, 2016.

[39] A. Berger, "Magnetic resonance imaging," *BMJ*, vol. 324, no. 7328, p. 35, Jan 2002.

[40] J. D. Roberts, *ABCs of Fourier Transform Nuclear Magnetic Resonance*. University Science Books, Sausalito CA, 2000.

[41] M. H. Levitt, *Spin Dynamics: Basics of Nuclear Magnetic Resonance*. Wiley, 2013.

[42] M. Zaiss and P. Bachert, "Chemical exchange saturation transfer (CEST) and MR Z-spectroscopy in vivo: a review of theoretical approaches and methods," *Phys Med Biol*, vol. 58, no. 22, pp. R221–269, Nov 2013.

[43] R. Reimer, P. M. Parizel, J. F. M. Meaney, and F. A. Stichnoth, Eds., *Clinical MR Imaging: A Practical Approach*, 3rd ed. Springer Science & Business Media, Berlin, Germany, 2010.

[44] D. W. McRobbie, E. A. Moore, and M. J. Graves, Eds., *MRI from Picture to Proton*, 3rd ed. Cambridge University Press, Cambridge, UK, 2017.

[45] J. P. Wansapura, S. K. Holland, R. S. Dunn, and W. S. Ball, "NMR relaxation times in the human brain at 3.0 Tesla," *J Magn Reson Imaging*, vol. 9, no. 4, pp. 531–538, Apr 1999.

[46] P. A. Boulby and F. J. Rugg-Gunn, *T2: The Transverse Relaxation Time*. John Wiley and Sons, Ltd, 2004.

[47] E. D. Bigler, *Neuroimaging I: Basic Science*. Springer Science & Business Media, Berlin, Germany, 1996.

[48] M. A. Bernstein, K. F. King, and X. J. Zhou, *Handbook of MRI Pulse Sequences*. Elsevier Academic Press, 2004.

[49] M. A. Brown and R. C. Semelka, *MRI: Basic Principles and Applications*, 4th ed. John Wiley & Sons, Inc., 2011.

[50] D. W. McRobbie, E. A. Moore, M. J. Graves, and M. R. Prince, *MRI: From Picture to Proton*, 2nd ed. Cambridge University Press, Cambridge, UK, 2006.

[51] S. Heiland, "From A as in Aliasing to Z as in Zipper: Artifacts in MRI," *Clinical Neuroradiology*, vol. 18, no. 1, pp. 25–36, Mar 2008.

[52] R. N. Scheidegger, "Methods for chemical exchange saturation transfer magnetic resonance imaging," Ph.D. dissertation, Harvard-MIT Division of Health Sciences and Technology, Massachusetts Institute of Technology, February 2013. [Online]. Available: http://hdl.handle.net/1721.1/79251

[53] J. Wang, L. He, H. Zheng, and Z. L. Lu, "Optimizing the magnetization-prepared rapid gradient-echo (MP-RAGE) sequence," *PLoS ONE*, vol. 9, no. 5, p. e96899, 2014.

[54] J. V. Hajnal, D. J. Bryant, L. Kasuboski, P. M. Pattany, B. De Coene, P. D. Lewis, J. M. Pennock, A. Oatridge, I. R. Young, and G. M. Bydder, "Use of fluid attenuated inversion recovery (FLAIR) pulse sequences in MRI of the brain," *J Comput Assist Tomogr*, vol. 16, no. 6, pp. 841–844, 1992.

[55] K. H. Klages, J. and, "Section 3.39 - nuclear magnetic resonance in drug discovery," in *Comprehensive Medicinal Chemistry*. Elsevier, 2007, pp. 901 – 920.

[56] J. Cavanagh, W. J. Fairbrother, A. G. Palmer, M. Rance, and N. J. Skelton, "Chapter 8 - experimental NMR relaxation methods," in *Protein NMR Spectroscopy*, second edition ed. Burlington: Academic Press, 2007, pp. 679 – 724.

[57] C. K. Jones, A. Huang, J. Xu, R. A. Edden, M. Schar, J. Hua, N. Oskolkov, D. Zaca, J. Zhou, M. T. McMahon, J. J. Pillai, and P. C. van Zijl, "Nuclear Overhauser enhancement (NOE) imaging in the human brain at 7T," *Neuroimage*, vol. 77, pp. 114–124, Aug 2013.

[58] N. McVicar, A. X. Li, D. F. Goncalves, M. Bellyou, S. O. Meakin, M. A. Prado, and R. Bartha, "Quantitative tissue pH measurement during cerebral ischemia using amine and amide concentration-independent detection (AACID) with MRI," *J. Cereb. Blood Flow Metab.*, vol. 34, no. 4, pp. 690–698, Apr 2014.

[59] M. Cuperlovic-Culf, "Chapter 3 - Experimental methodology," in *NMR Metabolomics in Cancer Research*. Woodhead Publishing, 2013, pp. 139 – 213.

[60] A. X. Li, R. H. Hudson, J. W. Barrett, C. K. Jones, S. H. Pasternak, and R. Bartha, "Four-pool modeling of proton exchange processes in biological systems in the presence of MRI-paramagnetic chemical exchange saturation transfer (PARACEST) agents," *Magn Reson Med*, vol. 60, no. 5, pp. 1197–1206, Nov 2008.

[61] D. E. Woessner, S. Zhang, M. E. Merritt, and A. D. Sherry, "Numerical solution of the Bloch equations provides insights into the optimum design of PARACEST agents for MRI," *Magn Reson Med*, vol. 53, no. 4, pp. 790–799, Apr 2005.

[62] M. A. Chappell, M. J. Donahue, Y. K. Tee, A. A. Khrapitchev, N. R. Sibson, P. Jezzard, and S. J. Payne, "Quantitative Bayesian model-based analysis of amide proton transfer MRI," *Magn Reson Med*, vol. 70, no. 2, pp. 556–567, Aug 2013.

[63] Y. Msayib, G. W. J. Harston, Y. K. Tee, N. P. Blockley, T. W. Okell, S. Payne, P. Jezzard, J. Kennedy, , and M. A. Chappell, "Assessing the suitability of common NOE modelling approximations in quantitative imaging of hyperacute stroke.

ESMRMB 2015, 32nd Annual Scientific Meeting," *Magnetic Resonance Materials in Physics, Biology and Medicine*, vol. 28, no. 442, pp. 277–418, Oct 1–3 2015.

[64] Y. K. Tee, A. A. Khrapitchev, N. R. Sibson, S. J. Payne, and M. A. Chappell, "Evaluating the use of a continuous approximation for model-based quantification of pulsed chemical exchange saturation transfer (CEST)," *J. Magn. Reson.*, vol. 222, pp. 88–95, Sep 2012.

[65] T. Jin, J. Autio, T. Obata, and S.-G. Kim, "Spin-locking versus chemical exchange saturation transfer mri for investigating chemical exchange process between water and labile metabolite protons," *Magn Reson Med*, vol. 65, no. 5, pp. 1448–1460, 2011.

[66] X. Song, A. A. Gilad, S. Joel, G. Liu, A. Bar-Shir, Y. Liang, M. Gorelik, J. J. Pekar, P. C. M. van Zijl, J. W. M. Bulte, and M. T. McMahon, "Cest phase mapping using a length and offset varied saturation (lovars) scheme," *Magn Reson Med*, vol. 68, no. 4, pp. 1074–1086, 2012.

[67] J. S. Lee, R. R. Regatte, and A. Jerschow, "Isolating chemical exchange saturation transfer contrast from magnetization transfer asymmetry under two-frequency rf irradiation," *J. Magn. Reson.*, vol. 215, pp. 56–63, Feb 2012.

[68] Z. Zu, E. A. Louie, E. C. Lin, X. Jiang, M. D. Does, J. C. Gore, and D. F. Gochberg, "Chemical exchange rotation transfer imaging of intermediate-exchanging amines at 2 ppm," *NMR Biomed*, vol. 30, no. 10, 2017.

[69] N. N. Yadav, C. K. Jones, J. Hua, J. Xu, and P. C. M. van Zijl, "Imaging of endogenous exchangeable proton signals in the human brain using frequency labeled exchange transfer imaging," *Magn Reson Med*, vol. 69, no. 4, pp. 966–973, 2013.

[70] J. Xu, N. N. Yadav, A. Bar-Shir, C. K. Jones, K. W. Chan, J. Zhang, P. Walczak, M. T. McMahon, and P. C. van Zijl, "Variable delay multi-pulse train for fast chemical exchange saturation transfer and relayed-nuclear overhauser enhancement MRI," *Magn Reson Med*, vol. 71, no. 5, pp. 1798–1812, May 2014.

[71] K. Yan, Z. Fu, C. Yang, K. Zhang, S. Jiang, D. H. Lee, H. Y. Heo, Y. Zhang, R. N. Cole, J. E. Van Eyk, and J. Zhou, "Assessing Amide Proton Transfer (APT) MRI Contrast Origins in 9 L Gliosarcoma in the Rat Brain Using Proteomic Analysis," *Mol Imaging Biol*, vol. 17, no. 4, pp. 479–487, Aug 2015.

[72] T. Jin, P. Wang, X. Zong, and S. G. Kim, "MR imaging of the amide-proton transfer effect and the pH-insensitive nuclear overhauser effect at 9.4 T," *Magn Reson Med*, vol. 69, no. 3, pp. 760–770, Mar 2013.

[73] F. Kogan, M. Haris, A. Singh, K. Cai, C. Debrosse, R. P. Nanga, H. Hariharan, and R. Reddy, "Method for high-resolution imaging of creatine in vivo using chemical exchange saturation transfer," *Magn Reson Med*, vol. 71, no. 1, pp. 164–172, Jan 2014.

[74] J. Zhou, X. Hong, X. Zhao, J. H. Gao, and J. Yuan, "APT-weighted and NOE-weighted image contrasts in glioma with different RF saturation powers based on magnetization transfer ratio asymmetry analyses," *Magn Reson Med*, vol. 70, no. 2, pp. 320–327, Aug 2013.

[75] S. Saito, Y. Mori, N. Tanki, Y. Yoshioka, and K. Murase, "Factors affecting the chemical exchange saturation transfer of Creatine as assessed by 11.7 T MRI," *Radiol Phys Technol*, vol. 8, no. 1, pp. 146–152, Jan 2015.

[76] A. Singh, M. Haris, K. Cai, H. Hariharan, and R. Reddy, "Chemical exchange transfer imaging of creatine," *Proc. Intl. Soc. Mag. Reson. Med.*, 2011.

[77] K. L. Desmond, F. Moosvi, and G. J. Stanisz, "Mapping of amide, amine, and aliphatic peaks in the CEST spectra of murine xenografts at 7 T," *Magn Reson Med*, vol. 71, no. 5, pp. 1841–1853, May 2014.

[78] K. J. Ray, J. R. Larkin, Y. K. Tee, A. A. Khrapitchev, G. Karunanithy, M. Barber, A. J. Baldwin, M. A. Chappell, and N. R. Sibson, "Determination of an optimally sensitive and specific chemical exchange saturation transfer MRI quantification metric in relevant biological phantoms," *NMR Biomed*, vol. 29, no. 11, pp. 1624–1633, Nov 2016.

[79] V. R. Sheth, G. Liu, Y. Li, and M. D. Pagel, "Improved pH measurements with a single PARACEST MRI contrast agent," *Contrast Media Mol Imaging*, vol. 7, no. 1, pp. 26–34, 2012.

[80] X.-Y. Zhang, F. Wang, T. Jin, J. Xu, J. Xie, D. F. Gochberg, J. C. Gore, and Z. Zu, "Mr imaging of a novel NOE-mediated magnetization transfer with water in rat brain at 9.4T," *Magn Reson Med*, vol. 78, no. 2, pp. 588–597, 2017.

[81] X. Y. Zhang, F. Wang, A. Afzal, J. Xu, J. C. Gore, D. F. Gochberg, and Z. Zu, "A new NOE-mediated MT signal at around -1.6ppm for detecting ischemic stroke in rat brain," *Magn Reson Imaging*, vol. 34, no. 8, pp. 1100–1106, Oct 2016.

[82] J. Lu, J. Zhou, C. Cai, S. Cai, and Z. Chen, "Observation of true and pseudo NOE signals using CEST-MRI and CEST-MRS sequences with and without lipid suppression," *Magn Reson Med*, vol. 73, no. 4, pp. 1615–1622, Apr 2015.

[83] E. Terreno, J. Stancanello, D. Longo, D. D. Castelli, L. Milone, H. M. Sanders, M. B. Kok, F. Uggeri, and S. Aime, "Methods for an improved detection of the MRI-CEST effect," *Contrast Media Mol Imaging*, vol. 4, no. 5, pp. 237–247, 2009.

[84] M. Zaiss, J. Xu, S. Goerke, I. S. Khan, R. J. Singer, J. C. Gore, D. F. Gochberg, and P. Bachert, "Inverse Z-spectrum analysis for spillover-, MT-, and T1 -corrected steady-state pulsed CEST-MRI–application to pH-weighted MRI of acute stroke," *NMR Biomed*, vol. 27, no. 3, pp. 240–252, Mar 2014.

[85] M. Zaiss and P. Bachert, "Exchange-dependent relaxation in the rotating frame for slow and intermediate exchange – modeling off-resonant spin-lock and chemical exchange saturation transfer," *NMR Biomed*, vol. 26, no. 5, pp. 507–518, May 2013.

[86] J. Xu, M. Zaiss, Z. Zu, H. Li, J. Xie, D. F. Gochberg, P. Bachert, and J. C. Gore, "On the origins of chemical exchange saturation transfer (CEST) contrast in tumors at 9.4 T," *NMR Biomed*, vol. 27, no. 4, pp. 406–416, Apr 2014.

[87] C. K. Jones, D. Polders, J. Hua, H. Zhu, H. J. Hoogduin, J. Zhou, P. Luijten, and P. C. van Zijl, "In vivo three-dimensional whole-brain pulsed steady-state chemical exchange saturation transfer at 7 T," *Magn Reson Med*, vol. 67, no. 6, pp. 1579–1589, Jun 2012.

[88] C. K. Jones, A. J. Huang, and P. C. van Zijl, "Exchange-relayed nuclear overhauser effect MRI," *Proc. Intl. Soc. Mag. Reson. Med.*, vol. 19, no. 2735, 2011.

[89] C. Jones, D. Polders, J. Hua, H. Hoogduin, H. Zhu, J. Zhou, and P. van Zijl, "3D whole brain pulsed CEST acquisition at 7T," *Proc. Intl. Soc. Mag. Reson. Med.*, vol. 19, 2011.

[90] Y. K. Tee, G. W. Harston, N. Blockley, R. Frost, T. W. Okell, S. Thandeswaran, F. Sheerin, P. Jezzard, J. Kennedy, J. F. Payen, and M. Chappell, "Can nuclear overhauser enhancement mediated chemical exchange saturation transfer (NOE CEST) offer a new insight in acute stroke diagnosis?" *Proc. Intl. Soc. Mag. Reson. Med.*, 2015.

[91] G. Stanisz, A. Kecojevic, M. Bronskill, and R. Henkelman, "Characterizing white matter with magnetization transfer and T2," *Magn Reson Med*, vol. 42, no. 6, pp. 1128–1136, 1999.

[92] R. M. Henkelman, G. J. Stanisz, and S. J. Graham, "Magnetization transfer in MRI: a review," *NMR Biomed*, vol. 14, no. 2, pp. 57–64, Apr 2001.

[93] R. Grossman, J. Gomori, K. Ramer, F. Lexa, and M. Schnall, "Magnetization transfer: theory and clinical applications in neuroradiology." *Radiographics : a review publication of the Radiological Society of North America, Inc*, vol. 14, no. 2, pp. 279–290, 1994.

[94] M. Zaiss, P. Kunz, S. Goerke, A. Radbruch, and P. Bachert, "MR imaging of protein folding in vitro employing nuclear-Overhauser-mediated saturation transfer," *NMR Biomed*, vol. 26, no. 12, pp. 1815–1822, Dec 2013.

[95] D. Paech, M. Zaiss, J. E. Meissner, J. Windschuh, B. Wiestler, P. Bachert, J. O. Neumann, P. Kickingereder, H. P. Schlemmer, W. Wick, A. M. Nagel, S. Heiland, M. E. Ladd, M. Bendszus, and A. Radbruch, "Nuclear overhauser enhancement mediated chemical exchange saturation transfer imaging at 7 Tesla in glioblastoma patients," *PLoS ONE*, vol. 9, no. 8, p. e104181, 2014.

[96] H. Y. Heo, Y. Zhang, D. H. Lee, X. Hong, and J. Zhou, "Quantitative assessment of amide proton transfer (APT) and nuclear overhauser enhancement (NOE) imaging with extrapolated semi-solid magnetization transfer reference (EMR) signals: Application to a rat glioma model at 4.7 Tesla," *Magn Reson Med*, vol. 75, no. 1, pp. 137–149, Jan 2016.

[97] H. Y. Heo, Y. Zhang, S. Jiang, D. H. Lee, and J. Zhou, "Quantitative assessment of amide proton transfer (APT) and nuclear overhauser enhancement (NOE) imaging with extrapolated semisolid magnetization transfer reference (EMR) signals: II. Comparison of three EMR models and application to human brain glioma at 3 Tesla," *Magn Reson Med*, vol. 75, no. 4, pp. 1630–1639, Apr 2016.

[98] H. Y. Heo, C. K. Jones, J. Hua, N. Yadav, S. Agarwal, J. Zhou, P. C. van Zijl, and J. J. Pillai, "Whole-brain amide proton transfer (APT) and nuclear overhauser enhancement (NOE) imaging in glioma patients using low-power steady-state pulsed chemical exchange saturation transfer (CEST) imaging at 7T," *J Magn Reson Imaging*, vol. 44, no. 1, pp. 41–50, Jul 2016.

[99] Y. Msayib, G. W. J. Harston, Y. K. Tee, F. Sheerin, N. P. Blockley, T. W. Okell, P. Jezzard, S. Payne, J. Kennedy, and M. Chappell, "Repeatability study of APT CEST quantification techniques for identification of ischaemic penumbra in stroke," *Proc. Intl. Soc. Mag. Reson. Med.*, vol. 25, no. 3752, 2017.

[100] M. A. Chappell, T. W. Okell, and M. Jenkinson, *Short Introduction to MRI Physics for Neuroimaging*, one ed., ser. Oxford Neuroimaging Primers, M. Jenkinson and M. A. Chappell, Eds. Oxford University Press, 2017.

[101] T. Tourdias, V. Dousset, I. Sibon, E. Pele, P. Menegon, J. Asselineau, C. Pachai, F. Rouanet, P. Robinson, G. Chene, and J. M. Orgogozo, "Magnetization transfer imaging shows tissue abnormalities in the reversible penumbra," *Stroke*, vol. 38, no. 12, pp. 3165–3171, Dec 2007.

[102] M. A. Chappell, A. R. Groves, and M. W. Woolrich, "The FMRIB variational Bayes tutorial: Variational Bayesian inference for a non-linear forward model," FMRIB Centre, University of Oxford, Tech. Rep. TR08MC1, 2008.

[103] M. A. Chappell, A. R. Groves, B. Whitcher, and M. W. Woolrich, "Variational Bayesian inference for a nonlinear forward model," *Signal Processing, IEEE Transactions on*, vol. 57, no. 1, pp. 223–236, 2009.

[104] E. Liepinsh and G. Otting, "Proton exchange rates from amino acid side chains–implications for image contrast," *Magn Reson Med*, vol. 35, no. 1, pp. 30–42, Jan 1996.

[105] K. J. Ray, G. Karunanithy, A. Baldwin, M. A. Chappell, and N. R. Sibson, "Separation of intracellular and extracellular z-spectra by diffusionCEST," *Proc. Intl. Soc. Mag. Reson. Med.*, vol. 24, no. 0302, 2016.

[106] M. K. Bader and S. Palmer, "What's the "hyper" in hyperacute stroke? Strategies to improve outcomes in ischemic stroke patients presenting within 6 hours," *AACN Adv Crit Care*, vol. 17, no. 2, pp. 194–214, 2006.

[107] K. J. Ray, J. R. Larkin, B. A. Sutherland, G. W. Harston, A. Baldwin, A. M. Buchan, P. Jezzard, J. Kennedy, M. A. Chappell, , and N. R. Sibson, "Investigation into the origin of the APT MRI signal in ischemic stroke," *Proc. Intl. Soc. Mag. Reson. Med.*, vol. 25, no. 3739, 2017.

[108] J. S. O'Brien and E. L. Sampson, "Lipid composition of the normal human brain: gray matter, white matter, and myelin," *J. Lipid Res.*, vol. 6, no. 4, pp. 537–544, Oct 1965.

[109] X. Zhao, Z. Wen, F. Huang, S. Lu, X. Wang, S. Hu, D. Zu, and J. Zhou, "Saturation power dependence of amide proton transfer image contrasts in human brain tumors and strokes at 3 T," *Magn Reson Med*, vol. 66, no. 4, pp. 1033–1041, Oct 2011.

[110] S. Goerke, M. Zaiss, D. Longo, F. Garello, E. DiGregorio, J. Breitling, M. E. Ladd, and P. Bachert, "Cest signals of lipids," *Proc. Intl. Soc. Mag. Reson. Med.*, vol. 25, no. 0201, 2017.

[111] Y. K. Tee, B. Abidin, A. Khrapitchev, B. A. Sutherland, J. Larkin, K. J. Ray, G. W. Harston, A. M. Buchan, J. Kennedy, N. R. Sibson, and M. Chappell, "CEST and NOE signals in ischemic stroke at 9.4T evaluated using a lorentzian multi-pool analysis: a drop, an increase or no change?" *Proc. Intl. Soc. Mag. Reson. Med.*, vol. 25, no. 3782, 2017.

[112] J. Zhou and van Zijl P. C., "Chemical exchange saturation transfer imaging and spectroscopy," *Progress in Nuclear Magnetic Resonance Spectroscopy*, vol. 48, pp. 109–136, April 2006.

[113] Z. Zu, K. Li, V. A. Janve, M. D. Does, and D. F. Gochberg, "Optimizing pulsed-chemical exchange saturation transfer imaging sequences," *Magn Reson Med*, vol. 66, no. 4, pp. 1100–1108, Oct 2011.

[114] J. Hua, C. K. Jones, J. Blakeley, S. A. Smith, P. C. van Zijl, and J. Zhou, "Quantitative description of the asymmetry in magnetization transfer effects around the water resonance in the human brain," *Magn Reson Med*, vol. 58, no. 4, pp. 786–793, Oct 2007.

[115] J. H. Thomas and E. D. Wills, *Wills' Biochemical Basis of Medicine*, 2nd ed., B. Gillham, Ed. Butterworth & Co.Publishers Ltd., 1989.

[116] J. L. DeRuck, *White matter*, ser. Encyclopedia of the Neurological Sciences (Second Edition), Reference Module in Neuroscience and Biobehavioral Psychology. Elsevier, 2014, no. 759Ű762.

[117] X. Y. Zhang, J. Xie, J. Xu, H. Li, J. C. Gore, and Z. Zu, "A new MT signal at -1.6ppm via NOE-mediated saturation transfer." *Proc. Intl. Soc. Mag. Reson. Med.*, no. 23, p. 999, 2015.

[118] I. Y. Zhou, E. Wang, J. S. Cheung, X. Zhang, G. Fulci, and P. Z. Sun, "Quantitative chemical exchange saturation transfer (CEST) MRI of glioma using Image Downsampling Expedited Adaptive Least-squares (IDEAL) fitting," *Sci Rep*, vol. 7, no. 1, p. 84, 03 2017.

[119] G. Jia, R. Abaza, J. D. Williams, D. L. Zynger, J. Zhou, Z. K. Shah, M. Patel, S. Sammet, L. Wei, R. R. Bahnson, and M. V. Knopp, "Amide proton transfer MR

imaging of prostate cancer: a preliminary study," *J Magn Reson Imaging*, vol. 33, no. 3, pp. 647–654, Mar 2011.

[120] J. Zhou, E. Tryggestad, Z. Wen, B. Lal, T. Zhou, R. Grossman, S. Wang, K. Yan, D. X. Fu, E. Ford, B. Tyler, J. Blakeley, J. Laterra, and P. C. van Zijl, "Differentiation between glioma and radiation necrosis using molecular magnetic resonance imaging of endogenous proteins and peptides," *Nat. Med.*, vol. 17, no. 1, pp. 130–134, Jan 2011.

[121] S. Goerke, M. Zaiss, P. Kunz, K. D. Klika, J. D. Windschuh, A. Mogk, B. Bukau, M. E. Ladd, and P. Bachert, "Signature of protein unfolding in chemical exchange saturation transfer imaging," *NMR Biomed*, vol. 28, no. 7, pp. 906–913, Jul 2015.

[122] M. Zaiss, J. Windschuh, S. Goerke, D. Paech, J. E. Meissner, S. Burth, P. Kickingereder, W. Wick, M. Bendszus, H. P. Schlemmer, M. E. Ladd, P. Bachert, and A. Radbruch, "Downfield-NOE-suppressed amide-CEST-MRI at 7 Tesla provides a unique contrast in human glioblastoma," *Magn Reson Med*, Jan 2016.

[123] T. W. Okell, M. A. Chappell, M. E. Kelly, and P. Jezzard, "Cerebral blood flow quantification using vessel-encoded arterial spin labeling," *J. Cereb. Blood Flow Metab.*, vol. 33, no. 11, pp. 1716–1724, Nov 2013.

[124] Y. K. Tee, A. A. Khrapitchev, N. R. Sibson, S. J. Payne, and M. A. Chappell, "Optimal sampling schedule for chemical exchange saturation transfer," *Magn Reson Med*, vol. 70, no. 5, pp. 1251–1262, Nov 2013.

[125] S. M. Smith, M. Jenkinson, M. W. Woolrich, C. F. Beckmann, T. E. Behrens, H. Johansen-Berg, P. R. Bannister, M. De Luca, I. Drobnjak, D. E. Flitney, R. K. Niazy, J. Saunders, J. Vickers, Y. Zhang, N. De Stefano, J. M. Brady, and P. M. Matthews, "Advances in functional and structural MR image analysis and implementation as FSL," *Neuroimage*, vol. 23 Suppl 1, pp. S208–219, 2004.

[126] M. Jenkinson, C. F. Beckmann, T. E. Behrens, M. W. Woolrich, and S. M. Smith, "FSL," *Neuroimage*, vol. 62, no. 2, pp. 782–790, Aug 2012.

[127] M. W. Woolrich, S. Jbabdi, B. Patenaude, M. Chappell, S. Makni, T. Behrens, C. Beckmann, M. Jenkinson, and S. M. Smith, "Bayesian analysis of neuroimaging data in FSL," *Neuroimage*, vol. 45, no. 1 Suppl, pp. S173–186, Mar 2009.

[128] M. W. Woolrich, P. Chiarelli, D. Gallichan, J. Perthen, and T. T. Liu, "Bayesian inference of hemodynamic changes in functional arterial spin labeling data," *Magn Reson Med*, vol. 56, no. 4, pp. 891–906, Oct 2006.

[129] A. R. Groves, M. A. Chappell, and M. W. Woolrich, "Combined spatial and non-spatial prior for inference on MRI time-series," *Neuroimage*, vol. 45, no. 3, pp. 795–809, Apr 2009.

[130] G. W. J. Harston, D. Minks, F. Sheerin, S. J. Payne, M. Chappell, P. Jezzard, M. Jenkinson, and J. Kennedy, "Optimizing image registration and infarct definition in stroke research," *Annals of Clinical and Translational Neurology*, vol. 4, no. 3, pp. 166–174, 2017.

[131] M. Jenkinson, P. Bannister, M. Brady, and S. Smith, "Improved optimization for the robust and accurate linear registration and motion correction of brain images," *Neuroimage*, vol. 17, no. 2, pp. 825–841, Oct 2002.

[132] D. N. Greve and B. Fischl, "Accurate and robust brain image alignment using boundary-based registration," *Neuroimage*, vol. 48, no. 1, pp. 63–72, Oct 2009.

[133] S. M. Smith, "Fast robust automated brain extraction," *Hum Brain Mapp*, vol. 17, no. 3, pp. 143–155, Nov 2002.

[134] Y. Zhang, M. Brady, and S. Smith, "Segmentation of brain MR images through a hidden Markov random field model and the expectation-maximization algorithm," *IEEE Trans Med Imaging*, vol. 20, no. 1, pp. 45–57, Jan 2001.

[135] M. Haris, K. Cai, A. Singh, H. Hariharan, and R. Reddy, "In vivo mapping of brain myo-inositol," *NeuroImage*, vol. 54, no. 3, pp. 2079 – 2085, 2011.

[136] M. Kim, J. Gillen, B. A. Landman, J. Zhou, and P. C. van Zijl, "Water saturation shift referencing (WASSR) for chemical exchange saturation transfer (CEST) experiments," *Magn Reson Med*, vol. 61, no. 6, pp. 1441–1450, Jun 2009.

[137] W. Zhu, "P-values competition," *Journal of Sport and Health Science*, vol. 5, no. 1, pp. 77–79, March 2016.

[138] Y. Msayib, G. W. J. Harston, K. J. Ray, J. R. Larkin, B. A. Sutherland, F. Sheerin, N. P. Blockley, T. W. Okell, P. Jezzard, A. Baldwin, N. R. Sibson, J. Kennedy, and M. Chappell, "Downfield CEST signals of the ischaemic core in quantitative imaging of hyperacute stroke, ESMRMB 2017, 34th Annual Scientific Meeting," *Magnetic Resonance Materials in Physics, Biology and Medicine*, vol. 30, no. 447, Oct 2017.

[139] M. A. Chappell, A. R. Groves, B. J. MacIntosh, M. J. Donahue, P. Jezzard, and M. W. Woolrich, "Partial volume correction of multiple inversion time arterial spin labeling MRI data," *Magn Reson Med*, vol. 65, no. 4, pp. 1173–1183, Apr 2011.

[140] R. H. Hashemi, W. G. Bradley, and C. J. Listanti, *Magnetic Resonance Imaging: The Basics*, 3rd ed. Philadelphia, USA: Lippincott Williams & Wilkins, 2010.

[141] A. A. O. Carneiro, G. R. Vilela, D. B. d. Araujo, and O. Baffa, "MRI relaxometry: methods and applications," *Brazilian Journal of Physics*, vol. 36, pp. 9 – 15, 03 2006.

[142] J. G. Sled and G. B. Pike, "Quantitative imaging of magnetization transfer exchange and relaxation properties in vivo using MRI," *Magn Reson Med*, vol. 46, no. 5, pp. 923–931, Nov 2001.

[143] W. D. Rooney, G. Johnson, X. Li, E. R. Cohen, S. G. Kim, K. Ugurbil, and C. S. Springer, "Magnetic field and tissue dependencies of human brain longitudinal 1H2O relaxation in vivo," *Magn Reson Med*, vol. 57, no. 2, pp. 308–318, Feb 2007.

[144] J. P. Korb and R. G. Bryant, "Magnetic field dependence of proton spin-lattice relaxation times," *Magn Reson Med*, vol. 48, no. 1, pp. 21–26, Jul 2002.

[145] K. Nael, T. P. Trouard, S. R. Lafleur, E. A. Krupinski, N. Salamon, and C. S. Kidwell, "White matter ischemic changes in hyperacute ischemic stroke: voxel-based analysis using diffusion tensor imaging and MR perfusion," *Stroke*, vol. 46, no. 2, pp. 413–418, Feb 2015.

[146] Y. Wang, G. Liu, D. Hong, F. Chen, X. Ji, and G. Cao, "White matter injury in ischemic stroke," *Prog. Neurobiol.*, vol. 141, pp. 45–60, 06 2016.

[147] M. P. Goldberg and B. R. Ransom, "New light on white matter," *Stroke*, vol. 34, no. 2, pp. 330–332, Feb 2003.

[148] V. P. Grover, M. M. Crossey, J. A. Fitzpatrick, B. K. Saxby, R. Shaw, A. D. Waldman, M. Y. Morgan, and S. D. Taylor-Robinson, "Quantitative magnetic resonance imaging in patients with cirrhosis: a cross-sectional study," *Metab Brain Dis*, vol. 31, no. 6, pp. 1315–1325, Dec 2016.

[149] M. E. Steenweg, N. I. Wolf, W. N. van Wieringen, F. Barkhof, M. S. van der Knaap, and P. J. Pouwels, "Quantitative MRI in hypomyelinating disorders: Correlation with motor handicap," *Neurology*, vol. 87, no. 8, pp. 752–758, Aug 2016.

[150] W. Jiang, I. Y. Zhou, L. Wen, X. Zhou, and P. Z. Sun, "A theoretical analysis of chemical exchange saturation transfer echo planar imaging (CEST-EPI) steady state solution and the CEST sensitivity efficiency-based optimization approach," *Contrast Media Mol Imaging*, vol. 11, no. 5, pp. 415–423, Sep 2016.

[151] B. Quesson, E. Thiaudiere, C. Delalande, J. F. Chateil, C. T. Moonen, and P. Canioni, "Magnetization transfer imaging of rat brain under non-steady-state conditions. Contrast prediction using a binary spin-bath model and a super-lorentzian lineshape," *J. Magn. Reson.*, vol. 130, no. 2, pp. 321–328, Feb 1998.

[152] O. E. Mougin, R. C. Coxon, A. Pitiot, and P. A. Gowland, "Magnetization transfer phenomenon in the human brain at 7 T," *Neuroimage*, vol. 49, no. 1, pp. 272–281, Jan 2010.

[153] C. Morrison and R. M. Henkelman, "A model for magnetization transfer in tissues," *Magn Reson Med*, vol. 33, no. 4, pp. 475–482, Apr 1995.

[154] G. J. Stanisz, E. E. Odrobina, J. Pun, M. Escaravage, S. J. Graham, M. J. Bronskill, and R. M. Henkelman, "T1, T2 relaxation and magnetization transfer in tissue at 3T," *Magn Reson Med*, vol. 54, no. 3, pp. 507–512, Sep 2005.

[155] M. Zaiss, B. Schmitt, and P. Bachert, "Quantitative separation of CEST effect from magnetization transfer and spillover effects by Lorentzian-line-fit analysis of z-spectra," *J. Magn. Reson.*, vol. 211, no. 2, pp. 149–155, Aug 2011.

[156] T. V. Perneger, "What's wrong with Bonferroni adjustments," *BMJ*, vol. 316, no. 7139, pp. 1236–1238, Apr 1998.

[157] G. W. J. Harston, D. Carone, Y. Msayib, A. Baldwin, M. A. Chappell, and J. Kennedy, "Identifying cerebral injury in acute stroke using metabolic imaging biomarkers," *National Institute for Health Research Stroke Research Workshop, Clare College, Cambridge*, September 2017.